Investigation of crystal field, magnetic frustration and magnetization reversal effects in $4f$ and $3d$ oxides

by

Abhijit Bhat Kademane

Thesis submitted in fulfillment of
the requirements for the degree of
PHILOSOPHIAE DOCTOR
(PhD)

University
of Stavanger

Faculty of Science and Technology
Department of Mathematics and Physics
2022

Abstract

This thesis deals with the investigation of single-ion excitations, magnetic frustration, and magnetization reversal phenomena. We have employed neutron scattering, μ^+SR, and computational methods for these studies.

Inverse spinel oxide Co_2VO_4 belongs to the family of spinel vanadates where cobalt and vanadium ions occupy the spinel B-site equally. This system exhibits magnetization reversal for temperatures below 65 K. Magnetization studies reveal three anomalies involving collinear and non-collinear ferrimagnetism phase and magnetization reversal crossover. Neutron diffraction analysis of Co_2VO_4 unveils that the evolution of relative balance between the two sublattice moments leads to ferrimagnetic phase and magnetization reversal. DFT calculation and μ^+SR results suggest delocalization -localization crossover as the underlying microscopic mechanism for magnetization reversal.

Rare earth oxide $SrTm_2O_4$ belongs to the family of $SrLn_2O_4$ where two inequivalent Tm^{3+}s form two zig-zag chains along the orthorhombic c-axis. An earlier study on $SrTm_2O_4$ reports the absence of long- or short-range order down to 65 mK. The crystal fields and exchange interactions in $SrTm_2O_4$ were studied to examine the absence of order. The crystal fields in $SrTm_2O_4$ were modeled using DFT and the effective charge (EC) model. The EC model describes the system well and suggests $|J, m_J\rangle = |6, 0\rangle$ dominates the ground state of both Tm^{3+} s. The exchange interactions extracted from low-energy dispersing excitations using random phase approximation suggest that Tm2 chains are frustrated and Tm1 chains could form dimers. The critical ratio calculated from exchange interaction indicates $SrTm_2O_4$ cannot undergo a thermal second-order phase transition confirming the absence of order. μ^+SR results show oscillations in polarization evolution spectra; these are typically

associated with muon precession due to the system's long-range order. Modeling precession frequency vs. temperature reveals that these oscillations originate due to nuclear hyperfine enhancement. Additionally, the magnetic field application induces long-range order, with Tm2 function as polarized paramagnet whereas Tm1 above $4\,\mathrm{T}$ transitions into XY-AFM phase.

In memory of Dr. K. S. Umesh

Acknowledgements

This journey between 2017-2022 was most memorable, at times filled with self-doubt and, other times, an eye-opening experience, overall filled with incredible life-changing experiences. This journey would not have been possible without exceptional co-travelers and people from the past.

First of all, I would like to acknowledge my Ph.D. advisor Diana Lucia Quintero Castro, for giving me a fantastic opportunity to work on this project and introducing me to neutron scattering. She has been my only point of contact at Stavanger for all my queries. She has patiently answered my questions and given me the freedom and support to try other techniques. She was gracious enough to join most beamline experiments and read my drafts despite her commitments. As a new group, we didn't have many facilities locally, but she ensured that I always found the right people who could help us with these measurements. Beyond the professional front, she has been a great mentor—also, thanks for inviting me to break bread with her family on several occasions. I have no words for her kindness.

I want to thank my co-supervisor, Rasmus Toft-Petersen. He has patiently answered all my naïve questions and encouraged me to focus on learning rather than running behind results. He has shown utmost patience towards my rookie mistakes and taught me the correct ways. Despite his busy schedule, he always found time for our weekly meetings and joined me at beamtime. I have learned much about science and beyond from our conversations during Berlin, Grenoble, and Copenhagen trips.

I thank all the collaborators who have helped me during my Ph.D. studies. First of all, thanks to David Vaknin, Churna Bhandari, and Durga Paudyal. I have learned a lot from our meetings between July-November 2021, where they spent many hours with me working on the manuscript. I am grateful to Konrad Siemensmeyer and

x

Table of Contents

1   Introduction to Thesis

Condensed matter systems offer fertile ground to observe multiple complex phenomena. Complex physics emerges in these systems due to the correlation between various system constituents. In the late '60s, Phil Anderson, in his seminal article "*More is different*" highlighted that the behavior of assemblies of interacting entities cannot be explained as a simple extrapolation of the behavior of individual constituents [1]. The article significantly established the importance and usefulness of fundamental research in condensed matter, especially in strongly correlated systems. Ever-since, the publication has been the guiding light for studying complex phenomena in condensed matter systems.

Magnetism in condensed matter is one of the oldest scientific fields, which is growing at a rapid phase due to its scientific precedence and technological relevance. Magnetism has been at the forefront of technological advances since time immemorial. In recent years, it has spearheaded the quantum revolution with promising ideas such as spintronics and multiferroicity. There are other fresh concepts, such as orbitonics with potential technological realization. The magnetic condensed matter systems provide a perfect breeding ground for unusual physics on the scientific front aswell. These systems have a variety of geometry, dimensionality, anisotropies, and strength and signs of interactions that can compete to evolve into exotic behavior such as magnetic frustration. Apart from exotic behaviors, many classical aspects such as orbital ordering have not been fully understood yet. Here I have taken two such systems belonging to $3d$ and $4f$ oxide families to understand their unique physics.

This thesis presents magnetism aspects of $3d$ and $4f$ oxide, Co_2VO_4 and $SrTm_2O_4$. The **Co_2VO_4** belongs to the family of spinel vanadates where the vanadium and cobalt ions share the spinel B-site. The magnetism of this system was the very first time reported by Menyuk *et al.* back in 1960 [2]. Menyuk and his coworkers observed an anoma-

1

lous magnetization behavior where the magnetization changed its sign (magnetization reversal) while cooling the sample. We probed this system with modern tools and methodologies to get a deeper insight into the question, **Why does Co_2VO_4 undergo magnetization reversal?**

The **$SrTm_2O_4$** belongs to family of rare-earth oxides $SrLn_2O_4$. Karundasa and coworkers synthesized members of this family and studied their magnetic behavior for the first time [3]. They discovered that this family hosts interesting physics due to various competing interactions arising from the unique geometric arrangement of atoms. The $SrTm_2O_4$ was previously studied by Haifeng Li *et al*. [4], where they found that $SrTm_2O_4$ did not show either long or short-range order down to 65 mK. Interestingly, within $SrLn_2O_4$ family, it was only $SrTm_2O_4$ that did not show any order. So, we decided to find the answer to the question, **Why does $SrTm_2O_4$ not order?**

Here I have prepared a compilation thesis based on the publications produced from the research work performed during the last four years. We have used neutron scattering, polarized muon spectroscopy, density functional theory calculation, and thermodynamic measurements to probe the magnetism in these systems. The thesis is structured as follows,

Chapter 2 provides an introduction to the theory of magnetism. Primary interactions such as single-ion, two-ion, and nuclear magnetism are discussed briefly in the first part. The introduction to magnetism is followed by a brief account of magnetization reversal, singlet magnetism, and magnetic frustration.

Chapter 3 describes the primary methods used in the thesis. The chapter consists of a description of neutron scattering, neutron instrumentation, muon spin relaxation, and density functional theory.

Chapter 4 is the cover chapter to article '*Magnetization reversal driven by electron localization-delocalization crossover in the inverse spinel Co_2VO_4*'. This chapter summarizes the article and provides a detailed

account of magnetic structure determination from neutron powder diffraction data. Additionally, results such as hysteresis curves, heat capacity, and AC-susceptibility are presented.

Chapter 5 is the cover chapter to article '*Crystal field effects in the zig-zag chain compound SrTm$_2$O$_4$*'. This chapter summarizes the article and provides a detailed account of crystal field determination using Wannier functions. Additionally, a brief description of the DFT+μ method used to determine the muon stopping site is provided.

Chapter 6 describes diffused scattering results, modeling and implication of dispersing excitation, critical ratio, nuclear hyperfine enhancement, and magnetic field induced order in SrTm$_2$O$_4$. This chapter covers the unpublished results from SrTm$_2$O$_4$. Additionally, in the beginning of the chapter brief description of methods is provided.

Last chapter (Chapter 7) summarizes entire thesis.

I would like to bring it to attention of the reader that, the thesis follows natural flow of research progression.

2 Theoretical Background

2.1 Single-ion Magnetism

2.1.1 Free-ion Magnetism

Magnetism is a pure quantum mechanical property that emerges due to the intrinsic angular momentum of the electrons from unfilled shells. These electrons possess spin '$s = \frac{1}{2}$' and orbital angular momentum 'l,' and additionally the total angular momentum 'j' given by the sum of spin and orbital angular momentum, as shown in Figure 2.1(a).

Consequently, the spin and the orbital and total angular momentum have magnetic moments given respectively as follows:

$$\mu_s = -g_s \cdot \mu_B \cdot s, \quad \mu_l = -\mu_B \cdot l, \quad \& \quad \mu_j = \mu_s + \mu_l. \tag{2.1}$$

Here, μ_B is the Bohr magneton given by $\mu_B = \frac{e\hbar}{2m_e}$ and g_s is the gyromagnetic ratio ≈ 2. The absolute value μ_j is given by $\left|\mu_j\right| = g_j \cdot \mu_B \sqrt{j(j+1)}$, where g_j is a Landé **g** factor.

As shown in Figure 2.1 (a), spin and orbital angular momentum are vector quantities whose respective magnetic moments point in opposite directions. However, the total angular momentum j is not parallel to the associated magnetic moments μ_j, as the spin and orbital magnetic moments have a different coefficient of proportionality to the respective angular momentum.

In the case of atoms with multiple electrons in the unfilled shells, their collective total angular momentum 'J' can be calculated by vector addition. The vector addition of spin and orbital angular momentum can be performed in two different ways, depending on the strengths of the spin-orbit coupling. The energy of the coupling is given by '$\xi s \cdot l$' where ξ is the spin-orbit coupling constant. When the spin-orbit cou-

5
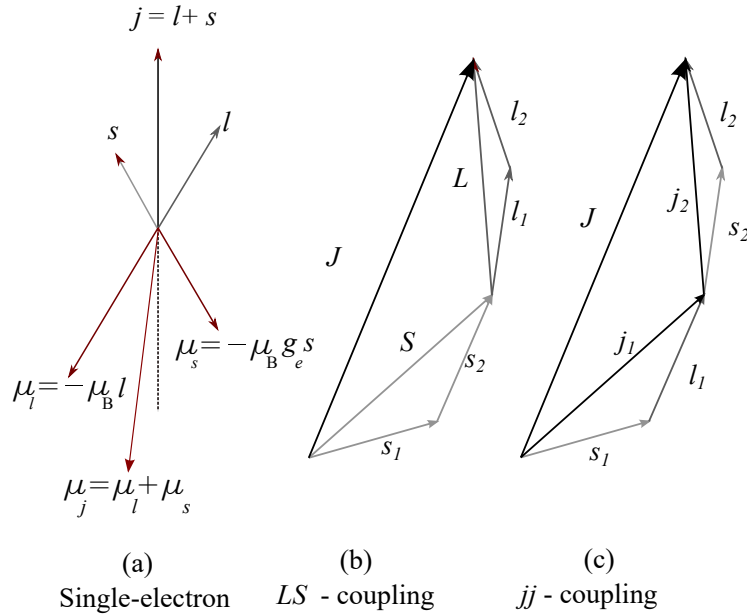
Figure 2.1: Vector model of the electron total, the spin, and the orbital and angular momentum and the magnetic moments associated with them. (b) Vector model of the total electron angular momentum within *LS* coupling approach and (c) *jj*-coupling approach.

pling is weak, the *J* is given by $J = S + L$, where $S = \sum_i s_i \quad L = \sum_i l_i$ (Fig. 2.1(b)). This treatment is called *LS*- or *Russell - Saunders* coupling. On the other hand, when the spin-orbit coupling is strong, the total angular momentum should be calculated as a sum of the total angular momentum of all individual electrons. This treatment is called the *j - j -* coupling scheme (Fig. 2.1(c)).

In the absence of spin-orbit coupling, multiple electronic states degenerate. However, in the presence of spin-orbit coupling, this degeneracy gets lifted. The total angular momentum *J* can take values from $|L - S|$ to $L + S$, depending on the electronic state. Therefore, the electronic ground state needs to be determined to describe the single-ion magnetism. The electronic ground state or ground state multiplet is predicted by applying the following rules sequentially:

1. Maximize the total spin angular momentum S.

2. Maximize the total orbital angular momentum L.

3. The total angular momentum J depends on the filling of the shell. For less than half-filled shell, $J = |L - S|$ and otherwise $J = L + S$.

These empirical rules are called 'Hund's rules'. The first and second rules aim at reducing the Coulomb energy, while the third rule minimizes the energy of the spin-orbit coupling [5]. The multiplets are usually represented by so-called *'term symbols'*, which are given by $^{2S+1}L_J$. In Table 2.1 Hund's rule has been applied to the magnetic ions relevant to this thesis to identify the ground state multiplets under spin-orbit coupling.

$l = 2, m_l =$	-2	-1	0	1	2	S	L	J	$^{2S+1}L_J$
V^{4+} $3d^1$	↓					$\frac{1}{2}$	2	$\frac{3}{2}$	$^2D_{\frac{3}{2}}$
Co^{2+} $3d^7$	↓↑	↓↑	↓	↓	↓	$\frac{3}{2}$	3	$\frac{9}{2}$	$^4F_{\frac{9}{2}}$

$l = 3, m_l =$	-3	-2	-1	0	1	2	3	S	L	J	$^{2S+1}L_J$
Tm^{3+} $4f^{12}$	↓↑	↓↑	↓↑	↓↑	↓↑	↓	↓	1	5	6	$^3H_6$

Table 2.1: Application of Hund's rule on V^{4+}, Co^{2+}, & Tm^{3+}, to determine the respective ground state multiplet.

2.1.2 Crystalline Electric Fields

When a magnetic ion is placed in a crystalline environment, the energy profile of electronic states changes drastically. The isolated magnetic ion discussed earlier has spherical symmetry. However, the spherical symmetry is violated when the atom is in a crystalline environment. The violation of the spherical symmetry leads to the lifting of multiplet degeneracy. Such splitting of the multiplet caused by the local crystalline environment is called *'crystal field splitting'*. The corresponding

site symmetry determines the type of splitting and the character of the corresponding levels.

The coulomb energy due to electron-electron interaction, spin-orbit coupling energy, and crystal field energy, depending on their strengths, define the multiplet structure of d and f group elements [5]. Thus, understanding the crystal fields is the first step to understanding magnetism in these systems.

The crystal field splitting can be modeled using the following parameterized Hamiltonian:

$$\mathcal{H} = \sum_{k,q} B_q^{(k)} O_q^{(k)} \tag{2.2}$$

Where $B_q^{(k)}$ are the crystal field parameters in so called Stevens normalization, and $O_q^{(k)}$ the Stevens operators [6]. The Stevens operators are represented in (J_x, J_y, J_z) coordinates, and the definition of these operators can be found in Refs. [7, 8]. Here, the task is to determine the $B_q^{(k)}$ parameters. The site symmetry of the magnetic ion limits the number of parameters by retaining only invariant parameters under the site symmetry. The $B_q^{(k)}$ parameters retained by various point group symmetries can be found in Ref. [7] (in Table 7). The Hamiltonian in Eq. 2.2 can be either determined by adjusting these parameters to observable quantities (experimentally) or can be theoretically modeled from first principles.

The method where the $B_q^{(k)}$ are adjusted with respect to the experimental observables is referred to as the '*Stevens operator*' approach. The Stevens operator approach is very successful in describing the $B_q^{(k)}$s of the magnetic ion with high site symmetry. However, this procedure yields degenerate sets of parameters for systems involving low symmetry [9]. On the other hand, theoretical methods can overcome the overparameterization problem in the Stevens operator approach. In the simplest scenario, it is sufficient to consider a model where the electric

field due to the *point charge* environment surrounding the ion is governed by the site symmetry [10]. This model proposed by Hutchings is called as '*Point charge*' model(or Electrostatic point charge model) [10]. A similar approach was earlier proposed by Bethe in '20s [11]. This crystal field model ignores any overlap between the charge cloud on the magnetic ion and the surroundings. Additionally, this model can be used in conjunction with experimentally observable quantities to optimize the charge position to arrive at the best set of $B_q^{(k)}$. However, point charge model fails to account for covalent bonding with the ligands and the finite extent of charges on the ions [10].

Some exciting improvements have been made to the electrostatic point charge model to account for covalency. The *Effective charge model* tries to mimic covalent effects by changing both the position and the magnitude of the charges [12, 13]. This model can be optimized by considering an effective point charge with adjustable charge amount and distance to the metal ion with respect to experimental observables [14]. Uldry *et al.*'s improvisation of the point charge model with intermediate coupling considerations and limited parameters is another successful modification to the point charge model [15]. There are other successful models also for these problems, such as Malkin's *Exchange charge* model [16] which is reasonably successful in the case of systems involving $4f$ electrons.

There are purely *ab initio* methods apart from phenomenological models such as point charge model. One such prominent model uses the Wannier functions constructed from density functional theory (DFT) based on electronic structure calculations, to represent atomic-like orbitals within a periodic crystal [17–20]. The Wannier functions thus constructed incorporate all the effects of crystal potential [20]. This method has been used quite successfully in the case of many rare-earth oxides [19, 21].

9

2.1.3 Energy Scales and Coupling

In the calculation of multiplet splitting, it is crucial to account for Coulomb term ($\mathcal{H}_{ee}$), spin-orbit term ($\mathcal{H}_{SO}$), and crystal field ($\mathcal{H}_{CF}$) term, depending on their strengths.

In the case of *Russell - Saunders* coupling the Coulomb term dominates, while the spin-orbit term is weaker than Coulomb term and stronger than the crystal field term i.e., $\mathcal{H}_{ee} \gg \mathcal{H}_{SO} \gg \mathcal{H}_{CF}$. In this case the crystal field term is treated as a small perturbation and only the lowest energy multiplet is considered. Consequently, the Stevens normalization for crystal field term expressed in equation 2.2 is relevant for this situation [22]. On the other hand, with *j-j* coupling the spin-orbit interaction dominates $\mathcal{H}_{SO} \gg \mathcal{H}_{ee}$, and thus there is no multiplet structure. In this case only J is used to label the states [7].

When Coulomb, spin-orbit, and the crystal field terms are of similar strengths ($\mathcal{H}_{ee} \approx \mathcal{H}_{SO} \approx \mathcal{H}_{CF}$) *Intermediate coupling* scheme can be implemented [5]. In this scheme, higher multiplets are considered in addition to the ground state multiplet. If the crystal field interaction is relatively weak, multiplet structure remains but the eigenstates end-up being a mixture of *LS*-states (due to the SO interaction), with only J distinguish the states. When crystal field interaction is large, J-mixing can occur, resulting in the loss of a distinct multiplet structure [7]. In intermediate coupling scheme, Stevens normalization breaks down [22] and so called Wybourne normalization [23] of the crystal field Hamiltonian must be used.

2.1.4 Magnetism in $3d$ and $4f$ Systems

Magnetism in both $3d$ (transition metals, along with $4d$ & $5d$) and $4f$ (rare-earth elements) arises due to unpaired electrons. However, the main distinction comes from the position of $3d$ and $4f$ orbitals. In transition metals, the $3d$ orbital is the outermost, and the orbital momentum is often quenched. On the other hand, $4f$ orbitals are deep inside, filled $5s$ and $5p$. Thus the $4f$ electrons are more strongly lo-

calized close to the atomic core. Additionally, an anisotropic $4f$ orbital results in highly anisotropic magnetic properties in these systems [24].

Another important distinction between $3d$ and $4f$ systems is that in the case of $4f$ systems the crystal field splitting is much weaker compared to spin-orbit splitting, while in the $3d$ system crystal field splitting is stronger [8].

2.2 Two-ion Interactions

The crystal fields, along with spin-orbit and Coulomb interaction, can be considered as *single-ion* interactions as they are unaffected by the magnetic state of neighboring ions. On the other hand, the *two-ion* interactions couple the electrons clouds between two magnetic ions.

2.2.1 Magnetic Exchange Interaction

The exchange interaction is electrostatic force between two neighboring spins, arising as a consequence of Pauli's exclusion principle [25]. The Pauli's exclusion principle states that the exchange interaction in case of three dimensional spins is given by the Heisenberg Hamiltonian as follows:

$$\mathcal{H}_{ex} = -\frac{1}{2} \sum_{ij} \mathcal{J}(ij)\mathbf{S}_i\mathbf{S}_j, \tag{2.3}$$

where '$\mathcal{J}$' is the coupling constant. If $\mathcal{J} > 0$, the energy is minimized by a parallel angular momentum configuration, and such arrangement is called ferromagnetic. On the other hand, when $\mathcal{J} < 0$, energy is minimized by an anti-parallel angular momentum configuration, and such arrangement is called antiferromagnetic. Additionally, the exchange interaction between two angular momentum operators can happen due to different mechanisms. In this regard, the exchange interactions are divided into direct, indirect, and a subset of indirect exchange called superexchange and itinerant exchange.

The exchange interaction between two neighboring magnetic atoms arising due to interaction between the respective electrons is called a *direct* exchange. Direct exchange seems most forthright way to establish interaction between neighboring spins. However, it is far more complicated. For example, in $4f$ systems, there is no direct overlap between neighboring $4f$ electron clouds due to their strong localization [25].

The *indirect* exchange in ionic solids is mediated by a non-magnetic ion between two non-adjacent magnetic ions. Such interactions are called *superexchange*. In metallic systems, a localized magnetic moment spin-polarizes a conduction electron which in turn polarizes adjacent localized moment at a distance 'r' from the first moment. This mechanism is called *itinerant exchange* or *RKKY interaction*. Direct and indirect exchange interactions are typically stronger than the magnetic dipole interactions discussed below.

Dzyaloshinskii—Moriya Interaction

Another important anisotropic interaction is the Dzyaloshinskii–Moriya interaction (DMI) [26]. This interaction originates from spin-orbit coupling and is expressed as follows:

$$\mathcal{H}_{DMI} = \mathbf{D}_{\alpha\beta}^{\mathrm{DM}} \cdot \left(\mathbf{S}_\alpha \times \mathbf{S}_\beta \right), \qquad (2.4)$$

where the orientation of the $\mathbf{D}_{\alpha\beta}^{\mathrm{DM}}$ vector is directed by the crystal symmetry [26].

2.2.2 Magnetic Dipolar Interactions

Analogous to electric dipoles, magnetic moments can be considered equivalent to magnetic dipoles. Thus the interaction between two magnetic moments becomes one of the natural considerations among two-ion interactions [8]. This interaction is directly dependent on the moment size and the distance between the magnetic ions. The dipolar interaction is anisotropic, and the strength of the interaction is weak

compared to the exchange interaction. The dipole–dipole interaction is defined using the following Hamiltonian:

$$\mathcal{H}_{dd} = -\frac{1}{2} \sum_{ij} \left\{ \sum_{\alpha\beta} \mathbf{S}_i^\alpha \, \mathcal{J}_{\alpha\beta}^{\mathrm{D}}(ij) \mathbf{S}_j^\beta \right\} \tag{2.5}$$

where $\mathbf{S}_i^\alpha (\alpha = 1, 2, 3)$ are the three components of the angular momentum and $\mathcal{J}_{\alpha\beta}^{\mathrm{D}}(ij)$ the dipole interaction. The dipole interaction is given as follows:

$$\frac{\mathcal{J}_{\alpha\beta}^{\mathrm{D}}(ij)}{(g_J\mu_{\mathrm{B}})^2} = \frac{3\left(R_i^\alpha - R_j^\alpha\right)\left(R_i^\beta - R_j^\beta\right) - \delta_{\alpha\beta}\left|\mathbf{R}_i - \mathbf{R}_j\right|^2}{\left|\mathbf{R}_i - \mathbf{R}_j\right|^5} \tag{2.6}$$

Here, $\mathbf{R}_i$ denotes the lattice vector of the i th magnetic ion, g_J the Landé factor, and μ_{B} the Bohr magneton [27].

2.2.3 Magnetic Order and Magnetic Structures

At low temperatures, with minimum thermal fluctuations, interactions between sites result in long-ranged order. This order starts emerging through a phase transition at temperatures which in comparison with exchange interactions are relatively low. There are various ways this ordering can come about; ferromagnetic(↑↑), antiferromagnetic (↑↓), ferrimagnetic (↑ ↓), or non-collinear order (↖↗) such as helical structures [25]. As seen in atomic structures, the periodic arrangement of magnetic moments can be defined using wave-vector dependent exchange Hamiltonian. Assuming only one magnetic atom in the unit-cell, Fourier transformation of the real-space exchange Hamiltonian in equation 2.3 can be written as follows:

$$\mathcal{H} = -\frac{1}{2} \sum_k \mathcal{J}_k \mathbf{S}^k \cdot \mathbf{S}^{-k}, \tag{2.7}$$

where $\mathcal{J}_k$ and $\mathbf{S}^k$ are given by

$$\mathcal{J}_{\mathbf{k}} = N^{-1} \sum_{\mathbf{r}_i, \mathbf{r}_j} \mathcal{J}_{ij} \exp\left[i\mathbf{k} \cdot (\mathbf{r}_i - \mathbf{r}_j)\right]$$

$$\mathbf{S}^{\mathbf{k}} = N^{-1/2} \sum_{\mathbf{r}} \mathbf{S}_i \exp(i\mathbf{k} \cdot \mathbf{r}_i)$$

(2.8)

The minimum of $\mathcal{H}$ occurs at wavevector $\mathbf{k}$ that maximizes $\mathcal{J}_k$ [28]. The wavevector gives the periodicity of the magnetic structure. For a general $\mathbf{k}$, a helical order is stabilized, and for $\mathbf{k} = 0$, it is the ferromagnetic order [29].

Unlike the crystal structure, the symmetry governing the magnetic structure should involve both the positions and orientation of the magnetic moment. An addition symmetry operation is introduced to standard symmetry operations, called the 'time-reversal' operator. By combining spatial and time-reversal operators, for each non-magnetic crystallographic point group there can be 122 magnetic point groups (MPGs) [30]. Similarly, 1651 distinct magnetic space groups (MSGs) are identified. These magnetic space groups are known as *Shubnikov* or *Heesch* groups.

Additionally, the magnetic structure can be described based on the atomic unit cell in terms of basis vectors and propagation vectors [31]. This method depends on the basic principle that magnetic structures can be described by the periodic repetition of a magnetic unit cell. Here the magnetic unit cell is described based on the atomic unit cell. The 'propagation vector' $\mathbf{k}$ helps in describing the relationship between moment orientations of equivalent magnetic atoms in different atomic unit cells [32]. This idea can be illustrated for the moment distribution m_j associated with the atom j in the crystal unit cell with the lattice translation vector $\mathbf{t}$, as

$$\mathbf{m}_j = \sum_k \psi_j^{\mathbf{k}} e^{-2\pi i \mathbf{k} \cdot \mathbf{t}}$$

(2.9)

where $\psi_j^{\mathbf{k}}$ are the basis vectors (projections of the magnetic moment

along the crystallographic axes) corresponding to wave vector **k** in the first Brillouin zone of the crystal structure. Such magnetic structures can have multiple propagation vectors that can be commensurate or incommensurate with respect to the periodicity of the atomic unitcell. A detailed explanation of this method can be found in the article by Bertaut in Ref. [31].

2.3 Nuclear Magnetism

Analogous to an electron's magnetic moment, the nucleus has a magnetic moment resulting from the total angular momentum of the nucleus. The total angular momentum of the nucleus is called '*nuclear spin*'(I). The nuclear magnetic moment associated with nuclear spin is given by the following equation:

$$\mu_I = -g_I \cdot \mu_N \cdot \boldsymbol{I}, \tag{2.10}$$

where g_I are the nuclear g-factors and μ_N is the nuclear magneton; $\mu_N = \frac{e\hbar}{2m_p}$ (m_p= mass of proton). Since mass of proton is three orders of magnitude larger than the mass of electron, μ_N is three orders of magnitude smaller than μ_B. Consequently the nuclear magnetic moment is very small compared to the electron's magnetic moment [25].

Hyperfine Interaction

Inside an atom, nuclear moment and electron moment can interact magnetically. This interaction is very weak and is called '*hyperfine interaction*' [33]. The hyperfine interaction can arise due to μ_N sitting in a collective internal magnetic field '**B**$_{el}$' produced by μ_J of all electrons. This produces an energy term -$\mu_N \cdot$ **B**$_{el}$. Since **B**$_{el} \propto J$, the hyperfine interaction term can be written as follows:

$$\mathcal{H}_{HF} = A_J I \cdot J, \tag{2.11}$$

15

where A_J is a parameter that measures the strength of the hyperfine interaction [25].

In certain systems, with paramagnetic electronic ground state, magnetic field application can induce order (polarization). For such systems, the induced electronic order in turn induces an effective magnetic field at the nuclei due to the hyperfine interaction. This induced hyperfine field amplifies the effects of the applied field by at least two orders of magnitude [34].

2.4 Magnetization Reversal

Magnetization of a system can be defined as the sum of the magnetic moments of all its constituent atoms per unit volume [35]. The magnetization (M) is measured by applying a magnetic field (B) along a direction. In certain materials, the temperature dependence of magnetization was found to undergo a crossover from a positive to a negative value with respect to the applied magnetic field as in Figure 2.2. Such a phenomenon is termed '*magnetization reversal*' or negative magnetization.

Kumar *et al*. in their review on magnetization reversal [35] have identified five possible ways the magnetization reversal may come about.

1. Negative exchange coupling between two or more ferromagnetic sublattices.

2. Negative exchange coupling between canted antiferromagnetic sublattices.

3. Negative exchange coupling between ferromagnetic or canted-antiferromagnetic and paramagnetic sublattices.

4. Interfacial exchange coupling between ferromagnetic and antiferromagnetic phases.

5. Imbalance of spin and orbital moments.
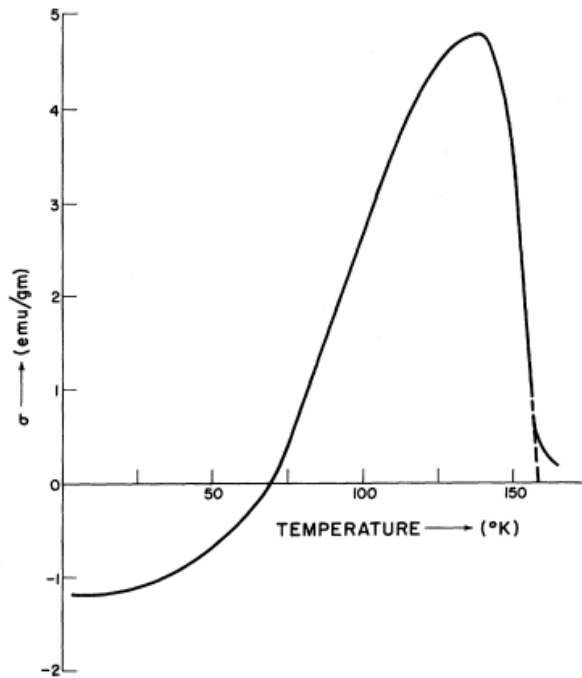
Figure 2.2: Temperature dependence of magnetization of Co_2VO_4 measured at 700 Oe. Reprinted from Ref. [2] with permission to reuse. License number: RNP/22/MAR/051376 © 1960, by the American Physical Society.

The most common condition is negative exchange coupling between ferromagnetic sublattices. Néel [36] proposed a phenomenological theory called '*molecular field theory*' to explain magnetic compensation in systems involving unequal ferromagnetic sublattice with negative exchange coupling. This treatment was found to be successful in explaining the magnetization reversal in many oxides [35].

2.5 Singlet Ground State Magnetism

The singlet state can be defined as a state with paired electrons. The nonmagnetic singlet ground state can happen due to many reasons.

Prominent among these is the crystal field splitting. In rare-earth ions with an even number of electrons ('non-Kramers ions'), the crystal-field-only ground state is often a singlet. In these systems, the crystal field completely removes the ground-state multiplet degeneracy by splitting the multiplet into (2J+1) singlets. Such systems order only if the exchange interaction energy is stronger than the crystal field energy. In these cases, the order does not occur through the process of alignment of permanent moments, but instead happens through a polarization instability of the crystal-field singlet ground state [37]. Note that in rare-earth systems, usually, the exchange interactions and crystal fields are of similar strengths. Thus the ratio of exchange to crystal field energy can reveal if these systems can order or not.

Alternatively, singlet state can emerge due to magnetic ions forming dimers. Here usually the ground-state is singlet and the first excited state is a triplet state. If $\mathcal{J}_{\text{Inter}}$ intradimer exchange is significantly smaller than the interdimer exchange $\mathcal{J}_{\text{Intra}}$, this system would remain nonmagnetic and can be treated as composed of singlet units (represented by an ellipse in Figure 2.3) [24].

In these systems, a magnetic ordering could be achieved if the dimer can be promoted to an excited state. This phenomenon can be realized with the application of magnetic fields. If a magnetic field 'B' were applied along the z-direction, the triplet state would undergo Zeeman splitting. For instance, in a system with a ground state singlet $|J = 0\rangle$ with the first excited triplet state $|J = 1\rangle$ separated by Δ, the $|J_z = \pm 1\rangle$ would split in applied magnetic field B. Here $|J_z = +1\rangle$ has energy of $E_{|J_z=+1\rangle} = \Delta - g_J \mu_B B$ and $E_{|J_z=-1\rangle} = \Delta + g_J \mu_B B$. We see that for the fields greater than $\Delta/g_J \mu_B, |J_z = +1\rangle$ would go below the singlet $|J = 0\rangle$. This would result in an abrupt transition to a fully polarized ordered state [24]. The earlier situation is very valid when the intradimer exchange is smaller than the interdimer exchange. However, there is always a finite interdimer interaction leading to dispersion of magnetic excitation [24]. In these situations, increasing the magnetic field would decrease the gap, and at critical field B_{c1} the gap is zero at
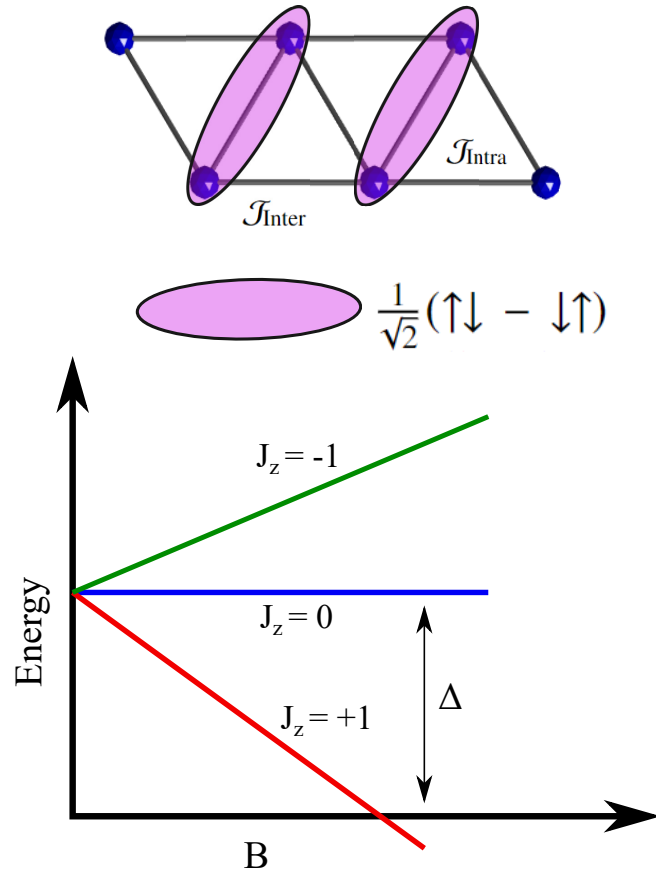
Figure 2.3: Dimerization in zig-zag chain systems with $\mathcal{J}_{\text{Inter}} < \mathcal{J}_{\text{Intra}}$. Here the ellipses represent a singlet unit of spins $\frac{1}{\sqrt{2}}(\uparrow\downarrow - \downarrow\uparrow)$. Magnetic field induced order in systems with singlet groundstate and triplet excited sate.

a certain wave vector Q. This would result in an ordered ground state (depending on the wave vector Q), as ferromagnetic, antiferromagnetic, or spiral structures [24].

2.6 Magnetic Frustration

As discussed earlier, the presence of two-ion interactions usually leads to long-range magnetic order. However, in some peculiar systems, there could be several equally possible microscopic configurations leading to a disordered ground state. One of the reasons for this situation could be competition between different interactions combined with special lattice geometry. If the system fails to order, unusual states as in 'spin-ice' might emerge [38]. However, these systems often try to reduce the entropy by unfolding several unconventional mechanisms. For instance, the system can stabilize the order by choosing an energy minimum governed by fluctuations; such a mechanism is referred to as 'order-by-disorder'[39]. Thus a system is considered '*frustrated*' if competition between different interactions in the system cannot be simultaneously satisfied.

For example, in a triangular lattice (Fig. 2.4(a)) with antiferromagnetic interaction, it is impossible to satisfy all the interactions simultaneously. Thus it is difficult to form an ordered state. Similarly, other possible geometries conducive to magnetic frustration are presented in Figures 2.4(b-d).

It is well known that at high temperatures the magnetic susceptibility of a system obeys the Curie–Weiss law, i.e., $\chi \propto [T - \theta_{\mathrm{CW}}]^{-1}$, where θ_{CW} is the Curie–Weiss temperature. Here the Curie–Weiss temperature represents the sum of all interactions involved. In an unfrustrated system, ordering temperature T_{N} is close to θ_{CW}. On the other hand, in frustrated systems ordering temperature is far smaller than the Curie–Weiss temperature, i.e., $\theta_{CW} \gg T_{\mathrm{N}}$, because in a frustrated case an ordered state (if realized at all) would gain only a small fraction of the exchange energy. Thus the parameter $f = \theta_{CW}/T_{\mathrm{N}}$ can be used for characterizing the degree of frustration. The ratio 'f' for unfrustrated systems is ~ 1 and for frustrated ones it is $f \gg 1$ [40]. A strongly frustrated system should have a large value of f and should behave as a normal paramagnet for $T > \theta_{CW}$. The system could be ordered for
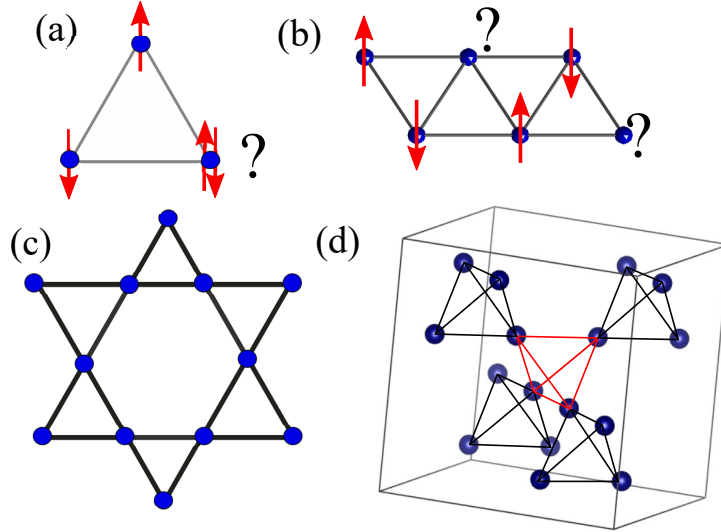
Figure 2.4: Magnetic frustration in different dimensionalities. (a) Triangular lattice with antiferromagnetic interactions where all interactions cannot be satisfied simultaneously. (b) Quasi-one-dimensional zig-zag chain. (c) Two-dimensional Kagome lattice. (d) Three dimensional pyrochlore lattice.

temperatures below T_N, whereas in the region $T_N < T < \theta_{CW}$ a short-range correlation might emerge. In this region, the system is referred to as a collective paramagnet [24].

Typically, frustrated magnets in applied magnetic fields show unique characteristics called 'magnetization plateau'. In a zig-zag lattice, as in Figure 2.4(b), the exchange interactions along the rungs and legs corresponding to $\mathcal{J}_1$ and $\mathcal{J}_2$ respectively are antiferromagnetic making it frustrated. This system can be visualized as a combination of adjacent triangles as in Figure 2.4(a). If the two corners are coupled antiferromagnetically, the third corner is frustrated (marked as '?'). If a small magnetic field 'B_{c1}' is applied to such a system, parallel to the ↑, the 'undecided' spin would point upwards. This emerges as a $\frac{1}{3}$ plateau on the M vs. B curve. On further increasing the field, the ↓ also points up, making the entire system ferromagnetic [24]. Such a plateau is often
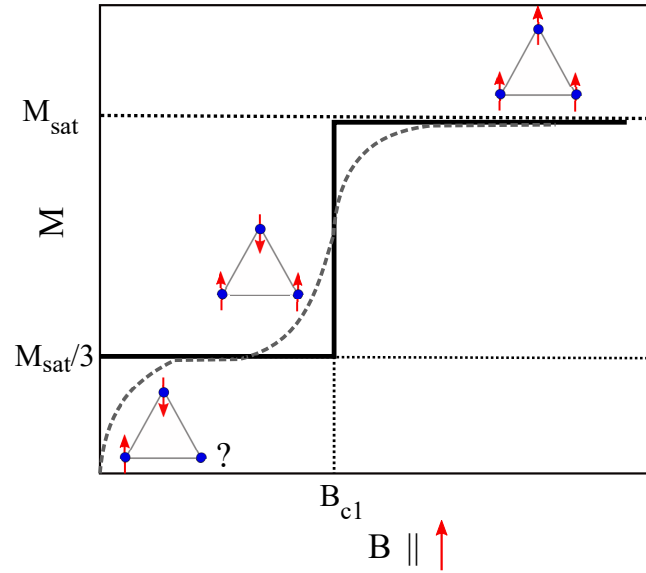
Figure 2.5: Schematic representing evolution of magnetization on triangular lattice with Ising spins.

spotted in frustrated systems with one-dimensional spins, also called 'Ising' type [41]. Figure 2.5 presents magnetization plateau formation in a triangular lattice with Ising spins.

3   Methods

This chapter is devoted to a brief description of the Neutron Scattering, polarized muon spectroscopy, and DFT methods that were used to probe the magnetism in $SrTm_2O_4$ and Co_2VO_4.

The neutron section of this chapter is largely inspired from books by G. L. Squires [42], S.W. Lovesey [43, 44] and Lectures by K. Lefmann at NNSP-SwedNess Neutron School 2018, Tartu [45]. The polarized muon spectroscopy part of this chapter is inspired from the book by A. Yaouanc and P. Dalmas de Reotier [46] and Lecture notes by A. Amato [47]. The quantum chemistry methods part of the chapter is inspired from the book by S. Cottenier [48].

3.1   Neutron Scattering

Neutrons are subatomic particles whose interaction with matter can act as a versatile tool to probe atomic arrangements and magnetic states along with their respective dynamics. Neutrons are scattered by the nucleus of an atom, revealing the atomic structure, while the neutron spin interacts with electron spin,via dipolar interactions, providing information on spin arrangement. Additionally, neutrons (thermal neutrons) have de Broglie wavelengths of the order of inter-atomic distances (~ 1 Å) and energy scales similar to elementary excitations (~ 10 meV). Thus, neutrons can simultaneously provide static and dynamic information of atomic and magnetic structures of the probed system. Additionally, neutrons possess neutral charge, which allows them to penetrate deep into a material and probe the bulk of the sample.

3.1.1   Principles of Neutron Scattering

In a neutron scattering experiment, properties of the incident (E_i, k_i) and final (E_f, k_f) neutrons can be used to understand the the energy
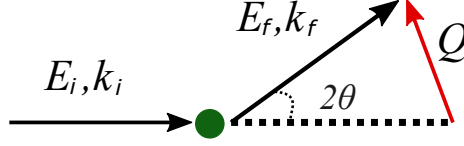
Figure 3.1: The scattering triangle, showing incoming neutrons with wave vector k_i, scattered neutrons with k_f, and the scattering vector $Q = k_f - k_i$. The scattering angle, 2θ, is twice Bragg angle θ.

($\hbar\omega$) and momentum transferred ($\hbar Q$) to the sample. These experiments are governed by the laws of momentum and energy conservation:

$$\hbar\omega = E_f - E_i \tag{3.1}$$

$$\hbar Q = \hbar(k_f - k_i) \tag{3.2}$$

An elastic neutron scattering experiment measures a neutron that has scattered without any energy exchange between the neutron and the sample ($\hbar\omega = 0$). From scattering triangle in Figure 3.1 one can derive condition for elastic scattering in crystalline systems. This condition is called as Bragg law,

$$n\lambda = 2d\sin\theta. \tag{3.3}$$

Elastic scattering (or Diffraction) technique is used to study atomic and magnetic structures.

On the other hand, in inelastic scattering experiments there is a change in energy after a neutron scatters from the system ($\hbar\omega \neq 0$). The loss of gained energy from the inelastic process provides information on the dynamic effects such as phonons and magnons. Thus in any neutron scattering experiment the main task is determination of the probability that a neutron with a wave vector k_i is scattered into a state with wave vector k_f (Fig 3.2). This probability of scattered intensity can be quantified by partial differential cross-section,
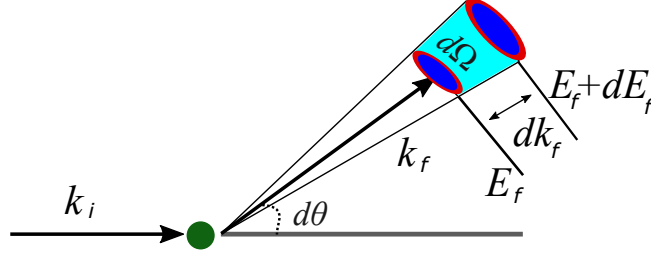
Figure 3.2: Representation of a neutron scattering. Incoming monochromatic beam of neutrons, with energy E_i and wave vector k_i, is scattered by the sample (green circle). The partial differential scattering cross-section, defined by Eq. 3.4, is the number of neutrons per second and per incoming flux, that are being scattered into the small solid angle $d\Omega$ around the direction defined by k_f, and with an energy between E_f and $E_f + dE_f$.

$$\frac{d^2\sigma}{d\Omega dE_f} = \frac{1}{\Phi} \frac{\text{no. of neutrons scattered per sec. into solid angle } d\Omega \text{ with energies } \left[E_f; E_f + dE_f\right]}{d\Omega dE_f}$$

(3.4)

Where σ is the neutron scattering cross-section given by scattered neutron flux per incident neutron flux (Φ). Thus the partial differential cross-section quantifies the number of neutrons scattered in a small solid angle $d\Omega$ with an energy between E_f and $E_f + dE_f$.

The differential cross-section is defined as,

$$\frac{d\sigma}{d\Omega} = \int dE_f \frac{d^2\sigma}{d\Omega dE_f}.$$

(3.5)

Which is the number of neutrons per second scattered into a solid angle $d\Omega$ in the given direction divided by the incomming flux.

Neutron scattering cross-section can originate from two types of processes, namely coherent and incoherent processes. The coherent scat-

tering cross-section describes the neutrons scattered by the collective behavior in the scattering system, as in the case of Bragg peaks, phonons, or magnon excitations. The incoherent scattering cross-section represents the neutrons which are scattered by the individual, uncorrelated fluctuations that would not produce interference effects.

Fermi's golden rule

When a neutron scatters, it can cause transitions from one quantum state to another within the system, but it does not modify the nature of the states themselves. Thus the neutron acts as a very weak perturbation to the scattering system. As a consequence, the partial differential cross-section can be obtained from Fermi's golden rule. Using this rule, Eq. 3.4 can be written as follows:

$$\left(\frac{\mathrm{d}^2\sigma}{\mathrm{d}\Omega\mathrm{d}E_f}\right)_{i\to f} = \frac{k_f}{k_i}\left(\frac{m}{2\pi\hbar^2}\right)^2 \left|\langle \mathbf{k}_f, \sigma_f, v_f | \mathcal{V} | \mathbf{k}_i, \sigma_i, v_i \rangle\right|^2 \delta\left(\hbar\omega + E_i - E_f\right)$$

(3.6)

where the initial and final quantum states of the system are represented by v, $\mathbf{k}$ is the momentum carried by a neutron, and σ is the neutron spin state; $\mathcal{V}$ is the scattering potential.

Nuclear scattering

For the scattering due to neutron interactions with a nucleus, scattering potential is given by this equation:

$$\mathcal{V}_n\left(\mathbf{r}_j\right) = \frac{2\pi\hbar^2}{m}b_j\delta\left(\mathbf{r}_j\right),$$

(3.7)

where b_j is the scattering length of the jth nucleus at position $\mathbf{r}_j$. The partial differential cross-section of nuclear scattering for a periodic arrangement of nuclei is given as follows:

$$\left(\frac{\mathrm{d}^2\sigma}{\mathrm{d}\Omega\mathrm{d}E_f}\right)_{\mathrm{nuc}} = \frac{k_f}{k_i}\frac{1}{2\pi\hbar}\sum_{jj'}b_jb_{j'}\int_{-\infty}^{\infty}\mathrm{d}t\,e^{-i\omega\alpha}\left\langle e^{i\mathbf{Q}\cdot[\mathbf{r}_j(0)-\mathbf{r}_{jj}(t)]}\right\rangle,$$

(3.8)

where $\langle...\rangle$ represents the thermal average. The nuclear potential $\mathcal{V}_n$ does not affect the spin state σ of the neutron, and thus there is no neutron spin component in $\left(\frac{\mathrm{d}^2\sigma}{\mathrm{d}\Omega\mathrm{d}E_f}\right)_{\mathrm{nuc}}$. Ignoring incoherent scattering for sake of simplicity, and by defining

$$N(\mathbf{Q},t) = \sum_j b_j e^{i\mathbf{Q}\cdot\mathbf{r}_j(t)},$$

(3.9)

the partial differential cross section in Eq. 3.8 is written as

$$\left(\frac{\mathrm{d}^2\sigma}{\mathrm{d}\Omega\mathrm{d}E_f}\right)_{\mathrm{nuc}} = \frac{k_f}{k_i}\frac{1}{2\pi\hbar}\int_{-\infty}^{\infty}\mathrm{d}t\,e^{-i\omega t}\left\langle N(\mathbf{Q},0)N^{\dagger}(\mathbf{Q},t)\right\rangle.$$

(3.10)

Similarly, for elastic case, the nuclear differential cross section (Eq. 3.5) can be written as,

$$\left(\frac{\mathrm{d}\sigma}{\mathrm{d}\Omega}\right)_{\mathrm{nuc}} = N\frac{(2\pi)^3}{V_0}\sum_{\tau}\delta(\mathbf{Q}-\tau)\,|F_N(\mathbf{Q})|^2,$$

(3.11)

where N is number of atoms in the crystal, V_0 is volume of the unit-cell, and $F_N(\mathbf{Q})$ the nuclear structure factor. The nuclear structure factor, summed over over the ions at position $\mathbf{d}$ in the unitcell, is give by,

$$F_N(\mathbf{Q}) = \sum_d b_d e^{i\mathbf{Q}\cdot\mathbf{d}}e^{-W_d},$$

(3.12)

where e^{-W_d} is the Debye-Waller factor, that considers average thermal displacement of the ions around their equilibrium position [42, 43].

27

Magnetic scattering

The neutron by virtue of its spin possesses a magnetic dipole moment $\mu_n = -\gamma\mu_N\sigma$, where γ is the neutron gyromagnetic ratio, μ_N is the nuclear magneton, and σ is the Pauli matrix. Similarly, by virtue of its spin the electron possesses magnetic dipole moment defined by equation 2.1. The scattering potential for magnetic scattering due to the magnetic field **B** generated at a position **R** both by the electron spin dipole moment and by the electron's momentum **p** is given by this equation:

$$\mathcal{V}_m = -\gamma\mu_N\mu_B\sigma \cdot \left[\nabla \times \left(\frac{\mathbf{s}\times\mathbf{R}}{R^3}\right) + \frac{1}{\hbar}\frac{\mathbf{p}\times\mathbf{R}}{R^3}\right] \tag{3.13}$$

Here the first term represents spin angular momentum and the second orbital angular momentum. The double differential cross-section for unpolarized neutrons is given as follows:

$$\left(\frac{\mathrm{d}^2\sigma}{\mathrm{d}\Omega\mathrm{d}E_f}\right)_{\mathrm{mag}} = \frac{k_f}{k_i}\frac{(\gamma r_0)^2}{2\pi\hbar}\sum_{\alpha\beta}\left(\delta_{\alpha,\beta} - \frac{Q_\alpha Q_\beta}{|\mathbf{Q}|^2}\right)\sum_{jj'}\frac{1}{4}g_j g_{j'} f_j(\mathbf{Q}) f_{j'}^*(\mathbf{Q})$$
$$\times \int \mathrm{d}t e^{-i\omega t}\left\langle e^{i\mathbf{Q}\cdot[\mathbf{r}_j(0)-\mathbf{r}_{j'(t)}]}\right\rangle \left\langle S_j^\alpha(0)S_{j'}^\beta(t)\right\rangle \tag{3.14}$$

$f_j(\mathbf{Q})$ is the magnetic form factor of the ion j. The neutron magnetic form factor has a very strong Q dependency. $S_j^\alpha(t)$ is the α component of the magnetic moment of the ion j [44]. It is crucial to note that the magnetic scattering is sensitive to the components of the moments which are perpendicular to the momentum transfer **Q**.

The $\left(\frac{\mathrm{d}^2\sigma}{\mathrm{d}\Omega\mathrm{d}E_f}\right)_{\mathrm{mag}}$ can be defined in terms of $\mathbf{M}(\mathbf{Q},t)$ which is the spatial Fourier transform of the magnetization density $\mathbf{M}(\mathbf{r},t)$.

$$\left(\frac{\mathrm{d}^2\sigma}{\mathrm{d}\Omega\mathrm{d}E_f}\right)_{\mathrm{mag}} = \frac{k_f}{k_i}\frac{1}{2\pi\hbar}\int \mathrm{d}t e^{-i\omega t}\left\langle \mathbf{M}_\perp(\mathbf{Q},0)\cdot\mathbf{M}_\perp^\dagger(\mathbf{Q},t)\right\rangle. \tag{3.15}$$

The elastic magnetic cross-section for a commensurate structure with a single magnetic site can be written as,

$$\left(\frac{d\sigma}{d\Omega}\right)_{\text{mag}} = N\frac{(2\pi)^3}{V_0} \sum_{\tau} \left(pf(\mathbf{Q})e^{-W}\right)^2 |\mathbf{F}_{M\perp}(\mathbf{Q})|^2 \, \delta(\mathbf{Q} - \boldsymbol{\tau}) \quad (3.16)$$

where $f(\mathbf{Q})$ is the magnetic form-factor for the magnetic ions.

At this juncture I would like to define the polarization factors

$$\mathbf{P}_x(\mathbf{Q}) = \widehat{\mathbf{Q}} \times \left(\mathbf{e}_x \times \widehat{\mathbf{Q}}\right) = \left(1 - \widehat{Q}_x^2, -\widehat{Q}_x\widehat{Q}_y, -\widehat{Q}_x\widehat{Q}_z\right)$$
$$\mathbf{P}_y(\mathbf{Q}) = \widehat{\mathbf{Q}} \times \left(\mathbf{e}_y \times \widehat{\mathbf{Q}}\right) = \left(-\widehat{Q}_x\widehat{Q}_y, 1 - \widehat{Q}_y^2, -\widehat{Q}_y\widehat{Q}_z\right) \quad (3.17)$$
$$\mathbf{P}_z(\mathbf{Q}) = \widehat{\mathbf{Q}} \times \left(\mathbf{e}_z \times \widehat{\mathbf{Q}}\right) = \left(-\widehat{Q}_x\widehat{Q}_z, -\widehat{Q}_y\widehat{Q}_z, 1 - \widehat{Q}_z^2\right)$$

where $\widehat{\mathbf{Q}} = \mathbf{Q}/Q$ is a unit vector directed in the direction of the scattering vector [49].

In Chapter 6, during the analysis of the magnetic structures, I will use these terms to determining the direction of the magnetic moments.

In Equation 3.16 the

$$\mathbf{F}_{M\perp}(\mathbf{Q}) = \widehat{\mathbf{Q}} \times \left[\mathbf{F}_M(\mathbf{Q}) \times \widehat{\mathbf{Q}}\right]$$
$$= \mathbf{P}_x(\mathbf{Q})F_M^x(\mathbf{Q}) + \mathbf{P}_y(\mathbf{Q})F_M^y(\mathbf{Q}) + \mathbf{P}_z(\mathbf{Q})F_M^z(\mathbf{Q}), \quad (3.18)$$

where the magnetic structure factor is given by [49],

$$\mathbf{F}_M(\mathbf{Q}) = \left(F_M^x(\mathbf{Q}), F_M^y(\mathbf{Q}), F_M^z(\mathbf{Q})\right) = \sum_d \mathbf{m}_d e^{i\mathbf{Q}\cdot\mathbf{r}_d} \quad (3.19)$$

3.2 Neutron Scattering Instruments

In this section I briefly introduce neutron diffraction and neutron spectroscopy instrumentation.

There are two distinct ways of producing neutrons at high flux neutron scattering facilities. One of these is neutron-induced *nuclear fission* in a nuclear reactor. The other method is called *spallation*, where neutrons are ejected from a heavy nucleus because of bombardment by high-energy protons.

3.2.1 Neutron Diffractometer

In this work I present neutron diffraction experiments performed using E6 [50] and E9[51] at HZB, POWGEN [52] at SNS, and DMC [53] at PSI. In this section I offer a brief overview of a neutron powder diffractometer without getting into the specifications.

A diffractometer measures the differential cross-section $d\sigma/d\Omega$, by counting the number of neutrons scattered into a small solid angle $d\Omega$ at an angle 2θ to the direction of the incident beam. Thus a neutron diffraction experiment can be used to study nuclear or magnetic Bragg scattering. There are two types of diffractometers: angle-dispersive and energy dispersive procedures. Angle dispersive procedure is typically operated on a continuous neutron source, whereas the energy dispersive procedure is implemented in case of pulsed neutron sources. Among the instruments used in this thesis, E6, E9, and DMC use angle dispersive procedures, while POWGEN uses the energy dispersive procedure. The energy dispersive procedure is also called as time-of-flight diffraction experiments [45, 54].

Figure 3.3 presents a typical angle dispersive (fixed wavelength) neutron powder diffractometer. In this diffractometer a monochromator (pyrolytic graphite (PG), germanium, or copper) is used to select a specific wavelength from a white neutron beam. The collimators are used to improve beam divergence. These neutrons are then scattered by sample and the intensity of the scattered beam is measured as a function of the scattering angle 2θ using an arc shaped detector. These detectors have many channels, each covering a narrow range of scattering angle. The background neutrons are suppressed using a radial col-
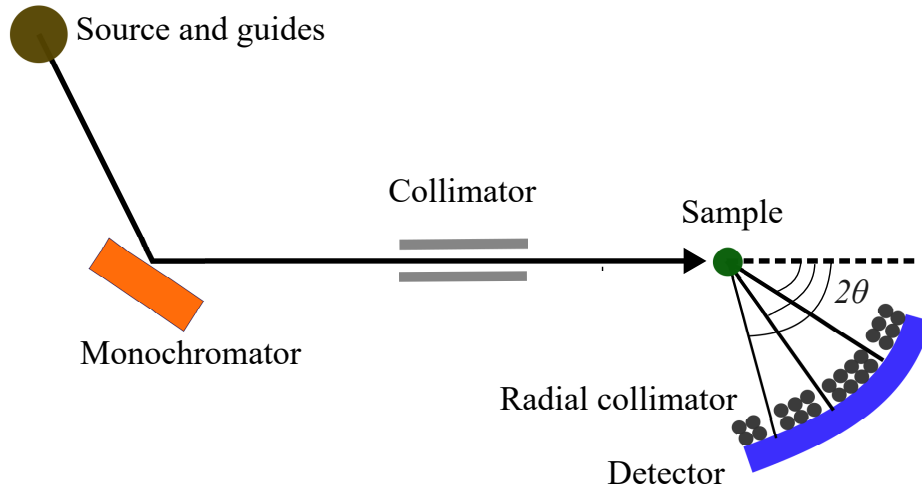
Figure 3.3: Schematics of an angle dispersive neutron powder diffractometer.

limator. A typical neutron powder diffractogram is plotted as intensity vs 2θ. It is crucial to note that the resolution of such a diffractometer varies with the scattering angle. The peaks are broadest at high scattering angles. Additionally, there are instances of magnetic peaks at low scattering angle owing to the magnetic form factor.

In the energy-dispersive (fixed angle) procedure a pulsed source delivers white neutron beams directly on the sample. Here the neutron wavelength changes with time, with the shortest wavelength neutrons arriving earliest. At any given moment in time, Bragg scattering happens from several lattice spaces, while the scattering angle from any reflection only increases with time as wavelength increases. Here the relationship between time-of-flight and wavelength is given by this equation:

$$t = 252.78 \, L \, \lambda \tag{3.20}$$

Where t is time-of-flight in μS, L is total flight length in meters, and λ is wavelength in Å. In these instruments choppers are used to precisely define the wavelength band of the beam impinging on the sample. To

achieve good resolution of the Bragg peaks the moderator is usually thin, and the flight path is very long. In these instruments to maximize the count rate there are a large number of position and time sensitive detectors covering large angles [45, 54].

Of the diffractometers used in this thesis, E6, E9, and DMC are angle dispersive instruments, whereas the POWGEN is a time-of-flight instrument.

3.2.2   Neutron Triple Axis Spectrometer (TAS)

In this thesis I present results from the cold neutron-TAS at HZB, called FLEXX-V2 [55].

The neutron triple axis (TAS) is one of the versatile neutron spectroscopy instruments. The TAS determines both initial and final neutron energy to calculate the energy transfer ΔE ($=E_i - E_f$). These instruments are called triple axis instruments because neutron direction changes three times from scattering, before detection. First, the monochromator selects E_i from incoming white beam by Bragg scattering at $2\theta_M$, next the sample scatters the beam by scattering angle 2θ, and finally the analyzer determines E_f by Bragg scattering at angle $2\theta_A$.

Figure 3.4 presents the schematics of a typical TAS. The TAS is placed away from cold or thermal neutron sources and the neutrons are transported via a neutron guide such that the stray background is lower. This beam is directed by monochromator to select the neutron energy. Beryllium filters are used to avoid higher order scattering. The neutron beam is scattered by the sample (single crystals). The analyzer selects the final neuron energy by Bragg reflection. The neutrons are collected by the single detector [45, 54].

Typically, in a TAS the data is collected point by point, unless a multi-channel analyzer is used. The TAS can be adjusted to measure any scattering vector Q and energy transfer ΔE by selecting three scattering angles $2\theta_M, 2\theta$, and $2\theta_A$ and vertical rotation ω of the sample.
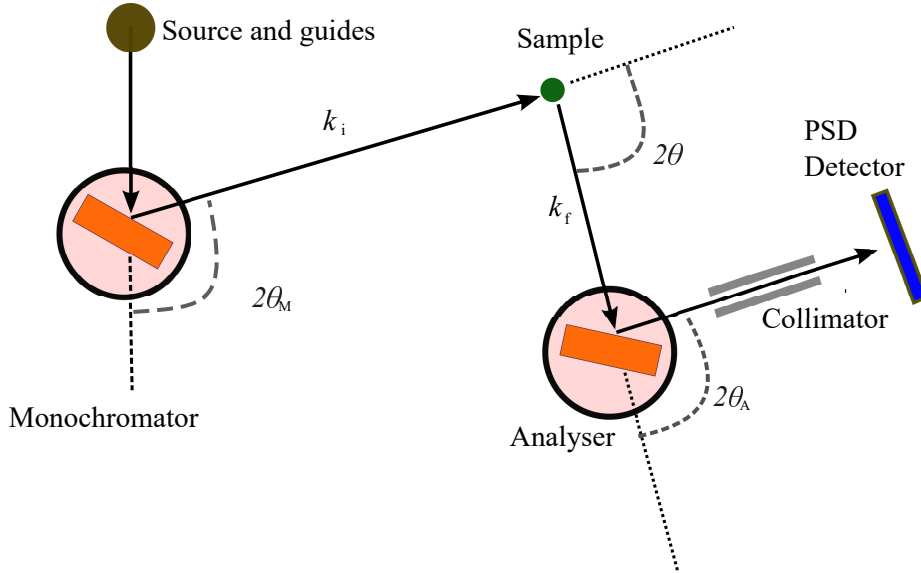
Figure 3.4: Schematics of a typical neutron triple axis spectrometer.

Typically, either incident or final energy is fixed to arrive at ΔE and 2 dimensions of Q by manipulating four angles.

3.2.3 Neutron Time-of-flight Spectrometer (TOF)

In this thesis I present the results from a MAPS [56] spectrometer at ISIS and D7 at ILL [57], a diffused scattering spectrometer with $XYZ-$polarization analysis.

In this technique either initial or final energy needs to be selected, using either Bragg reflecting crystals or choppers. Thus the TOF spectrometers can be divided as direct geometry and indirect geometry spectrometers. In direct geometry spectrometers the incoming neutrons are monochromized by chopper systems and the time-of-flight is used to determine final energy E_f, Whereas in indirect geometry spectrometers the sample is hit with a white beam and scattered neutrons of particular energy (E_f) are selected using analyzer. Finally, the E_i is determined by time-of-flight [45, 54].
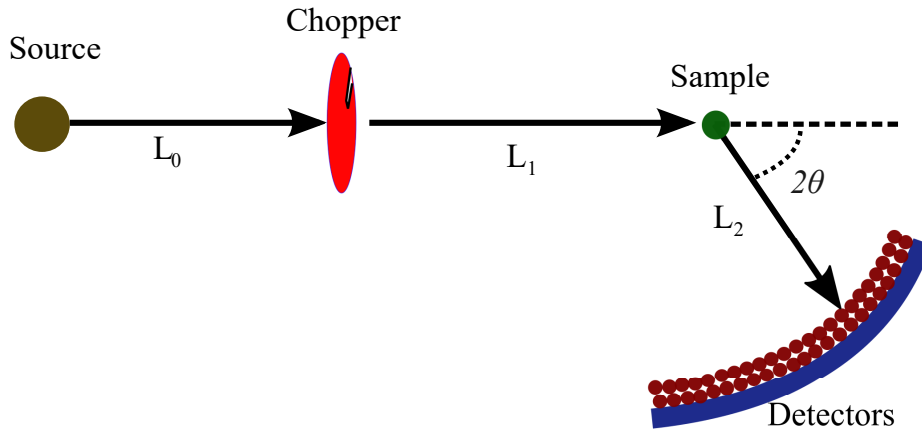
Figure 3.5: Schematics of a typical direct geometry neutron time-of-flight spectrometer.

Figure 3.5 presents the schematic representation of a direct geometry TOF spectrometer. In case of TOF spectrometers the detectors are typically meant to cover a large range of scattering angles. The detectors record the angular position of the scattered neutrons and the time at which they are counted. The time is used to obtain the final neutron energy, while the time and detector position define Q [45, 54].

3.3   Muon Spin Relaxation

Polarized muon spectroscopy is a complementary technique to neutron scattering. Polarized muons provide another avenue to probe magnetic systems without applying a magnetic field. The muons can be used as highly sensitive local probes to study magnetic order and fluctuations. Polarized muons implanted in the sample are influenced by the local magnetic environment, which determines the muon depolarization. By studying the time evolution of muon polarization, one can understand the nature of the magnetic environment in the muon's vicinity. The oscillations in muon time spectrum provide information on the magnitude and direction of the local field, while the damping of muon polarization provides information on the dynamics.

3.3.1 Muon Production

Muons can be produced from various high-energy processes. However, polarized muon spectroscopy requires low-energy muons. Accelerated protons, p, are collided into a target made of light elements such as carbon or beryllium. This results in a pion, π, that decays into a muon. This process is summarized below, wherein n represents neutrons:

$$p + p \rightarrow p + n + \pi^+ \tag{3.21}$$

Based on how the proton is accelerated, there are two ways to produce muons: (quasi-) continuous sources based on cyclotron and pulsed muon sources based on the synchrotron. Each has its strengths and limitations. TRIUMF and PSI are (quasi-) continuous muon sources that have high timing resolution, whereas ISIS and J-PARC are pulsed muon sources with high data rates and can measure for longer times [46, 47].

The π^+ thus produced is short-lived and decays into μ^+ and muon neutrino ν_μ.

$$\pi^+ \rightarrow \mu^+ + \nu_\mu \tag{3.22}$$

The π^+ has zero spins, and the ν_μ has definite helicity h = -1. As a consequence of conservation of angular momentum, μ^+ is fully spin-polarized with spin direction opposite to its flight direction. Such muons are called surface muons because they are typically generated from pions decaying at rest in the surface layer of a target. These muons usually have an energy of $\sim 4.2\,\text{MeV}$. The μ^+ then decays into a positron, neutrino, and muon antineutrino.

$$\mu^+ \rightarrow e^+ + \nu_e + \bar{\nu}_\mu \tag{3.23}$$

35

This positron is also correlated with the angular momentum of the muon. Here, the positron with maximum energy takes the angular momentum of the decaying muon, since the right-handed muon antineutrino and left-handed electron neutrino angular momentum cancel. The angular distribution of emitted positrons with respect to the muon spin at the time of decay is given as follows:

$$N(\theta) = N_0(1 + \beta \cos \theta) \tag{3.24}$$

where $\beta = 1$ for the maximum possible positron energy (52.8MeV) and $\beta = 1/3$ when averaged over all possible energies. Thus, by observing a substantially large number of decay events, the time-dependence of the spin-polarization of an ensemble of muons may be deduced. The emitted positrons are detected by an array of detectors or two detectors, based on pulsed or continuous sources respectively, placed in the forward and backward direction for Longitudinal field measurements [47].

3.3.2 Muon Precession and Relaxation

In a polarized muon experiment, one is interested in the time evolution of muon polarization. Considering a muon initial polarization along the z-axis in magnetic field B, its spin will precess around B with Larmor frequency $\omega = \gamma_\mu B$, where the gyromagnetic ratio is $\gamma_\mu = 2\pi \times 135.5 \text{MHz/T}$. The time evolution of its z-component of polarization $P_z(t)$ is then given by this equation:

$$P_z(t) = \cos^2 \theta + \sin^2 \theta \cos \omega t \tag{3.25}$$

Where θ is the angle between B and the z-axis. The powder average is given as follows:

$$P_z(t) = \frac{1}{3} + \frac{2}{3} \cos \left(\gamma_\mu B t \right) \tag{3.26}$$

1/3 denotes the fraction of spins parallel to the initial muon polarization, which therefore do not precess.

3.3.3   Longitudinal and Zero field μ^+SR

In this report, DOLLY, GPS [58], and LTF instruments from PSI, and EMU [59] instrument from ISIS were used.

In the Longitudinal field μ^+SR measurements, the detectors are arranged in forward (behind the sample) and backward (front of the sample) directions, as shown in Figure 3.6. The polarization is measured directly by observing the relative counts of the forward and backward detectors using the asymmetry function.

$$A(t) = \frac{N_{\text{B}}(t) - \alpha N_{\text{F}}(t)}{N_{\text{B}}(t) + \alpha N_{\text{F}}(t)} \tag{3.27}$$

where N_B and N_F denote the number of counts in the forward and backward detectors respectively and 'α' is the calibration constant. 'α' is usually determined experimentally by applying a very small transverse field. Note that $A(t) = a_0 P_Z(t)$ where a_0 is initial asymmetry and $P_Z(t)$ is polarization.

In the Longitudinal Field Muon Spin Relaxation (LF-μ^+SR) experiment, an external magnetic field is applied parallel to the initial direction of the muon spin polarization. Here one measures the time evolution of the muon polarization along its original path. Additionally, with the same experimental setting, Zero Field Muon Spin Relaxation (ZF-μ^+SR) can be performed in the absence of an external field. ZF-μ^+SR is a very sensitive method of detecting weak internal magnetism that arises due to ordered magnetic moments or random fields that are static or fluctuating with time. The capability of studying materials in zero external fields gives μ^+SR a unique edge over other techniques [46, 47].

3.4   Density Functional Theory

Density functional theory (DFT) is one of the forerunner in *ab-initio* electronic structure calculations. Calculating the total electronic energy
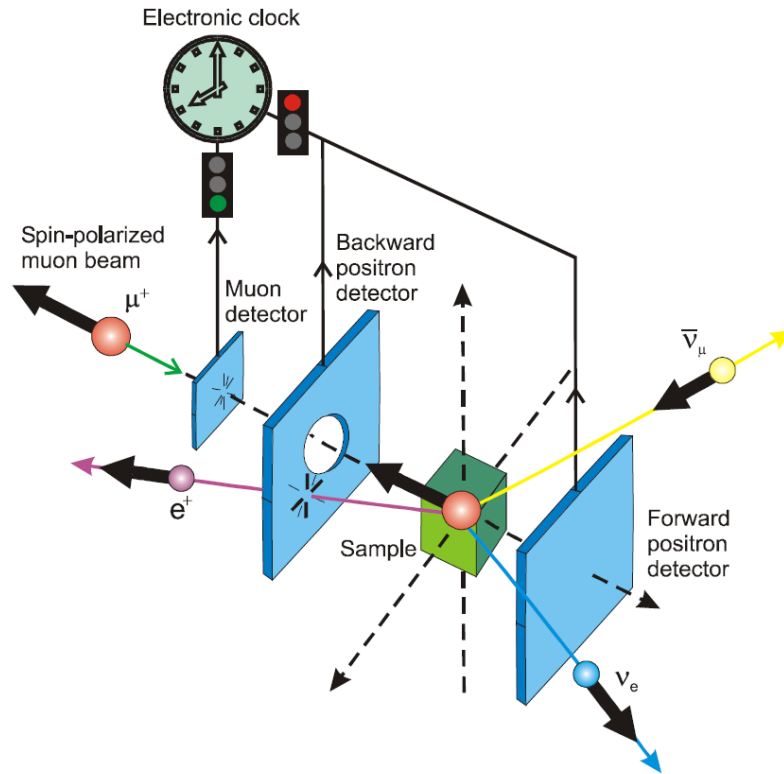
Figure 3.6: Experimental setup of Longitudinal field geometry. Reused from Ref. [60] with permission.© Jeff Sonier.

via the many-electron Schrödinger wave equation is a near-impossible problem due to the several interactions that need to be taken into account. However, DFT overcomes these shortcomings by considering the many-body system as a functional of electron density. In this regard, Hohenberg and Kohn proposed two theorems that laid the foundation for DFT.

1. The external potential V_{ext} is uniquely determined by the ground state electronic density $n(\mathbf{r})$, and the total energy E without the external potential energy contribution is a unique and universal functional of n.

2. The exact ground state density $n_0(\mathbf{r})$ minimizes the total energy functional $E[n]$ in the space of all possible functions $n(\mathbf{r})$.

Thus the energy of the many-body electronic system can be rewritten as follows:

$$E[n] = F[n] + \int d\mathbf{r} V_{\text{ext}}(\mathbf{r}) n(\mathbf{r}) \qquad (3.28)$$

Where $F[n]$ is a universal functional (independent of the external potential), and the many-body ground state density minimizes the energy $E[n]$. As a consequence of the first theorem, all properties of the system can be determined, in principle, by just knowing the ground state density alone. The second theorem suggests that approximations to E and n can be found variationally.

Kohn and Sham suggested that instead of optimizing the $E[n]$ with respect to the density, an auxiliary system of noninteracting electrons can be considered as in the Hamiltonian, as follows:

$$\hat{H}_{\text{KS}} = -\frac{\hbar^2}{2m_e} \nabla^2 + V_{\text{KS}}(\mathbf{r}) \qquad (3.29)$$

satisfying

$$\left[-\frac{\hbar^2}{2m_e} \nabla^2 + V_{\text{KS}}(\mathbf{r}) \right] \phi_i(\mathbf{r}) = \epsilon_i \phi_i(\mathbf{r}) \qquad (3.30)$$

with the N lowest-lying solutions having a corresponding ground state density given by this equation:

$$n(\mathbf{r}) = \sum_i^N |\phi_i(\mathbf{r})|^2 \qquad (3.31)$$

The ground state density of the interacting system can be expressed in terms of the Kohn–Sham orbitals: Here, one can optimize the energy functional $E[n]$ with respect to the ϕ_i instead of the density. Thus,

one can write the universal functional in terms of the non-interacting system as follows:

$$F[n] = T_{\text{KS}}[\{\phi_i\}] + E_{\text{KS}}[n] + E_{\text{xc}}[n] \qquad (3.32)$$

Where T_{KS} is Khon–Sham kinetic energy and Hartree energy E_{H} is given by this equation:

$$E_{\text{KS}}[n] = \frac{1}{2} \int \mathrm{d}\mathbf{r}\mathrm{d}\mathbf{r}' \frac{n(\mathbf{r})n(\mathbf{r}')}{|\mathbf{r} - \mathbf{r}'|} \qquad (3.33)$$

The exchange-correlation term $E_{\text{xc}}[n]$ contains all the parts of the universal functional that are not captured by the noninteracting kinetic energy and Hartree energy. By defining the Hartree potential V_{KS} and exchange-correlation potential $V_{\text{xc}}(= \frac{\delta E_{\text{xc}}}{\delta n(\mathbf{r})})$, the Kohn–Sham equations can be written as follows:

$$\left(-\frac{1}{2}\nabla^2 + V_{\text{ext}}(\mathbf{r}) + V_{\text{KS}}(\mathbf{r}) + V_{XC}\right)\phi_n(\mathbf{r}) = \epsilon_n\phi_n(\mathbf{r}) \qquad (3.34)$$

Where the Kohn–Sham potential V_{KS} is given by the functional derivative of the total energy functional $E_{\text{KS}}[n]$ with respect to the electron density, and it is the sum of the true external (nuclei) potential and an effective one-electron potential which replaces the electron–electron interaction. Various approximate functionals, such as the local density approximation (LDA), generalized gradient approximations (GGA), and hybrid functionals, are used for V_{XC}.

Many different approaches have been proposed to solve the Khon–Sham equation. In this study, Planewave–Pseudopotential approach as implemented in `Quantume Espresso` [61] and the all-electron approach (APW+lo) as implemented in `WIEN2k` [48, 62] were used based on the required accuracy and computational resources.

4   Magnetization Reversal in Co$_2$VO$_4$

This chapter is devoted to the study of magnetism in Co$_2$VO$_4$. This project was initially conceived by D. Vaknin and later taken over and supervised by R. Toft-Petersen. D. Vaknin's group synthesized the sample at the AMES lab as described in Ref. [63]. K. Siemensmeyer measured the bulk properties. The zero-field neutron diffraction measurements were performed by C. M. Naveen Kumar and P. Das. The theory calculations were performed by C. Bhandari and D. Paudyal. I was involved in neutron scattering measurements in the applied field with R. Toft-Petersen and A. Hoser and μ^+SR measurements with S. Cottrell. D. L. Quintero Castro and R. Toft-Petersen provided support with analysis of bulk and neutron data. I analyzed and interpreted all the experimental data and wrote the manuscript (excluding the theory section).

This chapter discusses magnetism and the underlying physics involved in magnetic compensation in Co$_2$VO$_4$.

4.1   Spinel Vanadate family

The spinel family consists of a large group of compounds having the general formula AB_2X_4 (Fig. 4.1) [64] with the same crystal structure as the homonymous mineral. Typical spinel compounds consist of anions 'X'(either O^{2-}, S^{2-}, or Se^{2-}) and cations 'A' and 'B' that can be accommodated by various transition-metal or rare-earth ions. The spinel structure is usually cubic at ambient temperature, containing eight formula units, i.e., 8 A-, 16 B-, and 32 X-. Typically, A-site cations have tetrahedral crystal field environment, while B-site cations form an octahedral environment. In addition to normal spinels of type AB_2X_4, one can also find inverted spinels of type $B(AB)X_4$ (Fig. 4.2) [64], where 50% of the B-sites are occupied by the same ion as the A-site.

41
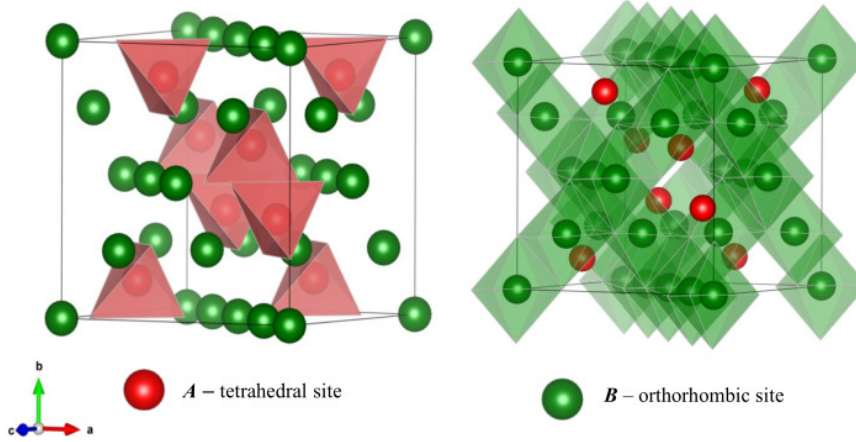
Figure 4.1: Spinel AB_2X_4 with tetrahedral A-site and octahedral B-site.

Co$_2$VO$_4$ belongs to an exciting family of spinel vanadates. Members of this family, such as MnV$_2$O$_4$, FeV$_2$O$_4$,and CoV$_2$O$_4$, have been known to host interesting physics ranging from structural and orbital to magnetic ordering [65–68]. Additionally, CoV$_2$O$_4$ has been a critical focus in the study of orbital glass physics [69], and "ice rules" have been realized in MnV$_2$O$_4$ and FeV$_2$O$_4$, with canting of Vanadium spins making $65.12°$ and $54.7°$ with respect to the c-axis respectively [65, 66].

Inverse spinel systems are known to host unique physics as well. It was in Fe$_3$O$_4$ where the metal to insulator transition ('Verwey transition') was first discovered [70, 71]. Phil Anderson discusses structural ordering in Fe$_3$O$_4$ which later led to conceptualization of spin-ice [72]. K. P. Belov proposed the 'weak magnetic sublattice' model to explain low-temperature anomalies and compensation behavior in some systems such as Fe$_3$O$_4$[71, 73]. He proposed that the low-temperature magnetization compensation in Fe$_3$O$_4$ is due to the formation of weak sublattice by the hopping electrons. As the temperature is lowered, the hopping electrons tend to localize, with their net magnetization going antiparallel to the system, which decreases the net magnetization of the
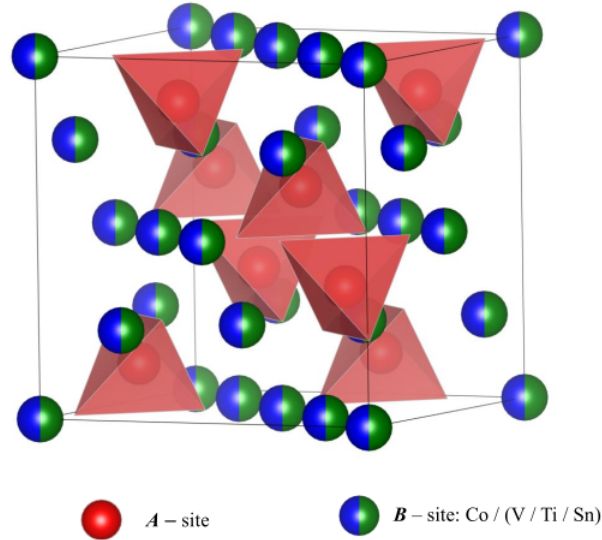
Figure 4.2: Spinel AB_2X_4 with tetrahedral A-site and octahedral B-site.

system.

Additionally, other inverse spinels such as Co$_3$O$_4$, Co$_2$SnO$_4$, and Co$_2$TiO$_4$ have been extensively studied for magnetization reversal and hosting a semi-spin glass phase [74–76]. On the other hand, inverse spinel vanadates have been less scrutinized for magnetism, unlike their spinel counterparts and other inverse spinel cobaltates. Nevertheless, Co$_2$VO$_4$ and Fe$_2$VO$_4$ are extensively studied for battery and catalytic applications [77, 78].

Magnetization reversal (MR) is a crossover of magnetization from a positive value to a negative value as a function of temperature below the magnetic ordering temperature of the material, as shown in Figure 2.2. The MR phenomenon most commonly manifests as compensation between negatively coupled ferromagnetic sublattices [35].

The MR in Co$_2$VO$_4$ was first reported by Menyuk *et al.* [2] in the 60s (Fig. 2.2). They observed a sign change of the magnetization as a function of temperature in the applied magnetic field of 0.07 T

around 70 K. Along with the MR phenomenon, they also saw ferrimagnetic ordering at $T_C = 158$ K. To explain the observed magnetization, they identified five possible magnetic interactions based on cation distribution $Co^{2+}[Co^{2+}V^{4+}]O_4$. Using phenomenological Goodenough–Kanamori rules, they hypothesized the relative strengths of the interactions as follows:

- The $A-B$ interactions involving only Co^{2+} ions are the strongest interactions, irrespective of their spin canting. In this case $A - B$ interaction has a negative sign (Antiferromagnetic interaction).

- If $A - B$ interactions involving $Co^{2+}-O-V^{4+}$ and $B - B$ interactions involving $V^{4+}-O-V^{4+}$ are of comparable strengths, then the vanadium ions undergo canting, resulting in a net moment.

Menyuk and his coworkers also speculated that the observed MR could be due to canted vanadium with net moment antiparallel to that of the cobalt ions on the A- site, but with different temperature dependence. We approached this old problem to answer the following questions:

1. Is the canted vanadium with net moment antiparallel to cobalt ions the cause of MR; i.e., does the vanadium ordering at a different temperature than the Cobalt ions tip the balance and cause compensation?

2. If the above is true, what could be the fundamental reason for such behavior by the Vanadium spins?

3. What is the effect of an applied magnetic field on MR phenomena; i.e., is the observed MR magnetic field a field induced phenomenon or a temperature-dependent phenomenon?

4.2   Manuscript: Summary

The magnetism in Co_2VO_4 is probed with neutron diffraction, magnetization, and muon spin relaxation measurements, supplemented by

density functional theory (DFT) calculations. The magnetization measurements reveal three main temperature anomalies, beginning with the collinear ferrimagnetic transition at T_C followed by non-collinear transition T_{NC} and finally MR crossover at T_{MR}. The neutron powder diffraction and subsequent magnetic structure refinement unveil two antiparallel ferromagnetic sublattices, belonging to magnetic ions on two distinct crystal lattice sites, where the relative balance between the two sublattices determines the net ferromagnetic moment in the unit cell. As the evolution of the ordered moment with temperature differs between the two sublattices, the net ferromagnetic moment reaches a maximum at T_{NC} and reverses its sign at T_{MR}.

The DFT results suggest that the underlying microscopic mechanism for the reversal is a delocalization of the unfilled $3d$ electrons on B sublattice just below T_C, followed by a gradual localization as the temperature is lowered. This delocalized-localized crossover is supported by muon spectroscopy results, as strong T_1-relaxation observed below T_C indicates fluctuating internal fields.

4.3 Co$_2$VO$_4$ Atomic Structure

Rietveld refinement of neutron diffraction and XRD data (at 300 K) of the synthesized Co$_2$VO$_4$ confirm the cubic $Fd\bar{3}m$ symmetry. The nuclear structure at 300 K was verified by D. Vaknin's group at AMES lab. However, impurity phases were not identified. The neutron powder diffraction (NPD) was performed with the time-of-flight powder diffractometer POWGEN at SNS, ORNL. The measurements were carried out with neutrons of central wavelengths of 1.333 and 3.731 Å for the respective frames, with a bandwidth of ~1 Å at 60 Hz chopper frequency. The sample was loaded in a vanadium can which was attached to the cold end of a cryostat to reach temperatures in the range $2 \leq T \leq 300$ K.

Neutron powder diffraction in the applied magnetic fields was performed using E6 and E9 diffractometers at the BER II reactor at the
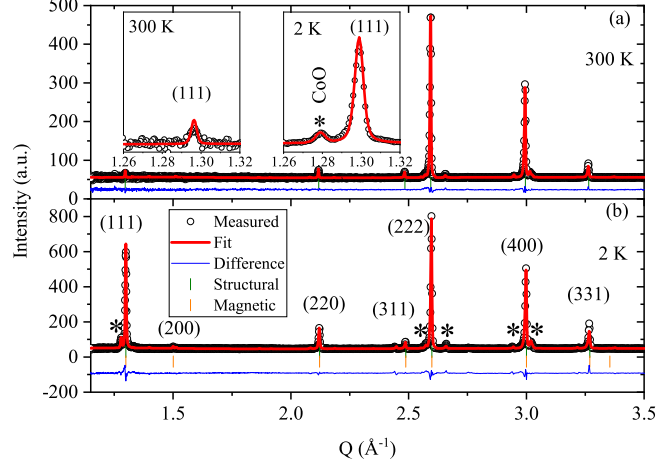
Figure 4.3: Neutron diffraction patterns and fits from the Rietveld refinement. The asterisk indicates impurity peaks. Measure NPD patterns (a) T = 300 K and (b) T = 2 K corresponding to the data collected with center wavelengths 3.731 Å. (a) insets show evolution of incommensurate magnetic impurity peak ($Q=1.28 Å^{-1}$) of CoO.

Helmholtz-Zentrum Berlin. Powder sample amounting to 3.5 g was dispersed in the deuterated methanol–ethanol mixture, which freezes into an amorphous glass upon cooling and fixes the powder orientation while applying a magnetic field. The E6 diffractometer was used to perform the temperature scans ranging from 15-200 K with an applied magnetic field of 0.25 T and 2 T with wavelength 2.44 Å and the E9 diffractometer was used to perform temperature scans ranging from 50-250 K with an applied magnetic field of 0, 0.05, and 0.5 T with wavelength 1.81 Å following field cooled protocol.

4.3.1 Impurity Phases

In neutron diffraction data at 300 K below 3.5 $Å^{-1}$, four peaks were not identified by the cubic $Fd\bar{3}m$ phase of Co₂VO₄, i.e., 2.56, 2.66, 2.94, and 3.03 $Å^{-1}$. On further investigation we found that the peaks at 2.56

and 2.94 Å^{-1} originate from CoO, which is an unused precursor in the synthesis process. Here CoO structural phase is identified as cubic 225.$Fm\bar{3}m$, The peak 2.56 Å^{-1} is indexed as (111) and 2.94 Å^{-1} as (200) with respect to spacegroup $Fm\bar{3}m$.

The temperature evolution of neutron diffraction patterns shows another interesting impurity. A peak centered at Q=1.28Å^{-1} posed challenges in indexing neutron diffraction patterns (Fig. 4.3). This peak absent at 300 K starts to emerge and evolve below ~ 250 K. The presence of this peak at low-Q and its proximity to the (111) (Q=1.3Å^{-1}) reflection makes understanding this peak crucial to arrive at a good magnetic structure refinement.

We propose that the peak at Q=1.28Å^{-1} in neutron diffraction data originates from the incommensurate magnetic structure of CoO. The magnetic structure of CoO has been debated for more than half a century [79, 80]. However, basis vector belonging to irreducible representation (Γ6) consistent with propagation vector $k = (1/2, 1/2, 1/2)$ and 225.$Fm\bar{3}m$ resolves emergence of the peak at Q=1.28Å^{-1} in the diffractogram. The basis vector was found using `BasIREPS`[81].

Additionally, low-temperature heat capacity anomalies have shown the formation of Co$_3$V$_2$O$_8$ (discussed in the next section). Formation of this phase explains occurrence of peaks 2.66 and 3.03 Å^{-1}. The Co$_3$V$_2$O$_8$ exists as orthorhombic 64.$Cmca$ [82, 83]. Co$_3$V$_2$O$_8$ undergoes transitions only below 11 K [84, 85].

4.3.2 Structural Transition

The spinel vanadate family is known to exhibit several successive structural transitions along with magnetic transitions[65, 86]. These structural transitions are interlinked with the orbital ordering as well. In the case of spinel counterpart CoV$_2$O$_4$, two such structural transitions are reported [68]. In this regard, it is crucial to look for such transitions in this system. In CoV$_2$O$_4$, structure transition from cubic phase to tetragonal phase is marked by broadening of the (400) peak.
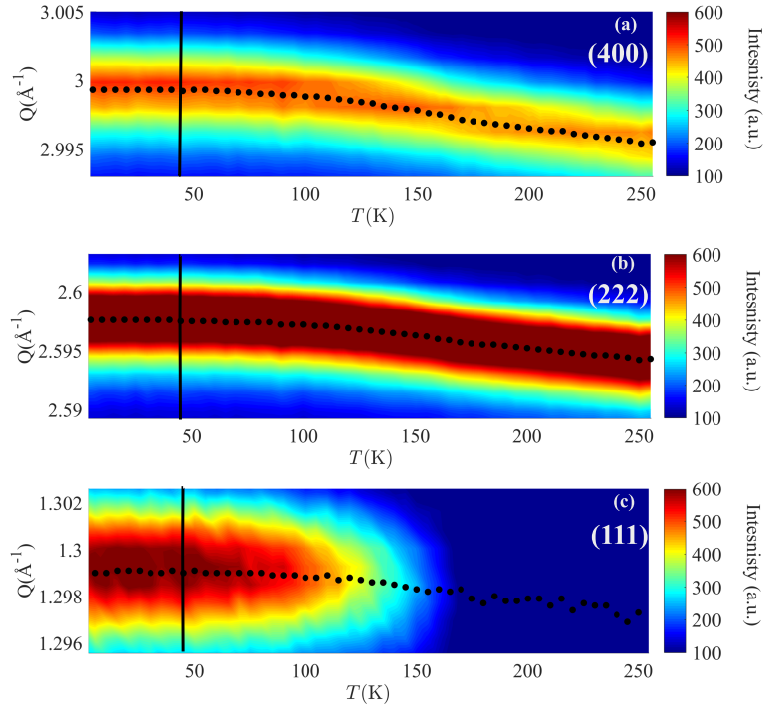
Figure 4.4: Temperature dependency of peak positions of (a) (400), (b) (222), and (c) (111). The color scheme represents the intensity scale. The scattered points represent the peak center obtained from peak fitting.

We do not observe any structural transition in our neutron diffraction data, unlike in the spinel counterpart. However, such structural transition cannot be ruled out, as the detection of these tiny distortions is limited by instrument resolution. On the other hand, Figure 4.4 presents temperature-dependent shifting of peak positions of (400), (222), and (111). The shifting of peak positions saturates at ~40 K. The shifting of peak positions indicates a uniform shrinking of the cubic unit cell.

48

4.4 Bulk Properties

In this section, I report the preliminary bulk characterization of Co$_2$VO$_4$. In the first part I describe magnetization vs. temperature reported in the manuscript, then anomalous hysteresis, and AC-Susceptibility results followed by metamagnetic behavior observed with heat capacity measurements.

4.4.1 Magnetization vs Temperature

Magnetization as a function of temperature was measured in field cooled (FC) and zero fields cooled (ZFC) measurements, with various applied fields in the range 0.03-8 T (Fig. 1 in the manuscript). The magnetization results show four temperature anomalies: the drastic increase in magnetization at T_C (C-Collinear), onset of a decreasing magnetization at T_{NC} (NC- Non-Collinear), magnetization reversal at T_{MR}, and finally low-temperature upturn in magnetization. Low-temperature upturn can be linked to the impurity phase originating from Co$_3$V$_2$O$_8$.

We have also established a considerable deviation between FC and ZFC measurements, which disappears completely with higher applied fields (~5 T). Most significantly, the observed magnetization reversal gets quenched in applied fields higher than ~0.25 T.

4.4.2 Magnetic Hysteresis

Figure 4.5 shows the magnetic hysteresis curves at selected temperatures, T = 5, 15, 75, 140, and 220 K. The hysteresis loops vary greatly over the range of temperatures. At the highest measured temperature (220 K), the expected paramagnetic behavior is observed, which is followed by a transition to the ferrimagnetic phase at 140 K, reaching a saturated moment of $\approx 0.4\mu_B$ at 4 T. However, it shows negligible hysteresis with the coercive field (H_c = 0.1 T). Close to T_{MR}, the system behaves very similarly to the paramagnetic phase, except for a small degree of hysteresis.
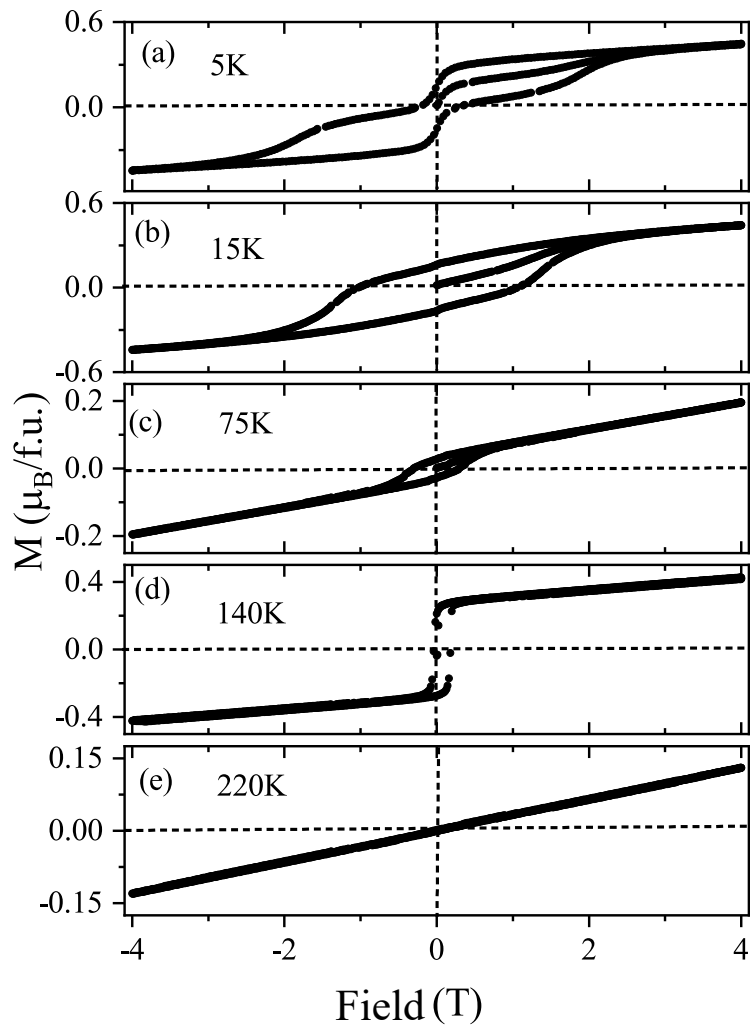
Figure 4.5: Magnetic hysteresis measurements at specified color-coded temperatures. The loops have been offset by 0.5 μ_B/ f.u. for clarity.

As the temperature is lowered, the system shows a pronounced hysteresis loop with a large H_c at 15 K. At this temperature, the observed curve resembles a "potbelly"(PB) shape. In such hysteresis loops, width becomes broader as the magnetization goes to zero and then closes down again at higher fields [87].
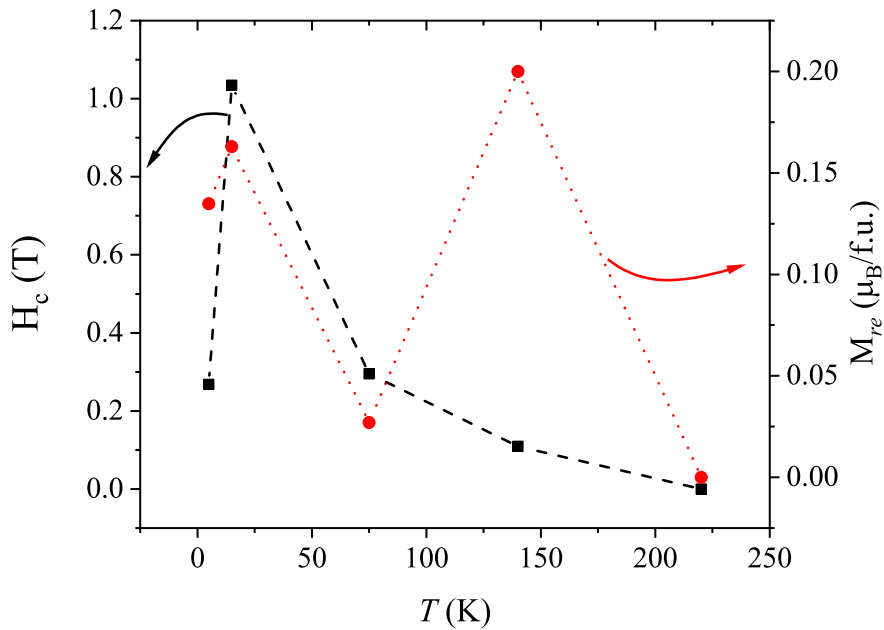
Figure 4.6: The temperature variation of coercive field (a) H$_c$ and remanence magnetization M$_{re}$

Upon further cooling down to 5 K, an unusual curve resembling a "wasp-waist" (WW) feature is observed. In this case, loop width narrows as the magnetization goes to zero and then opens up [87]. In general, such hysteresis loops are observed in mixed magnetic systems where they develop due to change in spin-exchange coupling between the cations [87–89]. Bennet *et al.*[87] have shown that WW loop can be obtained from two ferromagnetic sub-systems that are coupled oppositely, with one of them having a larger coercivity than the other,

and potbelly loop can be obtained from two oppositely coupled ferromagnetic sub-systems, where one of them has a smaller switching field distribution and higher coercivity than the other.
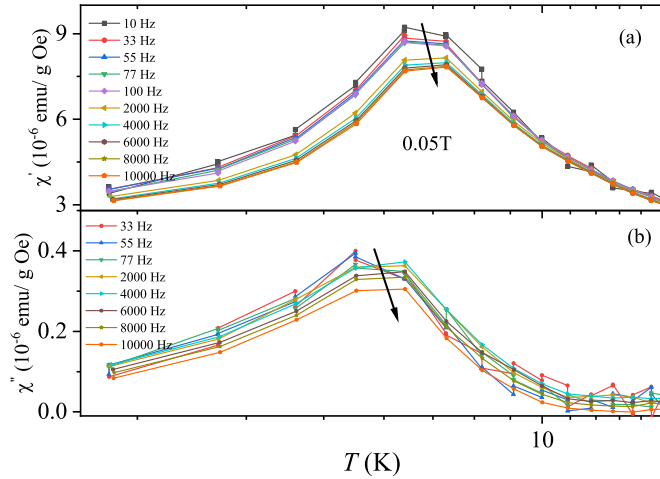
Figure 4.7: Temperature dependence of ac magnetic susceptibilities (a) $\chi'(T)$ (b) $\chi''(T)$ of Co$_2$VO$_4$ measured at various frequencies between 33 Hz and 10 kHZ; measured under FC protocol.

The PB and WW shapes are commonly spotted in single-domain/ superparamagnetic (SD/SP) systems. In this case, wasp-waisting loops require an SP contribution that saturates quickly, with a steeper initial slope relative to the SD, whereas the potbellied loops require a shallower slope [90]. However, the Co$_2$VO$_4$ sample used in theses measurements is polycrystalline, and loops do not exhibit squareness as in Ref. [90]. Therefore, the possibility of a single domain can easily be discarded. However, similar features in hysteresis have also been spotted among frustrated systems as well. There are several frustrated systems where chemical disorder in a system induces magnetic frustration, which is originated due to competition between negative and positive exchange coupling [91, 92].

In this sample, Co$_3$V$_2$O$_8$, one of the impurity phases in this sam-

ple (discussed in the next section), could be the reason for observed hysteresis. The Co$_3$V$_2$O$_8$ is popular frustrated system known for its Kagome structure. This system exhibits meta-magnetic anomalies at 11 K and 5 K [84, 85]. We conclude that PB and WW shapes of hysteresis could be due to the coexistence of the impurity phase.

Coercive field H$_c$ and remanence magnetization M$_{re}$ are shown in Figure 4.6. The standard definition of coercivity is given by H$_c$ = (H$^+$ − H$^-$) / 2, where H$^+$ and H$^-$ are the magnetic field values for which M = 0. The remanence M$_{re}$ is the magnetization value at H= 0.
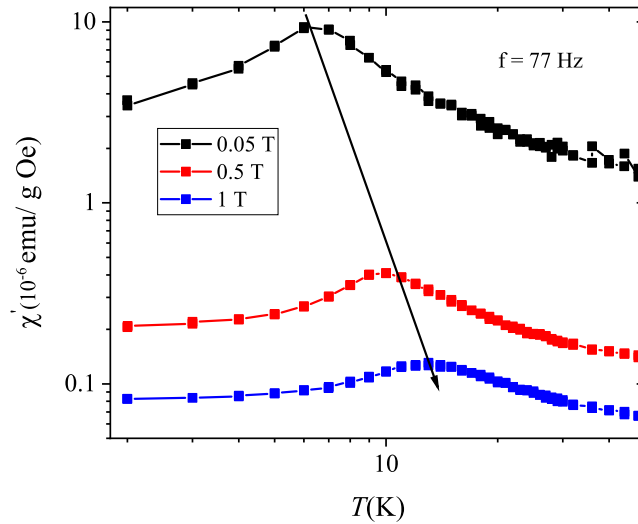
Figure 4.8: Temperature dependence of real part of ac magnetic susceptibilities $\chi^{'}(T)$ measured with applied field 0.05, 0.5, 1 T and f=77 Hz under FC protocol.

4.4.3 AC-susceptibility

The AC susceptibility measurement was performed on a powder sample pressed in the form of pellets, with an applied field of 0.05 T in FC. Both $\chi^{'}(T)$ and $\chi^{''}(T)$ show an anomaly, i.e., peak centered at

≈ 6 K. This peak has a small frequency dependency in case of both $\chi'(T)$ and $\chi''(T)$ (Fig. 4.7). Typically, such anomalous behavior is associated with a glassy transition [75]. Moreover, as shown in Figure 4.8, this peak moves toward higher temperature in the applied magnetic field, indicating that there is a field dependency associated with this anomaly.

4.4.4 Heat Capacity

However, similar meta-magnetic behavior is observed in heat capacity measurements of Co$_3$V$_2$O$_8$ at 11 K and 5 K [84, 85]. We conclude that the observed low-temperature behavior could have emerged from the impurity phase.
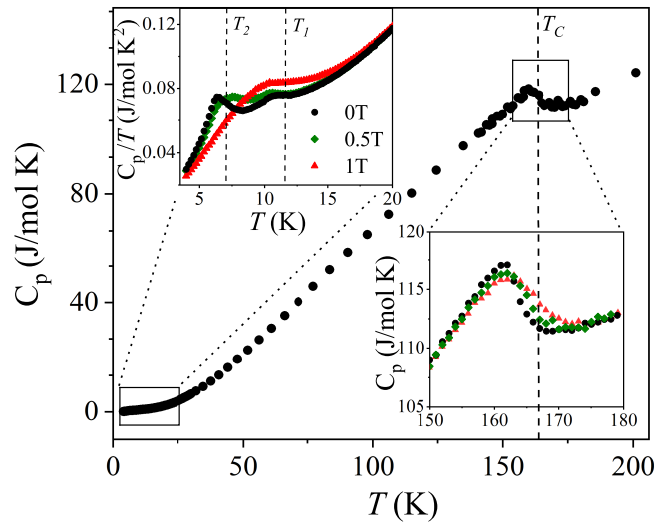
Figure 4.9: Heat Capacity C$_p$ as a function of temperature at applied fields in range 0–1 T. At low temperatures (2K-20K) there is a field dependent transition presented as C_p/T vs T for better visualization.

In Figure 4.9, the heat capacity of the powder sample pressed in as pellets is presented. This was measured in applied fields 0, 0.5, 1 T.

The anomaly observed at high temperature coincides with $T_C(=168\,\text{K})$ observed with magnetization measurements. Such a feature in heat capacity is termed as λ-anomaly(at T_{g_1}), which is a clear signature of second-order phase transition. In the applied fields, this anomaly broadens. No anomaly was observed at $T_{NC}(=148\,\text{K})$ or $T_{MR}(=65\,\text{K})$. Moreover, since the sign change in magnetization is a crossover phenomenon, no anomaly was expected at T_{MR}. However, there are more chances of spotting an anomaly at T_{NC} if phonon contributions could be subtracted from C_p.
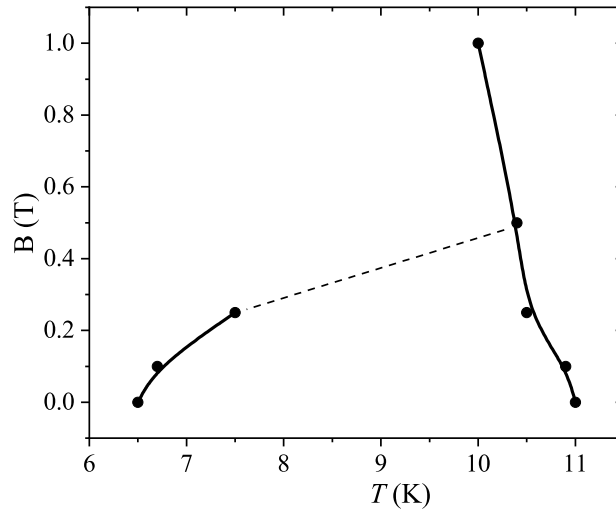
Figure 4.10: Phase diagram produced from heat capacity measurements. Dashed line indicates extrapolation.

At low temperature ($T < 20\,\text{K}$) in zero field, two anomalous features, one at $\approx 6\,\text{K}$ (T_{g_1}) and the other at $\approx 11\,\text{K}$ (T_{g_2}), can be spotted. As the applied field increases, both the anomalies move towards each other and finally merge at $10\,\text{K}$. Figure 4.10 shows a phase diagram constructed from capacity data as a function of temperature and applied magnetic field. This figure shows the merger of two anomalies, as discussed earlier. It is intriguing to note that the AC susceptibility shows

the shifting of T_{g_1}, while no signs of T_{g_2} can be spotted. These are the anomalies observed in the impurity phase Co$_3$V$_2$O$_8$ [84, 85].

4.5 Magnetic Structure Determination

This section describes how we arrived at the magnetic structure using irreducible representations and magnetic space groups.

4.5.1 Basis Vectors and Irreducible Representations

In order to restrict the refinement of the neutron powder data, we exclude the irreducible basis vectors, on both the *A*-and *B*-sites, that are inconsistent with the strongest observed peaks in the powder diffraction pattern. The basis vectors consistent with $Fd\bar{3}m$ and propagation vector $k = (0, 0, 0)$), found using BasIREPS [81] and SARAh[93], are presented in tables 4.1 and 4.2.

Table 4.1: Irreducible representation(IR) belonging to *A*-site (8b) for $Fd\bar{3}m$ and propagation vector $k = (0, 0, 0)$.

IR	BVs	(3/8, 3/8, 3/8)	(1/8, 5/8, 1/8)
	ψ_1	(0 0 1)	(0 0 1)
$\Gamma 10$	ψ_2	(1 0 0)	(1 0 0)
	ψ_3	(0 1 0)	(0 1 0)
	ψ_4	(0 0 1)	(0 0 -1)
$\Gamma 7$	ψ_5	(1 0 0)	(-1 0 0)
	ψ_6	(0 1 0)	(0 -1 0)

In tables 4.3 and 4.4, magnetic structure factors computed for corresponding basis vectors for *A*- and *B*-sites are presented. The $\Gamma 10$ basis vector for *A*-site constitutes ferromagnetic basis vectors in three orthogonal directions. Since the three directions are indistinguishable in a cubic symmetry, we have presented a normalized magnetic structure factor in the manuscript after averaging over three orthogonal directions.

Table 4.2: Irreducible representation (IR) belonging to B-site (16c) for $Fd\bar{3}m$ and propagation vector $k = (0, 0, 0)$.

IR	BVs	(0, 0, 0)	(3/4, 1/4, 1/2)	(1/4, 1/2, 3/4)	(1/2, 3/4, 1/4)
Γ10	ψ_1	(0 0 1)	(0 0 1)	(0 0 1)	(0 0 1)
	ψ_2	(1 1 0)	(-1 -1 0)	(1 -1 0)	(-1 1 0)
	ψ_3	(1 0 0)	(1 0 0)	(1 0 0)	(1 0 0)
	ψ_4	(0 1 1)	(0 1 -1)	(0 -1 1)	(0 -1 -1)
	ψ_5	(0 1 0)	(0 1 0)	(0 1 0)	(0 1 0)
	ψ_6	(1 0 1)	(1 0 -1)	(-1 0 -1)	(-1 0 1)
Γ7	ψ_7	(1 -1 0)	(-1 1 0)	(1 1 0)	(-1 -1 0)
	ψ_8	(0 1 -1)	(0 1 1)	(0 -1 -1)	(0 -1 1)
	ψ_9	(-1 0 1)	(-1 0 -1)	(1 0 -1)	(1 0 1)
Γ6	ψ_{10}	(1 -0.5 -0.5) + i (0 -0.87 0.87)	(-1 0.5 -0.5) + i (0 0.87 0.87)	(-1 -0.5 0.5) + i (0 -0.87 -0.87)	(1 0.5 0.5) + i (0 0.87 -0.87)
	ψ_{11}	(0.5 -1 0.5) + i (0.87 0 -0.87)	(-0.5 1 0.5) + i (-0.87 0 - 0.87)	(-0.5 -1 -0.5) + i (-0.87 0 0.87)	(0.5 1 -0.5) + i (0.87 0 0.87)
Γ3	ψ_{12}	(1 1 1)	(-1 -1 1)	(-1 1 -1)	(1 -1 -1)

Similarly, in case of *B*-site, in Γ10, the ferromagnetic basis vectors, i.e., ψ_1, ψ_3, ψ_5, and the anti-ferromagnetic basis vectors, i.e., ψ_2, ψ_4, ψ_6, are in three orthogonal directions. Similar treatment as explained earlier is applied to these sets as well.

Table 4.3: Magnetic structure factors computed are presented as $|F_{hkl}|^2$ (normalized) for the magnetic reflections (*hkl*) using Basis vectors (BVs) of the Irreducible representation(IR) belonging to *A*-site.

IR	BVs	F_{111}	F_{400}	F_{220}	F_{331}	F_{422}	F_{200}
	ψ_1	0.45	0.63	1	0.26	0.34	0
Γ10	ψ_2	0.45	0	0.5	0.14	0.14	0
	ψ_3	0.45	0.63	0.5	0.14	0.34	0
	ψ_4	0	0	0	0	0	0
Γ7	ψ_5	0	0	0	0	0	0
	ψ_6	0	0	0	0	0	0

Table 4.4: Magnetic structure factors computed are presented as $|F_{hkl}|^2$ (normalized) for the magnetic reflections (*hkl*) using Basis vectors (BVs) of the Irreducible representation(IR) belonging to *B*-site.

IR	BVs	F_{111}	F_{400}	F_{220}	F_{331}	F_{422}	F_{200}
	ψ_1	0.23	0.63	0	0.13	0	0
	ψ_2	0.03	0	0	0	0	0
Γ10	ψ_3	0.23	0	0	0.07	0	0
	ψ_4	0.08	0	0.03	0.04	0.02	0.08
	ψ_5	0.23	0.63	0	0.07	0	0
	ψ_6	0.08	0	0.03	0.04	0	0
	ψ_7	0.08	0	0.06	0	0	0
Γ7	ψ_8	0.2	0	0.03	0.04	0.03	0.08
	ψ_9	0.2	0	0.03	0.04	0	0
Γ6	ψ_{10}	0.32	0	0.06	0.09	0.03	0.11
	ψ_{11}	0.32	0	0.06	0.09	0.03	0.11
Γ3	ψ_{12}	0.02	0	0	0.04	0.01	0.05

4.5.2 Magnetic Space Groups (MSGs)

The magnetic structure was independently arrived at using magnetic space groups approach. In this regard, k-SUBGROUPSMAG and MAXMAGAN [94] tools provided in connection with Bilbao Crystallography Server were used [95].
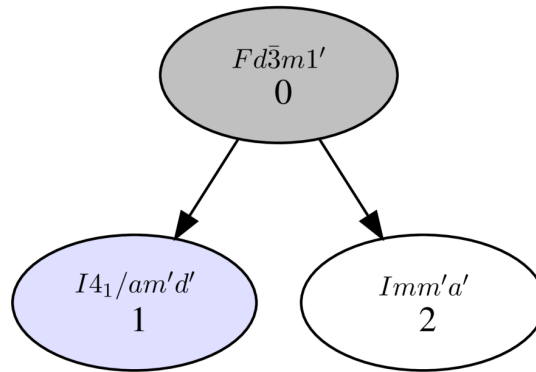
Figure 4.11: Graph obtained with k-SUBGROUPSMAG [94] of all possible magnetic symmetries for a magnetic ordering with propagation vector $k = (0, 0, 0)$ in a structure with space group $Fd\bar{3}m$ and Wyckoff positions $16c$ and $8b$. This listing is limited to only maximal subgroups.

Graph 4.11 shows only maximal subgroups corresponding to parent space group $Fd\bar{3}m$ and single propagation vector $k = (0, 0, 0)$ corresponding to Wyckoff positions $16c$ (*B*-site) and $8b$ (*A*-site). We could identify these system orders according to $141.557.I4_1/am'd'$ (representation mGM4+).

4.5.3 Zero Field NPD Refinement

The temperature scans of neutron powder diffraction (NPD) in zero-field measurements reveal major magnetic reflections such as (111) and (220) ordering at T_C and single (200) reflection ordering at T_{NC}. In order to understand the origin and behavior of said magnetic reflections, reasonable magnetic structure models that are consistent with the

propagation vector $k = (0, 0, 0)$ were identified using representational analysis approach and magnetic structure factor computation (and from MSGs). Incidentally, the identified magnetic structure is consistent with the magnetic structures of other spinel vanadates. All the basis vectors identified belong to IR $\Gamma 10$ for both A and B sites. The magnetic structure thus determined is constituted of ferromagnetic basis vector on A-site, ψ_A^1 (FM), and combination of ferromagnetic ψ_B^1 (FM) and anti-ferromagnetic ψ_B^2(AFM) bais vectors on B-site, represented as follows:

$$\vec{M}_A = \mu_{A(FM)} \cdot \vec{\psi}_A^1 \tag{4.1}$$

$$\vec{M}_B = \mu_{B(FM)} \cdot \vec{\psi}_B^1 + \mu_{B(AFM)} \cdot \vec{\psi}_B^2 \tag{4.2}$$

Where $\vec{M}_A$ and $\vec{M}_B$ are magnetic structures of A and B sublattices. $\mu_{A(FM)}$, $\mu_{B(FM)}$, and $\mu_{B(AFM)}$ are lengths of the moments that need to be refined with respect to neutron diffraction data. Here, ψ_B^2(AFM) always lies in the plane perpendicular to ψ_B^1 (FM). The computed structure factors suggest that ordering (200) reflection originates from ψ_B^2(AFM). Thus, emergence of (200) reflection at T_{NC} indicates canting of spins on B-site. However, the (200) reflection is an order of magnitude smaller than (111). Thus we expect the B-site moments to undergo only a tiny canting.

The zero field neutron diffraction data in range 2–300 K were used to refine lengths of the moments in Eqs. 4.1 and 4.2. The sign of refined moment lengths shows that A and B sub-lattices are antiferromagnetically coupled, which is consistent with expected ferrimagnetic ordering. Since the net contributions from ψ_B^2(AFM) cancel out, total moment μ_{total} can be considered simply as scalar sum of FM moments from A and B subalattices, represented as follows:

$$\mu_{total} = \mu_{A(FM)} + \mu_{B(FM)} \tag{4.3}$$

The μ_{total} as a function of the temperature follows low field magnetization perfectly. Thus, the observed magnetization reversal comes up as a relative balance between two sublattices, indicating that the magnetization reversal phenomenon can be observed without applying magnetic

fields. Furthermore, temperature dependency of μ_{total} obtained from the refinement of neutron diffraction results in the applied field of 2 T shows the killing of magnetization reversal phenomena. In this case $\mu_{\text{A(FM)}}$ is consistently longer than $\mu_{\text{B(FM)}}$ at all temperatures.

It is important to note here that individual magnetic contributions from *B*-site ions could not be distinguished decisively from the diffraction data. Thus the prominent role of Vanadium ordering as the cause for magnetization reversal as predicted by Menyuk *et al.* [2] cannot be tested.

4.5.4   Refinement of NPD Data in Magnetic Field

The neutron diffraction data in applied magnetic field from E6 and E9 were refined using the same model as zero-field but without the ψ_B^2(AFM) basis vector. As explained before, the reflection (200) is associated with the ordering of the ψ_B^2(AFM) basis vector. However, the (200) falls exactly on the diffused background originating from the ethanol–methanol mixture, which is used for sake of fixing the crystallites while applying magnetic fields. Thus the tiny peak (200) cannot be refined unambiguously. Accordingly, for field data the following model was used.

$$\vec{M}_A = \mu_{A(FM)} \cdot \vec{\psi}_A^1 \tag{4.4}$$

$$\vec{M}_B = \mu_{B(FM)} \cdot \vec{\psi}_B^1 \tag{4.5}$$

Figure 4.12 presents refined neutron diffraction data measured at 2 T and 140 K using E6 diffractometer with $\lambda = 2.66$ Å. The net magnetic moment calculated using Eq. 4.3 follows a similar trend as the magnetization measured with fields above 0.25 T. In this case, the *A* sublattice moments are consistently longer than the moments of *B* sublattice.

61
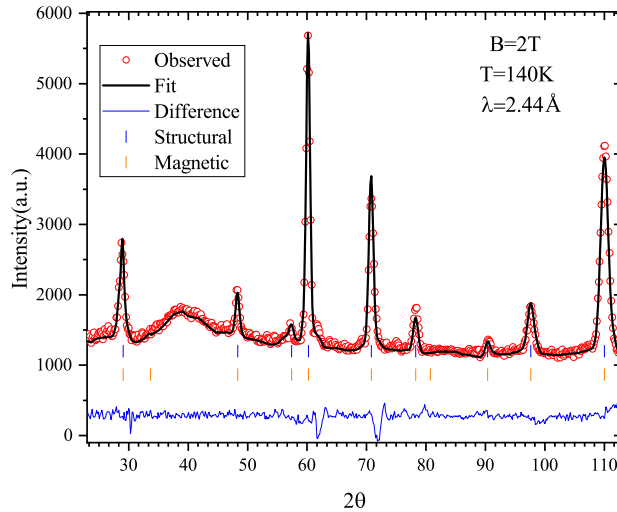
Figure 4.12: Neutron-diffraction patterns measured on E6 at 2 T and 140 K with wavelengths 2.44 Å and fits from the Rietveld refinement. The asterisk indicates impurity peaks.

4.6 Muon Spin Relaxation

The EMU spectrometer at ISIS Neutron and muon source was used to perform ZF-μ^+SR and LF-μ^+SR measurements on the polycrystalline Co$_2$VO$_4$ sample. The polycrystalline Co$_2$VO$_4$ sample amounting to 2.5g was placed in a titanium holder with an observation window of diameter 24mm. The silver mask was used to reduce the background.

The detector efficiency parameter 'α' was determined by performing weak transverse field measurement at high temperature, i.e., at T = 283K, a weak transverse field of 2 mT was applied to determine the 'α' = 1.0402. Asymmetry $A(t)$ is given by Eq. 3.27.

The ZF-μ^+SR temperature scans were performed at various temperatures in 10K–250K. The LF-μ^+SR measurements were performed at 250, 125, 75, and 10 K with applied fields of 5 mT, 50 mT, 0.2 T, and

0.3 T. In figure 4.13, the Asymmetry spectra are presented. For the reader's attention, it is crucial to note that in the manuscript the results are presented in terms of polarization instead of asymmetry for ease of interpretation, where $A(0) = 0.24$ equates to full polarization, i.e., $P_{z_1}(0) + P_{z_2}(0)$.
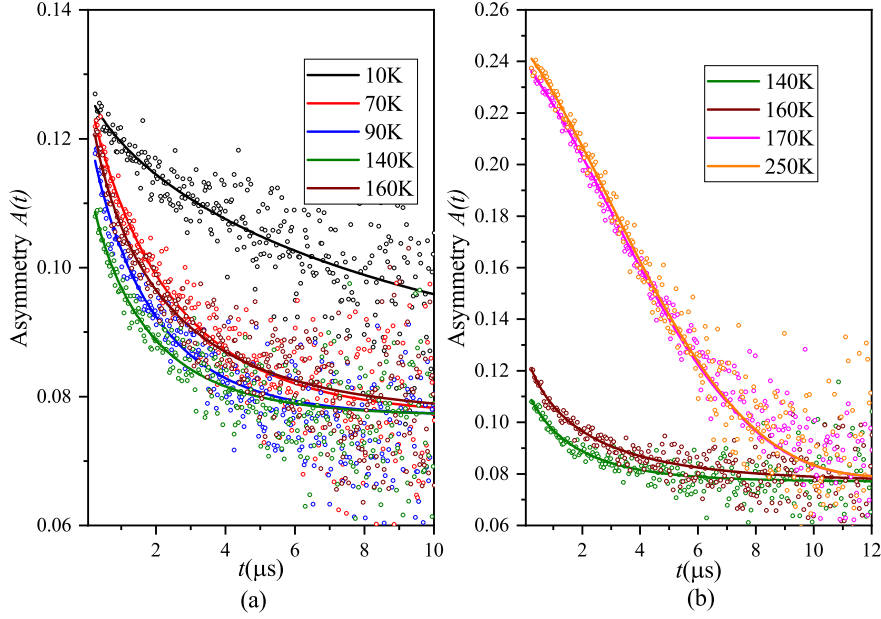
Figure 4.13: Representative ZF-μ^+SR Asymmetry vs time spectra for Co$_2$VO$_4$ polycrystalline sample.(a) $T \leq 160K$. (b) $140K \leq T \leq 250K$.

Normalized sample polarization when muons are stopped in the sample as a function of temperature for ZF-μ^+SR follows the magnetization results. However, interesting insights come from the relaxation rate 'λ' as a function of temperature. The relaxation rate is maximum in the proximity of T_{NC}. As the sample is cooled, the 'λ' drops significantly, i.e., strongest T_1-relaxation at 125 K, which decreases consistently while cooling down. Independently, the *ab-initio* DFT calculations showing *delocalized* calculation are akin to high temperature observations, while the *localized* calculations emulate sign change observed below T_{MR}. Thus, we conclude that the relaxation rate indi-

cates gradual charge localization on the *B*-site at low temperatures. These results presented an entirely new perspective to a fundamental understanding of the magnetization reversal phenomenon in this system.

Using K. P. Belov's 'Weak sublattice' model, we try to understand the microscopic reason for *delocalized–localized* crossover leading to the magnetization reversal phenomenon. Belov had used this model to explain the compensation behavior in Fe$_3$O$_4$ [73]. Following his arguments, we speculate that the delocalized electrons on *B*-site form a weak sublattice that goes parallel to *B*-site moment in the localization regime, i.e., for $T < 65$ K. This contribution of the weak sublattice to net moment shifts the balance in magnetization, creating the magnetization reversal crossover. On the other hand when the magnetic field greater than the strength of the weak sublattice is turned on, the weak sublattice moments tend to polarize along the applied field, i.e., going parallel to the *A*-site moments. The weak sublattice moments in this case favor *A*-site moments, thus killing the magnetization reversal. Based on the magnetization studies, we speculate that the strength of this weak sublattice cannot be greater than 0.25 T.

4.7 Conclusion & Outlook

Magnetization results are successful (Fig. 1 in the manuscript) in identifying collinear, non-collinear, and magnetization reversal temperature anomalies. However, the fourth anomaly at low temperature can be associated with one of the impurities, i.e., Co$_3$V$_2$O$_8$. This claim is supported by meta-magnetic behaviors of low-temperature heat capacity (Fig. 4.10) and hysteresis curves (Fig. 4.5).

Analysis of neutron diffraction shows that the interplay of *A*-site moments and *B*-site (net) out of plane moments indeed results in observed magnetization, including magnetization reversal crossover(Fig. 4 in manuscript). Application of magnetic field of 2 T makes *A*-site take the presidency, thus killing the magnetization reversal(Fig. 5 in

manuscript). These results are consistent with Néel's molecular field approach for ferrimagnetic compensation [36, 96].

Relaxation rate as a function of temperature (Fig. 6(b) in manuscript) observed in ZF-μ^+SR presents T_1-relaxation, that is maximum at T_{NC} and dropping sharply as the sample is cooled. This observation complements the DFT calculation; the DFT result suggests crossover from *delocalization* → *localization* of charges, leading to the observed magnetization reversal crossover.

Finally, the answers to the research questions framed at the beginning of this chapter can be summarized as follows:

1. Diffraction results and magnetic structure analysis were not able to distinguish between vanadium and cobalt spins. Thus we could only conclude that at T_C, both A- and B-site moments start ordering, and at T_{NC} B-site moments start canting. However, it is intriguing to notice that below T_{NC} the muon spin relaxation rate starts dropping, indicating that the B-site canting has some role in magnetization reversal. Spectroscopic measurements could help in distinguishing between the vanadium and cobalt spins on the B-site.

2. The fundamental driving mechanism for vanadium spin canting becomes irrelevant. However, we have provided the speculative model describing the microscopic mechanism for magnetization reversal.

3. The applied magnetic field studies with neutron diffraction and bulk measurements have shown that the magnetization reversal phenomenon is not field-dependent. Magnetic structure refinement has shown that the ferrimagnetic compensation between two sub-lattices is the main cause for magnetization reversal.

The results presented hitherto provide a consistent picture based on Magnetization, neutron diffraction, μ^+SR, and DFT calculation. However, I need to admit that there is still some information lacking for

a complete understanding of the magnetism in Co$_2$VO$_4$. The X-ray magnetic circular dichroism (XMCD) measurements at 5 T were performed by N. Anderson and D. Vaknin [97]. The preliminary analysis of these results has shown flipping of *B*-site V^{4+} and *A*-site Co^{2+} spins at 75 K. These results are not consistent with neutron diffraction, μ^+SR, and DFT. Thus, detailed analysis of the results and DFT modeling (using FDMNES) need to be performed to understand these results well.

Paper I

Magnetization reversal driven by electron localization-delocalization crossover in the inverse spinel Co_2VO_4.

Magnetization reversal driven by electron localization-delocalization crossover in the inverse spinel Co$_2$VO$_4$

Abhijit Bhat Kademane [1,*,†] Churna Bhandari [2,*,‡] Durga Paudyal [2,3] Stephen Cottrell,[4] Pinaki Das,[2] Yong Liu [2]
Yuen Yiu,[2] C. M. Naveen Kumar [5,6] Konrad Siemensmeyer [7] Andreas Hoser,[7] Diana Lucia Quintero-Castro,[1]
David Vaknin [2,8] and Rasmus Toft-Petersen [9,10,§]

[1]*Department of Mathematics and Physics, Universitetet i Stavanger, 4036 Stavanger, Norway*
[2]*Ames Laboratory, Iowa State University, Ames, Iowa 50011, USA*
[3]*Department of Electrical and Computer Engineering, Iowa State University, Ames, Iowa 50011, USA*
[4]*ISIS Facility, STFC Rutherford Appleton Laboratory, Harwell Science and Innovation Campus,
Chilton, Didcot, Oxon OX11 0QX, United Kingdom*
[5]*Institute of Solid State Physics, Vienna University of Technology, Wiedner Hauptstrae 810, 1040 Vienna, Austria*
[6]*AGH University of Science and Technology, Faculty of Physics and Applied Computer Science, 30-059 Kraków, Poland*
[7]*Helmholtz Zentrum Berlin für Materialien und Energie, D-14109 Berlin, Germany*
[8]*Department of Physics and Astronomy, Iowa State University, Ames, Iowa 50011, USA*
[9]*Department of Physics, Technical University of Denmark, DK-2800 Kongens Lyngby, Denmark*
[10]*European Spallation Source, Partikelgatan 2, 224 84 Lund, Sweden*

Neutron diffraction, magnetization, and muon spin relaxation measurements, supplemented by density functional theory (DFT) calculations are employed to unravel temperature-driven magnetization reversal in inverse spinel Co$_2$VO$_4$. All measurements show a second-order magnetic phase transition at $T_C = 168$ K to a collinear ferrimagnetic phase. Neutron diffraction measurements reveal two antiparallel ferromagnetic (FM) sublattices, belonging to magnetic ions on two distinct crystal lattice sites, where the relative balance between the two sublattices determine the net FM moment in the unit cell. As the evolution of the ordered moment with temperature differs between the two sublattices, the net magnetic moment reaches a maximum at $T_{NC} = 138$ K and reverses its sign at $T_{MR} = 65$ K. The DFT results suggest that the underlying microscopic mechanism for the reversal is a delocalization of the unfilled $3d$-shell electrons on one sublattice just below T_C, followed by a gradual localization as the temperature is lowered. This delocalized-localized crossover is supported by muon spectroscopy results, as strong T_1 relaxation observed below T_C indicates fluctuating internal fields.

DOI: 10.1103/PhysRevB.105.094408

I. INTRODUCTION

AB_2X_4-type spinel compounds, with tetrahedral A sites and octahedral B sites, have been an anchoring point for some of the earliest work on magnetism that led to the seminal Néel [1] and Yafet-Kittel [2] models. The spinel (and the inverse-spinel) compounds display a complex interplay among lattice, spin, charge, and orbital degrees of freedom [3], where intriguing phenomena emerge [4,5]. Indeed, interest in these systems persists, as they exhibit exotic magnetic phenomena, such as multiferroic effects and the spin-liquid state that result from spin-orbit coupling and geometric frustration associated with the pyrochlore sublattice of the B site [6,7].

Magnetization reversal (MR) is a crossover phenomenon, where the interplay of the ordering of two or more antiparallel magnetic sublattices results in spontaneous reversal of bulk

magnetization [8–10]. Additionally, the MR phenomenon can also occur due to an imbalance of spin and orbital moments. Néel [1] provided a phenomenological mean-field theory to explain the interplay of two antiparallel ferromagnetic (FM) sublattices in some ferrimagnetic systems. Subsequently, Belov [11,12] proposed the role of delocalized electrons acting as a weak magneto-electronic sublattice as a driving mechanism for compensation phenomena in magnetite.

A prototypical class of spinel compounds is the vanadate of type AV_2O_4 and its inverse-spinel counterpart A_2VO_4. At high temperatures, these systems form a cubic structure with space group $Fd\bar{3}m$. For AV_2O_4 with a nonmagnetic transition metal ion, such as Mg^{2+} or Zn^{2+}, in the A site, a cubic-to-tetragonal phase transition accompanied by an antiferromagnetic (AFM) phase has been reported [13,14]. On the other hand, magnetic ions on the A site, such as in MnV$_2$O$_4$, FeV$_2$O$_4$, or CoV$_2$O$_4$, show a multitude of structural and magnetic transitions by virtue of coupled spin and orbital degrees of freedom [15–19]. Specifically, for CoV$_2$O$_4$, orbital glasslike behavior has been reported [20,21] and *spin-ice rules* have been outlined in studies of MnV$_2$O$_4$ and FeV$_2$O$_4$ [15,16]. Additionally, CoV$_2$O$_4$ is

*These authors contributed equally to this work.
†abhijit.bhatkademane@uis.no
‡cbb@ameslab.gov
§rasp@fysik.dtu.dk

known to sit on the edge of the itinerant electron limit [22]. The inverse-spinel vanadate counterparts (of type A_2VO_4), which are more complex due to random cation distribution, have yet to be thoroughly explored. Indeed, the intriguing MR phenomenon was observed in inverse spinel Co_2VO_4 [8]. It has been proposed that the cation distribution of Co_2VO_4 is $Co_A^{2+}(Co^{2+}V^{4+})_B O_4^{2-}$ [8,23], which has been subsequently confirmed by x-ray photoelectron spectroscopy measurements in Ref. [24]. Additionally, magnetic interaction mechanisms in Co_2VO_4 have been proposed using semi-empirical rules for magnetic interactions in spinels [8,25]. While temperature-driven MR for Co_2VO_4 and Co_2TiO_4 has been experimentally explored [8,26–28], the fundamental driving mechanism behind MR in the inverse spinels remains to be understood.

Here, we examine the temperature evolution of magnetic structures using neutron diffraction, magnetization, polarized muon spectroscopy, and electronic structure calculations of Co_2VO_4. We establish multiple phase transitions in the magnetically ordered phase as well as temperature-driven MR. Neutron diffraction reveals the structure to be composed of two nearly balanced antiparallel FM sublattices, on the A and B sites, giving rise to a net ferrimagnetic phase that evolves with temperature. A significant difference between the temperature evolution of the ordered moment of the two sublattices causes a tipping of this balance, giving rise to a change in sign of the net magnetic moment in the unit cell.

To shed light on the underlying causes of such a tipping of the ferrimagnetic balance, we performed density functional theory (DFT) calculations, with *delocalized* calculation addressing the high-temperature phase, and *localized* calculation for low temperatures. The DFT results are shown to be consistent with MR. Using muon spectroscopy, dynamic T_1 relaxation is observed in an extended temperature interval just below T_C, indicative of magnetic moment fluctuations at high temperatures. These fluctuations support our interpretation of a gradual crossover between delocalization and localization of electrons as the underlying microscopic mechanism for the MR.

II. EXPERIMENTAL AND COMPUTATIONAL DETAILS

The polycrystalline sample of Co_2VO_4 was prepared using a solid-state reaction as described in Ref. [29]. The x-ray diffraction (XRD) measurement confirms the formation of Co_2VO_4 spinel. Rietveld refinement of neutron diffraction and XRD data (at 300 K) confirm the cubic $Fd\bar{3}m$ symmetry. Due to A/B site inversion ($A = 8b$ tetrahedral and $B = 16c$ octahedral) the formal chemical formula of Co_2VO_4 is $Co_\nu^{2+}V_{1-\nu}^{4+}[V_\nu^{4+}Co_{2-\nu}^{2+}]O_4$, where ν is the inversion parameter, and the B site cations are enclosed in brackets. The refinement yields that the degree of inversion $\nu \simeq 1$, i.e., the actual $Co_A^{2+}[V^{4+}Co^{2+}]_B O_4$, where Co^{2+} occupies the A site and the remaining Co^{2+} and V^{4+} are distributed evenly in the B site. Two impurity phases are identified. Peaks at 2.66 and 3.03 Å^{-1} correspond to the $Co_3V_2O_8$ phase [30], while peaks at 2.56 and 2.94 Å^{-1} corresponds to CoO structural phase. Additionally, at $T_N \simeq 290$ K, the CoO impurity phase orders into an AFM state that is incommensurate with its crystal structure corresponding to propagation vector $k = (\frac{1}{2}, \frac{1}{2}, \frac{1}{2})$

[31]. This phase can be identified from the magnetic peak at 1.28 Å^{-1}. Unlike the common spinel counterparts [15,18], we find no structural transitions in Co_2VO_4 at all measured temperatures. Nonetheless, we observed an insignificant shrinking of the unit cell that appears to saturate at $\approx$65 K.

Magnetization measurements were performed on a pellet of mass 6.15 mg and carried out using a superconducting quantum interference device (Quantum Design MPMS) magnetometer for various applied magnetic fields in the range of 0.03–7 T and 2–350 K, performing both zero-field-cooled (ZFC) and field-cooled (FC) measurements. Neutron powder diffraction (NPD) was performed on a 2 g polycrystalline sample on the time-of-flight powder diffractometer POW-GEN [32] located at the Spallation Neutron Source at Oak Ridge National Laboratory. The measurements were carried out with neutrons of central wavelengths 1.333 and 3.731 Å. The sample was loaded in a vanadium can which was attached to the cold end of a cryostat to reach temperatures in the range $2 \leqslant T \leqslant 300$ K. NPD in applied magnetic fields was performed using E6 [33] and E9 [34] diffractometers at the BER II reactor at the Helmholtz-Zentrum Berlin. Powder sample amounting 3.5 g was dispersed in deuterated methanol-ethanol mixture, which freezes into an amorphous glass upon cooling, and thereby fixes the powder orientation while applying a magnetic field. The E6 diffractometer was used to perform the temperature scans ranging from 15 to 200 K with an applied magnetic field of 0.25 and 2 T with wavelength 2.44 Å , and the E9 diffractometer was used to perform temperature scans ranging from 50 to 250 K with an applied magnetic field of 0, 0.05, and 0.5 T with wavelength 1.81 Å following FC protocol. Refinements of the diffraction data were carried out using FULLPROF [35].

The EMU spectrometer [36] at the ISIS Neutron and muon source was used to perform zero applied field muon spin relaxation (ZF-μ^+SR) and longitudinal field muon spin relaxation (LF-μ^+SR) measurements where the applied magnetic field and muon spin are collinear on the polycrystalline sample. The polycrystalline Co_2VO_4 sample amounting to 2.5 g was placed in a titanium holder with a 24-mm-diameter window. Muons falling outside the sample window were stopped in a silver mask, giving a nonrelaxing background. Here, 100% spin-polarized muons are produced by the source, implanted in the sample, and their time evolution measured. The time evolution of muon polarization is given by $P_z(t)$. A normalized sample polarization immediately after muon implantation $P_s(0)$ was obtained after background correction. The ZF-μ^+SR scans were performed at various temperatures in the 10–250 K range. To elucidate dynamic aspects, LF-μ^+SR measurements were performed at 250, 125, 75, and 10 K with applied fields of 0.005, 0.05, 0.2, and 0.3 T. The data were analyzed using the muon analysis module of MANTID [37].

To understand the MR in Co_2VO_4, we carried out two sets of first-principles electronic structure calculations: (i) *delocalized* and (ii) *localized*. The delocalized calculations were performed using DFT in conjunction with the generalized gradient approximation (GGA) for exchange-correlation functional in all-electron projected augmented plane-wave formalism implemented in the Vienna *Ab initio* Simulation Package including spin-orbit coupling (SOC) [38,39]. We
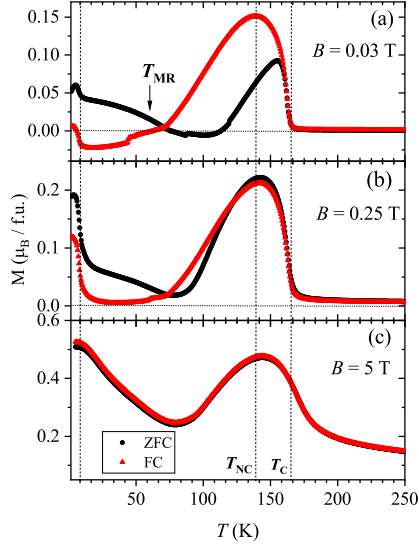
FIG. 1. Temperature dependence of zero-field-cooled (ZFC; black circle) and field-cooled (FC; red triangle) magnetization measurements performed for applied magnetic fields 0.03, 0.25, and 5 T. T_C and T_{NC} represent the transition temperatures to collinear and noncollinear magnetic structures, respectively, as explained in the text. Magnetization reversal temperature is represented by T_{MR} for $B = 0.03$ T

used a plane-wave cutoff energy of 500 eV and $4 \times 4 \times 4$ **k**-mesh for the Brillouin zone integration. Structure optimization is performed by randomly replacing 50% V_B with Co_B in the bulk CoV_2O_4 structure that has the lowest total energy among all the considered configurations.

III. RESULTS AND DISCUSSIONS

Figure 1 shows the temperature (T) dependence of the ZFC and FC magnetization (M) of Co_2VO_4 at applied magnetic field $B = 0.03$, 0.25, and 5 T. Four features are identified for $B = 0.03$ T. First, a sharp rise is observed at $T_C = 168(1)$ K (C = collinear) corresponding to ferrimagnetic response and, second, with an onset of a decrease at $T_{NC} = 138(8)$ K (NC = noncollinear), for both FC and ZFC. The third feature occurs at the temperature range $T_{MR} \sim 65$–130 K, where the magnetization reverses, dependent on the cooling protocol (i.e., FC or ZFC). Here, T_{MR} can also be refereed to as compensation temperature [1,11]. Finally, <20 K, there is an upturn in magnetization, suggestive of a metamagnetic behavior, likely due to the $Co_3V_2O_8$ impurity phase [40]. MR does not occur for fields $>\sim0.25$ T, and eventually, the ZFC and FC curves overlap for fields >5 T, and the temperature dependence becomes reversible.

The magnetization at T_C for $B = 0.1$ T is $0.2 \, \mu_B$/f.u. (not shown), which is lower than that of CoV_2O_4 [41]. A high spin configuration $S = \frac{3}{2}$ ($3 \, \mu_B$) for Co_A^{2+} and $S = 1$ ($2 \, \mu_B$) for

V_B^{3+} have been reported for CoV_2O_4 [18]. This indicates the reduced magnetization in Co_2VO_4 is due to antiparallel Co_A and Co_B/V_B (ferrimagnetic) assuming high spin configuration $S = \frac{3}{2}$, for Co^{2+} and $S = \frac{1}{2}$ for V_B, implying an oxidation state of 4+ for V. As discussed below, DFT calculations confirm the valence states of Co_B and V_B as well their magnetic ordering in the *localized solution*.

The NPD patterns for 140 and 25 K are presented in Figs. 2(a) and 2(b). Consistent with the aforementioned magnetic susceptibility, Fig. 3 shows the emergence of the (111) and (220) magnetic reflections at $T = 168(1)$ K. At a lower temperature [=138(2) K], a weak (200) magnetic reflection is also observed [inset of Fig. 2(a)]. We emphasize that (200) is forbidden by $Fd\bar{3}m$. In the case of MnV_2O_4, observation of (200) is linked to spin canting of the spinel B site and a structural transition [15]. The temperature dependence of the three magnetic Bragg reflections is shown in Fig. 3. These curves are fitted to a power law function. The critical temperature obtained for reflections (111) and (220) is $T_C = 167.8 \pm 0.4$ K and for (200) at $T_{NC} = 138.5 \pm 7.5$ K. We also note that the critical exponents associated with (111) and (200) are different, at 0.71 ± 0.02 and 0.5 ± 0.1, respectively.

To restrict the refinement of the neutron powder data, we exclude the irreducible basis vectors (BVs), on both the A and B sites, that are inconsistent with the strongest observed peaks in the powder diffraction pattern. These BVs are [for $Fd\bar{3}m$ and propagation vector $k = (0, 0, 0)$] found using BASIREPS [35] and SARAH [42]. We find that the simplest model consistent with both magnetization and powder diffraction data consists of BVs from the IR $\Gamma10$ with A- and B-sublattice moments arranged antiparallel. The magnetic representation in this case corresponds to Shubnikov space group $I4_1/am'd'$ (representation mGM4+) [43,44]. This picture is consistent with observations of other spinel vanadates [15,18] as well as recommendations made for magnetic interactions in Co_2VO_4 [8]. Table I lists $|F_{hkl}|^2$ for prominent magnetic reflections calculated using these BVs. Note that the intensity on (200) could be explained only by ψ_B^2 (AFM), while (220) has no contributions from ψ_B^1 (FM). As seen in Table I, FM order on the A site (ψ_A^1) gives rise to intensity in both the (220) and (111) reflections, while FM order on the B site (ψ_B^1) only gives rise to intensity on (111). The FM ordered moment on the A site can therefore be explicitly distinguished from that of the B site, and the relative magnitudes of the ordered moments can be directly extracted from the refinement. While the net ferrimagnetic moment can be directly deduced from NPD, it cannot distinguish individual contributions from Co_B and V_B. We note that combination of ψ_B^1 (c axis) and ψ_B^2(ab pane) leads to the commonly observed two-in-two-out configuration in pyrochlore structures [15].

The refinements of NPD data at $B = 0$ T at the temperature range 5–250 K yield the sublattice magnetic moments as shown in Fig. 4(a). To compare sublattice magnetizations, we present the refined magnetic moments normalized to formula units. Refined moments on A and B sites are labeled as $\mu_{A(FM)}$, $\mu_{B(FM)}$, and $\mu_{B(AFM)}$, respectively. The total moment $\mu_{total} = \mu_{A(FM)} + \mu_{B(FM)}$ is shown in Fig. 4(b). Contributions from $\mu_{B(AFM)}$(AFM, see Table I) cancel out and thus do not contribute to the total moment. As shown, μ_{total} as a function of temperature exhibits magnetic behavior that resembles the
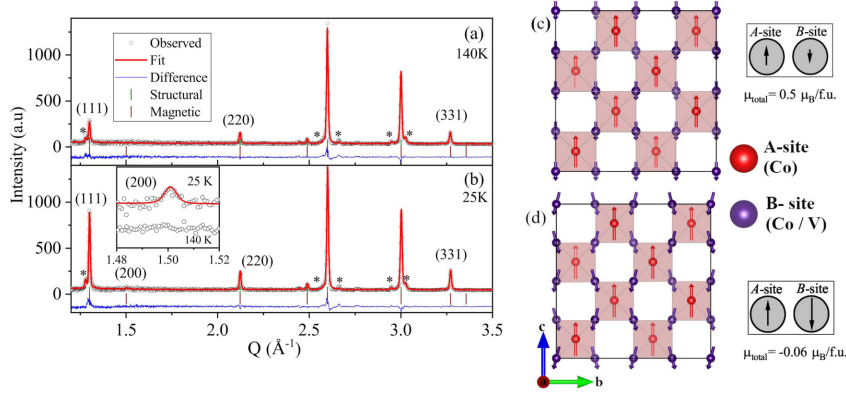
FIG. 2. Neutron diffraction patterns (NPD; black open circles), fits from the Rietveld refinement (red solid lines), and their differences (blue solid lines). The vertical bars are the expected Bragg peak positions as mentioned in the panels. The asterisks indicate impurity peaks. NPD observed (measured on POWGEN) (a) $T = 140$ K and (b) $T = 25$ K, corresponding to the data collected with center wavelengths 1.333 Å. In the inset of (b), one can see the emergence of (200) between 140 and 25 K. (c) Magnetic structure of Co_2VO_4 at 140 K. (d) Magnetic structure at 25 K. The A site is occupied by Co (red), whereas B site occupancy is shared between Co and V (purple).

magnetization shown in Fig. 1(a). The two sublattice magnetizations obtained at low temperature are similar, consistent with the B site [$Co^{2+}V^{4+}$] ground state electronic structure. Indeed Fig. 4(b) shows three identified temperatures in magnetization T_C, T_{NC}, and T_{MR}. Similar analysis of the diffraction patterns under magnetic field $B = 2$ T also yield distinguishable $\mu_{A(FM)}$ and $\mu_{B(FM)}$. However, μ_{total} at $B = 2$ T does not show MR (Fig. 5), as $\mu_{A(FM)}$ is always larger than $\mu_{B(FM)}$ for all temperatures, consistent with the observation >0.25 T (Fig. 1). It is not possible to extract $\mu_{B(AFM)}$ reliably in these measurements, as the defused signal from ethanol-methanol mixture overshadows the weak (200) peak.

To determine the possible dynamic origin of sublattice ordering, we employ polarized muon spectroscopy. The ZF-μ^+SR measurements were performed at various temperatures in the region 10–250 K. In the paramagnetic region ($T >$

FIG. 3. Temperature dependencies of integrated intensities of the Bragg peak (111), (220), and (200) reflections for $B = 0$ T. The solid lines represent respective power law fits. T_C features can be identified from the ordering of (111) and (220) and T_{NC} from ordering of (200).

T_C), the ZF-μ^+SR polarization spectra show temperature-independent relaxation with full polarization. This region is parameterized with static Kubo-Toyabe times exponential decay, accounting for nuclear and electronic moments [45]:

$$P_z(t) = P_{z_1}(0)\left[\exp\left(-\frac{\delta^2 t^2}{2}\right)(1 - \delta^2 t^2)\frac{2}{3} + \frac{1}{3}\right]$$
$$\times\, e^{-\lambda t} + P_{z_2}(0), \tag{1}$$

where P_{z_1} represents the polarization associated with the sample, and P_{z_2} is the nonrelaxing polarization from muons missing the sample, which could also include a nonrelaxed component present in the sample. Here, δ accounts for the relaxation rate due to the coupling of nuclear moments and muons and λ for the relaxation rate due to electron moments and muons coupling. At T_C, a sharp loss of the initial polarization is observed. This is typical for a magnetically

TABLE I. Magnetic structure factors computed are presented as $|F_{hkl}|^2$ (normalized) for the magnetic reflections (hkl) using basis vectors (BVs) of the irreducible representation (IR) belonging to A and B sites.

Site	IR		BVs	$|F_{111}|^2$	$|F_{200}|^2$	$|F_{220}|^2$	$|F_{331}|^2$
A site 8b	$\Gamma 10$	ψ_A^1 (FM)	(0 0 1) (0 0 1)	0.68	0	1.00	0.27
B site 16c	$\Gamma 10$	ψ_B^1 (FM)	(0 0 1) (0 0 1) (0 0 1) (0 0 1)	0.51	0	0	0.2
		ψ_B^2 (AFM)	(−1 −1 0) (1 1 0) (−1 1 0) (1 −1 0)	0.1	0.04	0.03	0.04

FIG. 4. (a) The magnitude of A- and B-sublattice moments obtained from Rietveld refinement for $B = 0\,\mathrm{T}$. (b) Total moment (per f.u.) calculated by adding ferromagnetic (FM) moments. Temperature dependence of total moment emulates the magnetization reversal as observed in magnetization measurement.

FIG. 5. (a) Magnitude of A- and B-sublattice moments obtained from Rietveld refinement for $B = 2\,\mathrm{T}$. (Inset) Total moment (per f.u.) calculated by adding moments along the c direction. Temperature dependence of total moment emulates magnetization for fields > 0.25 T.

ordered system, where the missing polarization is associated with strong electronic moments, giving rise to an unresolved precession signal owing to the finite muon pulse width at the source (ISIS). Below T_C, a one-component stretched exponential decay function is sufficient to parametrize the ordered region, i.e.,

$$P_z(t) = P_{z_1}(0)\exp[-(\lambda t)^\beta] + P_{z_2}(0). \tag{2}$$

In Eq. (2), P_{z_1} represents the polarization associated with the sample, and P_{z_2} is the nonrelaxing polarization from muons missing the sample, which could also include a non-relaxed component present in the sample. Here, λ is the relaxation rate and β the stretching exponent. When $\beta = 1$, Eq. (2) turns into simple exponential decay. We find that, above T_{MR}, the best fit to the data is obtained with β fixed at 1. However, below T_{MR}, acceptable fits could only be obtained fitting β as a free parameter.

Figure 6 shows the normalized sample polarization when muons are stopped in the sample ($t = 0$) and $P_s(0)$ and relaxation rate λ are extracted from ZF-μ^+SR data as a function of temperature. Below T_C, $P_s(0)$ is reduced to $\frac{1}{3}$ of its initial value ($T > T_C$). Intriguingly, there is a further loss of polarization as t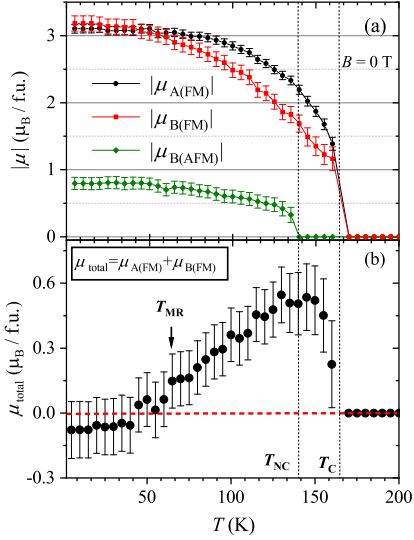he temperature is reduced below T_C, reaching a minimum at T_{NC} and only regaining the $\frac{1}{3}$ value of the initial polarization at T_{MR}. The broad dip between T_C and T_{MR} suggests that muons are experiencing changes in the magnetic structure right through the region. This is consistent with the corresponding peak in the relaxation rate, suggesting a spin fluctuation/reorientation process is driving an enhanced T_1

relaxation of the muon signal through this temperature region. Notably, there is no sharp peak in the relaxation rate at T_C, as one would expect for a typical magnetic phase transition. Fitting the low-temperature data ($T < 60$ K) with β as a free parameter shows β decreasing steadily, reaching a value ≈ 0.5 at 12 K. While we note that $\beta = 0.5$ could be a signature to glassy transition [46], typical for an inverse spinel at low temperatures [28,47], the $Co_3V_2O_8$ impurity phase is also
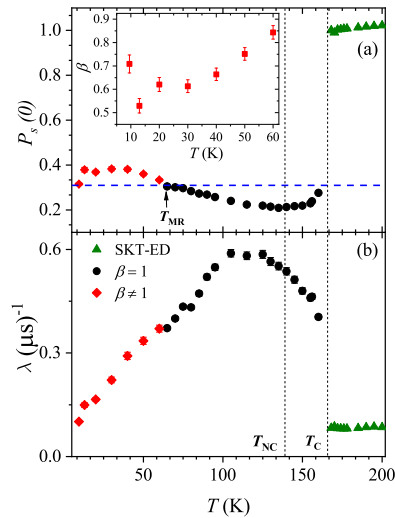
FIG. 6. (a) Initial polarization and (b) relaxation rate extracted from fits to the zero applied field muon spin relaxation (ZF-μ^+SR) polarization spectra. For $T < T_C$, fits are to Eq. (2), with β as a free parameter below T_{MR} (red points). Above T_C, fits are carried out to Eq. (1) (green points). Inset of (a) β vs T, where β reaches 0.5 at 12 K.
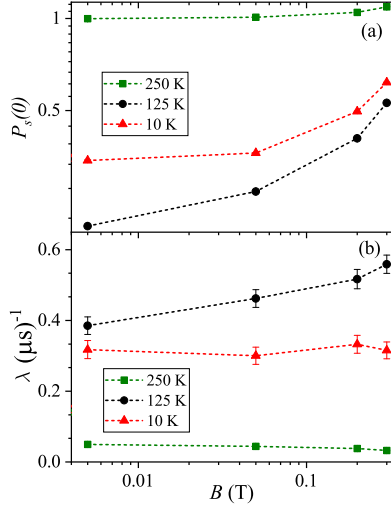
FIG. 7. (a) Initial polarization and (b) relaxation rate extracted from fits to the longitudinal field muon spin relaxation (LF-μ^+SR) polarization spectra with Eq. (2). At 125 K, complete decoupling was realized with a tiny field of 0.005 T. Due to instrument effects, $P_s(0)$ goes beyond 1 for higher fields.

likely to contribute to the measured behavior. Further work is needed to properly understand the low-temperature muon response.

Initial polarization and relaxation measurements for LF-μ^+SR up to 0.3 T were carried out at 10, 125, and 250 K. Values obtained for $P_s(0)$ and λ obtained from fitting the data to Eq. (2) with β fixed at 1 are shown in Fig. 7, with T_1 spin relaxation λ persisting at all temperatures to the highest fields measured. This suggests that spin dynamics are present at all temperatures, both in the paramagnetic regime above T_C and also in the ordered state. We note that the strongest relaxation is measured at 125 K, close to T_{MR}, a region where electron delocalization is predicted by DFT, and at this temperature, the relaxation rate [Fig. 7(b)] appears to increase with the applied field in contrast to results measured at 10 K. A clear recovery of the initial polarization is seen at the highest fields measured, although full decoupling is not achieved, with only 50% of the polarization being recovered. We suggest this is the result of both large internal fields and spin dynamics below T_C in this material.

To supplement the experimental results, we conduct *delocalized* and *localized* electronic structure calculations. For the delocalized calculations, we employ standard DFT with a GGA functional. In the localized calculations, we add the onsite electron correlation following the scheme of Dudarev *et al.* [48], in which only the effective value of onsite correlation ($U_{eff} = U - J = 4.5$ eV for 3d electrons of Co and V [49]) is meaningful. To be on equal footing, we also perform another calculation using the same value of U_{eff} and find the delocalized solution, which has higher total energy than in the

localized solution. As expected, the net magnetic moments do not change significantly with the use of U_{eff} in the delocalized results.

As shown below, the *localized* calculations are akin to the low-temperature ground state, whereas the *delocalized* ones correspond to the high-temperature ferrimagnetic phase. Both *localized* and *delocalized* calculations show similar magnetic moments for Co$_A$, while they are drastically different for Co$_B$ and V$_B$. These changes in the local magnetic moments are consistent with the low-temperature neutron diffraction results (Table II). The major contribution to the net magnetic moment is from spin (Table II), while the orbital contributions are small, and slight fluctuations for Co$_B$ are found (not shown). In the localized solution, we find canted spin structures for Co$_B$ and V$_B$ in qualitative agreement with the experimental results at 25 K (Table II). A notable prediction is the AFM alignment of Co$_A$ moments with respect to Co$_B$ with a small canting in the planar direction (Table II). For Co$_A$, the canting is not resolved experimentally. At the B site, the V$_B$ moments follow the Co$_B$ moments. These are remarkable changes in the frustrated magnetic structures of the well-known spinel vanadates, viz., FeV$_2$O$_4$ [16] and MnV$_2$O$_4$ [15], in which V$_B$ moments are two-in-two-out as observed experimentally. The calculated net magnetic moment parallel to the c direction is negative, in agreement with the low-temperature data. The discrepancy between theory and experiment in the magnitude of net magnetic moment is likely due to the choice of atomic sphere sizes used in the calculations, i.e., Co$_A$ moment $\sim$2.6 μ_B is smaller than the experiment 3.07 μ_B. We find 3d Co/V and O(2p) hybridization, which we argue may affect the magnetic moments on both Co and V. In calculations, the canting is small, which results in a large magnetic moment ($\sim$3.7 μ_B) along the z direction, which qualitatively agrees with the experiment (see Table II). Another possibility for the slight discrepancy is random occupancy of Co and V in the B sites.

Interestingly, the magnetic moments obtained with the delocalized solutions agree with the higher temperature data, indicating a more itinerant scenario [50]. The magnetic moments on the B site are sensitive to the choice of U_{eff} (i.e., localized or delocalized), while the moments on the A site remain relatively unchanged. Interatomic charge transfer from Co$_B$ to V$_B$ sites reduces the effective Co$_B$ moments. This delicate balance between Co$_A$, Co$_B$, and V$_B$ magnetic moments in the localized and delocalized limits presumably leads to the MR.

To demonstrate that the electronic configuration of Co is 3d^7 (i.e., Co^{2+}) and that of V$_B$ is 3d^1 (i.e., V^{4+}), we examine the partial density of states (PDOS) of each atom in the localized calculations. Figure 8 shows very well split-off $e_g\downarrow$ and $t_g\uparrow$ 3d states of Co$_A$ around the Fermi level due to the tetrahedral crystal field of oxygen atoms. In Co$_B$ and V$_B$, the splittings of the threefold t_{2g} states are less obvious. Because of the distorted octahedral crystal field effect [22], these states split into an a_{1g} and doubly degenerate e'_g, resulting in 3d^7, $S = \frac{3}{2}$ (occupying $e'_g\uparrow$) for Co$_B^{2+}$ as in Co$_A^{2+}$, and 3d^1, $S = \frac{3}{2}$ (occupying a_{1g}) for V$_B^{4+}$ in the localized limit as inferred from the current and earlier experiments [8]. An interesting change is in the vanadium oxidation state from V^{3+}(3d^2), which is common in the standard spinel compounds, to V^{4+}(3d^1)

TABLE II. Canted magnetic moment components (spin + orbital) (μ_x, μ_y, μ_z) of individual atom and total magnetic moments (μ_{total}) (per f.u.) in units of μ_B in Co_2VO_4 obtained from Rietveld refinement from zero field data and theory (GGA + SOC and GGA + SOC + U calculations). For oxygens, only the calculated moments are given.

Site	Atom	Experiment		Theory	
		140 K	25 K	GGA + SOC	GGA + U + SOC
A site	Co_A	(0, 0, 2.18(6))	(0, 0, 3.07(6))	(0, 0, 2.48)	(0.80, 0, 2.74)
B site	Co_B	NA	NA	(0, 0, −0.43)	(−0.81, |0.13|, −2.72)
	V_B	NA	NA	(0, 0, −1.29)	(−0.34, |0.02|, −1.02)
	$Co_B + V_B$	(0, 0, −1.68(2))	(|0.88(8)|, |0.88(8)|, −3.13(1))	(0, 0, −1.72)	(−1.15, |0.15|, −3.74)
X site	O	NA	NA	(0, 0, 0.09)	(0, 0, 0.02)
μ_{total} (μ_B/f.u.)		(0, 0, 0.50(8))	(0, 0, −0.06(7))	(0, 0, 1.14)	(−0.32, 0, −0.90)

with $S = \frac{1}{2}$, consistent with the magnetic moment [8] at low temperature. We note that Co_B^{2+} and V_B^{4+} moments change significantly in the delocalized solutions (Table II), which corresponds to high temperatures. Specifically, the magnetic moment on the Co_B is significantly reduced, suggesting a fluctuation of magnetic moment of Co_B between a low spin state Co^{3+} ($S = 0$) and a high spin state Co^{2+} ($S = \frac{3}{2}$). On the other hand, it is the opposite for V_B. This is expected because itinerant electrons can hop easily from Co_B to V_B due to a narrow splitting of t_{2g} states in both atoms. These results suggest that the inverse spinel undergoes charge fluctuations $[Co^{2+}][Co^{(2+\delta)+}V^{(4-\delta)+}]O_4$, where $\delta < 1$ above T_{MR}.

The T_1 relaxation observed with μ^+SR supplements the theoretical suggestion that the B-site ions undergo charge delocalization-to-localization crossover. A similar delocal-

ization mechanism was suggested by Belov [11] in inverse spinel magnetite Fe_3O_4 employing a so-called magneto-electronic sublattice model. Fe_3O_4 is well known for its metal-insulator transition or Verwey transition [51]. Belov [11,12] proposed an electronic hopping or delocalization on the B site creating the magneto-electronic sublattice with its magnetization antiparallel to that of the two combined sublattices, leading to a decreased spontaneous magnetization. Below T_{MR} in Co_2VO_4, the delocalized electrons would gradually localize, leading to $[Co^{2+}][Co^{(2+\delta)+}V^{(4-\delta)+}]O_4 \Rightarrow [Co^{2+}][Co^{2+}V^{4+}]O_4$ (where $\delta < 1$) and thus decreasing spontaneous magnetization $< 0 \mu_B$/f.u. This is consistent with the near-perfect compensation of the two sublattice magnetizations, coexisting with an AFM ordering of the V^{+4} moments.

IV. CONCLUSIONS

Our interest in inverse cobalt vanadium spinel springs from the highly unconventional temperature-dependent magnetization of the compound, where a spontaneous MR takes place. We have performed magnetization measurements and revealed at least three distinct anomalies. NPD analysis reveals two antiparallel magnetic structures, each belonging to magnetic ions on A and B sites. The relative balance of these two structural components in essence determines the net magnetic moment in the unit cell. However, the order parameter on one site develops more moderately than that on the other site. While in itself unusual, a tipping of the magnetic balance, caused by such site-specific magnetic fluctuation, gives rise to a spontaneous flipping of the magnetization as the temperature is lowered. The MR determined at zero field is sensitive to an applied magnetic field, such that, above $B \sim 0.25$ T, instead of a reversal, a minimum in the magnetization is apparent at T_{MR}.

The root cause of this site specificity is unveiled by DFT results. The DFT calculations were performed assuming delocalized and localized electrons. We argue that the MR is a consequence of the itineracy of Co and V electrons in the B site. The *delocalized* calculations, which we associate with the behavior of the high temperature of the system (around T_C), predict relatively small net magnetic moments on the B site compared with the A site, giving rise to the net ferrimagnetic moment observed near T_C. The DFT calculations also show that the Co moments on the A site are less sensitive to temperature change with electronic configuration $Co^{2+}(3d^7)$
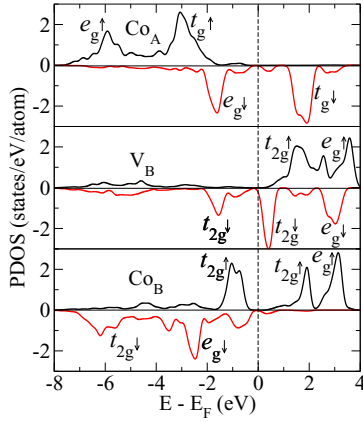
FIG. 8. Spin-resolved partial density of states (PDOS) of Co_A, Co_B, and V_B. The positive and negative values indicate PDOS of majority and minority spin electrons, respectively. The spins of Co_A are aligned antiferromagnetically with respect to Co_B and V_B. Both Co at A and B sites have $3d^7$ valence electrons, indicating the formation of a Co^{2+} ion. The distorted octahedral crystal field splits t_{2g} into a_{1g} and doubly degenerate e_g states at site B. For Co_B, two electrons occupy the lower e_g states forming a $S = \frac{3}{2}$ state, while for V_B, one electron occupies a_{1g}, yielding V^{4+} oxidation state with $S = \frac{1}{2}$.

with $S = \frac{3}{2}$. For the B site, the DFT calulations find mixed oxidation states for Co and V that at low temperatures tend toward their localized values, namely, Co^{2+} ($S = \frac{3}{2}$) (as in the A site) and V^{4+} ($S = \frac{1}{2}$). This suggests that the MR is likely driven by *delocalized*-to-localized crossover of the $3d$ electrons of the Co/V atoms in the B site. We note that quantitative disagreements between theory and experiment are expected owing to the complexities of this inverse spinel Co_2VO_4 and the random distribution of Co and V in the B site. Polarized muon spectroscopy as a function of temperature is consistent with the neutron diffraction and magnetization results but adds insights that have been predicted by our DFT calculations. It shows that highly delocalized-fluctuating magnetic moments at high temperatures gradually tend to localize at lower temperatures, in agreement with our DFT calculations.

[1] L. Néel, Propriétés magnétiques des ferrites; ferrimagnétisme et antiferromagnétisme, Ann. Phys. **12**, 137 (1948).

[2] Y. Yafet and C. Kittel, Antiferromagnetic arrangements in ferrites, Phys. Rev. **87**, 290 (1952).

[3] V. Tsurkan, H.-A. Krug von Nidda, J. Deisenhofer, P. Lunkenheimer, and A. Loidl, On the complexity of spinels: magnetic, electronic, and polar ground states, Phys. Rep. **926**, 1 (2021).

[4] Y. Yamasaki, S. Miyasaka, Y. Kaneko, J.-P. He, T. Arima, and Y. Tokura, Magnetic Reversal of the Ferroelectric Polarization in a Multiferroic Spinel Oxide, Phys. Rev. Lett. **96**, 207204 (2006).

[5] A. Ruff, Z. Wang, S. Zherlitsyn, J. Wosnitza, S. Krohns, H.-A. Krug von Nidda, P. Lunkenheimer, V. Tsurkan, and A. Loidl, Multiferroic spin-superfluid and spin-supersolid phases in MnCr₂S₄, Phys. Rev. B **100**, 014404 (2019).

[6] L. Balents, Spin liquids in frustrated magnets, Nature (London) **464**, 199 (2010).

[7] D. Bergman, J. Alicea, E. Gull, S. Trebst, and L. Balents, Order-by-disorder and spiral spin-liquid in frustrated diamond-lattice antiferromagnets, Nat. Phys. **3**, 487 (2007).

[8] N. Menyuk, K. Dwight, and D. G. Wickham, Magnetization Reversal and Asymmetry in Cobalt Vanadate (IV), Phys. Rev. Lett. **4**, 119 (1960).

[9] A. Kumar and S. Yusuf, The phenomenon of negative magnetization and its implications, Phys. Rep. **556**, 1 (2015).

[10] D. T. Adroja, S. Sharma, C. Ritter, A. D. Hillier, D. Le, C. V. Tomy, R. Singh, R. I. Smith, M. Koza, A. Sundaresan, and S. Langridge, Muon spin rotation and neutron scattering investigations of the B-site ordered double perovskite Sr₂DyRuO₆, Phys. Rev. B **101**, 094413 (2020).

[11] K. P. Belov, Ferrimagnets with a 'weak' magnetic sublattice, Usp. Fiz. Nauk [Sov. Phys. Usp.] **39**, 623 (1996).

[12] K. P. Belov, Electronic processes in magnetite (or, "Enigmas of magnetite"), Usp. Fiz. Nauk [Sov. Phys. Usp.] **36**, 380 (1993).

[13] S. Niitaka, H. Ohsumi, K. Sugimoto, S. Lee, Y. Oshima, K. Kato, D. Hashizume, T. Arima, M. Takata, and H. Takagi, A-Type Antiferro-Orbital Ordering with $I4_1/a$ Symmetry and Geometrical Frustration in the Spinel Vanadate MgV₂O₄, Phys. Rev. Lett. **111**, 267201 (2013).

[14] S.-H. Lee, D. Louca, H. Ueda, S. Park, T. J. Sato, M. Isobe, Y. Ueda, S. Rosenkranz, P. Zschack, J. Íñiguez, Y. Qiu, and R. Osborn, Orbital and Spin Chains in CoV₂O₄, Phys. Rev. Lett. **93**, 156407 (2004).

[15] V. O. Garlea, R. Jin, D. Mandrus, B. Roessli, Q. Huang, M. Miller, A. J. Schultz, and S. E. Nagler, Magnetic and Orbital Ordering in the Spinel MnV₂O₄, Phys. Rev. Lett. **100**, 066404 (2008).

[16] G. J. MacDougall, V. O. Garlea, A. A. Aczel, H. D. Zhou, and S. E. Nagler, Magnetic order and ice rules in the multiferroic spinel FeV₂O₄, Phys. Rev. B **86**, 060414(R) (2012).

[17] Q. Zhang, M. Ramazanoglu, S. Chi, Y. Liu, T. A. Lograsso, and D. Vaknin, Magnetic excitations and anomalous spin-wave broadening in multiferroic FeV₂O₄, Phys. Rev. B **89**, 224416 (2014).

[18] H. Ishibashi, S. Shimono, K. Tomiyasu, S. Lee, S. Kawaguchi, H. Iwane, H. Nakao, S. Torii, T. Kamiyama, and Y. Kubota, Small crystal distortion and long-range antiferro-orbital ordering in the spinel oxide CoV₂O₄, Phys. Rev. B **96**, 144424 (2017).

[19] Y. Nii, H. Sagayama, T. Arima, S. Aoyagi, R. Sakai, S. Maki, E. Nishibori, H. Sawa, K. Sugimoto, H. Ohsumi, and M. Takata, Orbital structures in spinel vanadates AV₂O₄(A = Fe, Mn), Phys. Rev. B **86**, 125142 (2012).

[20] R. Koborinai, S. E. Dissanayake, M. Reehuis, M. Matsuda, T. Kajita, H. Kuwahara, S.-H. Lee, and T. Katsufuji, Orbital Glass State of the Nearly Metallic Spinel Cobalt Vanadate, Phys. Rev. Lett. **116**, 037201 (2016).

[21] D. Reig-i-Plessis, D. Casavant, V. O. Garlea, A. A. Aczel, M. Feygenson, J. Neuefeind, H. D. Zhou, S. E. Nagler, and G. J.

MacDougall, Structural transition and orbital glass physics in near-itinerant CoV_2O_4, Phys. Rev. B **93**, 014437 (2016).

[22] A. Kismarahardja, J. S. Brooks, A. Kiswandhi, K. Matsubayashi, R. Yamanaka, Y. Uwatoko, J. Whalen, T. Siegrist, and H. D. Zhou, $Co[V]_2O_4$: A Spinel Approaching the Itinerant Electron Limit, Phys. Rev. Lett. **106**, 056602 (2011).

[23] D. B. Rogers, R. J. Arnott, A. Wold, and J. B. Goodenough, The preparation and properties of some vanadium spinels, J. Phys. Chem. Solids **24**, 347 (1963).

[24] C. Mu, J. Mao, J. Guo, Q. Guo, Z. Li, W. Qin, Z. Hu, K. Davey, T. Ling, and S.-Z. Qiao, Rational design of spinel cobalt vanadate oxide Co_2VO_4 for superior electrocatalysis, Adv. Mater. **32**, 1907168 (2020).

[25] D. G. Wickham and J. B. Goodenough, Suggestion concerning magnetic interactions in spinels, Phys. Rev. **115**, 1156 (1959).

[26] N. Sakamoto, Magnetic properties of cobalt titanate, J. Phys. Soc. Jpn. **17**, 99 (1962).

[27] S. Thota, M. Reehuis, A. Maljuk, A. Hoser, J.-U. Hoffmann, B. Weise, A. Waske, M. Krautz, D. C. Joshi, S. Nayak, S. Ghosh, P. Suresh, K. Dasari, S. Wurmehl, O. Prokhnenko, and B. Büchner, Neutron diffraction study of the inverse spinels Co_2TiO_4 and Co_2SnO_4, Phys. Rev. B **96**, 144104 (2017).

[28] S. Nayak, S. Thota, D. C. Joshi, M. Krautz, A. Waske, A. Behler, J. Eckert, T. Sarkar, M. S. Andersson, R. Mathieu, V. Narang, and M. S. Seehra, Magnetic compensation, field-dependent magnetization reversal, and complex magnetic ordering in Co_2TiO_4, Phys. Rev. B **92**, 214434 (2015).

[29] V. W. Rüdorff, G. Walter, and H. Becker, Über einige Ox-overbindungen und Doppeloxyde des vierwertigen Vanadins, Z. Anorg. Allg. Chem. **285**, 287 (1956).

[30] N. Qureshi, M. Zbiri, J. Rodríguez-Carvajal, A. Stunault, E. Ressouche, T. C. Hansen, M. T. Fernández-Díaz, M. R. Johnson, H. Fuess, H. Ehrenberg, Y. Sakurai, M. Itou, B. Gillon, T. Wolf, J. A. Rodríguez-Velamazan, and J. Sánchez-Montero, Experimental magnetic form factors in $Co_3V_2O_8$: a combined study of *ab initio* calculations, magnetic Compton scattering, and polarized neutron diffraction, Phys. Rev. B **79**, 094417 (2009).

[31] W. Jauch, M. Reehuis, H. J. Bleif, F. Kubanek, and P. Pattison, Crystallographic symmetry and magnetic structure of CoO, Phys. Rev. B **64**, 052102 (2001).

[32] A. Huq, J. P. Hodges, O. Gourdon, and L. Heroux, Powgen: A third-generation high-resolution high-throughput powder diffraction instrument at the spallation neutron source, Z. Kristallogr. Proc. **1**, 127 (2011).

[33] A. Buchsteiner and N. Stüßer, Optimizations in angular dispersive neutron powder diffraction using divergent beam geometries, Nucl. Instrum. Methods Phys. Res., Sect. A **598**, 534 (2009).

[34] A. Franz and A. Hoser, E9: The fine resolution powder diffractometer (FIREPOD) at BER II, J. Large-Scale Res. Facil. **3**, A103 (2017).

[35] J. Rodríguez-Carvajal, Recent advances in magnetic structure determination by neutron powder diffraction, Phys. B: Condens. Matter **192**, 55 (1993).

[36] S. R. Giblin, S. P. Cottrell, P. J. C. King, S. Tomlinson, S. J. S. Jago, L. J. Randall, M. J. Roberts, J. Norris, S. Howarth, Q. B. Mutamba, N. J. Rhodes, and F. A. Akeroyd, Optimising a muon spectrometer for measurements at the ISIS pulsed muon source, Nucl. Instrum. Methods Phys. Res., Sect. A **751**, 70 (2014).

[37] O. Arnold, J. Bilheux, J. Borreguero, A. Buts, S. Campbell, L. Chapon, M. Doucet, N. Draper, R. Ferraz Leal, M. Gigg, V. Lynch, A. Markvardsen, D. Mikkelson, R. Mikkelson, R. Miller, K. Palmen, P. Parker, G. Passos, T. Perring, P. Peterson *et al.*, Mantid-data analysis and visualization package for neutron scattering and μSR experiments, Nucl. Instrum. Methods Phys. Res., Sect. A **764**, 156 (2014).

[38] G. Kresse and J. Furthmüller, Efficient iterative schemes for *ab initio* total-energy calculations using a plane-wave basis set, Phys. Rev. B **54**, 11169 (1996).

[39] G. Kresse and D. Joubert, From ultrasoft pseudopotentials to the projector augmented-wave method, Phys. Rev. B **59**, 1758 (1999).

[40] Y. Yasui, Y. Kobayashi, M. Soda, T. Moyoshi, M. Sato, N. Igawa, and K. Kakurai, Successive magnetic transitions of the kagomé staircase compound $Co_3V_2O_8$ studied in various magnetic fields, J. Phys. Soc. Jpn. **76**, 034706 (2007).

[41] Y. Huang, Z. Yang, and Y. Zhang, Magnetic, structural, and thermal properties of CoV_2O_4, J. Phys.: Condens. Matter **24**, 056003 (2012).

[42] A. S. Wills, A new protocol for the determination of magnetic structures using simulated annealing and representational analysis (SARAh), Phys. B (Amsterdam, Neth.) **276-278**, 680 (2000).

[43] J. Perez-Mato, S. Gallego, E. Tasci, L. Elcoro, G. de la Flor, and M. Aroyo, Symmetry-based computational tools for magnetic crystallography, Annu. Rev. Mater. Res. **45**, 217 (2015).

[44] H. T. Stokes, D. M. Hatch, and B. J. Campbell, ISOTROPY software suite, https://iso.byu.edu/

[45] R. Kubo and T. Toyabe, *Magnetic Resonance and Relaxation* (North Holland, Amsterdam, 1967), Vol. 29, p. 59.

[46] I. A. Campbell, A. Amato, F. N. Gygax, D. Herlach, A. Schenck, R. Cywinski, and S. H. Kilcoyne, Dynamics in Canonical Spin Glasses Observed by Muon Spin Depolarization, Phys. Rev. Lett. **72**, 1291 (1994).

[47] S. Thota and M. S. Seehra, Co-existence of ferrimagnetism and spin-glass state in the spinel Co_2SnO_4, J. Appl. Phys. **113**, 203905 (2013).

[48] S. L. Dudarev, G. A. Botton, S. Y. Savrasov, C. J. Humphreys, and A. P. Sutton, Electron-energy-loss spectra and the structural stability of nickel oxide: an $LSDA + U$ study, Phys. Rev. B **57**, 1505 (1998).

[49] J. H. Lee, J. Ma, S. E. Hahn, H. B. Cao, M. Lee, T. Hong, H.-J. Lee, M. S. Yeom, S. Okamoto, H. D. Zhou, M. Matsuda, and R. S. Fishman, Magnetic frustration driven by itinerancy in spinel CoV_2O_4, Sci. Rep. **7**, 17129 (2017).

[50] C. Bhandari, M. E. Flatté, and D. Paudyal, Enhanced magnetic anisotropy in lanthanum M-type hexaferrites by quantum-confined charge transfer, Phys. Rev. Materials **5**, 094415 (2021).

[51] E. Verwey and P. Haayman, Electronic conductivity and transition point of magnetite ("Fe_3O_4"), Physica **8**, 979 (1941).

5 Crystal Fields in SrTm$_2$O$_4$

This chapter is devoted to the study of the crystal field and crystal field effects in SrTm$_2$O$_4$. The project was conceived and supervised by D. L. Quintero-Castro.

I synthesized the powder sample, while H. Li provided the single-crystal samples used in this study. I performed the DC-susceptibility measurements at Core Lab quantum materials, HZB. The pulsed-field measurements at High Magnetic Field Laboratory, HZDR were performed by a team comprising D. Gorbunov, C. Salazar Mejia, and myself. K. Siemensmeyer carried out the heat capacity measurements on the single-crystal sample.

The time-of-flight measurements on powder samples were performed on the MAPS instrument at ISIS Neutron and Muon Source, UK, as part of the rapid access proposal by R. Stewart. The μ^+SR experiments on powder samples on DOLLY, LTF, and GPS instruments at Swiss muon source (SμS), PSI were performed by D. L. Quintero-Castro, H. Li, H. Luetkens (DOLLY and GPS), and C. Baines (LTF).

I analyzed and interpreted all the data and carried out all the modeling, including DFT calculations. I wrote the first draft of the manuscript and was involved in subsequent revisions.

In this chapter, I provide background for the manuscript and summarize crystal field determination and μ^+SR results, with additional details that were not included in the manuscript.

5.1 Sr*Ln*$_2$O$_4$ family: A Background

SrTm$_2$O$_4$ belongs to the Sr*Ln*$_2$O$_4$ family (*Ln*: La, Ce, Pr, Nd, Sm, Eu, Gd, Tb, Dy, Ho, Er, Tm, Yb or Lu.), which crystallizes in the *Calcium ferrite* structure following orthorhombic *62.Pnam* spacegroup (ITA-settings) [98]. All the atoms sit on the Wyckoff site 4*c* corre-

sponding to monoclinic point group C_s. The magnetic sub-lattice consists of a network of interlinked distorted honeycombs (in *ab*-plane) and triangular ladders by two crystallographic in-equivalent *Ln^{3+}* (*Ln1* and *Ln2*). These ladders run along the *c*-axis of the orthorhombic *Pnam* crystal structure [3]. Typically, *c*-axis is the shortest ($\approx$ 3Å) compared to *a*- ($\approx$ 10Å) and *b*- ($\approx$ 12 Å) axes (Fig .5.1). These interesting geometric features allow this family to adopt intriguing pathways for exotic magnetic phenomena.
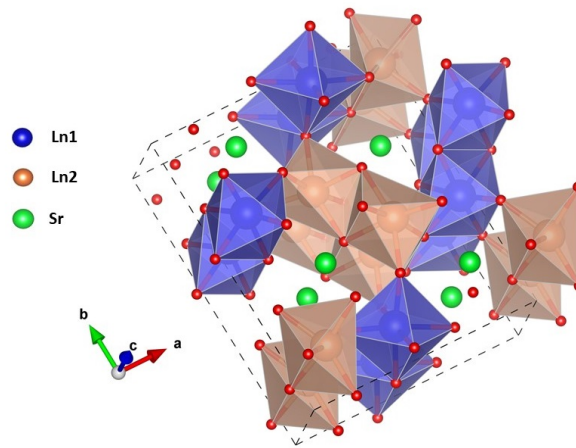
Figure 5.1: Network of honeycomb layers connected by triangular ladders as observed in Sr*Ln$_2$O$_4$*.

An essential feature of this honeycomb structure is that it has the lowest coordination number (i.e., 3) among two-dimensional systems. Another intriguing part is that the nearest-neighbor distances in this honeycomb are not identical. Hence, while considering only the nearest neighbors, the honeycomb is typically not frustrated. In contrast, the frustration can be induced with $\mathcal{J}_1$-$\mathcal{J}_2$-$\mathcal{J}_3$ situation by considering the next nearest neighbor. In this family, most commonly the frustration comes from 'zig-zag' ladders that run along the *c*-axis [99]. Magnetic frustration, low-dimensionality, strong single-ion anisotropy, and low-coordination numbers can compete to evolve into exotic physics observed in this family [3, 99].

Projection *ab*-plane of SrTm$_2$O$_4$ is presented in Fig .5.2, where the neighboring octahedra to the same type of Tm^{3+}s are connected by sharing an edge of the octohedra(closest in the plane), whereas the nearest in-equivalent Tm^{3+}s sites are only sharing a corner. These connections result in distorted honeycomb plane structures.
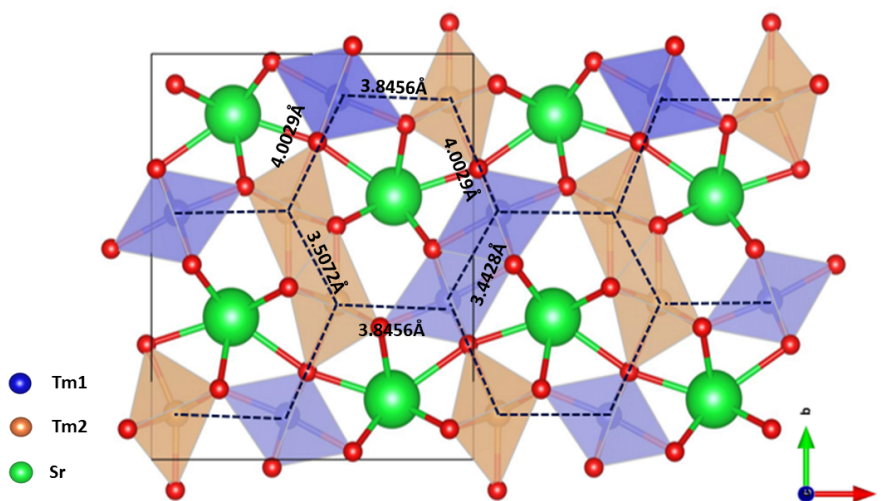
Figure 5.2: Network of honeycomb layers (ab-plane) connected by triangular ladders as observed in SrTm$_2$O$_4$, with distances according to Ref. [4].

In the Fig .5.3, there are two quasi one dimensional triangular ladders of in-equivalent Tm^{3+}s running parallel to the *c*-axis. The shortest distance between any Tm ions in the entire system is along the rails of the ladder (3.38 Å). This periodicity is the same for both Tm1 and Tm2 chains. The next nearest-neighbor distances are the quasi-1-dimensional zig-zag rungs. The Tm1 chains have the shortest zig-zag distances among both the chains (3.43 Å). The nearest-neighbor inter-ladder distances (3.83Å) are relatively larger compared to both intra-ladder (along rung and zig-zag) distances [4].

In general, *Ln*$^{3+}$ in Sr*Ln*$_2$O$_4$ are surrounded by a distorted octahedral oxygen environment (Fig .5.4). The oxygen ligand charge distribution
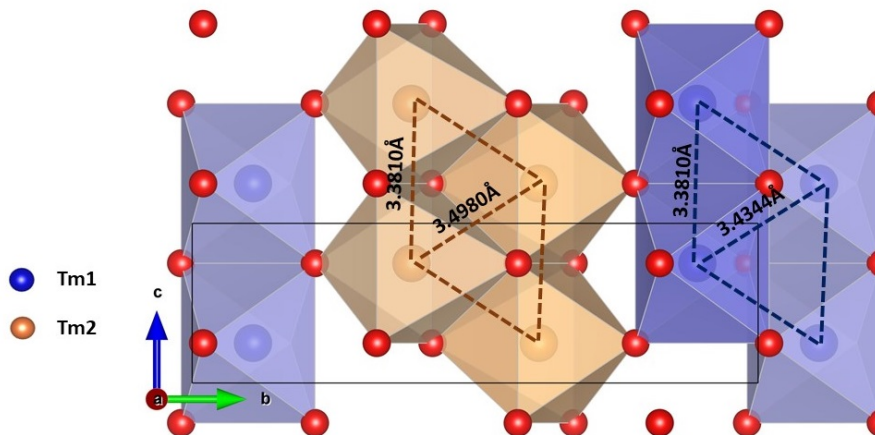
Figure 5.3: In equivalent zig-zag chains running parallel to the c-axis for SrTm$_2$O$_4$ Ref. [4].

lifts the degeneracy of ground state multiplet. The crystal field effects are instrumental to understanding the magnetic properties in this family [99]. The low lying crystal field levels play an important role in contributing to highly anisotropic magnetic properties in the form of single-ion anisotropy. The inequivalent Ln^{3+} ions lead to two unique sets of crystal field Hamiltonians. Determination of these Hamiltonians unambiguously is a non-trivial task by itself. Additionally, the low site symmetry (C_s) requires a large number of crystal field parameters (CFPs) to be determined. The 'Stevens operator approach' that involves adjusting CFPs is not sufficient to describe the single-ion properties unambiguously, as this method typically results in overparameterization [9].

5.1.1 Crystal Field Models for SrLn_2O$_4$

Very few attempts have been made to describe the crystal fields in the SrLn_2O$_4$ family. Up until the drafting of this thesis, successful descriptions of crystal fields in SrEr$_2$O$_4$, SrHo$_2$O$_4$, and SrDy$_2$O$_4$ (Fig
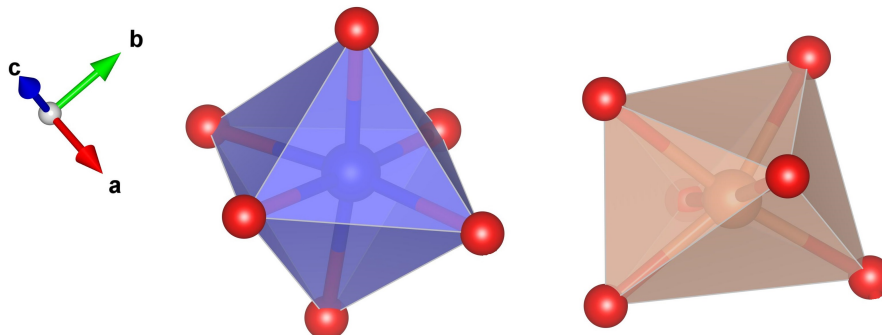
Figure 5.4: Distorted octahedral oxygen environment surrounding *Ln1* (blue) and *Ln2* (orange).

.5.5)have been reported in [100, 101].

In the case of the SrEr$_2$O$_4$, a sophisticated theoretical model called *'Exchange Charge Model'* was implemented to make an initial estimation of the CFPs. In this model, the crystal field Hamiltonian is considered as the sum of two terms. The first term describes the electrostatic interaction between an Er^{3+} and ligands as in the standard point charges model [10]. The second term is proportional to the overlap integrals between the wave functions of Er^{3+} and ligands. In addition to this, the experimental results from optical site-selective excitation and emission spectra measurements, electron paramagnetic resonance (ESR), and inelastic neutron scattering were used to adjust the CFPs accurately [100].

In the case of SrHo$_2$O$_4$ and SrDy$_2$O$_4$, a theoretical model based on point-charge calculations with a requirement of a minimum of adjustable parameters called crystal field scaling factor S_{xtal} was used [15]. Only the crystal field scaling factor S_{xtal} was refined by fitting the spectra. S_{xtal} captures the orbital overlay or covalency of atoms. The estimated S_{xtal} in SrDy$_2$O$_4$ for Dy1 = 0.35 and for Dy2 = 0.53 and in SrHo$_2$O$_4$ for Ho1 = 0.62 and for Ho2 = 0.70. Figure 5.5 presents a comparison of crystal field schemes for different members of the Sr*Ln*$_2$O$_4$ family.
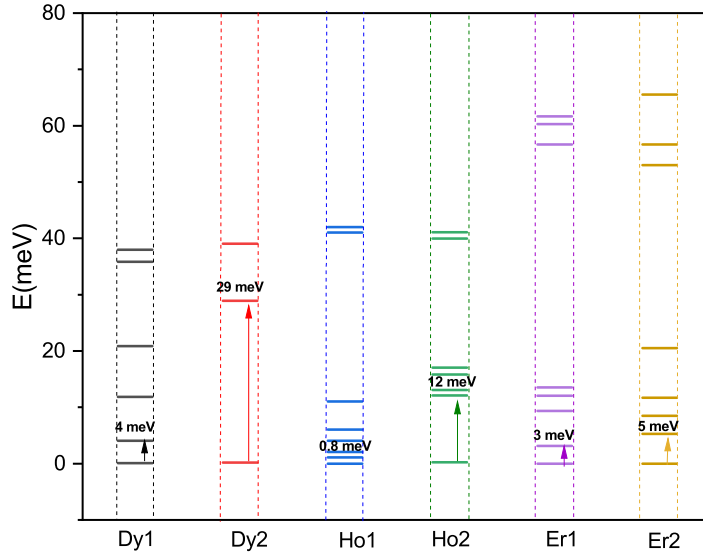
Figure 5.5: The Crystal Field Schemes for SrDy$_2$O$_4$, SrHo$_2$O$_4$ [101], and SrEr$_2$O$_4$ [100]

5.1.2 SrTm$_2$O$_4$ background

Previously, Haifeng Li *et al*. [4] reported a detailed study on the structure and magnetic properties of SrTm$_2$O$_4$. In their work they synthesized polycrystalline and single-crystal samples and performed structural analysis using neutron Laue diffraction and NPD. They have also performed magnetic characterization along with structural studies such as bulk properties and polarized neutron study. The structural studies using diffraction data have confirmed orthorhombic structure with two inequivalent Tm sites. Figures 5.2 & 5.3 present various Tm-Tm distances.

Haifeng Li *et al*. concluded that SrTm$_2$O$_4$ shows neither long nor short range magnetic order down to ~ 65mK. They attributed the mag-

netically disordered state to a strong anisotropic crystal field effect and inferred that such magnetic anisotropy may quench potential magnetic ordering. However, they do not provide crystal field study of SrTm$_2$O$_4$ to confirm their inference. In this regard, we decided to understand the crystal fields to confirm if it is only single-ion anisotropy or is due to competition between other interactions (discussed in Ref. [99]), leading to disordered ground state.

While Haifeng Li *et al*. [4] did not see any order, the μ^+SR measurements performed by D. L. Quintero Castro *et al*. showed oscillations in muon spectra. Such oscillations in muon spectra are usually attributed to muon precession due to magnetically ordered local environment [46].

To begin with, we intended to approach this project to answer the following questions:

1. What is the crystal field ground state? Is it same for both Tm1 and Tm2 sites?

2. How does the crystal field anisotropy looks like?

3. Why do muons show features of magnetic ordering, whereas the measurements performed by Haifeng Li *et al*. [4] refute any ordering down to 65 mK?

The first step to approaching this project would be to arrive at a model that describes the crystal fields of this system accurately. As discussed earlier, the crystal field schemes of the entire Sr*Ln*$_2$O$_4$ family are difficult to determine. However, crystal fields of SrTm$_2$O$_4$ are particularly difficult of access due to 13 singlets ($= J(J+1)$) expected from each Tm^{3+} within the ground-state multiplet. The limited number of transitions spotted with INS have made it difficult to fit the INS spectra to arrive at unambiguous parameters using Stevens operator approach. This satiated the need to approach this crystal field problem with *ab-initio* methods and other phenomenological methods such as effective charge model [12, 14].

5.2 Manuscript II Summary

The crystal field properties of the zig-zag chain compound SrTm$_2$O$_4$ are being studied using inelastic neutron scattering, heat capacity, magnetic susceptibility, magnetization, and polarized muon spectroscopy. To explain the single ion properties, Density Function Theory model (DFT model) and an effective charge model (EC model) were implemented. Additionally, muon spin rotation/relaxation μ^+SR spectra revealed oscillations, originating from muon precession due to long-range order of electronic spins. We understand these unique results by modeling the muon stopping site and estimating the impact of the muon implantation on crystal fields using point charge model.

This manuscript explains two interlinked problems associated with crystal fields in SrTm$_2$O$_4$. The first part details the determination of CFPs. The second part discusses the muon-induced distortion of crystal fields and extended critical regime of the ordering parameter in SrTm$_2$O$_4$ observed with μ^+SR.

5.3 Crystal field models

To understand the crystal fields in SrTm$_2$O$_4$ DC-magnetic susceptibility, Pulsed-field magnetization, heat capacity, and INS measurement were performed. Finally, two crystal field models were implemented and compared with experimental results.

5.3.1 Bulk Properties

The magnetic susceptibility (Figure 1(e,f) in the manuscript) as a function of the temperature of the single-crystal sample was measured in the temperature range 2-300 K and applied magnetic field of 0.1 T applied along a-,b-, and c-axes. The magnetic susceptibility thus obtained shows that the susceptibility along c-axis is at least two orders of magnitude smaller than other directions, which is a clear indicator

of strong anisotropy in this system. Additionally, no signs of short or long-range order were observed down to 2 K.
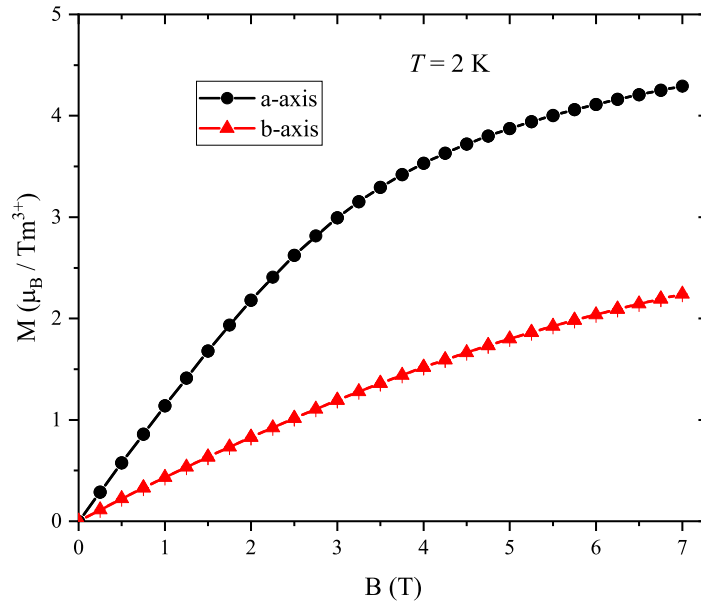
Figure 5.6: Low field magnetization measured with SQUID magnetometer. Results from these measurements were used to convert the pulsed field results from arbitrary units into absolute units.

The high field magnetization (Figure 1(b) in manuscript) of a single crystal sample up to 58 T was measured with the help of the pulsed magnetic field with field applied along *a*-,*b*-, and *c*-axes. The pulsed-field data was converted into absolute units using the continuous field magnetization measured using the SQUID magnetometer. In Figure 5.6 magnetization results from continuous fields are presented. The pulsed-field magnetization retains the low-field trends (continuous field) up to 58 T. The magnetization results clearly show that the *c*-axis is the hard axis, and the *a*-axis doesn't reach the theoretical saturation magnetization of 7 μ_B/f.u. (for Tm^{3+}). Unlike other members of the

family, [102] no anomalies in magnetization of SrTm$_2$O$_4$ were observed.

Heat capacity measurement was performed on the single crystal SrTm$_2$O$_4$. The phonon heat capacity was modeled using DFT methods to separate magnetic contribution to heat capacity. The first principles phonon heat capacity was extracted from phonon dispersion calculation using finite displacement method (FDM) implemented in `Phonopy` [103]. The preliminary optimized structure was obtained from the Materials Project database [104]. The distorted structure with force constants was obtained from PhononDB [105].
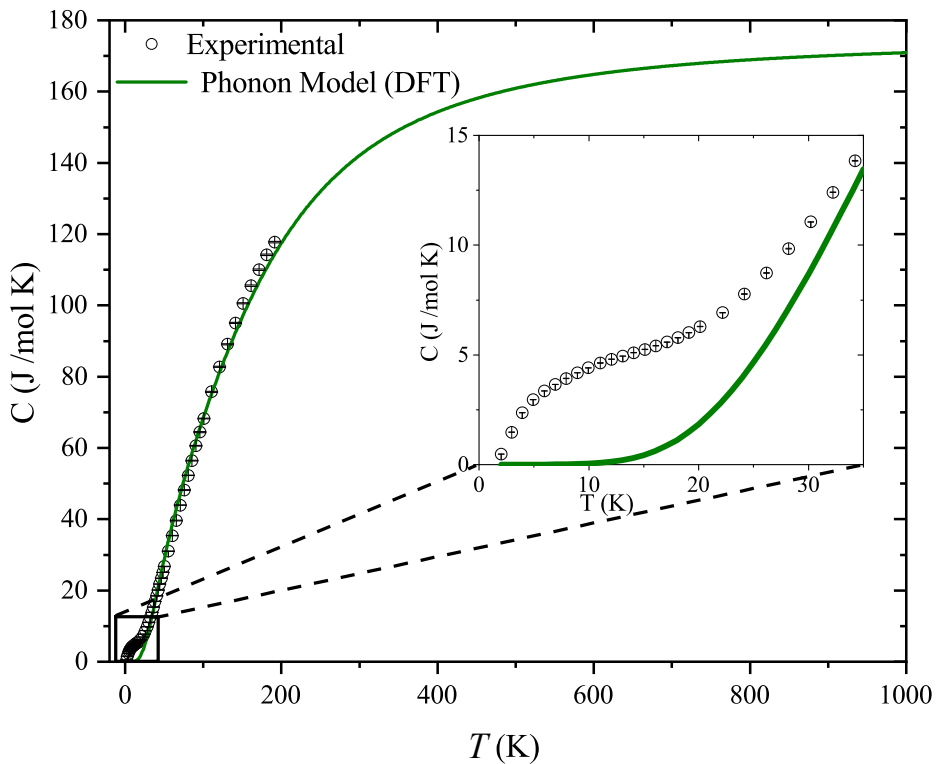
Figure 5.7: Phonon heat capacity [105] obtained from phonon dispersion calculation using FDM compared with the measured heat capacity. At low-temperatures.

The thermal properties were re-calculated using `Phonopy` [103], a post-processing program. The heat capacity thus obtained is compared with the measured heat capacity in Figure 5.7. Certainly, the low-temperature bump is indeed the 'Schottky anomaly' arising due to low-energy crystal field modes. It is clear that beyond 20 K, the phonon contributions to heat capacity get significantly stronger. To avoid introducing additional errors, the phonon background subtraction from the experimental data was not performed.

5.3.2 Inelastic Neutron Scattering: Crystal Field Levels

Inelastic neutron scattering measurements were performed using neutron time-of-flight instrument MAPS. In the low energy excitation spectra (E_i=26 meV), two dispersing excitations can be identified centered at 1.230(5) meV and 3.412(3) meV (Figure 2(b) in manuscript), whereas in the high energy range (E_i=130 meV), three excitations are identifiable centered at 23.72(4), 35.82(6), and 71.00(2) meV (Figure 2(a) in manuscript). Equation 5.1 was used to calculate |Q| dependency of magnetic form factor ($|f(|\mathbf{Q}|)|^2$).

$$f(|\mathbf{Q}|) = \langle j_0(|\mathbf{Q}|)\rangle + \frac{2-g}{g}\langle j_2(|\mathbf{Q}|)\rangle \qquad (5.1)$$

In equation 5.1, $f(|\mathbf{Q}|)$ is the magnetic form factor for rare earth ions under dipole approximation [7], where g= 1.16667 for Tm^{3+}. The coefficients corresponding to $\langle j_0(|\mathbf{Q}|)\rangle$ and $\langle j_2(|\mathbf{Q}|)\rangle$ were taken from Ref. [106]. Figure 5.8 presents |Q| dependency of the identified modes overlaid with $|f(|\mathbf{Q}|)|^2$. Both the low-energy modes (Fig. 5.8(a)), deviate from $|f(|\mathbf{Q}|)|^2$ vs |Q| behavior, as they are influenced by dynamic structure factor due to inter-ionic magnetic interaction. Details of this behavior are discussed in the next chapter. The mode centered at 71.00(2) meV has stronger phonon contributions due to the restricted |Q| range. Since all the modes follow $f(|\mathbf{Q}|)$ vs |Q| behavior in low |Q| regime well, they can be considered magnetic.
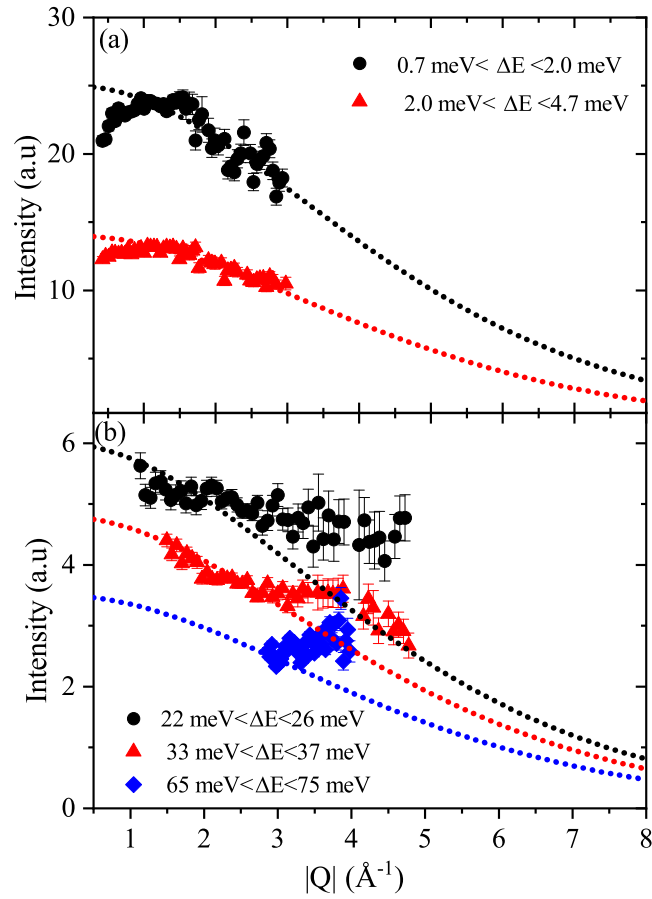
Figure 5.8: |Q| dependency of the identified modes in the spectra for (a) E$_i$ = 26 meV and (b) E$_i$ = 130 meV overlaid with square of magnetic form factor ($|F(|\mathbf{Q}|)|^2$) for Tm^{3+} calculated according to equation 5.1.

5.3.3 Crystal Field Parameters

Determination of CFPs in SrTm$_2$O$_4$ has been difficult due to low site symmetry. The site symmetry C_s requires fifteen CFPs per Tm^{3+} to define the crystal field Hamiltonian accurately. However, with INS measurements, only five excitation levels were identified ($<110\,$meV). Thus several attempts to optimize the parameter with respect to observed excitations led to degenerate sets of CFPs. Similarly, the point charge model was unsuccessful in describing the system accurately as it does not account for covalency effect. To overcome the shortcomings of Stevens operator method and point charge model, two advanced models were implemented. The first model uses *ab initio* DFT methods to extract the CFPs. The second model, an improvisation of the PC model, uses effective charge and positions to account for covalency effects [12, 14]. This model is called '*Effective charge model*' (EC model). Here I only discuss the methods involving the DFT model, with additional details.

Wannier functions method: DFT model

I implemented the method developed by Novák *et al.*[19] to determine the crystal fields in SrTm$_2$O$_4$. This method obtains Wannier functions by transforming Bloch functions calculated using all-electron DFT methods. The Wannier functions thus obtained represent atomic-like orbitals within periodic crystals. The crystal field Hamiltonian is expressed on the basis of Wannier functions, which is then expanded in a series of spherical tensor operators [19]. Henceforth in the thesis this model will be referred to as the DFT model.

The DFT model overcomes the shortcomings of the point charge model by accounting for covalency effects. Hybridization between the electronic orbitals of the rare earth ion and the surrounding ligands is compensated using charge transfer energy 'Δ' [19]. This procedure was successfully implemented for different rare-earth systems [21, 107–109]. Here, I describe the steps involved in the calculation of crystal fields using this method. Figure 5.9 presents a flow chart representing

the work flow of this computational procedure.

```
┌─────────────┐
│ First Step  │
└─────────────┘
      │
      ▼
┌─────────────┐
│   Second    │
│    Step     │
└─────────────┘
      │
┌─────────────┐  ┌─────────────┐
│  update Δ   │  │ Third Step  │
└─────────────┘  └─────────────┘
      │                │
      │                ▼
      │           ◇ Forth Step ◇
      │  no             │
      │                 │ yes
      │                 ▼
      │           ┌─────────────┐
      │           │    stop     │
      │           └─────────────┘
```
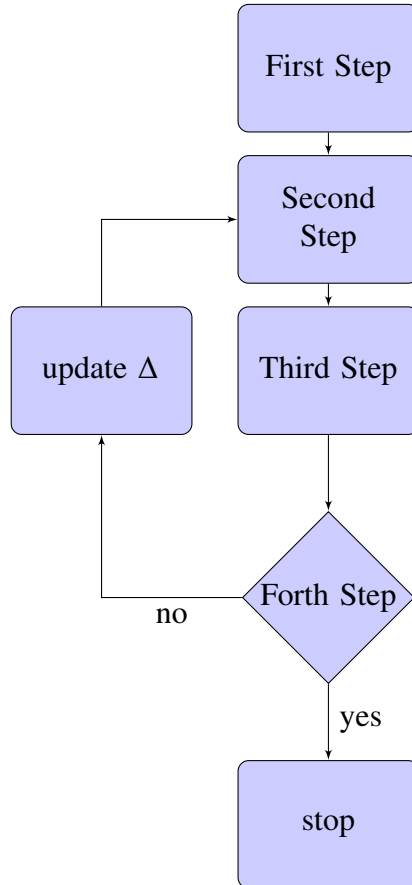
Figure 5.9: Work flow for DFT model.

In the **first step**, a standard self-consistent solution to the Khon–Sham equation of DFT was implemented using the augmented plane wave plus local orbitals (APW+lo) method using `WIEN2k` [62]. The exchange-correlation functional, the Perdew Burke Ernzerhof - Generalized Gradient Approximation (PBE-GGA) [110], was used in this calculation.

The experimental lattice parameters and atomic positions were considered according to Ref. [4] without performing any geometric optimization. The atomic sphere radii for Tm = 2.4 a.u, Sr = 2.24 a.u, and

O = 1.6 a.u were used. The eigenvalue problem was solved in 200 k-points (5 x 4 x 10) of the irreducible Brillouin zone with $\approx$ 4023 basis functions corresponding to RK$_{max}$ = 7. In this calculation, the 4f electrons were treated as core electrons (so-called open core method). This open core calculation at this stage is vital as it avoids nonphysical self-interactions that would dominate CFPs [19].
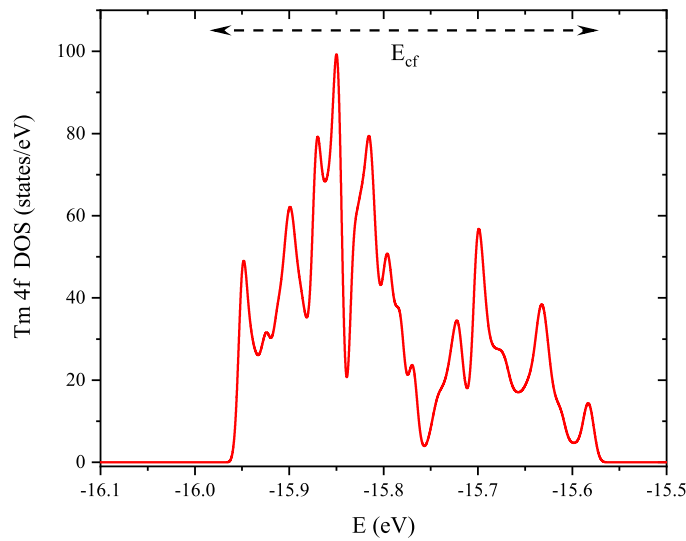
Figure 5.10: Density of states (DOS) of hybridized 4f orbitals for Δ = -1.22 eV (for representation). Here E$_{cf}$ is the energy difference between highest and lowest singlet sates. E$_{cf}$ consists of 28 f-orbitals coming from 4 equivalent Tm ions in the unit cell of SrTm$_2$O$_4$. Here, E$_{cf}$ is used to characterize the strength of the crystal field [19].

In the **second step** the effective crystal field Hamiltonian ($\mathcal{H}_{CF}$) for the 4f-electrons is constructed by considering the shape of the 4f-orbitals, the effective potential, and hybridization with the oxygen p-orbitals. Primarily, the 4f-orbitals are included in the valence basis set. Before the eigenvalue problem with the potential from the previous step is solved, the relative energy of the 4f and ligand states is modified by

introducing charge transfer energy 'Δ' (hybridization parameter). The Δ can be defined as follows:

$$\Delta \cong E_{tot}(4f^{(n+1)}, N_{val} - 1) - E_{tot}(4f^{(n)}, N_{val}) \qquad (5.2)$$

where n-is the number of electrons in 4f shell, N_{val} is the number of electrons in the valence band, $E_{tot}(4f^{(n)}, N_{val})$ is the ground state total energy, and $E_{tot}(4f^{(n+1)}, N_{val}-1)$ is the excited state energy [19]. Figure 5.10 presents the density of one-particle states projected on $4f$-orbitals. Several calculations were performed with Δ in the range of -0.68 to -13.8 eV.

In the **third step**, `Wien2Wannier` [111] interface and `Wannier90` [112] program were used to transform the 28 (=4 Tm atoms x 7 f-orbitals) Bloch states from $4f$ energy window to Wannier functions. It was found that in the case of both Tm1 and Tm2, quadratic spread of Wannier functions (Maximally localized Wannier functions (MLWF)) from the center of the atom were in the range of 0.3-0.4 Å^2. `Wannier90` provides a matrix of onsite Hamiltonian $\mathcal{H}_{4f}$.

$$\mathcal{H}_{4f} = E_{\text{avg}}I + \mathcal{H}_{cf} \qquad (5.3)$$

Here the traceless part of $\mathcal{H}_{4f}$ is the crystal field Hamiltonian $\mathcal{H}_{cf}$ [19].

$$\mathcal{H}_{cf} = \sum_{k,q} D_q^{(k)} C_{q(k)} \qquad (5.4)$$

To get the CFPs in Wybourne normalization ($D_q^{(k)}$) [23], $\mathcal{H}_{4f}$ was transformed into the basis of spherical harmonics and expanded as a 49-dimensional vector on the basis of spherical tensor operators, i.e.,

$$D_q^{(k)} = \frac{1}{n_{k,q}} \sum_{i=1}^{n} \sum_{j=i}^{n} \mathcal{H}_{cf}^{i,j} C_q^{(k),(i,j)} \qquad (5.5)$$

Where $n_{k,q} = \sum_{i=1}^{n} \sum_{j=i}^{n} C_q^{(k),(i,j)} C_q^{(k),(i,j)}$. The $C_q^{(k)}$ is defined as $C_q^{(k)}(\theta, \phi) = \sqrt{4\pi/(2q+1)} Y_q^{(k)}(\theta, \phi)$.
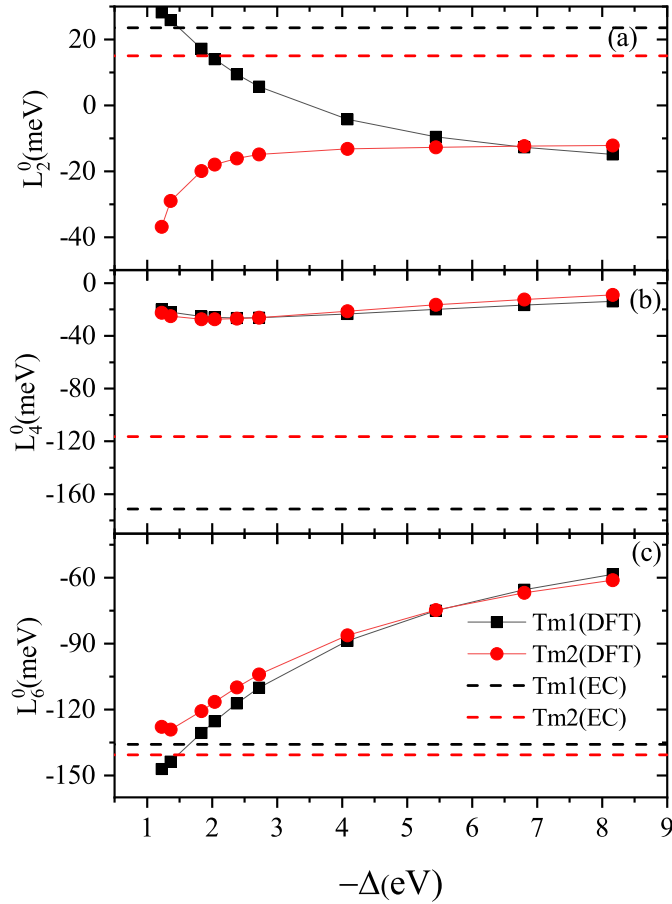
Figure 5.11: The CFPs L$_2^0$ (a), L$_4^0$ (b), and L$_6^0$(c) for both Tm1 (black) and Tm2 (red) as a function of 'charge transfer energy' (Δ). The CFPs are compared with the corresponding CFP obtained with effective charge model fitting (dashed lines). The CFPs are presented in Wybourne normalization according to Ref. [7].

Since $C_q^{(k)}$ are not Hermitian, CFPs $D_q^{(k)}$s turn out complex. In order to avoid imaginary operators, the $\mathcal{H}_{cf}$ was re-written in terms of $T_l^{(m)}$

as follows after performing several rotations:

$$\mathcal{H}_{cf} = \sum_{k,q} L_q^{(k)} T_q^{(k)} \tag{5.6}$$

Where $T_q^0 = C_q^0$, $\quad T_q^{\pm|k|} = \sqrt{\pm 1}\left[C_q^{-|k|} \pm (-1)^{|k|} C_q^{|k|}\right]$ [7]. However, this transformation of CFPs can be simply summarized as $L_q^0 = D_q^0, L_q^k = D_q^k, L_q^{-k} = iD_q^{-k}$. Figure 5.11 presents L_2^0, L_4^0, and L_6^0 as functions of Δ for both Tm1 and Tm2. There is a significant deviation from the same CFPs estimated using the effective charge model.

Finally, in **fourth step**, the Intermediate coupling scheme was used to define effective atomic Hamiltonian ($\mathcal{H}$).

$$\mathcal{H} = \mathcal{H}_{\text{FI}} + \mathcal{H}_{cf} \tag{5.7}$$

The contributions for Coulomb and spin-orbit interactions are constructed as $\mathcal{H}_{\text{FI}}$, i.e., Free ion Hamiltonian.

$$\begin{aligned}
\mathcal{H}_{\text{F1}} = {} & \zeta \sum_j l_j s_j + \alpha L^2 + \beta G\left(G_2\right) + \gamma G\left(R_7\right) \\
& + \sum_q \left(F^q f_q + P^q p_q + T^q t_q + M^q m_q\right)
\end{aligned} \tag{5.8}$$

where $\zeta = 2636\,\text{cm}^{-1}$ is the spin-orbit coupling constant, α, β, and γ are Trees and T^q are called Casimir's parameters standing for two- and three-body configuration interactions. Spin-orbit interactions are given by (M^q) and electrostatically correlated spin-orbit interactions by (P^q): both of these parameters are called Judd's parameters. Two-body electrostatic repulsions (F^q) are called Slater integrals [7, 113, 114]. In this work all these parameters were obtained from Ref. [115] based on Tm doped single crystal LaF$_3$.

The Ic1ion module in `McPhase` [7] was used to obtained eigenvalues and eigenfunctions and thermodynamic properties by considering 12 other multiplets along with ground state multiplet $^3H_6$. Figure 5.12

presents calculated eigenvalues plotted as a function of (Δ) and compared with measured values. This figure shows that the accurate value of Δ is equal to -1.83 eV.

Figure 5.13 presents calculated first eigenvalues for both Tm1 and Tm2 plotted as a function of (Δ). The first excited state comes from Tm2, and the second excited state from Tm1.

Limitations of Wannier function method

The Wannier function method is conceptually pleasing and has been successfully implemented for several $4f$ systems [21, 107–109]. This method is particularly successful in explaining crystal fields of insulating $4f$. However, the method was found to be not quite adequate in the case of SrTm$_2$O$_4$.

This model successfully predicted that the lowest dispersing mode originates from Tm2 while the second mode originates from Tm1. It has also successfully predicted the anisotropy, i.e., easy-axis anisotropy for Tm1 and easy-plane anisotropy for Tm2. However, the magnitude of anisotropy was not accurate. Moreover, other thermodynamic properties such as magnetization and magnetic susceptibility are not explained very well. The reasons could be as follows:

- Atomic positions used in the calculation were taken from NPD, without performing any geometric optimization. Geometric optimization of the structure could improve the accuracy of determined CFPs.

- Open core calculation should have retained $4f$ electrons in the core. Despite this the density $4f$ still leaks out.

- Also, the accuracy of this model is dependent on the correct choice of Δ. Finer steps of Δ between -1 and -2 eV should increase accuracy. A better estimation of Δ can be done with optical absorption results.

- Even though `Wannier90` calculates MWLFs, this does not guar-

97
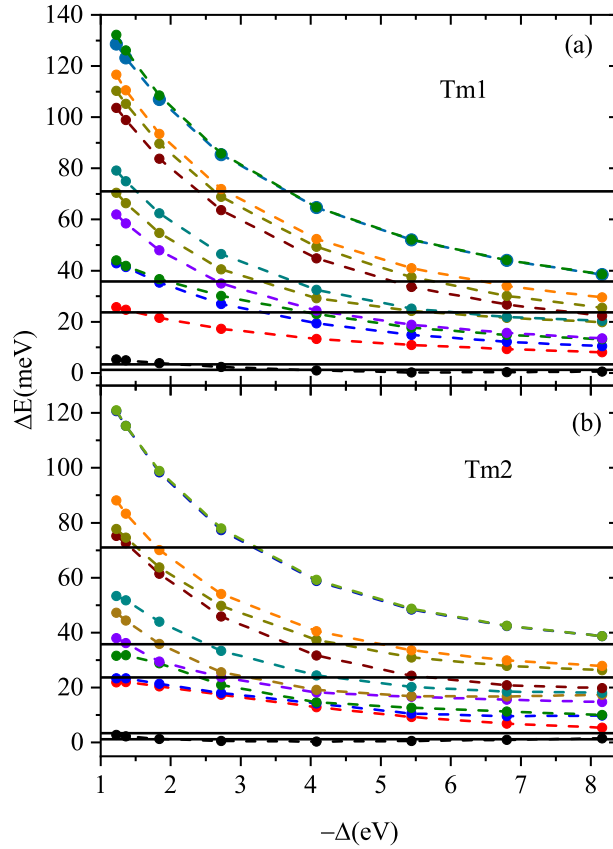
Figure 5.12: Calculated ground state multiplet $^3H_6$ as a function of Δ for Tm1 (a) and Tm2 (b). Straight lines correspond to measured excitations using neutron time-of-flight instrument MAPS.

antee that they will be centered on the crystallographic site of the Tm^{3+} ions [21]. Choice of other Wannier function schemes such as 'selectively localized Wannier functions' [116] or 'symmetry adapted Wannier functions' [117] should help to improve the method [21].
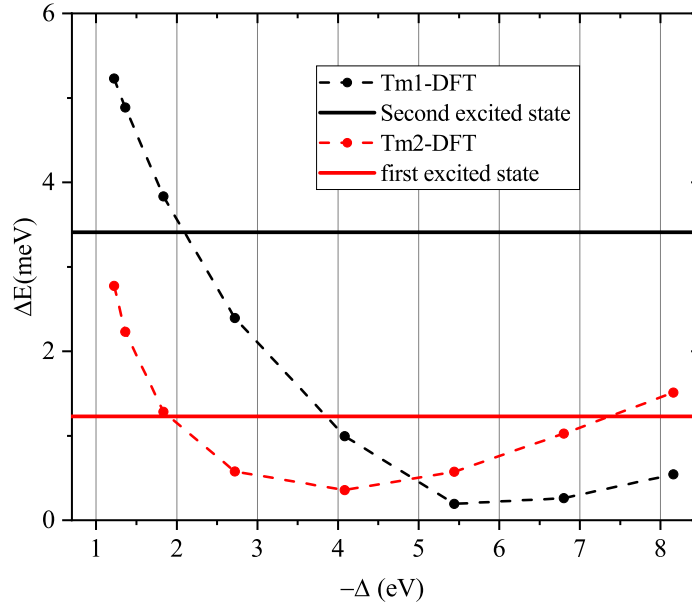
Figure 5.13: Calculated first excited state as function of 'charge transfer energy' (Δ) for Tm1 (black) and Tm2 (red). Straight lines correspond to measured excitations using neutron time-of-flight instrument MAPS. It is evident that the first excited state in the measured spectra corresponds to Tm2 and the second excited state to Tm1.

Despite the above shortcomings, this method has provided a tremendous preliminary understanding of the crystal field scheme and parameters. Such prior understanding has helped in implementing the effective charge model intelligently.

Single-ion anisotropy from EC model

The effective charge model was implemented as the DFT model failed to describe magnetization and susceptibility accurately. The EC model successfully determined magnetization, magnetic susceptibility, heat capacity, and INS reasonably. Effective charge (EC) model refinement
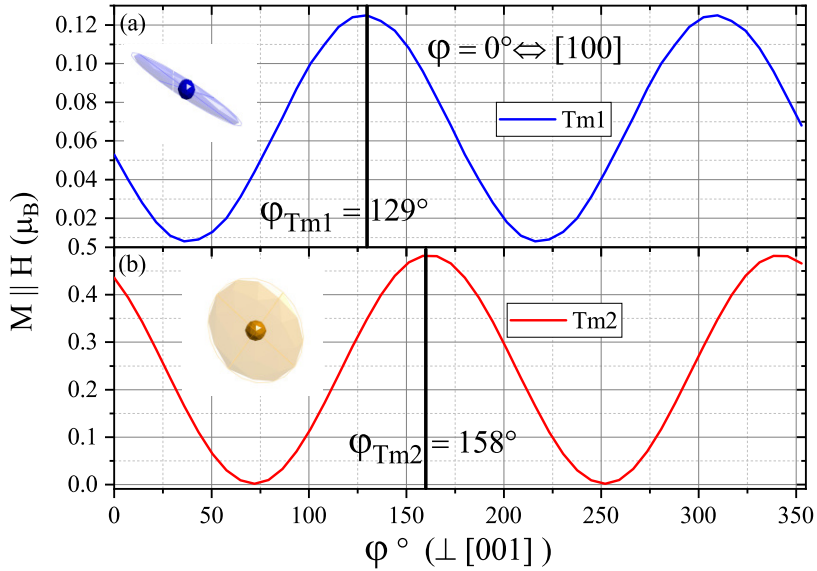
Figure 5.14: Anisotropy plot representing anisotropy modulation within *ab*-plane. Easy axis for Tm1 is at 129°, while for Tm2 it is at 158° with respect to *a*-axis.

could accurately determine single-ion anisotropy. Figure 5.14 represents the anisotropy modulation within *ab*-plane. As discussed in the manuscript, the Tm1 shows easy-axis anisotropy with easy-axis at 129° with respect to *a*-axis, whereas Tm2 shows easy-planer anisotropy with easy-axis at 158° with respect to *a*-axis.

5.4 Muon Spin Rotation/Relaxation

The zero-field (ZF) and longitudinal field (LF) μ^+SR measurements were performed on the polycrystalline samples of $SrTm_2O_4$. The ZF-μ^+SR results show oscillations in the spectrum, a signature of long-range magnetic order in the system [46]. However, the report by Haifeng Li *et al.*[4] and our diffraction results (in the next chapter) show no

short- or long-range order down to 65 mK. Thus, it is necessary to understand the origin of the oscillations in ZF-μ^+SR spectra of SrTm$_2$O$_4$.

5.4.1 Zero Field Muon Spin Rotation/Relaxation

The ZF-μ^+SR measurements were performed in the temperature range 19 mK-250 K. At low temperatures ($T < 100$ K) three unique features can be observed: oscillations due to muon precession, 2/3 relaxation, and 1/3 relaxation. Thus the spectra were modeled using the following equation:

$$a_0 P_Z^{\text{exp}}(t) = a_0 \left[\frac{1}{3} e^{-\lambda_L t} + \frac{2}{3} e^{(-\lambda_T t)} \cos(2\pi v t) \right] \qquad (5.9)$$

where a_0 is the initial asymmetry and $P_Z^{\text{exp}}(t)$ the polarization and v is the muon precession frequency due to local field. λ_L (L = longitudinal) and λ_T (T = transverse) are the relaxation rates parallel and perpendicular to the local field. The mean value of local field experienced by a muon at its stopping site B_{loc} were obtained using $2\pi v = \gamma_\mu B_{loc}$, where γ_μ is the gyromagnetic ratio of the muon (0.1355MHz/mT) [46]. The B_{loc} is typically used as an ordering parameter [46]. For higher temperatures, i.e., $T > 100$ K, 1/3 relaxation tail and parts of 2/3 relaxation tail for $T > 150$ K move beyond the instrument's time window. Longitudinal relaxation is also called T_1- relaxation, which typically originates from spin-lattice processes, whereas transverse relaxation is called T_2-relaxation and originates from spin-spin relaxation process.

Muon precession frequency and thus derived B_{loc} as a function of temperature increase gradually, not showing typical power-law critical behavior observed in the second-order phase transition. Similar temperature behavior is observed in the case of λ_T, whereas λ_L is distributed around $0.01 (\mu s)^{-1}$) down to 10 K and sharply increases below 10 K.
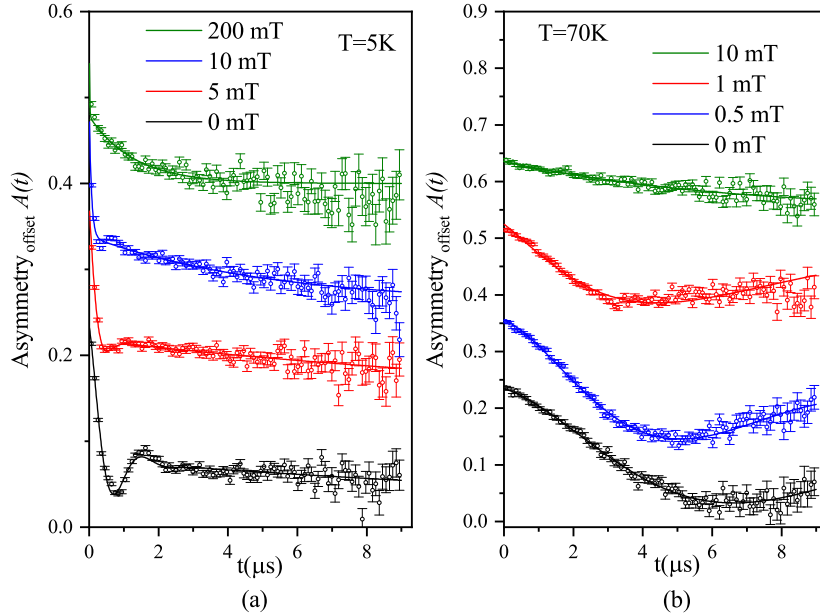
Figure 5.15: Longitudinal field dependency of muon spectra captures at 5 K (a) and 70 K (b).

5.4.2 Longitudinal Field Decoupling

The longitudinal decoupling measurements were made at 5K and 70K. From the Figure 5.15 it is evident that the oscillations in asymmetry spectra are quenched in the applied fields of 5 mT (at 5K). This observation is consistent with the internal field extracted from the model (4.4mT and 0.6mT, respectively). This indicates that the oscillations in the ZF-spectra indeed correspond to the internal field. However, at 5 K, even for a relatively high field of 200 mT the polarization is not entirely recovered, i.e., even with the application of longitudinal field 40 times stronger than the internal field, the polarization has not become time-independent. This implies that internal fields are fluctuating.

Fig .5.16 consists of plots of field dependency of ν, λ_T, and λ_L extracted from the fitting Eq: 5.9 to the asymmetry spectra at 5K. In-

102

terestingly, the 2/3 tail (hence λ_T) persists at fields higher than 5mT, where the precession frequency was quenched. Both λ_T and λ_L follow similar trends in the applied field where the asymmetry re-polarization does not quench at a high filed of 20 mT. Thus we can conclude that the observed internal field is constantly fluctuating.
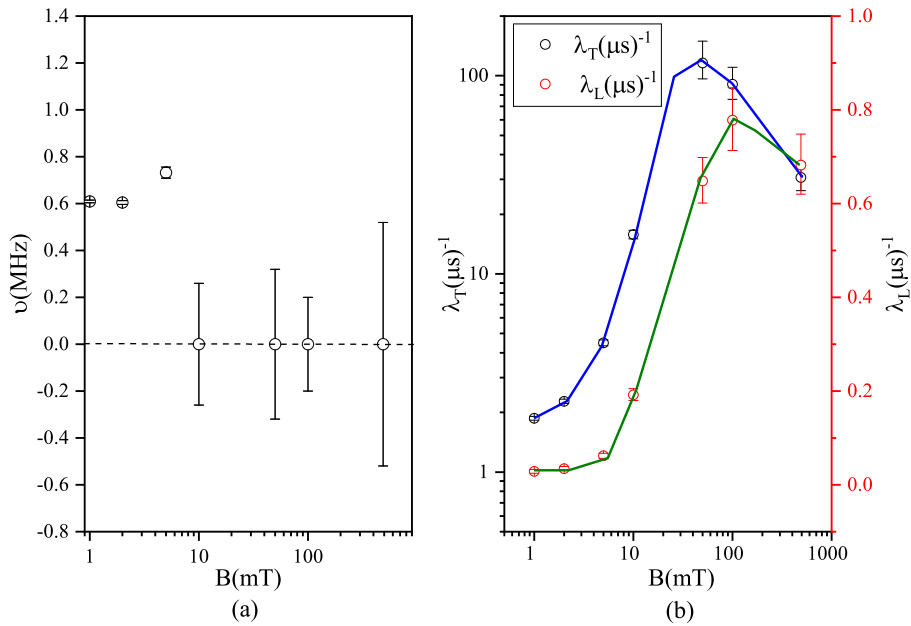
Figure 5.16: The results from fitting LF-μ^+SR data at 5 K to equation 5.9

5.4.3 Muon Stopping Site Calculation

Historically, a fundamental challenge in the interpretation of μSR data was to understand the muon stopping site [118, 119]. In particular, for SrTm$_2$O$_4$ the origin of the local field could not be identified straightaway. In this case, it becomes vital to identify the muon stopping site and thus understand the source of the internal field sensed by the muons.

In recent years various competent theoretical techniques have been de-

veloped to aid the muon site determination[120]; in particular the DFT based technique where the μ^+ is modeled after H$^+$ (proton) by geometric optimization [121]. This method is called DFT+μ technique.
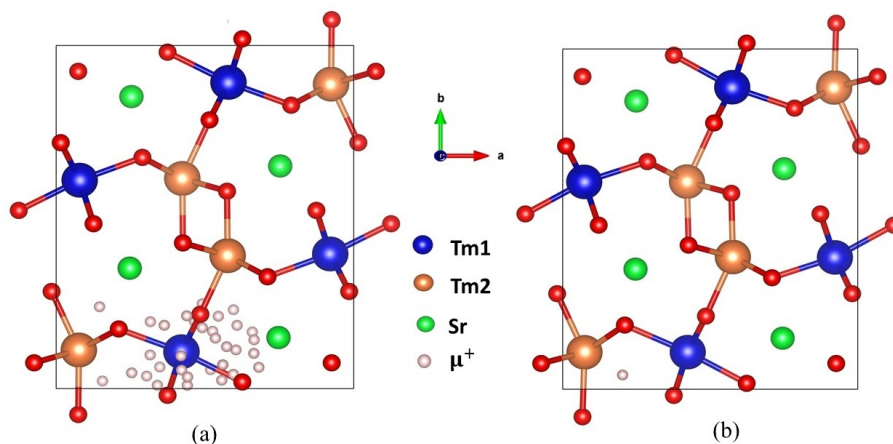
Figure 5.17: Representative set of starting muon positions in which the muons were relocated to symmetry-reduced subspace with 0.5 Åfor inter-muon distance and 1 Åfor muon-atom distance as a constraint. (a) represents 35 starting positions and (b) single optimized position.

The DFT calculations were conducted by following the recipe provided in Ref. [119] with the plane-wave pseudopotential based code QUANTUM ESPRESSO [61] using the generalized gradient approximation (GGA) exchange-correlation functional. Ions were modeled using ultrasoft pseudopotentials, and the muon was modeled by a norm-conserving hydrogen pseudopotential (provided graciously by Arne Ravandal). The Tm pseudopotential with the 4f electrons in the core (as in crystal field calculations) was chosen, as this calculation is computationally less demanding. The calculations were performed for SrTm$_2$O$_4$ in a single unit cell. The Mufinder [121] program was used to obtain the starting positions for muons. Two sets of starting positions were chosen. In the first set, the muons were distributed randomly within the unit cell by introducing the least inter-muon distances ($\mu-\mu$) and muon to atom distances (μ-atom) as constraints governing the random distri-

bution of muons. In the second set, randomly distributed muons were relocated to symmetry-reduced subspace, specifying the lowest inter-muon distances and the muon-atom distance. Figure 5.17(a) shows the initial starting position in the reduced sub-space of SrTm$_2$O$_4$ unit cell. The presence of a single muon stopping site (from experiments) was considered while preparing these starting position sets. This considera-tion was made as we observed a single precession frequency in the ZF measurements. Each of these systems was allowed to relax until all the forces were below 10^{-3}Ry/a.u. The calculations were performed with sets with several lowest inter-muon and muon-atom distances as con-straints. The calculation yields low-symmetry interstitial site [0.2092, 0.0448, 0.25] or its symmetry equivalent positions in 62.Pnam space group (the parent structure) (in case muon is distributed in the entire crystal). Figure 5.17(b) shows the optimized position in the reduced sub-space of SrTm$_2$O$_4$ unit cell. Note that this calculation considers only the diamagnetic muon states.

The muon-induced distortion impacts the crystal field levels. Qualita-tive estimation of muon-induced distortion on crystal field levels was carried out using the point charge model. Muon-induced distortion re-duces the gap size of Tm2 by 38% and Tm1 by 80%.

5.5 Conclusion

The crystal fields of SrTm$_2$O$_4$ were investigated using susceptibility, magnetization in pulsed fields, heat capacity, INS, and μ^+SR. Bulk property results indicate a strong anisotropy and show no ordering, down to 2 K. INS measurements were successful in identifying five excitations within 110 meV. Two crystal field models, the DFT and the EC models, were implemented to understand the single-ion properties. The DFT model predicts dominating $|6, 0\rangle$ for Tm1 and $|6, \pm 1\rangle$ for Tm2 ground states, whereas the EC model determines the ground state of both the inequivalent sites to ordain $|6, 0\rangle$ states. Both the mod-els predict easy-axis anisotropy for Tm1 and easy-plane anisotropy

for Tm2. The EC model predicts the magnetic properties reasonably well despite some small discrepancies at low temperatures, attributed to inter-ionic magnetic interactions.

ZF-μ^+SR results show oscillations in the asymmetry spectra, a standard signature of long-range order. However, the absence of power-law type critical behavior and lack of long or short-range order reported in Ref. [4] indicates that the observed ordering is a muon induced phenomenon. To quantify the impact of muon-induced distortion on the crystal field, the muon stopping site was determined using DFT+μ methods. Then the point charge model was used to estimate the crystal fields. The point charge model qualitatively determines how muon implantation can renormalize the gap size of the low energy crystal field levels by up to 80% on Tm1 and 38% on Tm2.

Furthermore, the muon precession frequency follows an exponential decay with a thermal activation gap of 11.3(3) K, the same as the gap to the first excited state measured with INS. This, together with the temperature dependence of the longitudinal field measurements, allows us to conclude that the observed relaxation is dynamic in origin and that the local field is rapidly fluctuating, making the muon experience a quasi-static local field.

Finally, answers to the research questions formulated at the beginning of this chapter can be summarized as follows:

- The EC crystal field model suggests both Tm1 and Tm2 to process non-magnetic ground-state with predominantly $|6, 0\rangle$ state.

- Crystal field models suggest easy-axis anisotropy for Tm1 and easy-plane anisotropy for Tm2 (in *ab*-plane). The *c*-axis remains the hard axis for both sites.

- The temperature dependence of the precession frequency and the relaxation rates in μ^+SR indicate that the system is in an extended critical regime, and the observed relaxation can be attributed to dynamic ground state.

Paper II

Crystal field effects in the zigzag chain compound $SrTm_2O_4$.

Research articles

Crystal field effects in the zig-zag chain compound SrTm$_2$O$_4$

A. Bhat Kademane [a,*], D.L. Quintero-Castro [a,b], K. Siemensmeyer [b], C. Salazar-Mejia [c], D. Gorbunov [c], J.R. Stewart [d], H. Luetkens [e], C. Baines [e], Haifeng Li [f,g]

[a] *University of Stavanger, 4021 Stavanger, Norway*
[b] *Helmholtz Zentrum Berlin für Materialien und Energie, D-14109 Berlin, Germany*
[c] *Hochfeld-Magnetlabor Dresden (HLD-EMFL), Helmholtz-Zentrum Dresden-Rossendorf, 01328 Dresden, Germany*
[d] *ISIS Neutron and Muon Source, Rutherford Appleton Laboratory, Didcot, OX11 0QX, UK*
[e] *Paul Scherrer Institut, 5232 Villigen PSI, Switzerland*
[f] *Jülich Center for Neutron Science, 52428 Jülich, Germany*
[g] *Joint Key Laboratory of the Ministry of Education, Institute of Applied Physics and Materials Engineering, University of Macau, Avenida da Universidade, Taipa, 999078, Macao*

ARTICLE INFO

ABSTRACT

The single ion properties of the zig-zag chain compound SrTm$_2$O$_4$ have been investigated using heat capacity, magnetic susceptibility, magnetization, inelastic neutron scattering, and polarized muon spectroscopy. Two crystal field models are employed to estimate the single ion properties; a Density Function Theory based model and an effective charge model based on the Hutchings point charge model. The latter describes our experimental results well. This model estimates an easy-axis anisotropy for one of the Tm^{3+} sites and an easy-plane anisotropy for the second site. It also predicts a mixed ground state with dominating $J = 0$ characteristics for both sites. Additionally, muon spin rotation/relaxation (μ^+SR) spectra reveal oscillations, typically a sign of long-range magnetic order. However, the temperature dependence of the precession frequency and the relaxation rates indicate that the system is in an extended critical regime and the observed relaxation is actually dynamic.

1. Introduction

It was previously thought that rare-earth-based magnetic systems were well described in terms of classical long-range order of the total angular momentum and that unconventional magnetic phases were only realized in pure spin systems. However, that picture is rapidly changing, as it has been shown that crystal field effects together with magnetic frustration, low coordination, dipolar interactions, and low dimensionality can cast the perfect ground for exotic phenomena in rare-earth systems, such as cooperative paramagnetism [1], potential spin liquid phases [2,3], noncollinear order [4] and dimerization [5,6].

Unconventional magnetic phenomena have been reported for several members of the SrLn_2O$_4$ family of compounds, where Ln are rare earth ions [7–12]. These extend from long-range incommensurate structures in SrTb$_2$O$_4$ [13], coexisting distinctive types of short-range orders in SrHo$_2$O$_4$ [14,15] and SrDy$_2$O$_4$ [14,16], and coexisting noncollinear long-range and short-range order in SrYb$_2$O$_4$ [17]. These compounds crystallize in the orthorhombic space group 62.*Pnam*, where two crystallographically inequivalent trivalent rare earth ions are surrounded by distorted oxygen octahedra, with monoclinic C_s site symmetry, and form two zig-zag chains running along the c-axis (Fig. 1(a)).

The low-lying crystal field scheme plays a key role in forming highly anisotropic magnetic properties in SrLn_2O$_4$ family [8]. However, determining the crystal field scheme has been a non-trivial task due to the two inequivalent Ln^{3+} in low symmetry environments. Nevertheless, successful modeling of the crystal field schemes for some members of this family has been reported [14,18].

In SrTm$_2$O$_4$ Tm^{3+} has electronic configuration [Xe] $4f^{12}$ (non-Kramers ion). A 13-fold degenerate ground state is expected for the lowest energy multiplet $^3H_6$ ($S = 1$, $L = 5$, and $J = 6$) for every Tm^{3+}. crystal field only ground state is usually a singlet for the systems involving non-Kramers rare earth ions, and there is no magnetic ordering down to the lowest temperatures [19]. This is in agreement with the results reported by Haifeng Li et al. [20], which shows the absence of short and long-range magnetic ordering in SrTm$_2$O$_4$ down to 60 mK.

Here, we present two aspects related to the single ion effects in SrTm$_2$O$_4$. In the first part, we report the results of our magnetic characterization through heat capacity, magnetization, magnetic susceptibility, inelastic neutron scattering (INS) measurements, and we implement

---

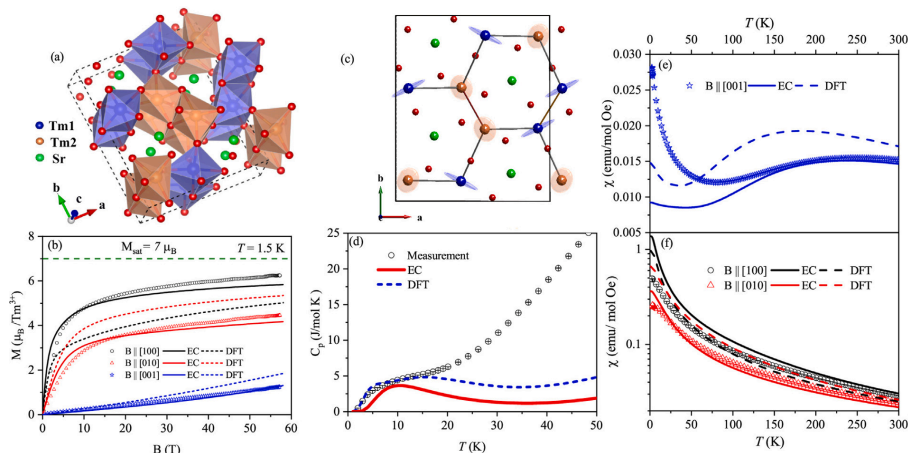**Fig. 1.** (Color online) (a) SrTm$_2$O$_4$ unit cell. Sr^{2+} ions are shown in green, O^{2-} in red, Tm1 in blue, and Tm2 in orange. Tm^{3+} zig-zag chains run along the c-axis and form a distorted honeycomb in ab-projection. (b) Measured magnetization (symbols) as a function of the magnetic field at 1.5 K, with magnetic fields applied along the main crystallographic axes. Calculated magnetization using the EC model (straight lines) and the DFT model (dashed lines). (c) Visual representations of g-tensor ellipsoid for Tm1 and Tm2 for the EC model. Tm1 shows easy-axis anisotropy while Tm2 shows easy-plane anisotropy. There is no component along the c-axis for both ions. (d) Low-temperature heat capacity of SrTm$_2$O$_4$(data open circles). The blue dashed line corresponds to the calculated Schottky anomaly using the DFT model, and the red solid line corresponds to the EC model. (e,f) Temperature dependence of DC magnetic susceptibility of SrTm$_2$O$_4$ (data shown as symbols) with a magnetic field of 0.1 T applied along (e) the c-axis and (f) a- and b-axes. The figures show the calculated susceptibility using the DFT model as dashed lines and the EC model as solid lines.

two crystal field models. In the second part, we present the observation of quasistatic order observed with muon spin rotation/relaxation (μ^+SR).

The standard method used in determining crystal fields involves searching for crystal field parameters (CFP) in parameter space that fit thermodynamic and spectroscopic properties. This procedure has multiple challenges. The major challenge is, degenerate sets of CFPs are expected for a low-symmetry non-Kramers system with multiple magnetic ions. To overcome these challenges, the crystal field problem in SrTm$_2$O$_4$ was approached with an *ab-initio* Density Functional Theory based model (DFT model) [21] and effective charge model (EC model) based on the point charge model (PC model) [22].

The DFT model is based on methodology proposed by Novák et al. [21]. In this method CFPs are obtained by using maximally localized Wannier functions (MWLF) with an all-electron DFT implementation. The advantage of this method is that, there is only one parameter that needs to be determined called 'charge transfer energy', Δ. The 'charge transfer energy' is estimated by,

$$\Delta \cong E_{tot}(4f^{(n+1)}, N_{val} - 1) - E_{tot}(4f^{(n)}, N_{val}) \tag{1}$$

where n-is number of electrons in 4f shell, N_{val} is number of electrons in the valence band, $E_{tot}(4f^{(n)}, N_{val})$ is the ground state total energy, and $E_{tot}(4f^{(n+1)}, N_{val} - 1)$ is the excited state energy. This method has been successfully implemented on several rare earth systems [21,23,24].

The EC model is based on Hutchings crystallographic PC model [25]. In this method, the crystallographic PC model was modified to account for oxygen's point charge with adjustable effective charge and effective radius. In our case, the crystallographic PC model with naive use of standard charge (i.e. $-2e$ for oxygen) and crystallographic coordinates at the position of the nucleus of oxygens did not result in an accurate prediction of the magnetic properties. Thus, oxygen charges and their displacement from crystallographic positions are fitted to INS spectra. This approach is more realistic compared to the crystallographic PC model and unlike the standard CFP fit approach avoids over-parameterization of fitted parameters. Similar semi-empirical improvisation has been successfully implemented for single-molecule magnets (SMM) [26] and for rare-earth pyrochlores [22].

In the second part, we present μ^+SR results. Typical static order in magnetic systems with zero fields μ^+SR (ZF-μ^+SR) manifests as oscillations in the asymmetry spectra. These oscillations are due to muon precessing in the internal magnetic field associated with magnetically ordered surroundings [27]. Similar observations in SrTm$_2$O$_4$ contradict the absence of magnetic order reported in Ref. [20]. Here, we prove that the quasistatic order observed in μ^+SR is due to a muon induced lattice distortion. In this work, we use *ab-initio* techniques to identify the muon stopping site and qualitatively discuss the impact of muon implantation on the crystal field with the aid of the PC model.

2. Methods

Powder SrTm$_2$O$_4$ samples were prepared according to Ref. [7], and single crystals were synthesized as described in Ref. [20]. A single crystal sample of mass 2.9 mg was used to measure the magnetization in the temperature range of 2–300 K with a magnetic field of 0.1 T applied along with main crystallographic directions. Heat capacity measurements were performed in a single-crystal sample of mass 49 mg in the temperature range of 2–200 K. These measurements were performed using a Physical Property Measurement System.

High-field magnetization was measured in a ^{4}He-flow cryostat up to 58 T using a coaxial pickup coil system [29]. The calibration to the absolute value of magnetization was done using a continuous field magnetometer in a commercial Superconducting Quantum Interference Device.

INS experiments were performed on a polycrystalline sample of mass 3.9 g at 5 K using the direct geometry neutron Time-of-Flight (TOF) instrument MAPS at ISIS [30]. The MAPS spectrometer was operated in two multi-rep modes yielding two incident energies (E_i) 26 meV and 130 meV using the sloppy chopper operated at 400 Hz.

The DFT model uses DFT derived Wannier functions, which takes the anisotropic shape features of f-orbitals into consideration [21,31]. The implementation procedure of this model for the APW+lo program, WIEN2k, was provided by Novák, et al. [21,32]. This procedure consists of two steps. In the first step, the standard self-consistent
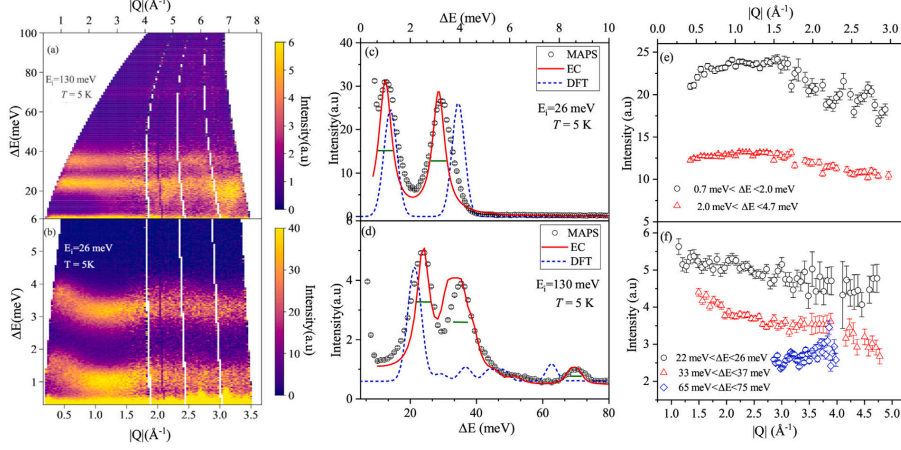
Fig. 2. (Color online) INS spectrum of powder SrTm$_2$O$_4$ as a function of momentum transfer (|Q|) and energy transfer (ΔE) with (a) E$_i$ = 130 meV and (b) E$_i$ = 26 meV. The spectrum was recorded using the MAPS spectrometer at 5 K. The color intensity scale indicates neutron counts, where purple stands for low counts and yellow high counts in arbitrary units. The gaps in the spectra are due to gaps between adjacent detectors. Integrated INS intensity (open symbols) as a function of energy transfer for (c) E$_i$ = 26 meV integrated in the range 0.7 Å^{-1} < Q < 2.5 Å^{-1} and (d) E$_i$ = 130 meV integrated in the range 1 Å^{-1} < Q < 4 Å^{-1}. Simulated spectra using the DFT (blue dashed line) and EC models (red solid line). Green lines refer to the calculated instrument resolution at the specific energy transfer [28]. |Q| dependency of the identified modes in the spectra for (e) E$_i$ = 26 meV and (f) E$_i$ = 130 meV.

solution of the Kohn–Sham equations of the DFT was performed with `WIEN2k` [32]. The PBE-GGA exchange–correlation functional was used for this calculation. The atomic sphere radii for Tm = 2.4 a.u, Sr = 2.24 a.u and O = 1.6 a.u were chosen. The number of basis sets amounted to ∼ 4023 (corresponding to $RKmax$ = 7.0), the number of k points in the irreducible part of the Brillouin zone was 200 (= 5×4×10). In this step, the Tm^{3+}(4f) states were considered as the core states (open core) to avoid non-physical self-interactions that would dominate the crystal field Hamiltonian. In the following step, f-electrons of one of the inequivalent Tm^{3+}were treated as valance states to allow their hybridization with the ligand orbitals (oxygen 2s and 2p). The relative position of 4f and ligand orbitals were adjusted by introducing a correction term Δ, which approximates the charge transfer energy. The non-self-consistent calculation was then performed, which yields the 4f Bloch states. These were transformed into Wannier functions using `Wannier90` and `Wien2wannier` [33,34]. This calculation yields the 4f local Hamiltonian, and it was then expanded in spherical tensor operators to obtain the CFPs, which are the expansion coefficients in Wybourne normalization [21,35]. Series of calculations with different Δ values in the range −0.68 eV to −13.6 eV were performed and compared with experimental results such as INS levels and bulk properties. The value of Δ = −1.83 eV was found to emulate the experimental results closely.

The EC model is based on the crystallographic PC model where the charge on oxygen ligands surrounding Tm^{3+} are considered as effective point charges lying between Tm-O bonds at effective radii. The starting values of effective charges are estimated by considering a net charge contribution to the oxygen by three Tm^{3+}and two Sr^{2+} coordinating with every oxygen. Subsequently, optimal effective charge and positions are obtained by fitting INS data using the code provided with Ref. [22] and `SIMPRE` [36]. The DFT model provides approximate estimations of crystal field levels that originate from Tm1 and Tm2. These estimations were considered to perform the fitting efficiently. Effective charges −0.468e and −0.725e and effective radii of 1.571 Å and 1.736 Å are obtained from fitting INS data for Tm1 and Tm2 respectively. The CFP's for DFT model and EC model in Stevens normalization are presented in Table 1.

Zero-field (ZF-) and longitudinal field (LF-) muon spin resonance μ^+SR measurements were performed with a polycrystalline sample, using the instruments DOLLY and LTF at the Swiss muon source (SμS), PSI. For the experiments, 2 g of polycrystalline sample was mixed with alcohol diluted GE varnish and attached to a silver plate for good thermalization. The LTF instrument with a dilution refrigerator was used to make two zero-field measurements at 19 mK and 1.4 K. ZF-measurements at several temperatures (between 2–250 K) were made on the DOLLY instrument. In addition, LF-measurements were made at 70 K and 5 K with several magnetic fields applied in the range 0.05 mT–0.5 T using DOLLY.

To understand the muon-induced effects, theoretical calculations (μ^+-DFT) were used to estimate the muon stopping site and the impact of muon on the local environment. The calculations were performed with the plane wave pseudopotential program `QUANTUM ESPRESSO` [37] using GGA exchange–correlation. Ions were modeled using ultrasoft pseudopotentials, and the muon was modeled by a norm-conserving hydrogen pseudopotential following the calculations in Ref. [38]. The calculations were performed in a single unit cell. The `Mufinder` was used to assign the starting positions for muons [39]. The system was allowed to relax until all the forces were below 10^{-3} Ry/a.u. The calculations were performed with sets of several lowest inter-muon and muon to atom distances as constraints. Effect of muon implantation on crystal fields were then quantified using Hutchings PC model by comparing crystal fields before and after muon implantation.

3. Results

3.1. Crystal field analysis

Magnetization results obtained from pulsed-field measurements at T = 1.5 K are compared with net magnetization obtained from DFT and EC models in Fig. 1(b). Magnetization with fields applied along the a- and b-axes increase quickly (< 10 T) and slow down eventually at higher fields. The c-axis remains the hard axis at all fields. The theoretical saturation moment for Tm^{3+}is 7 μ_B. However, magnetization

3

Paper II

Table 1

CFPs B_l^m (meV) in Stevens normalization for DFT model and EC model.

B_l^m	DFT Tm1	DFT Tm2	EC-Tm1	EC-Tm2
B_2^0	0.086866	−0.100362	0.118755	0.075761
B_2^2	0.344579	−0.553521	−0.06381	−0.253117
B_2^{-2}	0.114204	−0.576164	0.33965	0.477003
B_4^0	−0.000518	−0.000558	−0.003498	−0.002377
B_4^2	−0.018459	0.011757	−0.024412	0.0313
B_4^{-2}	−0.0184	0.014482	−0.011755	0.008587
B_4^4	−0.004236	0.00228	−0.000164	0.005889
B_4^{-4}	0.022274	0.016151	0.031696	0.016069
B_6^0	0.000046	0.000042	0.000048	0.000049
B_6^2	0.000152	0.000075	0.000001	0.000003
B_6^{-2}	0.000136	−0.000075	−0.000002	−0.000015
B_6^4	−0.000044	0.000105	−0.000043	0.000026
B_6^{-4}	−0.000138	−0.000061	−0.000131	−0.000146
B_6^6	0.000277	−0.000118	0.00016	0.000029
B_6^{-6}	−0.000083	0.00022	−0.000111	0.00004

along a-direction only reaches a maximum of $\sim 6.24\,\mu_B$ for maximum applied field. The measured slopes suggest that the sample is far from reaching magnetic saturation.

The magnetization for each crystal field model was derived by taking the average of magnetization of the two inequivalent sites. The EC model predicts magnetization trends with a slight deviation. This slight mismatch could be corrected by including the Weiss-molecular fields, implying significant contributions from magnetic interactions (not done here). The net magnetization from the DFT model does not predict the magnetization trends correctly.

A visual representation of g-tensor obtained from EC model for Tm1 and Tm2 is presented in Fig. 1(c). EC model predicts easy-axis anisotropy for Tm1 and easy-plane anisotropy (ab-plane) for Tm2. The model predicts the c-axis to be the hard axis for both Tm1 and Tm2. The DFT model also predicts similar anisotropy trends however these are not shown here. Similar distinct single ion anisotropy between inequivalent sites is a common occurrence in SrLn_2O$_4$ family [14,18].

Low-temperature heat capacity is presented in Fig. 1(d). A broad bump observed at low temperatures is a clear sign of a Schottky anomaly, implying the existence of low energy excitations. Above 20 K, phonon contributions to heat capacity get significantly stronger, making it difficult to distinguish any other magnetic contributions. Both crystal field models predict the Schottky anomaly fairly accurately indicating that the models predict the low energy excitations accurately.

Measured and calculated magnetic susceptibility, are shown in Figs. 1(e,f). These experimental results are a good indicator of the high magnetic anisotropy in this compound. The susceptibility along the c-axis is an order of magnitude smaller than for other directions, again reiterating that it is the hardest axis for magnetization. The susceptibility follows a paramagnetic behavior for temperatures below 50 K, followed by a broad peak centered at 220 K. On the other hand, the susceptibility for fields applied along the a- and b-axes follow a Curie–Weiss behavior all the way down to 50 K, where the curves start leveling off. None of the curves show any sign of a transition to a long range magnetic order. The EC model predicts susceptibility trends significantly well at high temperatures. At low temperatures however, it deviates from the experimental results. This could be due to unaccounted contributions from magnetic interactions.

Powder INS spectra measured at 5 K with incident energies 26 and 130 meV are presented as a function of momentum transfer (|Q|) and energy transfer (ΔE) in Figs. 2(a, b). The specific incident energies were chosen to cover the entire energy range in which the ground state multiplet expands (E < 110 meV). Integrated neutron scattering intensity as a function of energy transfer is presented in Figs. 2(c, d). In the low energy excitation spectra, two dispersing excitations can be identified centered at 1.230(5) meV and 3.412(3) meV with minima at $\sim 1.2\,\text{Å}^{-1}$. In the higher energy range, three excitations centered

at 23.72(4) meV, 35.82(6) meV and 71.00(2) meV are identified. The expected instrument resolution was calculated using `Mantid` [28] for each of the centers of the identified peaks. These are shown as green horizontal lines in Figs. 2(c,d). It can be noted that the all peaks are slightly broader than the resolution. This is expected for the lowest two modes, as they are dispersing. No dispersion can be seen however for the higher modes, and the slight broadening could be due to the overlapping of multiple excitations. Integrated intensity as a function of momentum transfer for each of these identified modes is plotted in Figs. 2(e,f). The decreasing intensity for increasing values of |Q| is an indicator of the magnetic nature of the excitations. It is important to note that the low energy modes (Fig. 2(e)) are influenced by the dynamic structure factor due to inter-ionic magnetic interactions, showing a maximum centered at 1.2 Å^{-1}. The |Q| of mode centered at 71 meV, does not show the typical magnetic form factor. This could be due to strong phonon contributions at the measured restricted |Q| range and energy transferred.

The fitted and calculated neutron powder scattering cross-section for EC and DFT models are presented in Figs. 2(c,d). The cross-sections were convoluted with the MAPS instrument resolution function using `Mantid` [28]. The EC model fits INS data well. A small disagreement is found around 30.492 meV, where the model calculates additional crystal field modes. Contrarily, the DFT model is successful in explaining only the low-energy excitations.

The first four eigenvalues and eigenvectors are reported in Table 2(a) and (b) for the DFT and EC models. J-mixing was observed within $|^3H_6, m_J\rangle$. The EC model predicts major contributions from $J = 0$ to the ground states of both the sites and $J = \pm 1$ dominates the first excited states. In contrast, in the DFT model, the major contribution to the Tm1 ground state comes from $J = 0$, while the ground state of Tm2 $J = \pm 1$ provides a major contribution. It is evident that among the low energy excitations, the first excited state originates from Tm2 while the second excited state comes from Tm1.

3.2. μ^+SR — Muon spin rotation and relaxation

ZF-μ^+SR asymmetry for selected temperatures are presented in Fig. 3(a). At low temperatures ($T < 100$ K), along with the relaxation part, there are oscillations with a single frequency that start developing and damps as the time evolves. At higher temperatures, these oscillations move beyond the instrument's time window, and only the relaxing part is available. The oscillations in the data are due to the muon precession as the muon experiences a static magnetic field in its immediate vicinity. Such oscillations are usually linked to long-range magnetic order, and a single frequency observation is the evidence for a single muon stopping site [27]. Despite this, there is no other evidence of long-range order in this compound, as discussed before.

The μ^+SR spectra were modeled using the polarization Eq. (2) for the entire temperature range (19 mK–250 K) [40].

$$a_0 P_Z^{exp}(t) = a_0\left[\frac{1}{3}e^{-\lambda_L t} + \frac{2}{3}e^{(-\lambda_T t)}cos(2\pi\nu t)\right] \qquad (2)$$

Where a_0 is the initial asymmetry and $P_Z^{exp}(t)$ the polarization and ν is the muon precession frequency. λ_L (L= longitudinal) and λ_T (T = transverse) are the relaxation rates parallel and perpendicular to the local field. In polycrystalline samples, the ratio of amplitudes between parallel and perpendicular components is 1 : 2 (fixed in Eq. (2)) [41]. The mean value of local field experienced by a muon at its stopping site B_{loc} can be obtained from the Larmor precession frequency using $2\pi\nu = \gamma_\mu B_{loc}$, where γ_μ is the gyromagnetic ratio of the muon (0.1355 MHz/mT) [27].
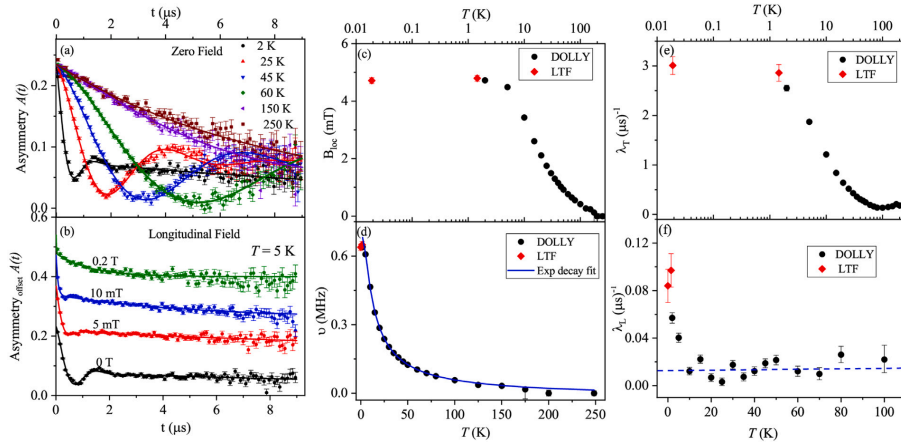
In polycrystalline samples, one can estimate λ_L by observing a 1/3 tail of the asymmetry spectra and λ_T a 2/3 tail. At low temperatures, the relaxation of both 1/3 and 2/3 tails is clearly visible. However, above 45 K, the 1/3 tail slowly shifts beyond 9 μs, the upper limit of the instrument, and vanishes completely above 100 K. Parts of the 2/3 tail

Table 2
Eigenvectors and Eigenvalues of the crystal field models.

(a) Tm1

Model	E (meV)	$\lvert0\rangle$	$\lvert\pm1\rangle$	$\lvert\pm2\rangle$	$\lvert\pm3\rangle$	$\lvert\pm4\rangle$	$\lvert\pm5\rangle$	$\lvert\pm6\rangle$
EC	0.000	0.695		0.0586		0.079		0.015
	3.143		0.4333		0.0295		0.0371	
	23.162		0.2411		0.1586		0.1003	
	30.492	0.0629		0.4041		0.0133		0.0512
DFT	0.000	0.5688		0.1108		0.0927		0.0041
	3.935		0.4467		0.0056		0.0408	
	21.608		0.0589		0.1849		0.2488	
	35.589	0.0258		0.1098		0.3591		
PC	0.000	0.6083		0.1577		0.0301		
	1.228		0.455		0.0281		0.011	
μ^+-PC	0.0000	0.4896		0.2133		0.0347		0.0087
	0.234		0.3951		0.0902		0.0087	

(b) Tm2

Model	E (meV)	$\lvert0\rangle$	$\lvert\pm1\rangle$	$\lvert\pm2\rangle$	$\lvert\pm3\rangle$	$\lvert\pm4\rangle$	$\lvert\pm5\rangle$	$\lvert\pm6\rangle$
EC	0.000	0.5597		0.1532		0.0499		0.017
	0.994		0.4029		0.0667		0.0304	
	32.997	0.0048		0.0355		0.1898		0.2724
	36.585		0.0256		0.1154		0.359	
DFT	0.000		0.4000		0.0006		0.0884	
	1.202	0.6537		0.13		0.0339		0.0027
	20.387	0.0076		0.0589		0.1849		0.2842
	21.379		0.1747		0.1508		0.1652	
PC	0.000	0.4423		0.2163		0.0508		
	0.388		0.369		0.107		0.0183	
μ^+-PC	0.0000	0.212		0.1630		0.0983		
	0.24		0.1965		0.1311		0.0574	

Fig. 3. (Color online) (a) ZF-μ^+SR spectra at selected temperatures. The solid lines represent the model described in Eq. (2). (b) LF-μ^+SR spectra at selected applied magnetic fields at 5 K. (c) Local field as a function of temperature extracted from the fitting to the ZF-μ^+SR data. (d) Muon precession frequency and exponential decay fit. Extracted transverse (e) and longitudinal (f) relaxation rates. The dashed line at $0.01(\mu s)^{-1}$ in (f) is a guide to the eye.

are not visible beyond 150 K. Hence our understanding of temperature dependence of ZF-relaxation rates and muon precession frequency is limited by the instrument time window.

The muon precession frequency ν and the B_{loc} are presented in Fig. 3(c,d). It is important to note that in a compound exhibiting no spontaneous magnetic order, B_{loc} is only different to zero in an applied magnetic field. Here, however, B_{loc} increases exponentially while cooling down, leveling off for temperatures below 2 K at 4.7 mT. There is no clear critical temperature, unlike any standard second-order phase transition to an ordered state. The muon precession frequency follows a similar trend, its temperature dependency has been fitted to an exponential decay function of the form $exp(-\delta/T)$ [42], where $\delta = 11.3(3)$ K (0.97 meV), seen as a blue line in Fig. 3(d). This activation temperature, δ, has coincidentally the same value of the gap to the first excited state.

The transverse and longitudinal muon spin relaxation rates extracted from the fits are presented in Figs. 3(e, f). λ_T is at least an order of magnitude faster than λ_L and has a similar temperature dependence as that of ν. However, λ_L remains almost constant, i.e., $0.01(\mu s)^{-1}$ above 10 K, and sharply increases below. The origin of the transverse component of the relaxation rate could either be due to the distribution of the local field or the dephasing of muon precession from fluctuation effects [41]. On the other hand, the longitudinal component is purely

due to fluctuations (dynamic effects). If the transverse component of the relaxation was due to static or quasi-static field distribution, then the field distribution should have narrowed as the local field (ordering parameter) reaches saturation. Nevertheless, we see that the relaxation rate increases as the local field increases saturating at 2 K. This behavior is a sign of an extended critical regime, similar to the one reported for TmNi$_2$B$_2$C [41].

Also, a consistent observation can be made in the case of the longitudinal field measurements. Fig. 3(b) shows the LF-μ^+SR time evolution spectra captured at $T = 5$ K with various applied magnetic fields in longitudinal geometry. This technique is used to determine whether the damping of muon polarization is caused due to the distribution of static fields or relaxation due to fluctuations [27]. The asymmetry spectra measured at several fields show that the oscillations are quenched at an applied field of 5 mT, which is close to B_{loc} value at 5 K. Nonetheless, there is no sign of relaxation quenching even at 0.2 T.

The muon stopping site was estimated using DFT based structural relaxation calculation, as explained in the methods section. A plane-wave pseudopotential program was used as it is relatively faster than all-electron DFT programs for structural relaxation. The presence of a single muon stopping site was considered as a single precession frequency was observed in the ZF measurements. The calculation yields a low symmetry interstitial site, as shown in Fig. 4(a). The effects of
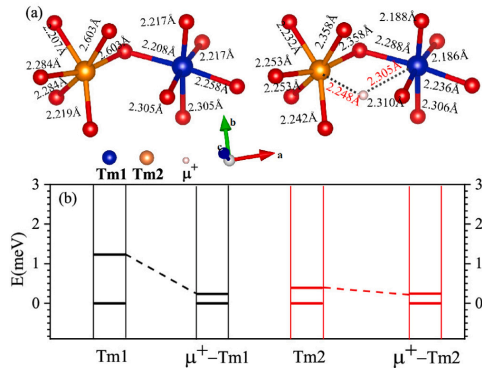
Fig. 4. (Color online) (a) Bond lengths comparisons before (extracted from Ref. [20]) and after muon implantation. (b) Impact of the muon-induced distortion in the crystal field scheme calculated using the PC model.

muon implantation on the crystal field scheme were modeled using the PC model and are shown in Fig. 4(b). Although the PC model is not accurate, it gives a qualitative distinction between the unperturbed and muon-perturbed crystal fields. The muon-induced distortion reduces the gap to the first excited state by $\sim 80\%$ for Tm1 and by $\sim 38\%$ for Tm2.

4. Conclusions

The crystal field properties of the non-Kramers compound $SrTm_2O_4$ were investigated using a combination of susceptibility, magnetization in pulsed fields, heat capacity, INS, and polarized muon spectroscopy. Two crystal field models, the DFT model, and the EC model are proposed to understand the single-ion properties. The DFT model foresees the ground state dominated by $J = 0$ for Tm1 and $J = \pm 1$ for Tm2 while the EC model determines the ground state of both the inequivalent sites to show predominantly $J = 0$ characteristics. Both the models predict easy-axis anisotropy for Tm1 and easy-plane anisotropy for Tm2. The EC model predicts the magnetic properties to great extent despite some small discrepancies at low temperatures, which can be attributed to inter-ionic magnetic interactions. These will be discussed in a separate report.

On the other hand, the DFT model is far from being perfect. Accuracy of the DFT model CFPs are strongly determined by the accurate determination of Δ. Although `Wannier90` program calculates MWLFs, it does not guarantee that they will be centered on the crystallographic site of the Tm^{3+} ions. To avoid this, calculations with other Wannier function formalism could be implemented as suggested in Ref. [23]. Additionally, even though open core calculations should restrain the $4f$ electrons in the core, some of their density can still leak out. Despite these shortcomings, the DFT model has provided a preliminary understanding of the crystal field schemes that have helped in making efficient fitting of INS spectra to arrive at the EC model.

ZF-μ^+SR results show oscillations in the asymmetry spectra, a standard signature of long-range order. However, the absence of standard critical behavior and absence of long or short-range order reported in Ref. [20] indicates that the observed ordering is a muon induced phenomenon. To quantify the impact of muon-induced distortion on the crystal field, the muon stopping site was determined using DFT techniques, and then the crystallographic PC model was used to estimate the crystal field. The PC model qualitatively determines how muon implantation can renormalize the gap size to the low energy crystal

field levels by up to 80% on Tm1 and 38% on Tm2. The renormalized gaps would take a value of $\approx 0.6\,meV$ ($\approx 7\,K$) for both ions. Having eventually an effective pseudo-doublet ground state. Similar observations have been made in the case of other non-magnetic non-Kramers ion-based systems [38,43,44] where it has been concluded that the observation of local fields was due to a muon-induced perturbation in the crystal field scheme. In these cases, however, hyperfine interactions play an important role.

Further insights are revealed by analyzing the temperature dependence of the muon precession frequency. The muon precession frequency follows an exponential decay with a thermal activation gap of $11.3(3)\,K$, which is the same as the gap to the first excited state measured with INS. This together with the temperature dependence of the longitudinal field measurements allow us to conclude that the observed relaxation is dynamic in origin and that the local field is rapidly fluctuating, making the muon experience a quasi-static local field.

CRediT authorship contribution statement

A. Bhat Kademane: Methodology, Validation, Formal analysis, Investigation, Writing – original draft, Visualization, Project administration. **D.L. Quintero-Castro:** Conceptualization, Investigation, Writing – original draft, Supervision, Writing – review & editing. **K. Siemensmeyer:** Investigation, Writing – review & editing. **C. Salazar-Mejia:** Investigation, Writing – review & editing. **D. Gorbunov:** Investigation, Writing – review & editing. **J.R. Stewart:** Investigation, Writing – review & editing. **H. Luetkens:** Investigation, Writing – review & editing. **C. Baines:** Investigation, Writing – review & editing. **Haifeng Li:** Conceptualization, Investigation, Investigation, Writing – review & editing.

Declaration of competing interest

The authors declare that they have no known competing financial interests or personal relationships that could have appeared to influence the work reported in this paper.

References

[1] J.S. Gardner, S.R. Dunsiger, B.D. Gaulin, M.J.P. Gingras, J.E. Greedan, R.F. Kiefl, M.D. Lumsden, W.A. MacFarlane, N.P. Raju, J.E. Sonier, I. Swainson, Z. Tun, Cooperative paramagnetism in the geometrically frustrated pyrochlore antiferromagnet $Tb_2Ti_2O_7$, Phys. Rev. Lett. 82 (1999) 1012–1015.

[2] Y. Shen, Y.-D. Li, H. Wo, Y. Li, S. Shen, B. Pan, Q. Wang, H.C. Walker, P. Steffens, M. Boehm, Y. Hao, D.L. Quintero-Castro, L.W. Harriger, M.D. Frontzek, L. Hao, S. Meng, Q. Zhang, G. Chen, J. Zhao, Evidence for a spinon Fermi surface in a triangular-lattice quantum-spin-liquid candidate, Nature 540 (7634) (2016) 559–562.

[3] S. Chillal, Y. Iqbal, H.O. Jeschke, J.A. Rodriguez-Rivera, R. Bewley, P. Manuel, D. Khalyavin, P. Steffens, R. Thomale, A.T.M.N. Islam, J. Reuther, B. Lake, Evidence for a three-dimensional quantum spin liquid in $PbCuTe_2O_6$, Nature Commun. 11 (1) (2020) 2348.

[4] V. Yu. Irkhin, Non-collinear magnetic structures and first-order magnetization process in rare-earth systems, J. Magn. Magn. Mater. 258–259 (2003) 228–230, Second Moscow International Symposium on Magnetism.

6

[5] K. Hara, S. Matsuda, E. Matsuoka, K. Tanigaki, A. Ochiai, S. Nakamura, T. Nojima, K. Katoh, Quantum spin state in the rare-earth compound YbAl$_3$C$_3$, Phys. Rev. B 85 (2012) 144416.

[6] G. Hester, H.S. Nair, T. Reeder, D.R. Yahne, T.N. DeLazzer, L. Berges, D. Ziat, J.R. Neilson, A.A. Aczel, G. Sala, J.A. Quilliam, K.A. Ross, Novel strongly spin-orbit coupled quantum dimer magnet: Yb$_2$Si$_2$O$_7$, Phys. Rev. Lett. 123 (2019) 027201.

[7] H. Karunadasa, Q. Huang, B.G. Ueland, J.W. Lynn, P. Schiffer, K.A. Regan, R.J. Cava, Honeycombs of triangles and magnetic frustration in SrL_2O$_4$ (L=Gd), Dy, Ho, Er, Tm, and Yb), Phys. Rev. B 71 (2005) 144414.

[8] O.A. Petrenko, Low-temperature magnetism in the honeycomb systems SrLn$_2$O$_4$ (review article), Low Temp. Phys. 40 (2) (2014) 106–112.

[9] N. Qureshi, O. Fabelo, P. Manuel, D.D. Khalyavin, E. Lhotel, S.X.M. Riberolles, G. Balakrishnan, O.A. Petrenko, Field-induced magnetic states in geometrically frustrated SrEr$_2$O$_4$, SciPost Phys. 11 (2021) 7.

[10] N. Qureshi, A.R. Wildes, C. Ritter, B. Fåk, S.X.M. Riberolles, M. Ciomaga Hatnean, O.A. Petrenko, Magnetic structure and low-temperature properties of geometrically frustrated SrNd$_2$O$_4$, Phys. Rev. B 103 (2021) 134433.

[11] N. Gauthier, A. Fennell, B. Prévost, A. Désilets-Benoit, H.A. Dabkowska, O. Zaharko, M. Frontzek, R. Sibille, A.D. Bianchi, M. Kenzelmann, Field dependence of the magnetic correlations of the frustrated magnet SrDy$_2$O$_4$, Phys. Rev. B 95 (2017) 184436.

[12] O. Young, G. Balakrishnan, P. Manuel, D.D. Khalyavin, A.R. Wildes, O.A. Petrenko, Field-induced transitions in highly frustrated SrHo$_2$O$_4$, Cryst. 9 (10) (2019).

[13] H.-F. Li, C. Zhang, A. Senyshyn, A. Wildes, K. Schmalzl, W. Schmidt, M. Boehm, E. Ressouche, B. Hou, P. Meuffels, G. Roth, T. Brückel, Incommensurate antiferromagnetic order in the manifoldly-frustrated SrTb$_2$O$_4$ with transition temperature up to 4.28 K, Front. Phys. 2 (2014) 42.

[14] A. Fennell, V.Y. Pomjakushin, A. Uldry, B. Delley, B. Prévost, A. Désilets-Benoit, A.D. Bianchi, R.I. Bewley, B.R. Hansen, T. Klimczuk, R.J. Cava, M. Kenzelmann, Evidence for SrHo$_2$O$_4$ and SrDy$_2$O$_4$ as model J_1-J_2 zigzag chain materials, Phys. Rev. B 89 (2014) 224511.

[15] J.-J. Wen, W. Tian, V.O. Garlea, S.M. Koohpayeh, T.M. McQueen, H.-F. Li, J.-Q. Yan, J.A. Rodriguez-Rivera, D. Vaknin, C.L. Broholm, Disorder from order among anisotropic next-nearest-neighbor ising spin chains in SrHo$_2$O$_4$, Phys. Rev. B 91 (2015) 054424.

[16] N. Gauthier, A. Fennell, B. Prévost, A.-C. Uldry, B. Delley, R. Sibille, A. Désilets-Benoit, H.A. Dabkowska, G.J. Nilsen, L.-P. Regnault, J.S. White, C. Niedermayer, V. Pomjakushin, A.D. Bianchi, M. Kenzelmann, Absence of long-range order in the frustrated magnet SrDy$_2$O$_4$ due to trapped defects from a dimensionality crossover, Phys. Rev. B 95 (2017) 134430.

[17] D.L. Quintero-Castro, B. Lake, M. Reehuis, A. Niazi, H. Ryll, A.T.M.N. Islam, T. Fennell, S.A.J. Kimber, B. Klemke, J. Ollivier, V.G. Sakai, P.P. Deen, H. Mutka, Coexistence of long- and short-range magnetic order in the frustrated magnet SrYb$_2$O$_4$, Phys. Rev. B 86 (2012) 064203.

[18] B.Z. Malkin, S.I. Nikitin, I.E. Mumdzhi, D.G. Zverev, R.V. Yusupov, I.F. Gilmutdinov, R. Batulin, B.F. Gabbasov, A.G. Kiiamov, D.T. Adroja, O. Young, O.A. Petrenko, Magnetic and spectral properties of the multisublattice oxides SrY$_2$O$_4$:Er^{3+} and SrEr$_2$O$_4$, Phys. Rev. B 92 (2015) 094415.

[19] B.R. Cooper, O. Vogt, Singlet ground state magnetism, J. Phys. Colloques 32 (1971) C1–958–C1–965.

[20] H.F. Li, A. Senyshyn, O. Fabelo, J. Persson, B. Hou, M. Boehm, K. Schmalzl, W. Schmidt, J.P. Vassalli, P. Thakuria, X. Sun, L. Wang, G. Khazaradze, B. Schmitz, C. Zhang, G. Roth, J.G. Roca, A. Wildes, Absence of magnetic ordering in the ground state of a SrTm$_2$O$_4$ single crystal, J. Mater. Chem. C 3 (2015) 7658–7668.

[21] P. Novák, K. Knížek, J. Kuneš, Crystal field parameters with wannier functions: Application to rare-earth aluminates, Phys. Rev. B 87 (2013) 205139.

[22] Z. Dun, X. Bai, M.B. Stone, H. Zhou, M. Mourigal, Effective point-charge analysis of crystal fields: Application to rare-earth pyrochlores and tripod kagome magnets R_3Mg$_2$Sb$_3$O$_{14}$, Phys. Rev. Res. 3 (2021) 023012.

[23] E. Mihóková, P. Novák, V.V. Laguta, Crystal field and magnetism with wannier functions: rare-earth doped aluminum garnets, J. Rare Ear. 33 (12) (2015) 1316–1323.

[24] P. Novák, J. Kuneš, K. Knížek, Crystal field of rare earth impurities in LaF$_3$, Opt. Mater. 37 (2014) 414–418.

[25] M.T. Hutchings, Point-charge calculations of energy levels of magnetic ions in crystalline electric fields, in: F. Seitz, D. Turnbull (Eds.), Solid State Physics, vol. 16, Academic Press, 1964, pp. 227–273.

[26] J.J. Baldoví, J.J. Borrás-Almenar, J.M. Clemente-Juan, E. Coronado, A. Gaita-Ariño, Modeling the properties of lanthanoid single-ion magnets using an effective point-charge approach, Dalton Trans. 41 (2012) 13705–13710.

[27] A. Yaouanc, P. Dalmas de Reotier, Muon Spin Rotation, Relaxation, And Resonance: Applications To Condensed Matter, Oxford University Press, Oxford, UK, 2011.

[28] O. Arnold, J.C. Bilheux, J.M. Borreguero, A. Buts, S.I. Campbell, L. Chapon, M. Doucet, N. Draper, R.F. Leal, M.A. Gigg, V.E. Lynch, A. Markvardsen, D.J. Mikkelson, R.L. Mikkelson, R. Miller, K. Palmen, P. Parker, G. Passos, T.G. Perring, P.F. Peterson, S. Ren, M.A. Reuter, A.T. Savici, J.W. Taylor, R.J. Taylor, R. Tolchenov, W. Zhou, J. Zikovsky, Mantid—Data analysis and visualization package for neutron scattering and μSR experiments, Nucl. Instrum. Methods Phys. Res. 764 (2014) 156–166.

[29] Y. Skourski, M.D. Kuz'min, K.P. Skokov, A.V. Andreev, J. Wosnitza, High-field magnetization of Ho$_2$Fe$_{17}$, Phys. Rev. B 83 (2011) 214420.

[30] R.A. Ewings, J.R. Stewart, T.G. Perring, R.I. Bewley, M.D. Le, D. Raspino, D.E. Pooley, G. koro, S.P. Waller, D. Zacek, C.A. Smith, R.C. Riehl-Shaw, Upgrade to the MAPS neutron time-of-flight chopper spectrometer, Rev. Sci. Instrum. 90 (3) (2019) 035110.

[31] A. Scaramucci, J. Ammann, N.A. Spaldin, C. Ederer, Separating different contributions to the crystal-field parameters using wannier functions, J. Phys. Conden. Matter. 27 (17) (2015) 175503.

[32] P. Blaha, K. Schwarz, F. Tran, R. Laskowski, G.K.H. Madsen, L.D. Marks, WIEN2K: An APW+lo program for calculating the properties of solids, J. Chem. Phy. 152 (7) (2020) 074101.

[33] A.A. Mostofi, J.R. Yates, G. Pizzi, Y.-S. Lee, I. Souza, D. Vanderbilt, N. Marzari, An updated version of wannier90: A tool for obtaining maximally-localised wannier functions, Comput. Phys. Comm. 185 (8) (2014) 2309–2310.

[34] J. Kuneš, R. Arita, P. Wissgott, A. Toschi, H. Ikeda, K. Held, Wien2wannier: From linearized augmented plane waves to maximally localized wannier functions, Comput. Phys. Comm. 181 (11) (2010) 1888–1895.

[35] B.G. Wybourne, Spectroscopic Properties Of Rare Earths, Interscience Publishers, 1965.

[36] J.J. Baldoví, S. Cardona-Serra, J.M. Clemente-Juan, E. Coronado, A. Gaita-Ariño, A. Palii, Simpre: A software package to calculate crystal field parameters, energy levels, and magnetic properties on mononuclear lanthanoid complexes based on charge distributions, J. Comput. Chem. 34 (22) (2013) 1961–1967.

[37] P. Giannozzi, S. Baroni, N. Bonini, M. Calandra, R. Car, C. Cavazzoni, D. Ceresoli, G.L. Chiarotti, M. Cococcioni, I. Dabo, A.D. Corso, S. de Gironcoli, S. Fabris, G. Fratesi, R. Gebauer, U. Gerstmann, C. Gougoussis, A. Kokalj, M. Lazzeri, L. Martin-Samos, N. Marzari, F. Mauri, R. Mazzarello, S. Paolini, A. Pasquarello, L. Paulatto, C. Sbraccia, S. Scandolo, G. Sclauzero, A.P. Seitsonen, A. Smogunov, P. Umari, R.M. Wentzcovitch, QUANTUM ESPRESSO: A modular and open-source software project for quantum simulations of materials, J. Phy. Condens. Matter. 21 (39) (2009) 395502.

[38] F.R. Foronda, F. Lang, J.S. Möller, T. Lancaster, A.T. Boothroyd, F.L. Pratt, S.R. Giblin, D. Prabhakaran, S.J. Blundell, Anisotropic local modification of crystal field levels in Pr-based pyrochlores: A muon-induced effect modeled using density functional theory, Phys. Rev. Lett. 114 (2015) 017602.

[39] B.M. Huddart, Muon stopping sites in magnetic systems from density functional theory, (Ph.D. thesis), Durham University, 2020.

[40] A.M. Mulders, P.C.M. Gubbens, U. Gasser, C. Baines, K.H.J. Buschow, Two types of magnetism in the magnetic superconductor TmNi$_2$B$_2$C related to the degree of carbon-site occupancy, Phys. Rev. B 57 (1998) 10320–10323.

[41] D.W. Cooke, J.L. Smith, S.J. Blundell, K.H. Chow, P.A. Pattenden, F.L. Pratt, S.F.J. Cox, S.R. Brown, A. Morrobel-Sosa, R.L. Lichti, L.C. Gupta, R. Nagarajan, Z. Hossain, C. Mazumdar, C. Godart, Competition between magnetism and superconductivity in TmNi$_2$B$_2$C observed by muon-spin rotation, Phys. Rev. B 52 (1995) R3864–R3867.

[42] M. Pregelj, A. Zorko, O. Zaharko, D. Arčon, M. Komelj, A.D. Hillier, H. Berger, Persistent spin dynamics intrinsic to amplitude-modulated long-range magnetic order, Phys. Rev. Lett. 109 (2012) 227202.

[43] F. Kayzel, J.J.M. Franse, P.C.M. Gubbens, A.A. Moolenaar, P. Dalmas De Réotier, A. Yaouanc, P. Bonville, P. Imbert, P. Pari, Quasi-static spin dynamics in the van-vleck paramagnet PrNi$_5$, Hyperfine Interact. 85 (1) (1994) 275–280.

[44] R. Feyerherm, A. Amato, A. Grayevsky, F.N. Gygax, N. Kaplan, A. Schenck, Crystal electric field next to a hydrogen-like interstitial— μ^+ in PrNi$_5$, Z. Phys. B Condens. Matter. 99 (1) (1995) 3–13.

7

115

6 Frustration & Field-Induced Phase in SrTm$_2$O$_4$

This chapter studies the magnetic exchange interaction and magnetic field-induced behavior of SrTm$_2$O$_4$. The project was conceived and supervised by D. L. Quintero-Castro.

XYZ-polarized neutron measurements were performed by R. Toft-Petersen, A. Wildes, and myself on D7 instrument at ILL. The low-energy INS measurements on single-crystal SrTm$_2$O$_4$ were carried out by D. L. Quintero-Castro, R. Toft-Petersen, J. Xu, and myself on the V2-FLEXX instrument at HZB.

The AC-susceptibility measurements were performed at Core Lab quantum materials, HZB by K. Siemensmeyer D. L. Quintero-Castro, and me. Powder NPD measurement in the applied magnetic field was performed on the DMC instrument at SINQ, PSI by D. L. Quintero-Castro, A. Gazizulina, V. Pomjakushin, and me.

I performed all the data analysis, modeling, and interpretation with support from D. L. Quintero-Castro.

6.1 Introduction

In the previous chapter, I have described the role of the crystal fields in the magnetism of SrTm$_2$O$_4$. The crystal field was successfully estimated using DFT and EC models. The EC model accurately captures the crystal fields of SrTm$_2$O$_4$, predicting the ground state of both Tm1 and Tm2 to be singlet $|6, 0\rangle$ and the first excited state $|6, \pm 1\rangle$. This model suggests that Tm1 has easy-axis anisotropy while Tm2 has easy-plane anisotropy. Additionally, the lowest dispersing mode ($\Delta E \approx 1\,\text{meV}$) was found to originate from Tm2, while the next mode ($\Delta E \approx 3\,\text{meV}$) originated from Tm1. These dispersing gapped excitations indicate that the exchange interactions could have a crucial role

117

in the magnetic properties of this system.
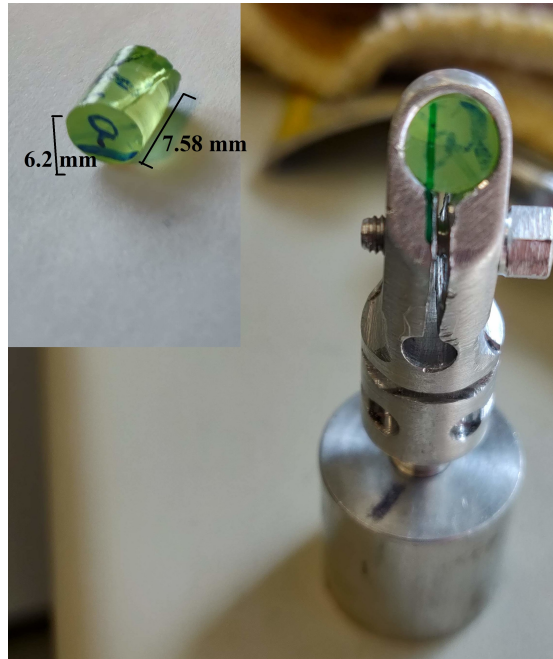
Figure 6.1: The single crystal SrTm$_2$O$_4$ mounted on the sample holder.

As discussed earlier, members of the Sr*Ln*$_2$O$_4$ family show diverse magnetic behavior. Most prominently, the importance of low-energy crystal field excitations was highlighted in Ref. [99], as also in the previous chapter of this thesis. Some of the members of this family show exotic ground states [122–127]. For example, in SrDy$_2$O$_4$ magnetic frustration and low dimensionality have prevented long-ranged magnetic ordering. This system is known to realize one-dimensional magnetic correlations along the chain direction, which is accounted for by the axial next-nearest-neighbor Ising model (ANNNI) [123]. Additionally, most of the members of this family show fascinating field-induced behavior [102, 128–131]. SrDy$_2$O$_4$ lacks long-short range magnetic order down to 60 mK. However, when the magnetic field was applied along the *b*-axis, the system exhibited a field-induced phase with a magnetization plateau at 1/3 of the saturation value [129, 131]. The

long-range ordered magnetic structure is shown to be identical to the one-dimensional ANNNI model in longitudinal fields [130].

However, SrTm$_2$O$_4$ behaves very differently compared to other members of the SrLn_2O$_4$ family. The SrTm$_2$O$_4$ is the only system, among the members studied until the drafting of this thesis, that does not show either long or short range order down to 65mK [4]. Unlike in most members of the family, the magnetization does not show 'plateau' formation, implying that the strongest contributor to magnetic anisotropy are mostly crystal fields. Additionally, low-energy modes in SrTm$_2$O$_4$ are dispersing, indicating that the ground state of the system cannot be ruled out as being crystal field only, without understanding the exchange interactions. In this regard, it is critical to model the dispersion to extract exchange interactions.

To begin with, we intended to approach the project to answer the following questions:

1. Which are the exchange interactions causing dispersing gapped excitations?

2. What are the implications of the exchange interactions?

3. Can the system be driven to thermal phase transition?

4. What are the consequences of oscillations observed in the muon spectra, in the light of exchange interactions?

The first step would be to verify the absence of any short-range order reported in Ref. [4] by observing the HL-plane which was not probed in Ref. [4]. Next, it would be vital to map and model the exchange interactions in various crystallographic directions. Furthermore, the influence of the applied field needs to be studied using NPD.

6.2 Experimental Details

The Quantum Design PPMS-ACMS was used to measure AC susceptibility. A single crystal sample of mass 49 mg was measured in the temperature range 2-200 K with the DC-magnetic fields of 1-14 T applied along the *c*-axis and frequencies in the range f =10 Hz-3 KHz. The measurements were performed in both field cooled (FC) and zero-field cooled (ZFC) protocols.

The magnetic structure in applied magnetic fields was studied using the neutron diffractometer DMC at SINQ-PSI [53] with a wavelength of 2.45 Å. A powder sample amounting to 5 g was pressed into pellets to fix the powder orientation while applying a magnetic field. The sample was measured under the ZFC protocol at 1.5, 30, and 120 K with 0 and 4.5 T applied magnetic fields. Subsequently, diffraction patterns were acquired in an applied magnetic field in the range $0 - 4.5$ T at 1.5 K. Additionally, diffraction patterns were also acquired at 4.5 T between $1.5 - 40$ K and at 120 K.

The low energy excitation spectra (<5 meV) were investigated using inelastic neutron scattering. The cold neutron triple-axis spectrometer FLEXX at HZB [55] was used to make these measurements. A large cylindrical single crystal of mass $\sim$ 3.2 g mounted on an aluminum sample holder was used for these experiments (Fig. 6.1). Constant wave-vector transfer Q-scans were preformed along $[0\,2\,L],[2\,0\,L]$, $[0\,K\,0]$, $[0\,2.5\,L]$, and $[0\,0\,L]$ with fixed final wave-vector k_f=1.3 Å^{-1} (E_f= 5 meV).

Uniaxial longitudinal neutron polarization analysis was carried out using the diffuse scattering spectrometer D7 at ILL [57] with a wavelength of 4.8 Å. The data were calibrated with vanadium and amorphous quartz. The non-time-of-flight mode was used to collect the data, leading to the extraction of the integrated scattering intensity with an incident energy of E$_i$ = 3.55 meV. Approximately 5 g of SrTm$_2$O$_4$ polycrystalline and a large cylindrical single crystal of mass $\sim$ 3.2 g (Fig. 6.1) with $(H, 0, L)$-plane on the scattering plane was used.
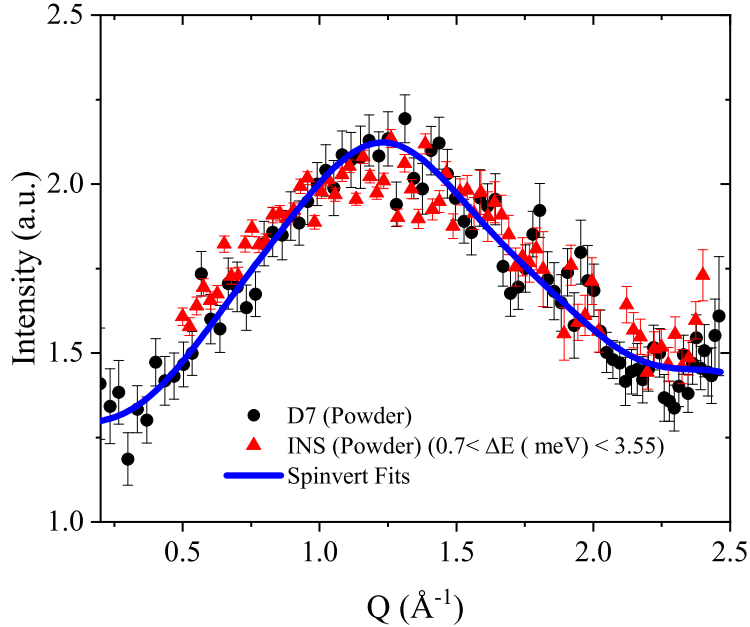
Figure 6.2: Magnetic powder patter obtained from D7 (black) overlaid with INS data (red) reported in previous chapter integrated between $0.7 < E_i < 3.55$ (meV). The blue line represents RMC fit using `Spinvert` [132, 133].

Equal counting times were spent for $x, y,$, and z polarization. The nuclear, magnetic, and nuclear spin-incoherent scattering cross sections were separated as a function of the wave-vector transfer Q using the $XYZ-$polarization analysis method described in Ref. [134].

6.3   Diffused Scattering

To confirm the lack of short-range order, we performed a polarized neutron experiment using the diffused scattering spectrometer D7 at the ILL [57] on both single crystal and polycrystalline samples. Figures 6.2 & 6.3 show the magnetic signal obtained out of XYZ-polarization

analysis as described in Ref. [134] for the polycrystalline sample and single-crystal, respectively. Diffused features in signal can be seen centered around $(0\,0\,0.66)$ on the $(H\,0\,L)$ plane in single crystal and at $|Q| \approx 1.3$ Å^{-1} in the polycrystalline sample. This signal seem to contradict the previously published D7 data measured on the $(H\,K\,0)$ plane [4], where no magnetic signal was found.
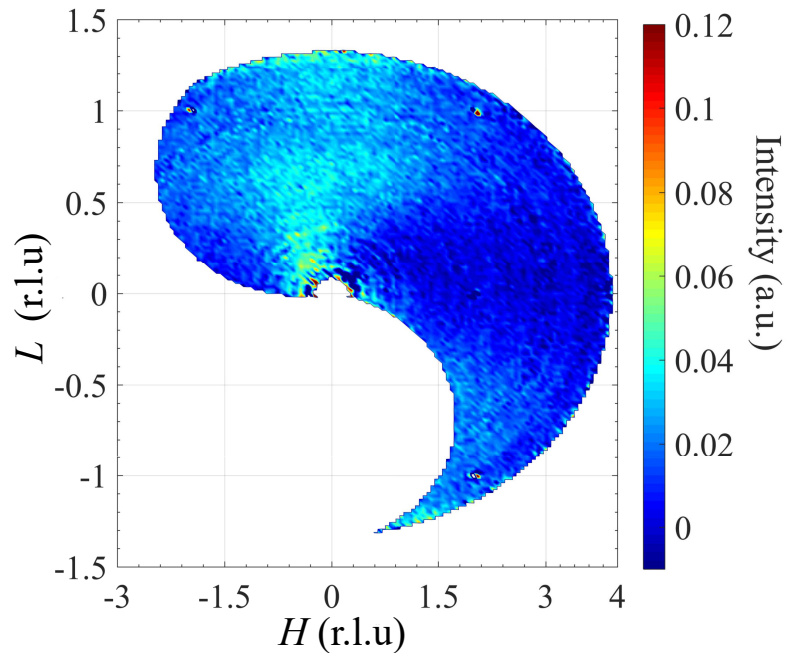
Figure 6.3: Pure magnetic signal after subtracting data from structural model. The color intensity scale indicates neutron counts, where blue stands for low counts and red for high counts in arbitrary units.

I have used reverse Monte-Carlo (RMC) refinement procedure using the `Spinvert` program [132, 133] to analyze the powder result, since the diffuse features in powder data cannot be modeled using conventional Rietveld refinement. The optimal 6 x 6 x 6 super-cell (1728 spins) is used with the spins initially lying on the *ab*-plane for both Tm^{3+} ions. This optimal super-cell was obtained by reconstructing the dynamic structure factors from RMC using the `Scatty` program [135]

and comparing it with single crystal data. Figure 6.4 presents single-crystal magnetic signal reconstructed from refined RMC model for 6 x 6 x 6 super-cell. The spin correlation function is plotted in Figure 6.5 as a function of the radial distance between the corresponding spin pair. These correlations are predominately antiferromagnetic (AFM) at shorter distances, where the nearest neighbors (NN) are the strongest interactions. The strongest ferromagnetic correlations are obtained for distances related to interchain (different Tm chains) exchange paths.
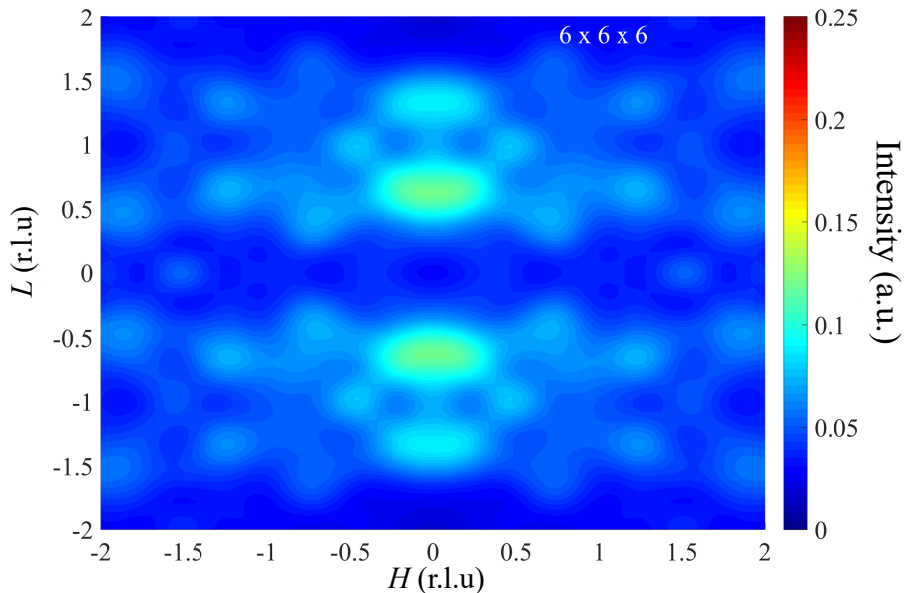
Figure 6.4: Single crystal dynamic structure factor reconstructed for RMC model using `Skatty` [135].The color intensity scale indicates neutron counts, where blue stands for low counts and red for high counts in arbitrary units.

The D7 data were acquired in the non-time of flight mode, where final-transfer energy is not analyzed. Thus it is necessary to investigate whether the spectral weight is in the elastic or inelastic channel. For this reason, inelastic neutron scattering data from the previous chapter was used as a comparison by integrating the spectrum in the transferred

energy region $0.7 < E < 3.55$ meV. Figure 6.2 shows the comparison. It is evident that the diffused signal originates from the low-energy excitations (< 3.55 meV), and no spectral weight can be linked to elastic diffuse scattering. Therefore, there is no indication of magnetic short-range order in this compound, in contrast to other members of this family. Thus we can conclude that our results are in consistent with polarized neutron results reported in Ref. [4].
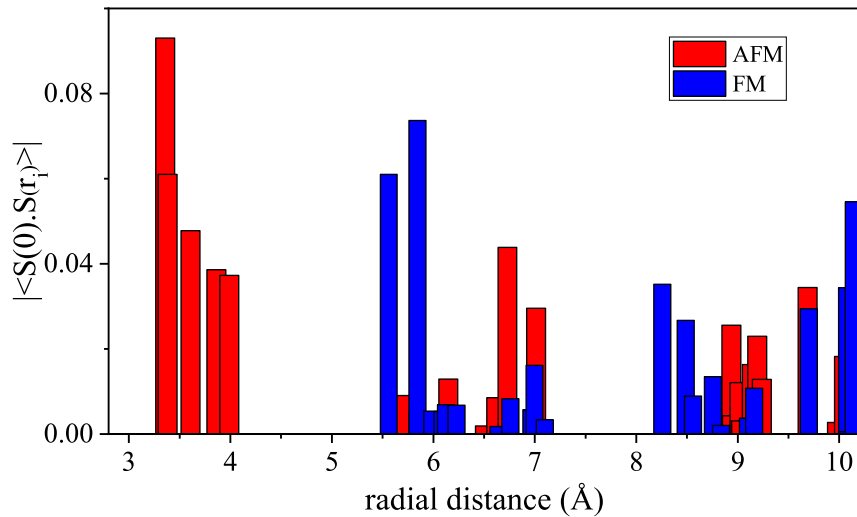
Figure 6.5: Spin correlation $|\langle S(0).S(r_i) \rangle|$ as a function of the radial distance r_i calculated from the refined RMC model for $T = 2$ K. The ferromagnetic interactions are marked by blue bars and antiferromagnetic interactions by orange bars.

6.4 Magnetic Exchange Interaction

We proceeded to investigate the wave-vector and energy dependency of the low energy magnetic excitations. INS measurements were performed along some of the reciprocal space directions using a triple axis
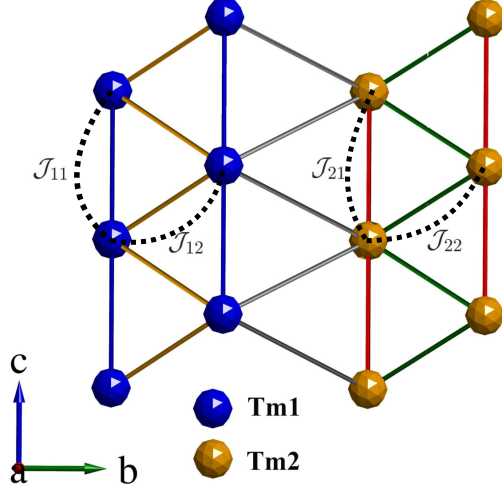
Figure 6.6: Tm1 (blue) and Tm2 (orange) zig-zag chains. In Tm1 chain NN interactions, ($\mathcal{J}_{11}$) are represented by blue lines and NNN interactions ($\mathcal{J}_{12}$) are represented by orange lines. In case of Tm2 chains the red lines represent NN interactions ($\mathcal{J}_{21}$) and green lines represent NNN interactions ($\mathcal{J}_{22}$).

spectrometer. The data extracted from these directions are shown in Figures 6.7 & 6.8. Spectra along $[2\,0\,L]$, $[0\,2.5\,L]$ (not shown), $[0\,2\,L]$ directions show dispersing gapped excitations with up to 4 branches below 4.5 meV, while spectra along $[0\,K\,0]$ and $[0\,0\,L]$ (not shown) show at least 4 non-dispersing modes. According to our crystal field calculations (from previous chapter), energy modes around 1 meV originate from Tm2 (calculated energy 0.994 meV), while the excitations around 3 meV originate from Tm1 crystal fields (calculated energy 3.143 meV). These excited states correspond to $|J, m_J\rangle = |6, \pm 1\rangle$. Both sets of modes show similar dispersion characteristics with shifted minima.

The dispersing excitations in SrTm$_2$O$_4$ are very different from the standard spin waves. Since the ground state is not ordered, these dispersions cannot be modeled using linear spin-wave theory. Hence I
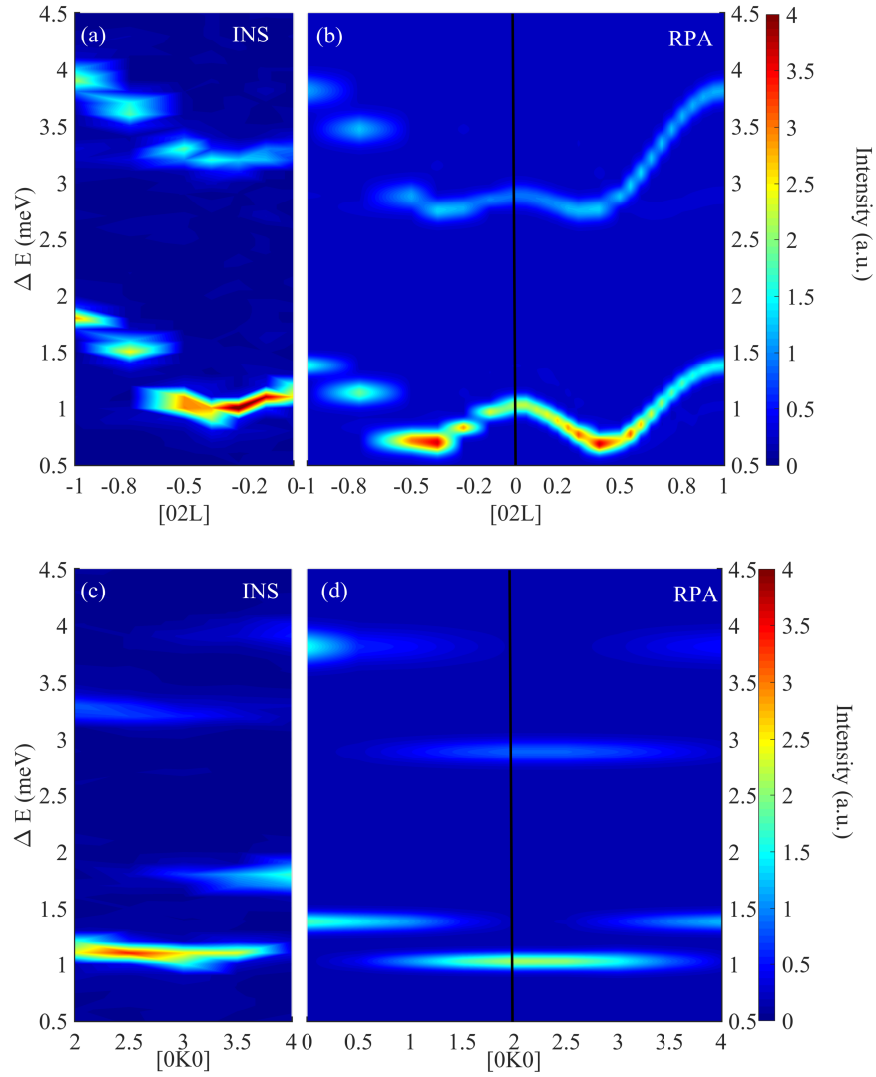
Figure 6.7: Magnon spectrum and RPA model along $[0\,2\,L]$ and $[0\,K\,0]$.

use the mean-field random phase approximation (MF-RPA) as implemented with *mcdisp* module in `McPhase` [7, 8, 136]. The following Hamiltonian is used to model the system:

$$\mathcal{H}_i = \sum_{n,kq} B_q^{(k)} O_q^{(k)} (\mathbf{J}_i) - \frac{1}{2} \sum_{ij} \mathcal{J}(ij)\mathbf{J}_i\mathbf{J}_i \qquad (6.1)$$

The first term in this equation is the crystal field term. The crystal field parameters are obtained from the previous chapter. The second term corresponds to the magnetic exchange interactions $\mathcal{J}(ij)$. Different possibilities were explored by including the interactions coming from the neighbors up to 6Å. In the best solution, it is only necessary to consider nearest and next-near neighbors, ignoring all other interactions, including inter-chain interactions. In this Hamiltonian, we ignore two-ion anisotropy, which is typically presented as 'Racah operators' [8], multi-pole interactions (eg. Eq. 2.5), and anti-symmetric exchange (eg. Eq. 2.4). Figure 6.6 presents the exchange path consideration for both Tm chains.

Table 6.1: RPA resulting magnetic exchange interactions and respective distances.

Site	$\mathcal{J}$(meV)		r_i(Å)		
Tm1	$\mathcal{J}_{11}$	-0.0132	r_1	3.3811	NN
	$\mathcal{J}_{12}$	-0.026	r_2	3.4212	NNN
Tm2	$\mathcal{J}_{21}$	-0.0048	r_1	3.3811	NN
	$\mathcal{J}_{22}$	-0.0043	r_3	3.4860	NNN

The exchange interactions were fitted to the experimental data using simulated annealing procedure implementation *simannfit* in `McPhase` [7, 136]. Table 6.1 presents the optimal exchange interactions obtained from fitting, and the corresponding distances. The simulated spectra are shown in Figures 6.7& 6.8. The calculation plots are extended beyond experimentally measured regions to capture the dispersion features in the respective directions. The simulation captures the features in the data to a large extent, with some identifiable discrepancies seen
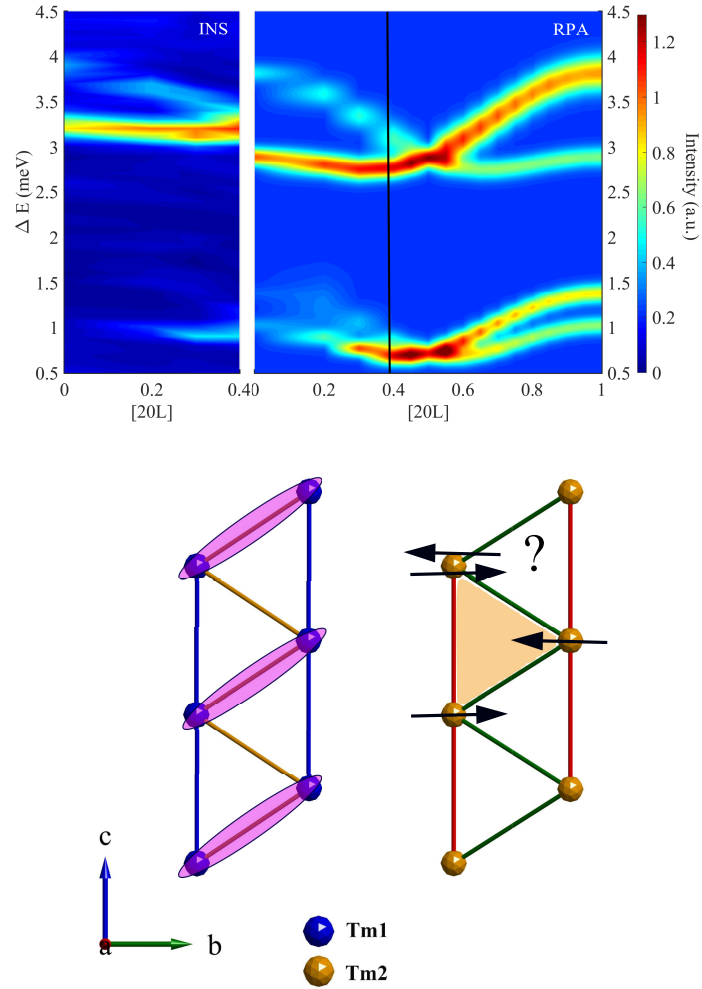
Figure 6.8: Magnon spectrum and RPA model along $[2\,0\,L]$. Pictorial representation of spin dimer for Tm1 and magnetic frustration for Tm2. The blue ellipses represent a singlet valence bond of spin. In Tm2 chain the magnetic frustration is captured withing the orange triangle using hypothetical spins represented as black arrows.

as energy shifts. For instance, modes along $[0\,K\,0]$ direction are approximately $0.4\,\mathrm{meV}$ shifted for the Tm2 mode, while the Tm1 mode

is shifted 0.35 meV. Additionally, the deviation of the model from the data is anisotropic, and linear corrections to the crystal field Hamiltonian have not improved the model. The obtained interactions are anti-ferromagnetic (Eq .6.1), in agreement with our RMC results for the NN and NNN (Fig. 6.5). These interactions are relatively fragile compared to the strength of crystal fields. Thus, in a future analysis it would be ideal to consider anisotropic exchange via dipolar interaction using Eq. 2.5.

6.4.1 Magnetic Frustration & Dimer Limit

The exchange interactions presented in Table 6.1 show that Tm2 chains have similar NN and NNN exchange interactions. Similar exchange interaction or $\frac{\mathcal{J}_{22}}{\mathcal{J}_{21}} \approx 1$ implies that the chain is frustrated. Figure 6.8 is a pictorial representation of magnetic frustration with the help of hypothetical spins presented as black arrows. The hypothetical spins are restricted to the *ab* plane by virtue of single-ion anisotropy. If Tm2 spins were to order within the orange triangle, the spin on the third corner would not be able to satisfy anti-ferromagnetic interactions simultaneously with respect to the remaining corners. Thus we deem the Tm2 chain to be frustrated [137, 138].

On the other hand, in Tm1 chains $\frac{\mathcal{J}_{12}}{\mathcal{J}_{11}} \approx 2$, implying that NNN interactions are twice as strong as NN interactions. Magnetic systems such as this with alternate strong and weak interactions can form dimers, where the strong interaction locks the pair of spins into a singlet state [139–141]. Figure 6.8 presents a visualization of dimer in Tm1 chains. In this chain, $\mathcal{J}_{12}$ is the intradimer interaction ($\mathcal{J}_{Intra}$), while the weak $\mathcal{J}_{11}$ interaction is the interdimer interaction ($\mathcal{J}_{Inter}$). So we deem Tm1 chains are in the dimer limit.

Systems such as this fall under the subgroup of dimer systems with large anisotropy [142, 143]. Golinelli *et al*. [142] have shown that the presence of strong anisotropy can significantly modify the excitation spectrum; thus, the exchange interactions alone will not be able

to quantify the gap size. In most cases the presence of nondiagonal matrix elements of magnetic dipoles between the nonmagnetic ground state and the excited magnetic state plays a major role. Depending on the type of anisotropy, the parallel or perpendicular applied fields determine the field induced order in these systems. Large-D (large single-ion anisotropy) dimer systems have been experimentally realized in pure spin system $NiCl_2 - 4\,SC(NH_2)_2$, where application parallel magnetic field resulted in *XY*-AFM phase [144, 145].

The magnetization vs. field results (from the previous chapter) were predominantly dominated by crystal fields and were unable to show 'plateau' features expected in frustrated systems. Thus, in systems such as SrTm$_2$O$_4$, the interplay of several unique interactions could make it challenging to decisively isolate the field induced phase transition involving magnon condensation, a typical trend in dimerized spin systems [146]. Despite such complications, SrTm$_2$O$_4$ shows magnetic field induced behavior and formation of *XY*-AFM phase with applied fields above 4 T. These results are presented in a subsequent section.

6.4.2   Critical Ratio and Soft-mode Limit

The soft-mode behavior for a dispersing excitation can be summarized as $E_Q \rightarrow 0$ where $T \rightarrow T_N$, where E_Q is the excitation energy at Q. To estimate the soft-mode limit of these dispersing excitations, a critical ratio can be defined based on methodology provided by Jensen *et al*. in Ref. [8, 147] assuming a two state model. First, I define

$$R(T) = 1 - \frac{\chi_T(0)}{\chi_T(Q, 0)} \tag{6.2}$$

where $\chi_T(0)$ is the non-interacting susceptibility and $\chi_T(Q, 0)$ is the static susceptibility at Q characterizing the ordered phase [147]. At a thermal second-order phase transition, i.e., at $T = T_N$, $R(T)$ becomes 1. Under RPA, Eq. 6.2 can be redefined as follows:

$$R(T) = 1 - \left(\frac{E_Q}{\Delta} \right)^2 = n_{01} R_0 \qquad (6.3)$$

where Δ is crystal field excitation between ground and first excited crystal field states, and $n_{01} = n_0 - n_1$ is the difference in population between the two sates. R_0 in Eq. 6.3 can be defined as follows:

$$R_0 = \frac{2M_\alpha^2 \mathcal{J}_{\alpha\alpha}(\mathbf{Q})}{\Delta} \qquad (6.4)$$

where $M_\alpha = |\langle 0| J_\alpha |1\rangle|$ [8] is the transition matrix element. Knowledge of R_0 gives estimation of the possibility of the system being driven to the soft-mode limit, i.e., the thermal second-order phase transition from paramagnetic state to an ordered state. From Eq. 6.3 we can see that when $R_0 > 1$ the soft-mode limit is achievable. In case of Pr, R_0 is calculated to be 0.96. The proximity of R_0 to 1 suggests that the Pr is very close to undergoing magnetic ordering [147].

The R_0s for SrTm$_2$O$_4$ are calculated by substituting the corresponding values for Tm2 and Tm1 in Eq. 6.4. For the lowest dispersing excitation, i.e., Tm2 level at 0.994 meV (= Δ), R_0 parameter is found to be 0.27, while for the next excited state at 3.143 meV originating from Tm1 $R_0 = 0.08$. Since $R_0 << 1$ at 2 K, implies that it is extremely hard to drive this system to second-order thermal phase transition (classical phase transition).

Additionally, estimated R_0s indicate that in SrTm$_2$O$_4$ at regime above 2 K the nuclear spin effects should not be neglected [147]. In Refs. [8, 33, 119, 148] it has been established that there are rare-earth systems where the hyperfine coupling to the nuclear spins can induce cooperative ordering of the combined electronic and nuclear moments. Usually, such behavior is limited to systems involving non-Kramer's ions where singlet ground-states are well-known and where two-ion coupling can be smaller than the threshold value for magnetic ordering, i.e., $R(T) = 1$ (or $R_0>1$). Another significant detail in the case

of non-Kramer's ions is that all of them have unpaired nuclear spins [148]. Thus it is vital to revisit the μ^+SR results presented in the last chapter, focusing on hyperfine effects.

6.5 Nuclear Hyperfine Enhancement

In this section, I revisit the ZF-μ^+SR results from the previous chapter, intending to understand the apparent ordering observed with muon precession frequency (ν) in the light of hyperfine effects.

In SrTm$_2$O$_4$ the muon precession frequency 'ν' grows consistently as a function of temperature. The critical parameter B$_{\text{loc}}$ calculated from ν is presented in the previous chapter. The internal field B$_{\text{loc}}$ does not show any standard critical behavior and reaches a trivial saturation value of 5 mT. We had modeled the 'ν vs T' using $exp(-\delta/T)$ to estimate the activation energy δ. However, the estimation of the critical ratio in the previous section of this chapter has shown that it is impossible to drive this system to the thermal phase transition. Thus it is decisive to understand the emergence of 'ν' and the peculiar temperature behavior of SrTm$_2$O$_4$ from the nuclear hyperfine perspective.

In Pr$_2$$B_2O_7$ (B = Sn, Zr, Hf), the static distribution of the internal field shows similar temperature dependency as internal fields in SrTm$_2$O$_4$. In these systems, it was shown that such behavior could be linked to hyperfine enhancement of nuclear spins of neighboring Pr ions, causing highly anisotropic distortion fields [119].

In our analysis of crystal fields, we have established that both Tm^{3+} have singlet ground-state with dominant $|J, m_J\rangle = |6, 0\rangle$ characteristics. For systems with singlet ground state and involving nuclear spin I, the Hamiltonian can be written according to the 'Bleaney model' [149]:

$$\mathcal{H} = \mathcal{H}_{\text{CF}} + g_J \mu_{\text{B}} (\boldsymbol{B} \cdot \boldsymbol{J}) + A_J (\boldsymbol{J} \cdot \boldsymbol{I}) - g_I \mu_{\text{B}} (\boldsymbol{B} \cdot \boldsymbol{I}), \qquad (6.5)$$

Where $\mathcal{H}_{\mathrm{CF}}$ denotes interactions with the crystal fields; the second term is the Zeeman interaction of the ion with electronic angular momentum $\hbar J$. The third term represents magnetic hyperfine interaction with a nucleus of angular momentum $\hbar I$ and the last term is the nuclear Zeeman interaction term.

In SrTm$_2$O$_4$ $\mathcal{H}_{\mathrm{CF}}$ has produced a singlet ground state with low lying excited state in case of both Tm1 and Tm2 with energy gap Δ. Using this model, one can arrive at the magnetic moment using the formalism reported in ref. [119].
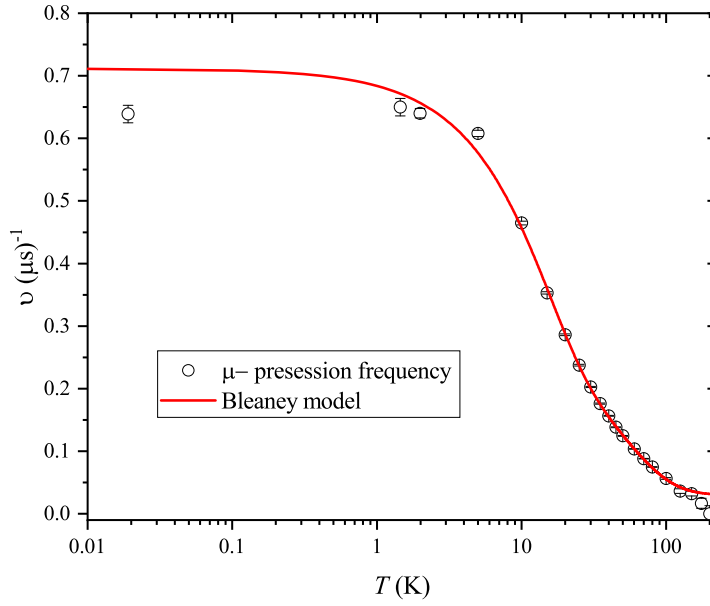

Figure 6.9: Muon precession frequency (black circles) as a function of temperature and fitted Bleaney [149] two state model (red line).

For ZF-μ^+SR the applied field $B_z = 0$, thus both the Zeeman terms are not relevant. This leads to the magnetic moment 'm' given by the following equation:

$$m = m_0 + \frac{\eta}{\tilde{\epsilon}} \tanh\left(\frac{\tilde{\varepsilon}}{k_B T}\right), \qquad (6.6)$$

where $m_0 = g_l \mu_B I_z$, $\quad \eta = g_J \mu_B M_\alpha^2 A_J I_z$, and $\tilde{\varepsilon} = \sqrt{(\Delta/2)^2 + (M_\alpha A_J I_z)^2}$ (where $\alpha^2 \leq J^2$) [119]. For ^{169}Tm $I_z = \frac{1}{2}$ and A_J = -394 MHz. The muon in this case is coupled to many neighbors *via* dipole-dipole interaction. Since dipole-dipole interactions are proportional to $\propto r^{-3}$ [119], it would be sufficient to consider only the nearest neighbor Tm atoms. According to our DFT+μ calculation (Fig. 5.17(b)), muon stops in the interstitial site between Tm1 and Tm2. Thus it suffices to consider a model in which dominant contributions to ν come from neighboring Tm1 and Tm2. Since the ordering parameter B$_{loc}$($\propto$ m) $\propto \nu$, we can model 'ν vs T' using the following equation:

$$\nu(T) = \sqrt{\left(\nu_{01} + \frac{\beta_1}{\tilde{\epsilon}_1} \tanh\left(\frac{\tilde{\epsilon}_1}{k_B T}\right)\right)^2 + \left(\nu_{02} + \frac{\beta_2}{\tilde{\epsilon}_2} \tanh\left(\frac{\tilde{\epsilon}_2}{k_B T}\right)\right)^2} \quad (6.7)$$

Where ν_{01}, ν_{03} and β_1, β_2 are scaled values of m_0 and η respectively and $\tilde{\varepsilon}_1, \tilde{\varepsilon}_2$ provide qualitative estimation of gap size [150]. Figure 6.9, presents ' ν vs T ' data fitted to Eq. 6.7. The gaps sizes estimated from the fit are 2.8 meV for Tm2 and 4.6 meV for Tm1.

In the previous chapter I have presented muon site determination using the DFT+μ technique and qualitative estimation muon induced distortion on crystal fields. The gap sizes estimated from ν vs T fits have similar magnitudes as the values obtained from PC model estimation from DFT+μ calculations. Following similar logic as presented in [119], considering the sensitivity of DFT+μ calculation, accuracy of PC-model of the crystal fields, and restrictions of the Bleaney model, we can conclude that the agreement is well within the inherent uncertainties.

The results from PC model of crystal fields show low-energy crystal field levels re-normalizing gap size, i.e., reducing the Tm1 gap size

134

by 80% and Tm2 gap size by 38% due to muon induced distortion . According to Eq. 6.6, $m \propto \Delta^{-1}$ implies that the closing of the first excited crystal field level plays the dominant role in enhancing nuclear spins. Thus we conclude that the observed oscillation in muon spectra can be associated with muon-induced 'nuclear hyperfine enhancement.' Similar nuclear hyperfine enhancement in systems involving ^{169}Tm was reported in TmPO$_4$ [151, 152].

6.6   Field Induced Order

In the previous section, I have demonstrated that Tm1-chains have the potential to dimerize. As explained earlier, the dimer spin system typically undergoes a field induced phase transition into the $XY-$AFM, which can be treated as magnon condensation [146]. However, in the case of rare-earth systems, there are not many candidates that exhibit the magnon condensation phase. For example, YbAl$_3$C$_3$ though expected to be a dimer does not exhibit magnon condensation [153], whereas Yb$_2$Si$_2$O$_7$ shows magnon condensation phase with critical fields ~ 0.4 and 1.4 T [154].

We try to investigate the field-induced phase in SrTm$_2$O$_4$ using AC-susceptibility and NPD.

6.6.1   AC Susceptibility

Figure 6.10(a) shows the real part of AC-susceptibility ($\chi^{'}$) in an applied magnetic field of different strength along the $c-$axis (perpendicular direction to the hard anisotropy axis). A broad peak emerges close to 4 T. In contrast, the imaginary part of AC-susceptibility ($\chi^{''}$) as a function of temperature does not exhibit any anomalies (not shown). The presence of a broad peak in $\chi^{'}$ and the absence of any anomalies in $\chi^{''}$ are indications of the emergence of AFM ordering [155, 156]. On the other hand, there is no deviation between ZFC and FC measurement protocols (not shown) and no frequency dependency (not shown). These behaviors suggest the absence of slow dynamics as in spin-glass
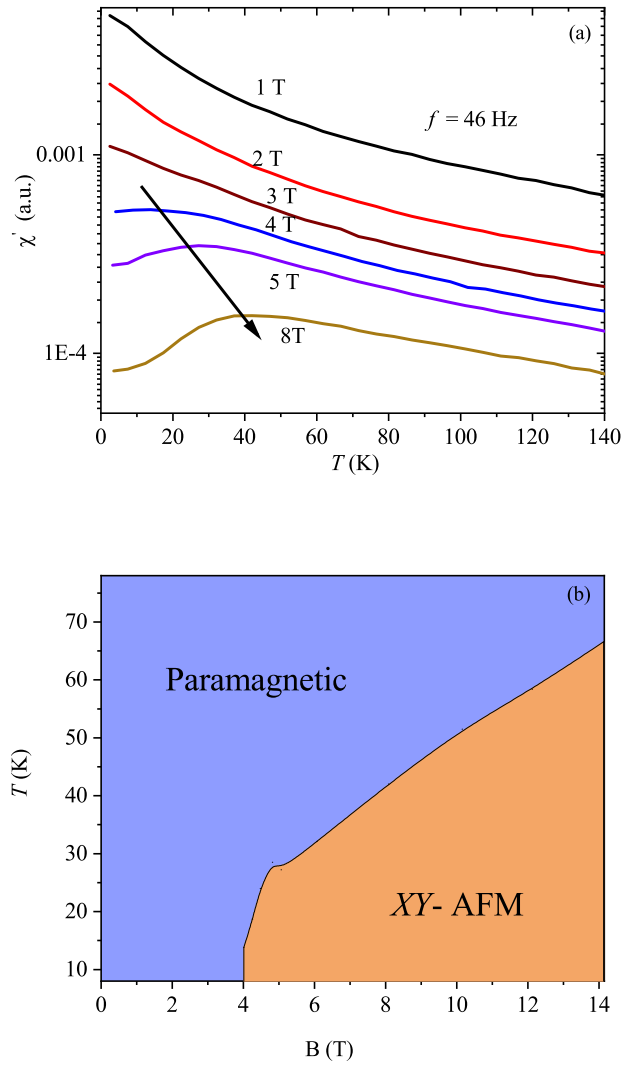
Figure 6.10: (a) Temperature dependency of χ' at various applied fields between 1-8 T. (b) Temperature vs magnetic field phase diagram obtained from the shifting χ' peak.

or spin-liquid systems [156]. Results shown in Figure 6.10(a) were measured with the field applied parallel to the hard axis (i.e., $c-$axis)

136

. Consequently, by virtue of the large moment size of Tm^{3+} and the magnetic field applied parallel to the hard axis, a large torque appears, forcing the sample to flip. Thus χ' in Figure 6.10(a) is represented in arbitrary units as they might not be very reliable.

The broad peak χ' starts emerging ~ 4 T, and as the magnetic field is increased starts to shift toward higher temperature. By tracking the position of this peak in T for various applied fields, we have constructed a magnetic phase diagram as a function of temperature and applied magnetic field. The phase diagram is presented in Fig.6.10(b). In the phase diagram, two phases can be identified: a paramagnetic phase and a field-induced phase that is AFM. This phase diagram very closely resembles the field vs. temperature phase diagram expected for the dimer spin system [146]. In that case, the first critical field B$_{c1} \sim 4$ T. However, within 1-14 T second critical field of *XY*-AFM phase B$_{c2}$ could not be tracked.

To understand the AFM phase in the applied field, we performed NPD.

6.6.2   Neutron Powder Diffraction

The NPD measurements on a polycrystalline sample of SrTm$_2$O$_4$ were performed at 120 K, 30 K, and 1.5 K at 0 T. Diffractogram measured at 1.5 K exhibits a broad feature in Q, that peaks at $|Q| \sim 1.3$ Å^{-1} along with sharper nuclear Bragg peaks. This broad feature was initially believed to originate due to short-range correlations. However, the analysis of diffused scattering data presented in the first section of this chapter shows that the diffused signals originate from the low-energy excited states. Thus the zero-field NPD data are consistent with Ref. [4] in predicting the absence of any magnetic ordering down to 65 mK.

However, with applied magnetic fields, some of the peaks in NPD data begin to order. Interestingly, the first critical field B$_{c1} \sim 4$ T predicted by χ' measurements is not consistent with the NPD data. Figure 6.11 presents field dependency of one of the magnetic peaks (121) at

Figure 6.11: Field dependency of (121) peak measured at 1.5 K.

$T = 1.5$ K. The (121) peak orders continuously in the applied field and critical field; in this case it is seemingly different from the B$_{c1}$ predicted by χ'. Thus, the NPD results need to be studied to separate the $XY-$AFM phase expected due to the dimerization of Tm1 chains and quenching of frustration in the Tm2 chain. In Tm2 chains, once the frustrations are quenched, we expect Tm2 moments to polarize in a preferred direction. With this hypothesis, I performed representational analysis to identify possible magnetic structures.

Magnetic Structure Determination

Figure. 6.12 presents the neutron diffraction patterns measured at 1.5 K and 4.5 T (scattered circles) with structural model overlaid (red lines). Pure magnetic intensities for all the peaks (blue line) were obtained by subtracting the structural model from the data. Peak (121) (with unresolved shoulders) is found to be the strongest. Relative strengths of intensities with respect to (121) for primary reflections are presented in Table. 6.2. As seen in Figure. 6.12, reflections (040), (120), and (121) get substantially enhanced in the applied magnetic field, whereas

reflections (011) and (111) emerge slightly in the presence of magnetic field.

Figure 6.12: Pure magnetic signal /blue lines) obtained after subtracting data at 4.5 T from structural model from 0 T and 1.5 K.

As mentioned earlier, in SrTm$_2$O$_4$ all atoms (also other atoms) occupy sites corresponding to wyckoff position 4c of *62. Pnam*, i.e., four similar kinds of atoms in a unit cell. Following Bertaut's method [31], we can identify four generic spin arrangements or basis vectors (BVs), namely F : (↑↑↑↑), C : (↑↑↓↓) , G : (↑↓↓↑), and A : (↑↓↑↓). I have calculated the magnetic structure factor F_{hkl} and polarization factor $\mathbf{P}_{hkl}$ in order to trace the contributions from the various basis vectors and to understand discrepancies in the critical behavior.

Table 6.2, suggests that the peaks (121) and (040) prefer significant contribution from F basis vector, whereas the peaks (120) and (111) have significant contribution from C basis vector. Unlike (120), (111)

Table 6.2: Absolute squares of magnetic structure ($|F_{hkl}|^2$) and polarization ($|\mathbf{P}_{hkl}|^2$) factor, and observed integrated magnetic intensity (Int.I) for key Bragg peaks. The factors are normalized to unit spin lengths. Integrated magnetic intensity is normalized.

| | $|F_{hkl}|^2$ | | | | $|\mathbf{P}_{hkl}|^2$ | | | |
| | F | C | G | A | | | | Int.I |
(hkl)	(↑↑↑↑)	(↑↑↓↓)	(↑↓↓↑)	(↑↓↑↓)	$x \, \|a$	$y \, \|b$	$z \, \|c$	(a.u.)
(120)	3.46	11.78	0.17	0.59	0.73	0.26	1	31.5
(011)	6.25	0	9.7	0	1	0.92	0.07	20.7
(111)	2.21	7.53	1.41	4.83	0.9	0.93	0.16	11.3
(040)	13.1	0	2.9	0	1	0	1	32.1
(121)	11.78	3.45	0.59	0.17	0.92	0.77	0.3	100

prefers *y* polarization with *C* basis vector instead of *x* polarization. Using magnetic representation analysis implemented in `BasIREPS` [81], possible magnetic structures (IRs) consistent with *62. Pnam* and propagation vector $k = (0,0,0)$ were found. The 8 IRs identified are $\Gamma_1(C_xF_y)$, $\Gamma_2(F_xC_y)$, $\Gamma_3(G_xA_y)$, $\Gamma_4(A_xG_y)$, $\Gamma_5(C_z)$, $\Gamma_6(F_z)$, $\Gamma_7(G_z)$, and $\Gamma_8(A_z)$.

To restrict the refinement of the NPD, I exclude the irreducible basis vectors that are inconsistent with the strongest observed peaks in the powder diffraction pattern. This is done by calculating the net structure factor in the commensurate case, i.e., $k = (0,0,0)$ can be written as follows:

$$\mathbf{F}_{hkl} = \mathbf{P}_{hkl}^x F_{hkl}^x + \mathbf{P}_{hkl}^y F_{hkl}^y + \mathbf{P}_{hkl}^z F_{hkl}^z \tag{6.8}$$

In Table 6.3, the net structure factor calculated for IRs by considering the structure factor of basis vectors and polarization factor are presented. All IRs with *z*-component can be easily excluded, since the *c*-axis is the hard axis and *c*‖*z* in SrTm$_2$O$_4$. This reduces the number of possible IRs to only $\Gamma_1 - \Gamma_4$. Among these IRs, Γ_1 and Γ_4 have no magnetic intensity for (040), and Γ_3 has an insignificant magnetic intensity on the strongest magnetic peak, i.e., (121). This mix

Table 6.3: Absolute squares of structure factor ($|\mathbf{F}_{hkl}|^2$). IR calculated for 62. *Pnam* for $k = (000)$, considering intra-chain interactions between two $4c$ zig-zag chains.

IRs	$|\mathbf{F}_{hkl}|^2$				
	(120)	(011)	(111)	(040)	(121)
Γ_1 (C_xF_y)	9.5	5.75	8.83	0	12.24
Γ_2 (F_xC_y)	5.59	6.25	8.99	13.1	13.49
Γ_3 (G_xA_y)	0.28	9.7	5.76	2.9	0.67
Γ_4 (A_xG_y)	0.47	8.92	5.66	0	0.61
Γ_5 (C_z)	11.78	0	1.2	0	1.04
Γ_6 (F_z)	3.46	0.44	0.35	13.1	3.53
Γ_7 (G_z)	0.17	0.68	0.23	2.9	0.18
Γ_8 (A_z)	0.59	0	0.77	0	0.05

and match procedure retains only Γ_2 as one of the allowed magnetic structures.

The magnetic representation in this case corresponds to Shubnikov space group (in OG setting) *62.447 Pna'm'* (representation mGM3+) [157]. The magnetic structure refinement was performed based on the following hypothesis:

- Tm2 chains are frustrated; thus, in the applied magnetic field, the frustration is quenched, and Tm2 moments polarize along a certain direction without undergoing a phase transition. This would mean that Tm2 moments are composed of FM basis vectors in the easy plane. To reduce the number of fitting parameters, we consider that the Tm2 moments are composed of the FM basis vector along x direction, i.e., F_x. In support of this hypothesis, polarization factor $\mathbf{P}^x_{hkl}$ is predominantly preferred in the case of basis vector F. However, one must note that FM y-component to Tm2 cannot be ruled out completely.

- Tm1 chains are dimerized, and therefore the expected ordered phase is *XY*-AFM Ref. [146]. Thus $\Gamma_2(F_x, C_y, 0)$ is used in the
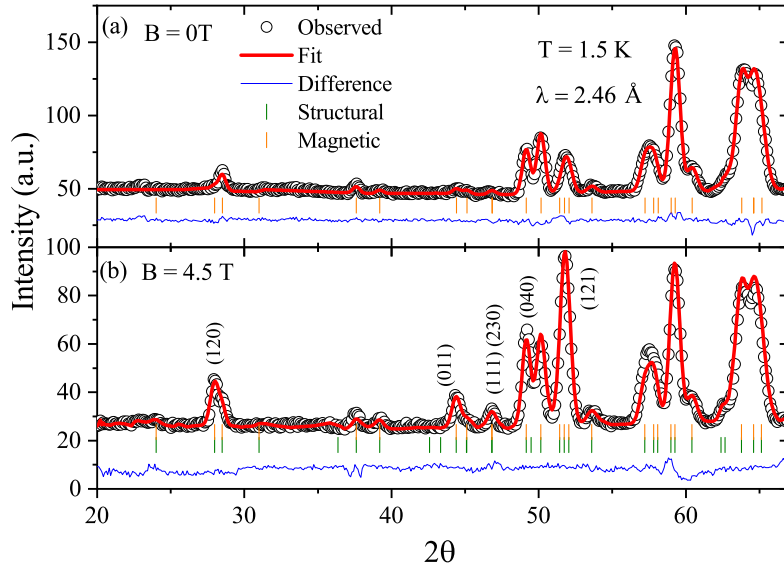
Figure 6.13: Neutron-diffraction patterns (black open circles), fits from the Rietveld refinement (red solid lines), and their differences (blue solid lines). The vertical bars are the expected Bragg peak positions as mentioned in the panels. NPD observed (measured on DMC diffractometer) at T =1.5 K and (a) B = 0 T and (b) B = 4.5 T corresponding to the data collected with neutron wavelengths 2.46 Å.

refinement.

The NPD patterns were refined using `FullProf` [81] and `JANA2006` [157], and the results are shown in Fig.6.13. Additionally, in the applied magnetic field, the powder sample has a preferred orientation (100). This preferred orientation is consistent with magnetization results. Table 6.4 presents the refined moments for the pattern at 4.5 T and 1.5 K. Figure 6.14 presents the refined magnetic structure in *ab*-plane. The ordered phase is *XY*-AFM for Tm1 sublattice and polarized ferromagnetic behavior is seen in Tm2 sublattice, confirming our hypothesis. Additionally, refined moments in Table 6.4 are consistent

with the magnetization vs field data presented in the previous chapter.

Table 6.4: IR, Basis vectors, refined moments (μ_B/Tm^{3+}) at 4.5 T and 1.5 K. The refinement achieved χ^2 = 5.84 and Magnetic R-factor = 10.08.

Site	IRs	Basis vectors	$(|\mu_x|, |\mu_y|, |\mu_z|)$
Tm1	Γ_2	$(F_x, C_y, 0)$	(2.07(03),0.79(2),0)
Tm2		$(F_x, 0, 0)$	(4.22(04),0,0)
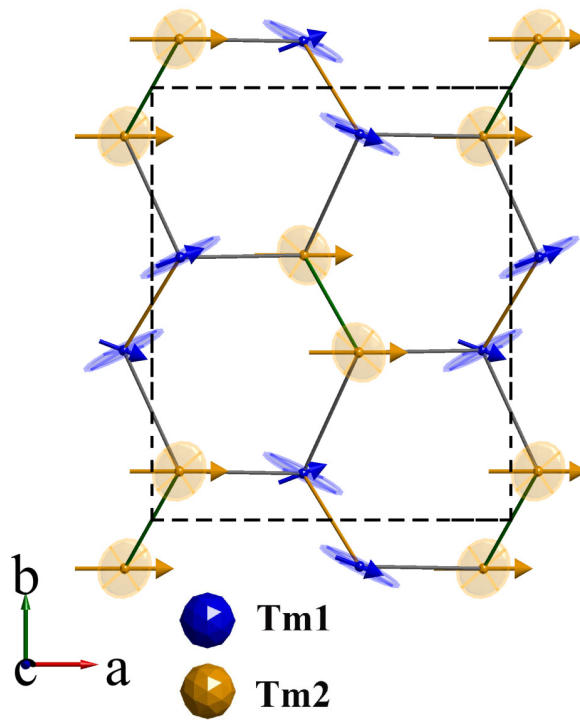
Figure 6.14: Distorted honeycomb arrangement of Tm1 and Tm2 chains with refined moments at 4.5 T overlaid with ground-state single-ion anisotropy from previous chapter.

Critical Behavior
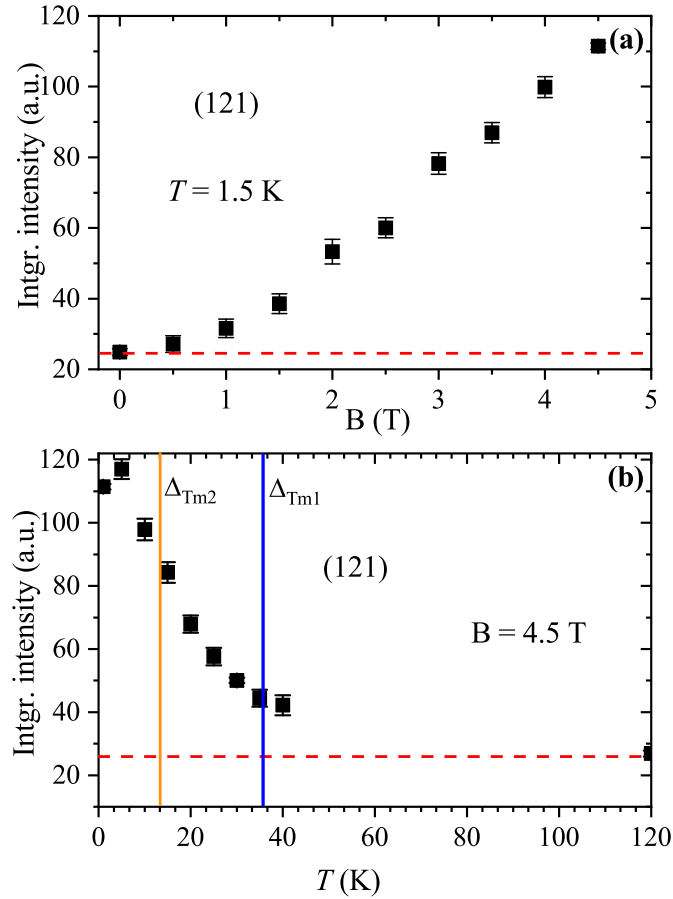
Figure 6.15: (a) Field evolution of integrated intensity of (121) at $T = 1.5$ K. (b) Temperature evolution of integrated intensity of (121) at B = 4.5 T. The blue and orange lines mark the gap-size (in K) for Tm1 and Tm2 excitations, respectively. The red dashed line corresponds to integrated intensity value corresponding to 0 T and 1.5 K.

In this section I present critical behavior of magnetic peaks (121) and

(120). Figures 6.15 (a,b) show the temperature evolution at B = 4.5 T and field evolution at T = 1.5 K of integrated intensity of (121). In Figures 6.16(a,b) a color-map of the field evolution at T=1.5 K and temperature evolution at B = 4.5 T of (120) are presented.

The field-dependent critical behavior of (121) and (120) are studied to understand the superficial discrepancy between NPD and AC Susceptibility results. Peak (121) is the strongest magnetic peak and as shown in Figures 6.11 and 6.15 (a) seems to emerge spontaneously as the magnetic field is increased. On the other hand, peak (120) starts to emerge beyond 2 T. Both the peaks behave differently compared to AC Susceptibility in this regard. However, the magnetic structure presented in Table 6.2 indicates significant contributions from F basis vector to both (121) and (120). This implies that the polarized Tm2 moments could cause different onset fields for (121) and (120). Thus, it is evident that there is no discrepancy between AC susceptibility and NPD results. Despite F basis vector contributions, the temperature dependency of (121) peak at 4.5 T gives a crucial detail on the XY-AFM phase.

At this juncture the eventual step would be to see what this critical behavior means, from the perspective of dimer systems. The dimer behavior in YbAl₃C₃ was shown in Refs. [158, 159]. However, Ref. [153] shows that instead of the typical XY-AFM expected in dimer systems, there was an unusual field-induced ordered state whose onset temperature was far exceeding the spin gap energy. This conclusion was arrived at by observing the temperature dependency integrated intensity of (200) peak at 12 T. In Figure 6.15(b) the (120) at 40 K ($\approx$ 3.3 meV) peak does not reach the integrated intensity value at 1.5 K and 0 T. This discrepancy can again be attributed to the polarizing Tm2 moments. So we conclude that in SrTm₂O₄ the origin of the XY-AFM phase can be associated with the dimerization of Tm1 chains. The slight discrepancy can be attributed to crystal field effects and polarization of Tm2 moments in the applied field. However, associating this XY-AFM phase to the singlet–triplet transition seen in the magnon

condensation would be unfeasible with the current understanding of this system. Thus to map the critical fields exclusively and to study the magnon condensation it would be crucial to identify a magnetic reflection with no contribution from F.

6.7 Conclusions & Outlook

In this chapter I have discussed magnetism originating from magnetic exchange interactions. The magnetic diffused scattering results have revealed that the system does not exhibit short-range correlations down to 2 K. The diffused signal in powder pattern and $(H\,0\,L)$ plane in single-crystal originates exclusively from integration of the elastic channel. The diffused signal in the $(H\,0\,L)$ plane indicates that the exchange correlations in SrTm$_2$O$_4$ are two-dimensional or quasi-one-dimensional with dominating AFM interactions among close neighbors.

Furthermore, the dispersing excitations were mapped using a single crystal along several crystallographic directions in reciprocal space. The first and second excited modes originating from Tm2 and Tm1 chains were found to disperse along $[2\,0\,L]$, $[0\,2.5\,L]$ (not shown), $[0\,2\,L]$ directions. These dispersions were modeled using RPA. The results show that NN and NNN interaction in both ladders are AFM in nature. Similar NN and NNN Intra-chain interactions ($\frac{\mathcal{J}_{22}}{\mathcal{J}_{21}} \approx 1$) in Tm2 ladder lead to absolute frustration whereas in Tm1 ladder, $\frac{\mathcal{J}_{12}}{\mathcal{J}_{11}} \approx 2$ indicates the ladder is in dimer limit. Calculation of the critical ratio has shown that SrTm$_2$O$_4$ cannot be driven to a thermal second-order phase transition. Insights obtained from the calculation of critical ratio have shown that the observed oscillations in ZF-μ^+SR spectra are signs of nuclear hyperfine enhancement due to muon induced distortion.

SrTm$_2$O$_4$ shows a magnetic field induced transition above 4 T. NPD results have shown that Tm1 chains in dimer limit lead to ordered *XY*-AFM phase in the applied field, while in the frustrated Tm2 chains the moments are polarized along the applied field.

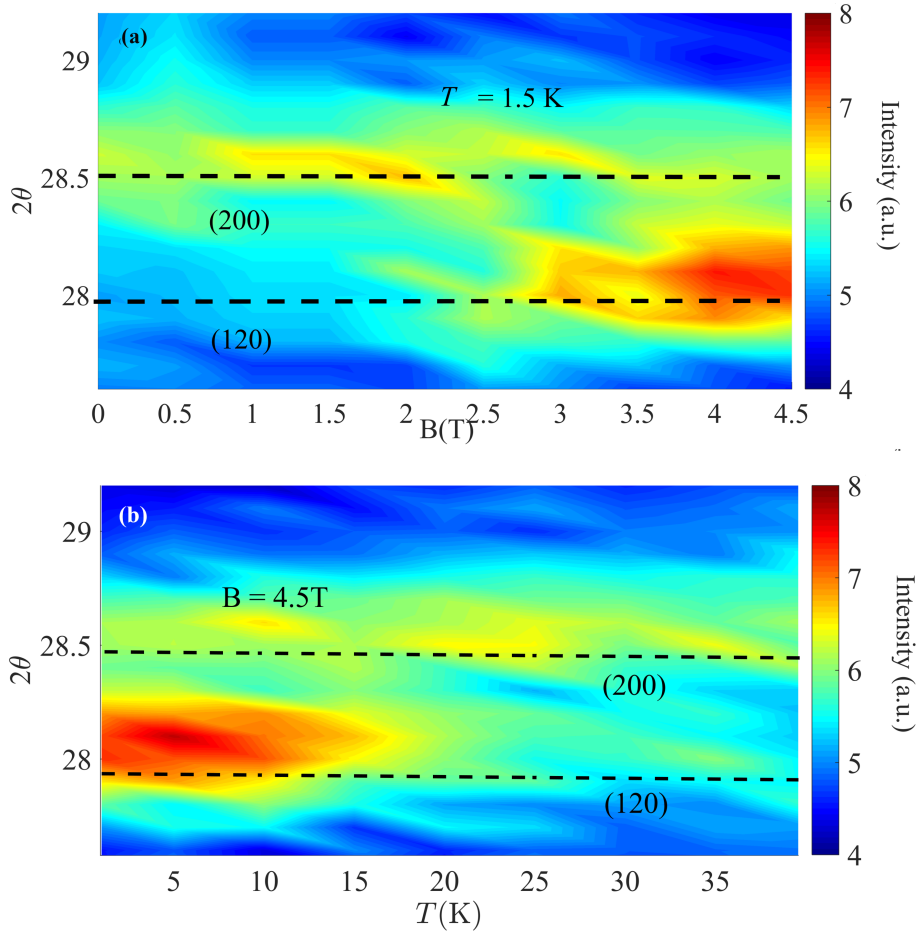Figure 6.16: (a) Field dependency of (200) and (120) peaks measured at T=1.5 K. (b) Temperature dependency of (200) and (120) peaks measured at B =4.5 T.

Finally, the research questions raised at the beginning can be addressed as follows:

1. The NN and NNN exchange interactions in both ladders are anti-ferromagnetic in nature and are the primary interactions leading to the observed dispersion.

2. The ratio of exchange interactions $\frac{\mathcal{J}_{22}}{\mathcal{J}_{21}} \approx 1$ in case of Tm2 indicates that this chain is frustrated, whereas in Tm1 $\frac{\mathcal{J}_{12}}{\mathcal{J}_{11}} \approx 2$, indicates that the $\mathcal{J}_{12}$ interactions could lead to dimerization.

3. Calculation of the critical ratio has shown that SrTm$_2$O$_4$ cannot be driven to a thermal phase transition. However, Tm1 chains in dimer limit has led to the magnetic field induced phase transition with critical field B$_{c1} \approx 4$ T.

4. Insignificant critical ratio altogether excludes the possibility of thermal phase transition involving electronic moments. This insight led to the estimation of nuclear spin enhancement in ^{169}Tm as a consequence of muon-induced distortion of crystal field levels. Thus the oscillations in ZF-μ^+SR can be associated with nuclear hyperfine enhancement.

Thus it is very clear that like other non-Kramers ion systems, in SrTm$_2$O$_4$ the crystal field effects are strongest. However, magnetic exchange interactions play a decisive role in the magnetic field induced behavior of the system. Until now, the analysis and interpretation of results have been consistent across various probes. However, the following extension might provide deeper insights into complicated systems involving multiple interactions, such as SrTm$_2$O$_4$:

- Dimerization of Tm1 chains need to be estimated decisively. Mapping of dispersing excitation in the applied magnetic field can provide better understanding on this dimerization.

- Estimation of B$_{c2}$ has to be made. The accurate mapping of field induced phase could be done with heat capacity or ultrasound velocity measurements in applied magnetic field.

- The critical behavior of the field induced phase needs to be studied with a theoretical framework.

7 Summary & Perspective

This thesis provides the results of experimental and theoretical investigations of the magnetic properties of Co_2VO_4 and $SrTm_2O_4$.

Our interest in Co_2VO_4 originates from its anomalous temperature-dependent magnetization, where a magnetization reversal crossover occurs. We have performed magnetization measurements and revealed at least four distinct anomalies; collinear ferrimagnetic phase at T_C, non-collinear ferrimagnetic phase at T_{NC}, magnetization reversal crossover at T_{MR} and upturn in magnetization for $T < 20$ K. The anomaly at low temperatures ($T < 20$ K) originates from the impurity phase of $Co_3V_2O_8$. Neutron powder diffraction and magnetic structure analysis reveal two antiparallel ferromagnetic structures, each belonging to magnetic ions on A- and B-sites. Magnetic structure refinement of neutron powder diffraction data shows that for temperatures above T_{MR} the A-site moment always leads, i.e., $\mu_{A(FM)} > \mu_{B(FM)}$. Whereas for $T < T_{MR}$, we find the trend reverses, i.e., $\mu_{A(FM)} < \mu_{B(FM)}$. Therefore, this relative balance of these two magnetic structures determines the net magnetic moment in the unit cell. However, the magnetization reversal determined at zero fields is sensitive to an applied magnetic field, such that above $B \sim 0.25$ T, instead of a reversal, a minimum in the magnetization is apparent at T_{MR}.

DFT results unveil the root cause of this site-specificity. The DFT calculations provide two ground state solutions, delocalized and localized, representing regions with $T > T_{MR}$ and $T < T_{MR}$ respectively. Polarized muon spectroscopy as a function of temperature is consistent with the neutron diffraction and magnetization results but adds new insights to DFT predictions. The relaxation rate as a function of temperature indicates T_1-relaxation drops as the system is cooled. These results suggest that highly delocalized-fluctuating magnetic moments at elevated temperatures gradually tend to localize at lower temperatures. Thus, we can conclude that the delocalized-to-localized crossover drives Co_2VO_4

to magnetization reversal.

$SrTm_2O_4$ is unique among the family of $SrLn_2O_4$ since it does not order down to 65 mK. We pursued this system to find out why does $SrTm_2O_4$ not order? Our first step was to understand the crystal field ground state in $SrTm_2O_4$.

We investigated the crystal field properties of the non-Kramers compound $SrTm_2O_4$ using a combination of susceptibility, magnetization in pulsed fields, heat capacity, and INS. The magnetization and susceptibility results show a strong anisotropy, with the c axis being the hard axis. Schottky anomaly features seen in heat capacity results indicate the presence of low energy excitations. The INS results show two dispersing low-energy excitations below 5 meV.

We proposed two crystal field models to explain the single ion properties: the DFT and the EC models. The DFT model predicts $|J, m_J\rangle = |6, 0\rangle$ ground state for Tm1 and $|J, m_J\rangle = |6, \pm1\rangle$ for Tm2 while the EC model determines the ground state of both the inequivalent sites to show predominantly $|J, m_J\rangle = |6, 0\rangle$ characteristics. Both the models predict easy-axis anisotropy for Tm1 and easy-plane anisotropy for Tm2. The EC model accurately predicts experimentally measured magnetization, heat capacity, and INS results. However, the calculated susceptibility for the EC model shows a small discrepancy at low temperatures. This discrepancy could be corrected by including two-ion contributions. On the other hand, the DFT model is far from perfect. Despite these shortcomings, the DFT model has provided a preliminary understanding of the crystal field schemes that have helped make efficient EC model optimization.

Our diffused scattering results from the polarized neutron instrument show a broad signal in powder and single-crystal data. Spin-correlation obtained from the reverse Monte Carlo modeling of powder results suggests dominating AFM interactions for nearest neighbors up to 5.5Å. This signal originates purely from the excitations, so we rule out the existence of short-range ordering in $SrTm_2O_4$.

150

Our crystal field models have estimated the first excited state to originate from Tm2 and the second excited state from Tm1. We modeled the low-energy dispersing excitations to extract exchange interaction terms using random phase approximation. We include the respective crystal field Hamiltonian while modeling the dispersion to account for the origin of these modes. RPA results suggest that the Tm2 chains are frustrated due to similar NN and NNN antiferromagnetic interactions. On the other hand, Tm1 chains have NNN interactions twice as strong as NN interactions. Thus, we suggest the Tm1 chain is within the dimer limit.

AC Susceptibility and neutron powder diffraction in applied magnetic fields indicate the emergence of *XY*-AFM phase above 4 T. We speculate that the observed magnetic field-induced phase might be originating from the Tm1 chain at the dimer limit. Additional spectroscopy measurements in the applied field could accurately tell if the system does exhibit a dimer behavior.

Critical ratios calculated from RPA results estimate if the system can undergo a thermal second-order phase transition. The critical ratio closer to one implies that systems have stronger exchange interactions, which can drive them to a thermal phase transition. However, $SrTm_2O_4$has a meager critical ratio for both Tm^{3+} s, indicating that the system cannot undergo a second-order phase transition. The critical ratio suggests that in $SrTm_2O_4$ crystal field effects are dominant. Additionally, the critical ratio indicates large chances of nuclear effects emerging in such systems.

Our ZF-μ^+SR results show oscillation in the time evolution of polarization (Asymmetry vs. time spectra). Typically, such oscillations are associated with muon precession in the presence of ordered surroundings, i.e., the probed system has a long-range order. However, our previous results show no ordering down to 2 K. To understand this peculiar behavior, we modeled the muon stopping site using DFT+μ techniques and estimated the effects of muon-induced distortion on crystal fields using a simple point charge model. These results show a renor-

malization of the gap in both Tm^{3+} s. Additionally, the temperature behavior of muon precession frequency shows anomalous critical behavior. Modeling this result suggests that the renormalization of the crystal field gap induces nuclear hyperfine enhancement. We conclude that the oscillations in ZF- μ^+SR spectra are due to nuclear hyperfine enhancement.

These investigations have given me a broader perspective on magnetism, neutron scattering, μ^+SR and computational methods. The most challenging part of this endeavor was modeling crystal fields in $SrTm_2O_4$. Based on my experience with crystal field modeling, I would like to put forward a few general propositions in front of the community.

- Understanding the crystal fields is key to knowing the magnetism in many Rare-earth and Transition metal systems. Difficulties in implementing a phenomenological approach to crystal field problems for systems involving low symmetry have been highlighted in this thesis and elsewhere. It would be beneficial to maintain a library for crystal field parameters. Such a library would provide intelligent starting parameters while making phenomenological optimization.

- In a Recent article, Berthusen *et al*. [160] have successfully implemented a convolutional neural network (CNN) algorithm for crystal field problems. This article has opened a new avenue to use machine learning (ML) approaches in crystal field problems. Implementing other algorithms, such as genetic algorithms, could be interesting. The use of machine learning tools could make the phenomenological determination of crystal field parameters smooth. The library of crystal fields mentioned in the last point could be beneficial.

- Wannier function method used in this thesis gave a preliminary understanding of crystal field parameters before the phenomenological approach was applied. If more experimentalists can use such methods, it would simultaneously help benchmark theoret-

ical methods while benefiting experimental determination. Thus, the easy accessibility of these methods could make it possible for experimentalists to use such methods.

List of papers

Following articles are included in the thesis

Paper I

A. B. Kademane, C. Bhandari, D. Paudyal, S. Cottrell, P. Das, Y. Liu, Y. Yiu, C. M. N. Kumar, K. Siemensmeyer, A. Hoser, D. L. Quintero-Castro, D. Vaknin, and R. Toft-Petersen. *Magnetization reversal driven by electron localization-delocalization crossover in the inverse spinel* Co_2VO_4.. *Phys. Rev. B*, 105 094408,Mar 2022

Paper II

A. Bhat Kademane, D. L. Quintero-Castro, K. Siemensmeyer, C. Salazar-Mejia, D. Gorbunov, J.R. Stewart, H. Luetkens, C. Baines, and Haifeng Li. Crystal field effects in the zigzag chain compound $SrTm_2O_4$.. *Journal of Magnetism and Magnetic Materials, page 169020,2022.*ISSN 0304-8853(2022)

Paper III

A. B. Kademane, D. L. Quintero-Castro, R. Toft-Petersen, K. Siemensmeyer, J. Xu, A . Gazizulina, V. Pomjakushin, A. Wildes and Haifeng Li. Magnetic frustration and magnetic field induced order in $SrTm_2O_4$. *To be submitted for publication in PHYSICAL REVIEW B.*

Following articles are not included in the thesis

Paper IV

A. Gazizulina, D. L. Quintero-Castro, Z. Wang, F. Duc, F. Bourdarot, K. Prokes, W. Schmidt, R. Daou, S. Zherlitsyn, N. Islam, N. Henrik Kolnes, **A. B. Kademane**, A. Schilling, and B. Lake. Neutron diffraction of field-induced magnon condensation in the spin-dimerized antiferromagnet $Sr_3Cr_2O_8$. *Phys. Rev. B, 104*.064430, Aug 2021.

Paper V

D. L. Quintero-Castro, J. Hincapie, **A. B. Kademane**, M. Jeong, M. Frontzek, A. Franz, R. Toft-Petersen, A. Ramachandran, and F. Yokaichiya. Magnetic Percolation in the Anisotropic and Frustrated Antiferromagnet $SrYb_2O_4$. *To be submitted for publication in Journal of Materials Chemistry C.*

References

[1] P. W. Anderson. More is different. *Science*, 177(4047):393–396, August 1972. URL `https://doi.org/10.1126/science.177.4047.393`.

[2] N. Menyuk, K. Dwight, and D. G. Wickham. Magnetization reversal and asymmetry in cobalt vanadate (IV). *Phys. Rev. Lett.*, 4:119–120, Feb 1960. URL `https://link.aps.org/doi/10.1103/PhysRevLett.4.119`.

[3] H. Karunadasa, Q. Huang, B. G. Ueland, J. W. Lynn, P. Schiffer, K. A. Regan, and R. J. Cava. Honeycombs of triangles and magnetic frustration in SrL_2O_4 ($L =$ Gd, Dy, Ho, Er, Tm, and Yb). *Phys. Rev. B*, 71:144414, Apr 2005. URL `https://link.aps.org/doi/10.1103/PhysRevB.71.144414`.

[4] H-F. Li, A. Senyshyn, O. Fabelo, J. Persson, B. Hou, M. Boehm, K. Schmalzl, W. Schmidt, J-P. Vassalli, P. Thakuria, X. Sun, L. Wang, G. Khazaradze, B. Schmitz, C. Zhang, G. Roth, J. G. Roca, and A. Wildes. Absence of magnetic ordering in the ground state of a $SrTm_2O_4$ single crystal. *Journal of Materials Chemistry C*, 3(29):7658–7668, 2015. URL `https://doi.org/10.1039/c5tc01607j`.

[5] E U Condon and G H Shortley. *The Theory of Atomic Spectra.* Cambridge University Press, Cambridge, England, 1959.

[6] K W H Stevens. Matrix elements and operator equivalents connected with the magnetic properties of rare earth ions. *Proceedings of the Physical Society. Section A*, 65(3):209–215, March 1952. URL `https://doi.org/10.1088/0370-1298/65/3/308`.

[7] M. Rotter, M. D. Le, J. Keller, L. G. Pascut, T. Hoffmann, M. Doerr, R. Schedler, F. Fabi né Hoffmann, S. Rotter, M. Banks, and N. Klüver. *McPhase - USERS MANUAL*,

2017. URL `https://www2.cpfs.mpg.de/~rotter/homepage_mcphase/manual/manual.html`.

[8] J. Jensen and A. R. Mackintosh. *Rare Earth Magnetism*. Oxford University Press, Oxford, UK, 1991. ISBN 9780198520276.

[9] C. Rudowicz and J. Qin. Can the low symmetry crystal (ligand) field parameters be considered compatible and reliable? *Journal of Luminescence*, 110(1-2):39–64, October 2004. URL `https://doi.org/10.1016/j.jlumin.2004.04.003`.

[10] M.T. Hutchings. Point-charge calculations of energy levels of magnetic ions in crystalline electric fields. In *Solid State Physics*, pages 227–273. Elsevier, 1964. URL `https://doi.org/10.1016/s0081-1947(08)60517-2`.

[11] H. Bethe. Termaufspaltung in kristallen. *Annalen der Physik*, 395(2):133–208, 1929. URL `https://doi.org/10.1002/andp.19293950202`.

[12] J. J. Baldoví, J. J. Borrás-Almenar, J. M. Clemente-Juan, Eugenio Coronado, and Alejandro G-A. Modeling the properties of lanthanoid single-ion magnets using an effective point-charge approach. *Dalton Trans.*, 41:13705–13710, 2012. URL `http://dx.doi.org/10.1039/C2DT31411H`.

[13] J. J. Baldoví, J. M. Clemente-Juan, and A. Gaita-Ariño. Simpre: Installation and user manual, 2014. URL `https://arxiv.org/abs/1407.6576`.

[14] Z. Dun, X. Bai, M. B. Stone, H. Zhou, and M. Mourigal. Effective point-charge analysis of crystal fields: Application to rare-earth pyrochlores and tripod kagome magnets $R_3Mg_2Sb_3O_{14}$. *Phys. Rev. Research*, 3:023012, Apr 2021. URL `https://link.aps.org/doi/10.1103/PhysRevResearch.3.023012`.

[15] A. Uldry, F. Vernay, and B. Delley. Systematic computation of crystal-field multiplets for x-ray core spectroscopies. *Physical*

Review B, 85(12), March 2012. URL https://doi.org/
10.1103/physrevb.85.125133.

[16] B.Z. Malkin. Crystal field and electron–phonon interaction
in rare-earth ionic paramagnets. In *Spectroscopy of Solids
Containing Rare Earth Ions*, pages 13–50. Elsevier, 1987. URL
https://doi.org/10.1016/b978-0-444-87051-3.
50008-0.

[17] S. V. Streltsov, A. S. Mylnikova, A. O. Shorikov, Z. V. Pchelk-
ina, D. I. Khomskii, and V. I. Anisimov. Crystal-field splitting
for low symmetry systems in *ab initio* calculations. *Phys. Rev.
B*, 71:245114, Jun 2005. URL https://link.aps.org/
doi/10.1103/PhysRevB.71.245114.

[18] M. W. Haverkort, M. Zwierzycki, and O. K. Andersen. Multi-
plet ligand-field theory using Wannier orbitals. *Phys. Rev. B*, 85:
165113, Apr 2012. URL https://link.aps.org/doi/
10.1103/PhysRevB.85.165113.

[19] P. Novák, K. Knížek, and J. Kuneš. Crystal field parameters with
wannier functions: Application to rare-earth aluminates. *Phys.
Rev. B*, 87:205139, May 2013. URL https://link.aps.
org/doi/10.1103/PhysRevB.87.205139.

[20] A. Scaramucci, J. Ammann, N. A. Spaldin, and C. Ederer. Sepa-
rating different contributions to the crystal-field parameters using
Wannier functions. *Journal of Physics: Condensed Matter*, 27
(17):175503, apr 2015. URL https://doi.org/10.1088/
0953-8984/27/17/175503.

[21] E. Mihóková, P. Novák, and V. V. Laguta. Crystal field
and magnetism with Wannier functions: rare-earth doped alu-
minum garnets. *Journal of Rare Earths*, 33(12):1316–1323,
2015. ISSN 1002-0721. URL https://doi.org/10.
1016/S1002-0721(14)60563-9.

[22] A. Furrer, J. Mesot, and T. Strässle. *Neutron Scattering in Con-
densed Matter Physics*. WORLD SCIENTIFIC, 2009. doi:

10.1142/4870. URL `https://www.worldscientific.com/doi/abs/10.1142/4870`.

[23] B. G. Wybourne. *Spectroscopic Properties of Rare Earths*. Interscience Publishers, 1965.

[24] D. I. Khomskii. *TRANSITION METAL COMPOUNDS*. Cambridge University Press, 2009. URL `https://doi.org/10.1017/cbo9781139096782`.

[25] S. J. Blundell. *Magnetism in Condensed Matter*. Oxford Master Series in Condensed Matter Physics. Oxford University Press, London, England, August 2001.

[26] T. Moriya. Anisotropic Superexchange Interaction and Weak Ferromagnetism. *Phys. Rev.*, 120:91–98, Oct 1960. URL `https://link.aps.org/doi/10.1103/PhysRev.120.91`.

[27] M. Rotter, A. Schneidewind, M. Doerr, M. Loewenhaupt, A. M. El Massalami, and C. Detlefs. Interpreting magnetic X-ray scattering on Gd-compounds using the McPhase simulation program. *Physica B: Condensed Matter*, 345(1):231–234, 2004. ISSN 0921-4526. URL `https://doi.org/10.1016/j.physb.2003.11.061`.

[28] J. N. Reimers. Diffuse-magnetic-scattering calculations for frustrated antiferromagnets. *Phys. Rev. B*, 46:193–202, Jul 1992. URL `https://link.aps.org/doi/10.1103/PhysRevB.46.193`.

[29] J. Xu. *Magnetic properties of rare earth zirconate pyrochlores*. Doctoral thesis, Technische Universität Berlin, Berlin, 2017. URL `https://depositonce.tu-berlin.de/bitstream/11303/7102/5/xu_jianhui.pdf`.

[30] D. B. Litvin, editor. *Magnetic Group Tables*. International Union of Crystallography, April 2013. URL `https://doi.org/10.1107/9780955360220001`.

[31] E. F. Bertaut. Representation analysis of magnetic structures. *Acta Crystallographica Section A*, 24(1):217–231, Jan 1968. URL https://doi.org/10.1107/S0567739468000306.

[32] A. Wills. Magnetic structures and their determination using group theory. *Le Journal de Physique IV*, 11(PR9):Pr9–133–Pr9–158, November 2001. URL https://doi.org/10.1051/jp4:2001906.

[33] M. A. H. McCausland and I. S. Mackenzie. Nuclear magnetic resonance in rare earth metals. *Advances in Physics*, 28(3):305–456, June 1979. URL https://doi.org/10.1080/00018737900101385.

[34] B. R. Cooper and O. Vogt. Singlet Ground State Magnetism. *Le Journal de Physique Colloques*, 32(C1):C1–958–C1–965, February 1971. URL https://doi.org/10.1051/jphyscol:19711343.

[35] A. Kumar and S.M. Yusuf. The phenomenon of negative magnetization and its implications. *Physics Reports*, 556:1–34, February 2015. URL https://doi.org/10.1016/j.physrep.2014.10.003.

[36] M. L. Néel. Propriétés magnétiques des ferrites ; ferrimagnétisme et antiferromagnétisme. *Annales de Physique*, 12(3):137–198, 1948. URL https://doi.org/10.1051/anphys/194812030137.

[37] Bernard R. Cooper. Magnetic properties of compounds with singlet ground state: Exchange correlation effects. *Phys. Rev.*, 163:444–459, Nov 1967. URL https://link.aps.org/doi/10.1103/PhysRev.163.444.

[38] L. Balents. Spin liquids in frustrated magnets. *Nature*, 464(7286):199–208, March 2010. URL https://doi.org/10.1038/nature08917.

161

[39] J. Villain, R. Bidaux, J.-P. Carton, and R. Conte. Order as an effect of disorder. *Journal de Physique*, 41(11):1263–1272, 1980. URL `https://doi.org/10.1051/jphys:01980004101101126300`.

[40] C. Lacroix, P. Mendels, and Fr. Mila, editors. *Introduction to Frustrated Magnetism*. Springer Berlin Heidelberg, 2011. URL `https://doi.org/10.1007/978-3-642-10589-0`.

[41] F. Heidrich-Meisner, I. A. Sergienko, A. E. Feiguin, and E. R. Dagotto. Universal emergence of the one-third plateau in the magnetization process of frustrated quantum spin chains. *Phys. Rev. B*, 75:064413, Feb 2007. URL `https://link.aps.org/doi/10.1103/PhysRevB.75.064413`.

[42] G. L. Squires. *Introduction to the Theory of Thermal Neutron Scattering*. Cambridge University Press, 2009. URL `https://doi.org/10.1017/cbo9781139107808`.

[43] S. W. Lovesey. *Theory of neutron scattering from condensed matter: Volume I: Nuclear scattering*. International Series of Monographs on Physics. Clarendon Press, Oxford, England, October 1986.

[44] S. W. Lovesey. *Theory of neutron scattering from condensed matter: Volume II: Polarization effects and magnetic scattering*. Theory of Neutron Scattering from Condensed Matter. Clarendon Press, Oxford, England, October 1986.

[45] K. Lefmann. Neutron Scattering: Theory, Experiment, and Simulations, October 2018.

[46] A. Yaouanc and P. D. de Reotier. *Muon Spin Rotation, Relaxation, and Resonance: Applications to Condensed matter*. International series of monographs on physics. Oxford University Press, Oxford, 2010. ISBN 9780199596478.

[47] A. Amato. Physics with Muons: From Atomic Physics to Solid State Physics, February 2021. URL `https://www.psi.ch/en/media/73526/download?attachment`.

162

[48] S. Cottenier. Density Functional Theory and the Family of (L)APW-methods: a step-by-step introduction. Instituut voor Kern- en Stralingsfysica, K.U.Leuven, Belgium, 2013. ISBN 978-90-807215-1-7.

[49] Thomas Bagger Stibius Jensen. *Magnetic structures, phase diagram and spin waves of magneto-electric LiNiPO₄*. PhD thesis, 2007. URL `https://orbit.dtu.dk/files/5000886/ris-phd-40.pdf`.

[50] A. Buchsteiner and N. Stüßer. Optimizations in angular dispersive neutron powder diffraction using divergent beam geometries. *Nuclear Instruments and Methods in Physics Research Section A: Accelerators, Spectrometers, Detectors and Associated Equipment*, 598(2):534–541, January 2009. URL `https://doi.org/10.1016/j.nima.2008.09.022`.

[51] A. Franz and A. Hoser. E9: The fine resolution powder diffractometer (FIREPOD) at BER II. *Journal of large-scale research facilities*, 3:A103, 2017. URL `http://dx.doi.org/10.17815/jlsrf-3-127`.

[52] A. Huq, J. P. Hodges, O. Gourdon, and L. Heroux. Powgen: A third-generation highresolution high-throughput powder diffraction instrument at the spallation neutron source. In *European Powder Diffraction Conference, August 2010, Darmstadt, Germany*, pages 127–136. OLDENBOURG WISSENSCHAFTSVERLAG, December 2011. URL `https://doi.org/10.1524/9783486991321-024`.

[53] P. Fischer, L. Keller, J. Schefer, and J. Kohlbrecher. Neutron diffraction at sinq. *Neutron News*, 11(3):19–21, 2000. URL `https://doi.org/10.1080/10448630008233743`.

[54] C. J. Carlile and B. T. M. Willis. *Experimental Neutron Scattering*. Oxford university press, 2013. ISBN 9780199673773.

[55] M. D. Le, M. Skoulatos, D. L. Quintero-Castro, R. Toft-Petersen, F. Groitl, K. C. Rule, and K. Habicht. The upgraded cold neutron three-axis spectrometer FLEXX at BER II

at HZB. *Neutron News*, 25(2):19–22, April 2014. URL `https://doi.org/10.1080/10448632.2014.902699`.

[56] R. A. Ewings, J. R. Stewart, T. G. Perring, R. I. Bewley, M. D. Le, D. Raspino, D. E. Pooley, G. Škoro, S. P. Waller, D. Zacek, C. A. Smith, and R. C. Riehl-Shaw. Upgrade to the MAPS neutron time-of-flight chopper spectrometer. *Review of Scientific Instruments*, 90(3):035110, March 2019. URL `https://doi.org/10.1063/1.5086255`.

[57] J. R. Stewart, P. P. Deen, K. H. Andersen, H. Schober, J.-F. Barthélémy, J. M. Hillier, A. P. Murani, T. Hayes, and B. Lindenau. Disordered materials studied using neutron polarization analysis on the multi-detector spectrometer, D7. *Journal of Applied Crystallography*, 42(1):69–84, Feb 2009. URL `https://doi.org/10.1107/S0021889808039162`.

[58] A. Amato, H. Luetkens, K. Sedlak, A. Stoykov, R. Scheuermann, M. Elender, A. Raselli, and D. Graf. The new versatile general purpose surface-muon instrument (GPS) based on silicon photomultipliers for μSR measurements on a continuous-wave beam. *Review of Scientific Instruments*, 88(9):093301, September 2017. URL `https://doi.org/10.1063/1.4986045`.

[59] S.R. Giblin, S.P. Cottrell, P.J.C. King, S. Tomlinson, S.J.S. Jago, L.J. Randall, M.J. Roberts, J. Norris, S. Howarth, Q.B. Mutamba, N.J. Rhodes, and F.A. Akeroyd. Optimising a muon spectrometer for measurements at the ISIS pulsed muon source. *Nuclear Instruments and Methods in Physics Research Section A: Accelerators, Spectrometers, Detectors and Associated Equipment*, 751:70–78, July 2014. URL `https://doi.org/10.1016/j.nima.2014.03.010`.

[60] J. E. Sonier. Muon Spin Rotation/Relaxation/Resonance (μSR). Brochure, 2002. URL `http://cmms.triumf.ca/intro/musr/muSRBrochure.pdf`.

[61] P. Giannozzi, S. Baroni, N. Bonini, M. Calandra, R. Car, C. Cavazzoni, D. Ceresoli, G. L. Chiarotti, M. Cococ-

164

cioni, I. Dabo, A. Dal Corso, S. de Gironcoli, S. Fabris, G. Fratesi, R. Gebauer, U. Gerstmann, C. Gougoussis, A. Kokalj, M. Lazzeri, L. Martin-Samos, N. Marzari, F. Mauri, R. Mazzarello, S. Paolini, A. Pasquarello, L. Paulatto, C. Sbraccia, S. Scandolo, G. Sclauzero, A. P. Seitsonen, A. Smogunov, P. Umari, and R. M. Wentzcovitch. QUANTUM ESPRESSO: a modular and open-source software project for quantum simulations of materials. *Journal of Physics: Condensed Matter*, 21(39):395502, sep 2009. URL `https://doi.org/10.1088/0953-8984/21/39/395502`.

[62] P. Blaha, K. Schwarz, F. Tran, R. Laskowski, G. K. H. Madsen, and L. D. Marks. WIEN2k: An APW+lo program for calculating the properties of solids. *The Journal of Chemical Physics*, 152(7):074101, February 2020. URL `https://doi.org/10.1063/1.5143061`.

[63] Von W. Rüdorff, G. Walter, and H. Becker. Über einige Oxoverbindungen und Doppeloxyde des vierwertigen Vanadins. *Zeitschrift für Anorganische und Allgemeine Chemie*, 285(3-6):287–296, June 1956. URL `https://doi.org/10.1002/zaac.19562850321`.

[64] E. J. W. Verwey and E. L. Heilmann. Physical Properties and Cation Arrangement of Oxides with Spinel Structures I. Cation Arrangement in Spinels. *The Journal of Chemical Physics*, 15(4):174–180, April 1947. URL `https://doi.org/10.1063/1.1746464`.

[65] V. O. Garlea, R. Jin, D. Mandrus, B. Roessli, Q. Huang, M. Miller, A. J. Schultz, and S. E. Nagler. Magnetic and Orbital Ordering in the Spinel MnV_2O_4. *Phys. Rev. Lett.*, 100:066404, Feb 2008. URL `https://link.aps.org/doi/10.1103/PhysRevLett.100.066404`.

[66] G. J. MacDougall, V. O. Garlea, A. A. Aczel, H. D. Zhou, and S. E. Nagler. Magnetic order and ice rules in the multiferroic spinel FeV_2O_4. *Phys. Rev. B*, 86:060414, Aug

2012. URL `https://link.aps.org/doi/10.1103/PhysRevB.86.060414`.

[67] Q. Zhang, M. Ramazanoglu, S. Chi, Y. Liu, T. A. Lograsso, and D. Vaknin. Magnetic excitations and anomalous spin-wave broadening in multiferroic FeV_2O_4. *Phys. Rev. B*, 89: 224416, Jun 2014. URL `https://link.aps.org/doi/10.1103/PhysRevB.89.224416`.

[68] H. Ishibashi, S. Shimono, K. Tomiyasu, S. Lee, S. Kawaguchi, H. Iwane, H. Nakao, S. Torii, T. Kamiyama, and Y. Kubota. Small crystal distortion and long-range antiferro-orbital ordering in the spinel oxide CoV_2O_4. *Phys. Rev. B*, 96: 144424, Oct 2017. URL `https://link.aps.org/doi/10.1103/PhysRevB.96.144424`.

[69] R. Koborinai, S. E. Dissanayake, M. Reehuis, M. Matsuda, T. Kajita, H. Kuwahara, S.-H. Lee, and T. Katsufuji. Orbital glass state of the nearly metallic spinel cobalt vanadate. *Phys. Rev. Lett.*, 116:037201, Jan 2016. URL `https://link.aps.org/doi/10.1103/PhysRevLett.116.037201`.

[70] E. J. Verwey, P. W. Haayman, and F. C. Romeijn. Physical Properties and Cation Arrangement of Oxides with Spinel Structures II. Electronic Conductivity. *The Journal of Chemical Physics*, 15(4):181–187, April 1947. URL `https://doi.org/10.1063/1.1746466`.

[71] Konstantin P Belov. Electronic processes in magnetite (or, "Enigmas of magnetite"). *Physics-Uspekhi*, 36(5):380–391, may 1993. URL `https://doi.org/10.1070/pu1993v036n05abeh002160`.

[72] P. W. Anderson. Ordering and Antiferromagnetism in Ferrites. *Phys. Rev.*, 102:1008–1013, May 1956. URL `https://link.aps.org/doi/10.1103/PhysRev.102.1008`.

[73] K. P. Belov. Ferrimagnets with a 'weak' magnetic sublattice. *Uspekhi Fizicheskikh Nauk (UFN) Journal*, 39(6):

166

623–634, 1996. URL `http://dx.doi.org/10.1070/PU1996v039n06ABEH000153`.

[74] S. Thota and S. Singh. Nature of magnetic ordering in cobalt-based spinels. In *Magnetic Spinels - Synthesis, Properties and Applicationsn*, chapter 4. InTech Open Bookseries, 2017. URL `https://www.intechopen.com/chapters/53006`.

[75] S. Nayak, S. Thota, D. C. Joshi, M. Krautz, A. Waske, A. Behler, J. Eckert, T. Sarkar, M. S. Andersson, R. Mathieu, V. Narang, and M. S. Seehra. Magnetic compensation, field-dependent magnetization reversal, and complex magnetic ordering in Co_2TiO_4. *Phys. Rev. B*, 92:214434, Dec 2015. URL `https://link.aps.org/doi/10.1103/PhysRevB.92.214434`.

[76] X. Liu, C.and Kan, X. Liu, Z. Zhang, and J. Hu. Magnetic compensation and critical behavior in spinel Co_2TiO_4. *Phys. Chem. Chem. Phys.*, 22:20929–20940, 2020. URL `http://dx.doi.org/10.1039/D0CP03713C`.

[77] C. Mu, J. Mao, J. Guo, Q. Guo, Z. Li, W. Qin, Z. Hu, K. Davey, T. Ling, and S-Z. Qiao. Rational design of spinel cobalt vanadate oxide Co_2VO_4 for superior electrocatalysis. *Advanced Materials*, 32(10):1907168, January 2020. URL `https://doi.org/10.1002/adma.201907168`.

[78] T. Yang, D. Xia, Z. Wang, and Y. Chen. A novel anode material of Fe_2VO_4 for high power Lithium ion battery. *Materials Letters*, 63(1):5–7, January 2009. URL `https://doi.org/10.1016/j.matlet.2008.08.012`.

[79] W. Jauch, M. Reehuis, H. J. Bleif, F. Kubanek, and P. Pattison. Crystallographic symmetry and magnetic structure of CoO. *Phys. Rev. B*, 64:052102, Jul 2001. URL `https://link.aps.org/doi/10.1103/PhysRevB.64.052102`.

[80] K. Tomiyasu, T. Inami, and N. Ikeda. Magnetic structure of CoO studied by neutron and synchrotron x-ray diffraction. *Phys. Rev.*

B, 70:184411, Nov 2004. URL `https://link.aps.org/doi/10.1103/PhysRevB.70.184411`.

[81] J. Rodríguez-Carvajal. Recent advances in magnetic structure determination by neutron powder diffraction. *Physica B: Condensed Matter*, 192(1):55–69, 1993. ISSN 0921-4526. URL `https://doi.org/10.1016/0921-4526(93)90108-I`.

[82] N. R. Wilson, O. A. Petrenko, and L. C. Chapon. Magnetic phases in the kagomé staircase compound $Co_3V_2O_8$ studied using powder neutron diffraction. *Phys. Rev. B*, 75:094432, Mar 2007. URL `https://link.aps.org/doi/10.1103/PhysRevB.75.094432`.

[83] N. Qureshi, M. Zbiri, J. Rodríguez-Carvajal, A. Stunault, E. Ressouche, T. C. Hansen, M. T. Fernández-Díaz, M. R. Johnson, H. Fuess, H. Ehrenberg, Y. Sakurai, M. Itou, B. Gillon, Th. Wolf, J. A. Rodríguez-Velamazan, and J. Sánchez-Montero. Experimental magnetic form factors in $Co_3V_2O_8$: A combined study of *ab initio* calculations, magnetic Compton scattering, and polarized neutron diffraction. *Physical Review B*, 79(9), March 2009. URL `https://doi.org/10.1103/physrevb.79.094417`.

[84] R. Szymczak, M. Baran, R. Diduszko, J. Fink-Finowicki, M. Gutowska, A. Szewczyk, and H. Szymczak. Magnetic field-induced transitions in geometrically frustrated $Co_3V_2O_8$ single crystal. *Phys. Rev. B*, 73:094425, Mar 2006. URL `https://link.aps.org/doi/10.1103/PhysRevB.73.094425`.

[85] Y. Yasui, Y. Kobayashi, M. Soda, T. Moyoshi, M. Sato, N. Igawa, and K. Kakurai. Successive Magnetic Transitions of the Kagomé Staircase Compound $Co_3V_2O_8$ Studied in Various Magnetic Fields. *Journal of the Physical Society of Japan*, 76(3): 034706, March 2007. URL `https://doi.org/10.1143/jpsj.76.034706`.

[86] Y. Nii, H. Sagayama, T. Arima, S. Aoyagi, R. Sakai, S. Maki, E. Nishibori, H. Sawa, K. Sugimoto, H. Ohsumi, and M. Takata. Orbital structures in spinel vanadates AV_2O_4(A= Fe,Mn). *Phys. Rev. B*, 86:125142, Sep 2012. URL `https://link.aps.org/doi/10.1103/PhysRevB.86.125142`.

[87] L. H. Bennett and E. Della Torre. Analysis of wasp-waist hysteresis loops. *Journal of Applied Physics*, 97(10):10E502, 2005. URL `https://doi.org/10.1063/1.1846171`.

[88] Peter J. W. Magnetic hysteresis in natural materials. *Earth and Planetary Science Letters*, 20(1):67–72, 1973. ISSN 0012-821X. URL `https://doi.org/10.1016/0012-821X(73)90140-4`.

[89] B. Debnath, A. Bansal, H. G. Salunke, A. Sadhu, and S. Bhattacharyya. Enhancement of Magnetization through Interface Exchange Interactions of Confined NiO Nanoparticles within the Mesopores of CoFe2O4. *The Journal of Physical Chemistry C*, 120(10):5523–5533, 2016. URL `https://doi.org/10.1021/acs.jpcc.5b12332`.

[90] L. Tauxe, T. A. T. Mullender, and T. Pick. Potbellies, wasp-waists, and superparamagnetism in magnetic hysteresis. *Journal of Geophysical Research*, 101:571–583, 1996. URL `https://doi.org/10.1029/95JB03041`.

[91] J. P. Palakkal, C. R. Sankar, A. P. Paulose, and M. R. Varma. Hopping conduction and spin glass behavior of La_2FeMnO_6. *Journal of Alloys and Compounds*, 743:403–409, 2018. ISSN 0925-8388. URL `https://doi.org/10.1016/j.jallcom.2018.01.210`.

[92] P. Singh, A. Pal, V. K. Gangwar, P. K. Gupta, Md. Alam, S. Ghosh, R. K. Singh, A. K. Ghosh, and S. Chatterjee. Wasp – Waisted loop and spin frustration in $Dy_{2-x}Eu_xTi_2O_7$ pyrochlore. *Journal of Magnetism and Magnetic Materials*, 518: 167364, 2021. ISSN 0304-8853. URL `https://doi.org/10.1016/j.jmmm.2020.167364`.

169

[93] A. S. Wills. A new protocol for the determination of magnetic structures using simulated annealing and representational analysis (SARAh). *Physica B: Condensed Matter*, 276-278: 680–681, March 2000. URL https://doi.org/10.1016/s0921-4526(99)01722-6.

[94] J.M. Perez-Mato, S.V. Gallego, E.S. Tasci, L. Elcoro, G. de la Flor, and M.I. Aroyo. Symmetry-Based Computational Tools for Magnetic Crystallography. *Annual Review of Materials Research*, 45(1):217–248, July 2015. URL https://doi.org/10.1146/annurev-matsci-070214-021008.

[95] Aroyo M.I., Perez-Mato J.M., Orobengoa D., Tasci E., De La Flor G., and Kirov A. Crystallography online: Bilbao crystallographic server. *Bulgarian Chemical Communications*, 43(2):183 – 197, 2011. URL https://www.scopus.com/inward/record.uri?eid=2-s2.0-80955140447&partnerID=40&md5=488772b9e21d2636a3952f66ae80ae84.

[96] L. Néel. Magnetism and Local Molecular Field, December 1971. URL https://doi.org/10.1126/science.174.4013.985.

[97] N. A. Anderson. *X-ray magnetic circular dichroism (XMCD) of metallic nano-structures on epitaxial graphene*. PhD thesis, 2021. URL https://doi.org/10.31274/etd-20210609-6.

[98] B. F. Decker and J. S. Kasper. The structure of calcium ferrite. *Acta Crystallographica*, 10(4):332–337, Apr 1957. URL https://doi.org/10.1107/S0365110X5700095X.

[99] O. A. Petrenko. Low-temperature magnetism in the honeycomb systems SrLn_2O$_4$ (review article). *Low Temperature Physics*, 40 (2):106–112, 2014. URL https://doi.org/10.1063/1.4865556.

[100] B. Z. Malkin, S. I. Nikitin, I. E. Mumdzhi, D. G. Zverev, R. V. Yusupov, I. F. Gilmutdinov, R. Batulin, B. F. Gabbasov, A. G. Kiiamov, D. T. Adroja, O. Young, and O. A.

Petrenko. Magnetic and spectral properties of the multisublattice oxides SrY_2O_4:Er^{3+} and $SrEr_2O_4$. *Phys. Rev. B*, 92: 094415, Sep 2015. URL https://link.aps.org/doi/10.1103/PhysRevB.92.094415.

[101] A. Fennell, V. Y. Pomjakushin, A. Uldry, B. Delley, B. Prévost, A. Désilets-Benoit, A. D. Bianchi, R. I. Bewley, B. R. Hansen, T. Klimczuk, R. J. Cava, and M. Kenzelmann. Evidence for $SrHo_2O_4$ and $SrDy_2O_4$ as model J_1-J_2 zigzag chain materials. *Phys. Rev. B*, 89:224511, Jun 2014. URL https://link.aps.org/doi/10.1103/PhysRevB.89.224511.

[102] N. Qureshi, O. Fabelo, P. Manuel, D. D. Khalyavin, E. Lhotel, S.X.M. Riberolles, G. Balakrishnan, and O. A. Petrenko. Field-induced magnetic states in geometrically frustrated $SrEr_2O_4$. *SciPost Phys.*, 11:7, 2021. URL https://scipost.org/10.21468/SciPostPhys.11.1.007.

[103] A. Togo and I. Tanaka. First principles phonon calculations in materials science. *Scripta Materialia*, 108:1–5, 2015. ISSN 1359-6462. URL https://www.sciencedirect.com/science/article/pii/S1359646215003127.

[104] The Materials Project. Materials data on $SrTm_2O_4$ by materials project, 7 2020. URL https://materialsproject.org/materials/mp-3446/.

[105] PhononDB. Phonon database at kyoto university: $SrTm_2O_4$, 2018. URL http://phonondb.mtl.kyoto-u.ac.jp/ph20180417/d003/mp-3446.html?highlight=srtm2o4.

[106] Magnetic form factors. URL https://www.ill.eu/sites/ccsl/ffacts/ffactnode1.html.

[107] P. Novák, J. Kuneš, and K. Knížek. Crystal field of rare earth impurities in LaF3. *Optical Materials*, 37:414–418, November 2014. URL https://doi.org/10.1016/j.optmat.2014.07.001.

[108] Z. Huesges, K. Kliemt, C. Krellner, R. Sarkar, H-H. Klauß, C. Geibel, M. Rotter, P. Novák, J. Kuneš, and O. Stockert. Analysis of the crystal electric field parameters of YbNi$_4$P$_2$. *New Journal of Physics*, 20(7):073021, jul 2018. URL `https://doi.org/10.1088/1367-2630/aace35`.

[109] H. Tsuchiura, T. Yoshioka, P. Novák, J. Fischbacher, A. Kovacs, and T. Schrefl. First-principles calculations of magnetic properties for analysis of magnetization processes in rare-earth permanent magnets. *Science and Technology of Advanced Materials*, 22(1):748–757, September 2021. URL `https://doi.org/10.1080/14686996.2021.1947119`.

[110] J. P. Perdew, K. Burke, and M. Ernzerhof. Generalized Gradient Approximation Made Simple. *Phys. Rev. Lett.*, 77:3865–3868, Oct 1996. URL `https://link.aps.org/doi/10.1103/PhysRevLett.77.3865`.

[111] J. Kuneš, R. Arita, P. Wissgott, A. Toschi, H. Ikeda, and K. Held. Wien2wannier: From linearized augmented plane waves to maximally localized Wannier functions. *Computer Physics Communications*, 181(11):1888–1895, nov 2010. URL `https://doi.org/10.1016%2Fj.cpc.2010.08.005`.

[112] A. A. Mostofi, J. R. Yates, G. Pizzi, Y-S. Lee, I. Souza, D. Vanderbilt, and N. Marzari. An updated version of wannier90: A tool for obtaining maximally-localised Wannier functions. *Computer Physics Communications*, 185(8):2309–2310, August 2014. URL `https://doi.org/10.1016/j.cpc.2014.05.003`.

[113] N. Magnani, G. Amoretti, A. Baraldi, and R. Capelletti. Crystal-field and superposition model analysis of :BaY f (= er, dy, nd). *The European Physical Journal B*, 29(1):79–84, September 2002. URL `https://doi.org/10.1140/epjb/e2002-00264-0`.

[114] S. Edvardsson and D. Åberg. An atomic program for energy levels of equivalent electrons: lanthanides and ac-

tinides. *Computer Physics Communications*, 133(2-3):396–406, January 2001. URL `https://doi.org/10.1016/s0010-4655(00)00171-5`.

[115] W. T. Carnall, G. L. Goodman, K. Rajnak, and R. S. Rana. A systematic analysis of the spectra of the lanthanides doped into single crystal LaF$_3$. *The Journal of Chemical Physics*, 90 (7):3443–3457, April 1989. URL `https://doi.org/10.1063/1.455853`.

[116] R. Wang, E. A. Lazar, H. Park, A. J. Millis, and C. A. Marianetti. Selectively localized Wannier functions. *Phys. Rev. B*, 90: 165125, Oct 2014. URL `https://link.aps.org/doi/10.1103/PhysRevB.90.165125`.

[117] R. Sakuma. Symmetry-adapted Wannier functions in the maximal localization procedure. *Phys. Rev. B*, 87:235109, Jun 2013. URL `https://link.aps.org/doi/10.1103/PhysRevB.87.235109`.

[118] R. Feyerherm, A. Amato, A. Grayevsky, F. N. Gygax, N. Kaplan, and A. Schenck. Crystal electric field next to a hydrogen-like interstitial— μ^+ in PrNi$_5$. *Zeitschrift für Physik B Condensed Matter*, 99(1):3–13, Mar 1995. ISSN 1431-584X. URL `https://doi.org/10.1007/s002570050002`.

[119] F. R. Foronda, F. Lang, J. S. Müller, T. Lancaster, A. T. Boothroyd, F. L. Pratt, S. R. Giblin, D. Prabhakaran, and S. J. Blundell. Anisotropic local modification of crystal field levels in pr-based pyrochlores: A muon-induced effect modeled using density functional theory. *Phys. Rev. Lett.*, 114:017602, Jan 2015. URL `https://link.aps.org/doi/10.1103/PhysRevLett.114.017602`.

[120] S. Sturniolo and L. Liborio. Computational prediction of muon stopping sites: A novel take on the unperturbed electrostatic potential method. *The Journal of Chemical Physics*, 153(4):044111, 2020. URL `https://doi.org/10.1063/5.0012381`.

[121] B. M. Huddart. *Muon stopping sites in magnetic systems from density functional theory*. PhD thesis, Durham University, 2020. URL `http://etheses.dur.ac.uk/13423/`.

[122] D. L. Quintero-Castro, B. Lake, M. Reehuis, A. Niazi, H. Ryll, A. T. M. N. Islam, T. Fennell, S. A. J. Kimber, B. Klemke, J. Ollivier, V. Garcia Sakai, P. P. Deen, and H. Mutka. Coexistence of long- and short-range magnetic order in the frustrated magnet $SrYb_2O_4$. *Phys. Rev. B*, 86:064203, Aug 2012. URL `https://link.aps.org/doi/10.1103/PhysRevB.86.064203`.

[123] N. Gauthier, A. Fennell, B. Prévost, A.-C. Uldry, B. Delley, R. Sibille, A. Désilets-Benoit, H. A. Dabkowska, G. J. Nilsen, L.-P. Regnault, J. S. White, C. Niedermayer, V. Pomjakushin, A. D. Bianchi, and M. Kenzelmann. Absence of long-range order in the frustrated magnet $SrDy_2O_4$ due to trapped defects from a dimensionality crossover. *Phys. Rev. B*, 95: 134430, Apr 2017. URL `https://link.aps.org/doi/10.1103/PhysRevB.95.134430`.

[124] O. Young, G. Balakrishnan, M. R. Lees, and O. A. Petrenko. Magnetic properties of geometrically frustrated $SrGd_2O_4$. *Phys. Rev. B*, 90:094421, Sep 2014. URL `https://link.aps.org/doi/10.1103/PhysRevB.90.094421`.

[125] J.-J. Wen, W. Tian, V. O. Garlea, S. M. Koohpayeh, T. M. McQueen, H.-F. Li, J.-Q. Yan, J. A. Rodriguez-Rivera, D. Vaknin, and C. L. Broholm. Disorder from order among anisotropic next-nearest-neighbor Ising spin chains in $SrHo_2O_4$. *Phys. Rev. B*, 91:054424, Feb 2015. URL `https://link.aps.org/doi/10.1103/PhysRevB.91.054424`.

[126] N. Qureshi, A. R. Wildes, C. Ritter, B. Fåk, S. X. M. Riberolles, M. Ciomaga Hatnean, and O. A. Petrenko. Magnetic structure and low-temperature properties of geometrically frustrated $SrNd_2O_4$. *Phys. Rev. B*, 103:134433, Apr 2021. URL `https://link.aps.org/doi/10.1103/PhysRevB.103.134433`.

174

[127] Hai-Feng Li, C. Zhang, A. Senyshyn, A. Wildes, K. Schmalzl, W. Schmidt, M. Boehm, E. Ressouche, B. Hou, P. Meuffels, G. Roth, and T. Brückel. Incommensurate antiferromagnetic order in the manifoldly-frustrated $SrTb_2O_4$ with transition temperature up to 4.28 k. *Frontiers in Physics*, 2:42, 2014. ISSN 2296-424X. URL http://journal.frontiersin.org/article/10.3389/fphy.2014.00042.

[128] O. Young, G. Balakrishnan, P. Manuel, D. D. Khalyavin, A. R. Wildes, and O. A. Petrenko. Field-Induced Transitions in Highly Frustrated $SrHo_2O_4$. *Crystals*, 9(10), 2019. ISSN 2073-4352. URL https://www.mdpi.com/2073-4352/9/10/488.

[129] T. H. Cheffings, M. R. Lees, G. Balakrishnan, and O. A. Petrenko. Magnetic field-induced ordering in $SrDy_2O_4$. *Journal of Physics: Condensed Matter*, 25(25):256001, may 2013. URL https://doi.org/10.1088/0953-8984/25/25/256001.

[130] N. Gauthier, A. Fennell, B. Prévost, A. Désilets-Benoit, H. A. Dabkowska, O. Zaharko, M. Frontzek, R. Sibille, A. D. Bianchi, and M. Kenzelmann. Field dependence of the magnetic correlations of the frustrated magnet $SrDy_2O_4$. *Phys. Rev. B*, 95: 184436, May 2017. URL https://link.aps.org/doi/10.1103/PhysRevB.95.184436.

[131] O. A. Petrenko, O. Young, D. Brunt, G. Balakrishnan, P. Manuel, D. D. Khalyavin, and C. Ritter. Evolution of spin correlations in $SrDy_2O_4$ in an applied magnetic field. *Phys. Rev. B*, 95:104442, Mar 2017. URL https://link.aps.org/doi/10.1103/PhysRevB.95.104442.

[132] J. A. M .Paddison, J. R. Stewart, and A. L. Goodwin. SPINVERT: a program for refinement of paramagnetic diffuse scattering data. *Journal of Physics: Condensed Matter*, 25(45): 454220, oct 2013. URL https://doi.org/10.1088/0953-8984/25/45/454220.

[133] J. A. M. Paddison and A. L. Goodwin. Empirical Magnetic Structure Solution of Frustrated Spin Systems. *Phys. Rev. Lett.*, 108:017204, Jan 2012. URL https://link.aps.org/doi/10.1103/PhysRevLett.108.017204.

[134] W. Schweika. XYZ-polarisation analysis of diffuse magnetic neutron scattering from single crystals. *Journal of Physics: Conference Series*, 211:012026, feb 2010. URL https://doi.org/10.1088/1742-6596/211/1/012026.

[135] J. A. M. Paddison. Ultrafast calculation of diffuse scattering from atomistic models. *Acta Crystallographica Section A*, 75(1):14–24, Jan 2019. URL https://doi.org/10.1107/S2053273318015632.

[136] M. Rotter, M. D. Le, J. Keller, L. G. Pascut, T. Hoffmann, M. Doerr, R. Schedler, F. Fabi né Hoffmann, S. Rotter, M. Banks, and N. Klüver. *McPhase - USERS MANUAL*, 2017. URL https://www2.cpfs.mpg.de/~rotter/homepage_mcphase/manual/manual.html.

[137] G. H. Wannier. Antiferromagnetism. the triangular ising net. *Phys. Rev.*, 79:357–364, Jul 1950. URL https://link.aps.org/doi/10.1103/PhysRev.79.357.

[138] A. P. Ramirez. Strongly Geometrically Frustrated Magnets. *Annual Review of Materials Science*, 24(1):453–480, 1994. URL https://doi.org/10.1146/annurev.ms.24.080194.002321.

[139] I. Affleck, T. Kennedy, E. H. Lieb, and H. Tasaki. Rigorous results on valence-bond ground states in antiferromagnets. *Phys. Rev. Lett.*, 59:799–802, Aug 1987. URL https://link.aps.org/doi/10.1103/PhysRevLett.59.799.

[140] T. Giamarchi. *Quantum Physics in One Dimension*. Oxford University Press, December 2003. URL https://doi.org/10.1093/acprof:oso/9780198525004.001.0001.

[141] Subir Sachdev. *Quantum Phase Transitions*. Cambridge University Press, 2009. URL `https://doi.org/10.1017/cbo9780511973765`.

[142] O. Golinelli, Th. Jolicoeur, and R. Lacaze. Dispersion of magnetic excitations in a spin-1 chain with easy-plane anisotropy. *Phys. Rev. B*, 46:10854–10857, Nov 1992. URL `https://link.aps.org/doi/10.1103/PhysRevB.46.10854`.

[143] J Ren, W-L You, and A M. Oleś. Quantum phase transitions in a spin-1 antiferromagnetic chain with long-range interactions and modulated single-ion anisotropy. *Phys. Rev. B*, 102:024425, Jul 2020. URL `https://link.aps.org/doi/10.1103/PhysRevB.102.024425`.

[144] V. S. Zapf, D. Zocco, B. R. Hansen, M. Jaime, N. Harrison, C. D. Batista, M. Kenzelmann, C. Niedermayer, A. Lacerda, and A. Paduan-Filho. Bose-einstein condensation of $s = 1$ nickel spin degrees of freedom in $NiCl_2 - 4SC(NH_2)_2$. *Phys. Rev. Lett.*, 96:077204, Feb 2006. URL `https://link.aps.org/doi/10.1103/PhysRevLett.96.077204`.

[145] S. A. Zvyagin, J. Wosnitza, C. D. Batista, M. Tsukamoto, N. Kawashima, J. Krzystek, V. S. Zapf, M. Jaime, N. F. Oliveira, and A. Paduan-Filho. Magnetic Excitations in the Spin-1 Anisotropic Heisenberg Antiferromagnetic Chain System $NiCl_2 - 4SC(NH_2)_2$. *Phys. Rev. Lett.*, 98:047205, Jan 2007. URL `https://link.aps.org/doi/10.1103/PhysRevLett.98.047205`.

[146] T. Giamarchi, C. Rüegg, and O. Tchernyshyov. Bose–einstein condensation in magnetic insulators. *Nature Physics*, 4(3):198–204, Mar 2008. ISSN 1745-2481. URL `https://doi.org/10.1038/nphys893`.

[147] J. Jensen. Spin fluctuations in a spin-1 paramagnet with easy-planar anisotropy: Application to praseodymium. *Journal of Physics C: Solid State Physics*, 15(11):2403–2415, apr

1982. URL `https://doi.org/10.1088/0022-3719/15/11/020`.

[148] A. Abragam and B. Bleaney. Enhanced nuclear magnetism: some novel features and prospective experiments. *Proceedings of the Royal Society of London. A. Mathematical and Physical Sciences*, 387(1793):221–256, 1983. URL `https://royalsocietypublishing.org/doi/abs/10.1098/rspa.1983.0059`.

[149] B. Bleaney. Enhanced nuclear magnetism. *Physica*, 69(1):317–329, 1973. ISSN 0031-8914. URL `https://doi.org/10.1016/0031-8914(73)90224-3`.

[150] F. Foronda. *Muon spin spectroscopy and high magnetic field studies of novel superconductors and magnetic materials*. PhD thesis, University of Oxford, 2017. URL `https://ora.ox.ac.uk/objects/uuid:55c7ed6b-af31-4b7b-8b64-217dcc6846ac`.

[151] C. Fermon, J.F. Gregg, J.-F. Jacquinot, Y. Roinel, V. Bouffard, G. Fournier, and A. Abragam. « enhanced » magnetism and nuclear ordering of 169Tm spins in $TmPO_4$. *Journal de Physique*, 47(6):1053–1075, 1986. URL `https://doi.org/10.1051/jphys:019860047060105300`.

[152] B. Bleaney, J. F. Gregg, C. H. A. Huan, I. D. Morris, and M. R. Wells. Further Studies of the Enhanced Nuclear Magnet $TmPO_4$. *Proceedings of the Royal Society of London. Series A, Mathematical and Physical Sciences*, 424(1867):245–254, 1989. ISSN 00804630. URL `http://www.jstor.org/stable/2398366`.

[153] D. D. Khalyavin, D. T. Adroja, P. Manuel, A. Daoud-Aladine, M. Kosaka, K. Kondo, K. A. McEwen, J. H. Pixley, and Qimiao Si. Field-induced long-range magnetic order in the spin-singlet ground-state system $YbAl_3C_3$: Neutron diffraction study. *Phys. Rev. B*, 87:220406, Jun 2013. URL `https://link.aps.org/doi/10.1103/PhysRevB.87.220406`.

[154] G. Hester, H. S. Nair, T. Reeder, D. R. Yahne, T. N. DeLazzer, L. Berges, D. Ziat, J. R. Neilson, A. A. Aczel, G. Sala, J. A. Quilliam, and K. A. Ross. Novel Strongly Spin-Orbit Coupled Quantum Dimer Magnet: $Yb_2Si_2O_7$. *Phys. Rev. Lett.*, 123: 027201, Jul 2019. URL `https://link.aps.org/doi/10.1103/PhysRevLett.123.027201`.

[155] M. Bałanda. AC Susceptibility Studies of Phase Transitions and Magnetic Relaxation: Conventional, Molecular and Low-Dimensional Magnets. *Acta Physica Polonica A*, 124(6):964–976, December 2013. URL `https://doi.org/10.12693/aphyspola.124.964`.

[156] C. V. Topping and S. J. Blundell. A.c. susceptibility as a probe of low-frequency magnetic dynamics. *Journal of Physics: Condensed Matter*, 31(1):013001, nov 2018. URL `https://doi.org/10.1088/1361-648x/aaed96`.

[157] V. Petříček, M. Dušek, and L. Palatinus. Crystallographic Computing System JANA2006: General features. *Zeitschrift für Kristallographie - Crystalline Materials*, 229(5): 345–352, April 2014. URL `https://doi.org/10.1515/zkri-2014-1737`.

[158] A. Ochiai, T. Inukai, T. Matsumura, A. Oyamada, and K. Katoh. Spin Gap State of S = 1/2 Heisenberg Antiferromagnet $YbAl_3C_3$. *Journal of the Physical Society of Japan*, 76(12): 123703, 2007. URL `https://doi.org/10.1143/JPSJ.76.123703`.

[159] Y. Kato, M. Kosaka, H. Nowatari, Y. Saiga, A. Yamada, T. Kobiyama, S. Katano, K. Ohoyama, H. S. Suzuki, N. Aso, and K. Iwasa. Spin-Singlet Ground State in the Two-Dimensional Frustrated Triangular Lattice: $YbAl_3C_3$. *Journal of the Physical Society of Japan*, 77(5):053701, 2008. URL `https://doi.org/10.1143/JPSJ.77.053701`.

[160] N. F. Berthusen, Y. Sizyuk, M. S. Scheurer, and P. P. Orth. Learning crystal field parameters using convolutional neural net-

works. *SciPost Phys.*, 11:11, 2021. URL `https://scipost.org/10.21468/SciPostPhys.11.1.011`.